

---

INVESTIGATION OF THE  
NONLINEAR OPTICAL PROPERTIES OF METAMATERIALS  
BY SECOND HARMONIC GENERATION

---

Dissertation  
zur  
Erlangung des Doktorgrades (Dr. rer. nat.)  
der  
Mathematisch-Naturwissenschaftlichen Fakultät  
der  
Rheinischen Friedrich-Wilhelms-Universität Bonn

vorgelegt von  
  
Mathieu Julien Gentile  
aus Saint-Etienne, Frankreich

Bonn, August 2013



Angefertigt mit Genehmigung der Mathematisch-Naturwissenschaftlichen Fakultät der Rheinischen Friedrich-Wilhelms-Universität Bonn

Bonn, August 2013

1. Gutachter: Prof. Dr. Manfred Fiebig  
2. Gutachter: Prof. Dr. Karl Maier

Tag der Promotion: 2013-09-23  
Erscheinungsjahr: 2013



A mes grands-parents,  
mes parents,  
et, je l'espère, mes futurs enfants.



Dans beaucoup de choix de la vie, il est difficile de savoir la part de la réaction contre et de l'inclination pour.

---

Pierre Bourdieu

Work like hell, tell everyone everything you know, close a deal with a handshake, and have fun.

---

Harold Edgerton



# Contents

<b>List of Figures</b>	<b>xiii</b>
<b>List of Tables</b>	<b>xvii</b>
<b>Acknowledgments</b>	<b>xix</b>
<b>Abstract</b>	<b>xxi</b>
<b>Introduction</b>	<b>1</b>
<b>1 Linear Optics Principles for Metallic Nanostructures</b>	<b>5</b>
1.1 Maxwell's Equations in Matter . . . . .	5
1.2 Dielectric Properties of Gold . . . . .	8
1.3 Optics of Metallic Nanostructures . . . . .	11
1.3.1 Particle Plasmon Classical Model . . . . .	12
1.3.2 Optical Manifestations: Scattering and Absorption . . . . .	16
1.3.3 Particle Plasmons Lifetime: Damping Mechanisms . . . . .	18
<b>2 Perturbative Nonlinear Optics</b>	<b>25</b>
2.1 Second Harmonic Generation . . . . .	25
2.2 Two-Photon Photoluminescence . . . . .	30
<b>3 Experimental Methods</b>	<b>33</b>
3.1 Samples . . . . .	33
3.1.1 Fabrication: Electron Beam Lithography . . . . .	33
3.1.2 Nonlinear Characterization: Nanostructured Gold on Glass . . . . .	36
3.1.3 Gold Nanostructures: SHG Tensor Components . . . . .	38
3.1.4 Nonlinear Optical Catalyst: Gold Nanowires on SHG Active Crystals . . . . .	43

3.1.5	<i>RMnO<sub>3</sub></i> and <i>Cr<sub>2</sub>O<sub>3</sub></i> : SHG Tensor Components . . . . .	47
3.2	Linear Characterization . . . . .	51
3.3	Laser System . . . . .	51
3.3.1	Regenerative Amplifier (RGA) . . . . .	52
3.3.2	Auto-Correlation Measurement . . . . .	53
3.3.3	Optical Parametric Amplifier (OPA) . . . . .	55
3.4	Optical Setup for SHG Spectroscopy . . . . .	58
3.5	Optical Setup for AFM Domain Topography . . . . .	61
3.6	Signal Normalization . . . . .	61
3.7	Sample Damage . . . . .	63
<b>4</b>	<b>Results and Discussion</b>	<b>65</b>
4.1	Linear Characterization . . . . .	65
4.1.1	Nanostructures on Glass . . . . .	65
4.1.2	Nanowires on Nonlinear Crystals and Glass . . . . .	68
4.2	Nonlinear Measurements . . . . .	70
4.2.1	SHG Character of the Emitted Light . . . . .	70
4.2.2	Bulk Material Nonlinear Spectroscopy . . . . .	72
4.2.3	SHG Characterization . . . . .	73
Size Effects: Spectral Dependence . . . . .	73	
Shape Effects: Geometrical Feature Dependence . . . . .	74	
Symmetry Effects: Interferences Dependence . . . . .	76	
Reproducibility Issues . . . . .	77	
4.2.4	SHG Amplification . . . . .	82
Functionality: AFM Measurements . . . . .	82	
Mechanism: FEL Measurements in <i>RMnO<sub>3</sub></i> . . . . .	85	
Mechanism: MD Contribution in <i>Cr<sub>2</sub>O<sub>3</sub></i> . . . . .	88	
Mechanism: Nanowires On Amorphous Glass . . . . .	92	
Near-Field Model Nanowire Model . . . . .	94	
	<b>Conclusion and Outlook</b>	<b>101</b>
<b>A</b>	<b>Spectra</b>	<b>103</b>
A.1	Linear Spectra . . . . .	103

## CONTENTS

---

A.2 $R\text{MnO}_3$ Reference SHG Spectra . . . . .	112
A.3 $\text{Cr}_2\text{O}_3$ Reference SHG Spectra . . . . .	113
<b>B Mathematica 8 Notebooks</b>	<b>115</b>
B.1 $\text{Cr}_2\text{O}_3$ SHG Model . . . . .	115
B.2 Nanowire-Mediated SHG Amplification Model . . . . .	116
<b>Bibliography</b>	<b>121</b>
<b>Publications and Presentations</b>	<b>135</b>
<b>Curriculum Vitae</b>	<b>137</b>



# List of Figures

1.1	Dielectric Function for Gold Versus Photon Energy . . . . .	10
1.2	Details of the Band Structure of Gold Near the Fermi Energy . . . . .	11
1.3	Skin Depth for Gold Versus Photon Energy . . . . .	12
1.4	Localized Surface Plasmon Formation in a Metallic Nanoparticle . . . . .	14
1.5	Time and Frequency Profile of a Damped Oscillation . . . . .	19
1.6	Decay Channels for a Particle-Plasmon . . . . .	20
1.7	Structure Size Dependence of the Plasmonic Resonance Position and Linewidth	22
2.1	Schematic Illustration of the SHG Process . . . . .	26
3.1	Fabrication Steps of the Electron Beam Lithography Process . . . . .	34
3.2	Geometry of the Building Blocks for the Investigated Metamaterials . . . . .	36
3.3	Normal Incidence SEM Micrographs of Gold Nanostructures on Glass . . . . .	38
3.4	Symmetry Elements of the Investigated Nanostructures . . . . .	39
3.5	Electric Field Amplification Mediated by a Plasmonic Wire . . . . .	44
3.6	Optical Layout for Chirped Pulse Amplification . . . . .	52
3.7	Optical Layout for the Autocorrelator . . . . .	54
3.8	Optical Layout for the Optical Parametric Amplifier . . . . .	56
3.9	Energy Spectrum of the Optical Parametric Amplifier (TOPAS-C Unit) . . . . .	57
3.10	Optical Layout for Nonlinear Spectroscopy . . . . .	59
3.11	Normalization Functions . . . . .	62
4.1	Linear Plasmonic Resonances for the Gold Nanostructures on Glass . . . . .	66
4.2	Electric Field Distribution Within and Around the Nanostructures . . . . .	67
4.3	Oblique Incidence SEM Micrographs of Gold Nanostructures on Glass . . . . .	67
4.4	Electric Field Distribution Within and Around a Gold Nanowire . . . . .	69

4.5	Oblique Incidence SEM Micrographs of Gold Nanostructures on $\text{Cr}_2\text{O}_3$ . . . . .	69
4.6	Linear Plasmonic Resonances for Gold nanowires on a Nonlinear Crystal . . . . .	69
4.7	Resonance Features of Nanowire Field Pairs on $\text{Cr}_2\text{O}_3$ . . . . .	70
4.8	Resonance Features of Nanowire Fields on Glass . . . . .	70
4.9	SHG Signal Intensity Versus Fundamental Intensity . . . . .	71
4.10	Monochromaticity of the Measured Signals . . . . .	71
4.11	Emission Polarization Anisotropy of the Measured Signals . . . . .	71
4.12	Normalized SHG Spectrum of a Plain Gold Film Illuminated at $45^\circ$ Incidence . .	72
4.13	Normalized SHG Spectra Comparison of Three Similar U-Shaped Metamaterials	74
4.14	SHG Spectra for a Variety of Metamaterial Designs . . . . .	75
4.15	SHG Acquisition Reproducibility on a U-Shaped Metamaterial Field . . . . .	77
4.16	Optical Microscope Inspection of a Damaged Metamaterial Field . . . . .	78
4.17	Normal Incidence SEM Micrographs of Damaged Gold Nanostructures on Glass	79
4.18	Alteration of the Linear Spectra After Laser Illumination . . . . .	79
4.19	Resistivity of Usual Plasmonic Metals Versus Temperature . . . . .	80
4.20	Optically-Induced Damage Observed on a PMMA-Impregnated Sample . . . . .	80
4.21	Antiferromagnetic Domain Topography of a Nanopatterned $\text{Cr}_2\text{O}_3$ Surface . . .	82
4.22	AFM SHG Anisotropies on $\text{RMnO}_3$ : Model versus Experiment . . . . .	84
4.23	SHG Signals Versus Temperature from (Un)Structured $\text{HoMnO}_3$ . . . . .	85
4.24	FEL SHG Anisotropies on $\text{RMnO}_3$ . . . . .	86
4.25	SHG Amplification Spectra from Metamaterial Fields Relative to the Bare Crystal	88
4.26	Normalized Anisotropy from Nanostructured Fields on $\text{Cr}_2\text{O}_3$ . . . . .	89
4.27	SHG Signal Spectral Correlation with the Linear Plasmonic Resonance . . . . .	89
4.28	SHG Strength and Contrast under Circular Polarization Excitations . . . . .	92
4.29	Normalized SHG Spectra from Nanowires on Glass . . . . .	93
4.30	SHG Strength versus Plasmonic Resonance for Nanowires on Glass . . . . .	93
4.31	Spatial Distribution of the Plasmonic Electric Field Around a Nanowire . . . . .	95
4.32	Dark Field Acquisition of a Nanostructured Field on $\text{Cr}_2\text{O}_3$ . . . . .	99
A.1	U-Shaped Metamaterial Linear Spectra vs Driving Light Polarization. . . . .	103
A.2	L-Shaped Metamaterial Linear Spectra vs Driving Light Polarization. . . . .	104
A.3	C-Shaped Metamaterial Linear Spectra vs Driving Light Polarization. . . . .	105
A.4	I-Shaped Metamaterial Linear Spectra vs Driving Light Polarization. . . . .	106

A.5 Z-Shaped Metamaterial Linear Spectra vs Driving Light Polarization. . . . .	107
A.6 Linear Spectra Sample DMF12 FZ YbMnO <sub>3</sub> , Field Homogeneity and Resonance Polarization Dependence . . . . .	108
A.7 Linear Spectra Sample DMF13 FG HoMnO <sub>3</sub> . . . . .	108
A.8 Linear Spectra Sample DMF15 FG YbMnO <sub>3</sub> . . . . .	108
A.9 Linear Spectra Sample DMF16 FZ YbMnO <sub>3</sub> . . . . .	109
A.10 Linear Spectra Sample DMF18 Cr <sub>2</sub> O <sub>3</sub> . . . . .	110
A.11 Linear Spectra Sample Wires on Glass . . . . .	111
A.12 <i>i</i> -Tensor SHG Contributions in YMnO <sub>3</sub> . . . . .	112
A.13 <i>c</i> -Tensor SHG Contributions in RMnO <sub>3</sub> . . . . .	112
A.14 <i>i</i> - and <i>c</i> -Tensor SHG Contributions in Cr <sub>2</sub> O <sub>3</sub> . . . . .	113



# List of Tables

3.1	Allowed Tensor Components for the Nanostructures on Glass . . . . .	40
3.2	Polarizing Optics Configurations for Accessible Tensor Components . . . . .	43
3.3	Allowed Tensor Components in $R\text{MnO}_3$ . . . . .	48
3.4	Allowed Tensor Components in $\text{Cr}_2\text{O}_3$ . . . . .	49
3.5	Spectral Output Ranges and Polarizations of the OPAs, Corresponding Filters . .	57
4.1	Plasmonic Wire Amplification Truth Table . . . . .	96



# Acknowledgments

The completion of this work has been only possible with the help, assistance, and support from a number of people. It is my pleasure to pay due to them at least in form of these words. I humbly acknowledge the breadth of perspective, knowledge, and experience that I have gained professionally, culturally, and personally.

For giving me the opportunity to work in his group and providing financial support, I would like to thank Prof. Dr. Manfred Fiebig. Also, I express my sincere gratitude to Prof. Dr. Karl Maier for kindly agreeing to co-referee this thesis, for his valuable tips, and for very interesting discussions about and beyond Physics. I am glad I could have a particular connection to his group, and that he always kept his door opened. I also thank Prof. Dr. Carsten Urbach and Prof. Dr. Moritz Sokolowski for being part of the examination board.

For providing access to his impressive group's resources, both material and human, I would like to thank Prof. Dr. Harald Giessen, from the University of Stuttgart. In particular, Dr. Mario Hentschel made decisive contributions, mastering the production of nanostructured samples. I kindly remember his time in our group, soon followed by a real appreciation of his sharing knowledge in a very efficient way from Stuttgart. Also, it has been a pleasure to work with Dr. Hongcang Guo, Dr. Richard Taubert and Bernd Metzger.

My appreciation goes to the members of the Hikari group at the University of Bonn. For their decisive contributions in fruitful work, I want to thank in particular Carsten Becher, Dr. Tim Hoffmann and Dr. Andrea Rubano. It has been a great pleasure to have daily interactions with them. They have always been present whenever I needed them, with answers, advices, encouragements, and actions. Also besides Physics, I have learned so much.

Likewise, I very much enjoyed the dynamics and nice atmosphere of the Maier group. They welcomed me as one of them. There, I always found a lively group of helpful people, eventually gathering around something delicious, or for a weekly badminton play, and, last but not least, for interesting discussions about Physics, or pretty much anything else. Sharing was key. I am glad I could come and take my mind off things.

Further thanks go to all members of the workshops, as well as the IT and administrative departments. They always helped me swiftly in a friendly and professional way. Although I am bound to forget some names, I would like to cite, for the mechanical workshop: Stefan Birkenbach, Hermann-Josef Eichler, Bert Kann, Josef Klaes, Dirk Lenz, Jörg Seul; for the electrical workshop: Albrecht D'Hein, Martin Kerp, Detlef Wolf; for the polishing workshop: Ulrich Böhning and, in Cologne, Max Baum and Luis Fels; for the IT and administrative organization:

Angela Anderson, Margret Balci, Andrea Kehr, Dr. Michel Lang, Armin Leiendecker, Dr. Gunnar Mertler, Barbara Mosblech, Mechthild Paus, Dr. Konrad Peithmann and, with a special thought, Claudia Seifert.

My thanks would not be complete if I did not mention my friends and family who have supported me along the way.

Je mesure la chance qui est la mienne d'avoir de tels parents. Mieux que quiconque, ils ont su me prodiguer les meilleurs conseils qui soient, ainsi qu'un confort affectif et matériel de chaque instant. Ils ont été un phare, alors même qu'au fur et à mesure de mes études je m'avançais en *terra incognita*. Ce travail est plus à leur honneur qu'au mien. Nul n'est besoin d'un quelconque titre pour être un modèle.

Enfin, je n'oublie pas ma "mie" Jessica, elle aussi toujours présente, aimante et prévoyante.

Je pense à *Nous* et suis heureux et confiant.

# Abstract

Metamaterials have attracted tremendous attention in the past decade because they allow researchers to engineer new optical properties by *designing* a new optical material. In particular, metamaterials are regarded as the key technology paving the way to an optical revolution, from medical applications to all-optical networks.

Metamaterials are sub-wavelength metallic nanostructures which owe their optical properties to the formation of a so-called *plasmon*, or collective electron oscillation. Each nanostructure can be regarded as a meta-atom forming an homogeneous optical material whose optical resonance features depend on three main parameters: The shape of the nanostructure, and the dielectric functions of both the material used and the surrounding environment.

Even though the nonlinear optical features are bound to play a central role for future applications, the underlying light conversion process has been unknown up to now. Moreover, hardly any of the plasmonic features found yet its way to an actual application.

In the present work, one makes use of the symmetry sensitivity and spectral information carried in the nonlinear process of second harmonic generation (SHG). Two types of investigations are carried out: First, gold nanostructures sharing symmetry feature variations are investigated to *characterize* the SHG in metamaterials. Second, simple gold nanowires are used to pattern the surface of an SHG-active host to investigate their *application* as an optical catalyst enhancing the SHG yield of the underlying crystal.

For the first time, broad SHG spectra are recorded from a variety of nanostructures sharing geometrical features. SHG is measured even from nanostructures described as centrosymmetric, or from tensor components expected to be symmetry forbidden. This work provides valuable insights into the potential role played by nanoscopic surface defects and irregularities resulting from the top-down electron-beam lithography (EBL) fabrication process.

The amplification model developed for the concept of an optical catalyst proves not to be sophisticated enough to fully explain the recorded SHG results. However, nanostructures fabricated on the surface of  $\text{RMnO}_3$  and  $\text{Cr}_2\text{O}_3$  crystals display tweaked SHG features with respect to the known features from these nonlinear model systems. This is a clear indication of convolutions of the plasmonic process with a sample-specific response. Although the exact process could not be pinpointed, a certain dependence of the SHG yield on the environment of the nanowires has been highlighted and requires to take a closer look in future investigations.



# Introduction

Metallic nanoparticles are known to mediate unusual optical properties since the ancient times of the late Roman Empire at least. This is attested by the Lycurgus Cup whose glass is made dichroic by tiny amounts of colloidal gold and silver [1]. The process has also been used e.g. in the colorful windows of medieval churches [2] despite the lack of a deeper physical understanding at the time. Partial explanation came in the last century only with the pivotal work of Mie [3] later allowing to interpret the underlying process as a particle plasmon mechanism: The illumination by light leads to plasmonic oscillations, i.e. coherent collective oscillations of the free electrons in the conduction band of the metal. Decades later, it was realized that these plasmonic excitations can be exploited to tailor the macroscopic optical properties nearly at will by controlling the nanostructures' design to form so-called *metamaterials*.

From initial theoretical investigations [4] to conceptual breakthrough [5] and actual realization [6] the concept of electromagnetic metamaterials is revolutionizing the field of optics. As for the examples above, they are composed of metallic building blocks with a size much smaller than the operating wavelength of the light [7–10]. The subwavelength period distinguishes metamaterials from photonic crystal structures whose special optical properties arise from photonic bandgaps. For metamaterials, optical features arise from a subwavelength interaction with the light spectrum, which mimics atoms or ions. The working range extends from microwaves and millimeter-sized designs, to the optical range with structures a few hundreds of nanometers large, typically fabricated in a top-down approach by electron beam lithography with gold on glass [11]. Tailored electromagnetic functionalities are obtained by controlling not only the dielectric function of the metal and of the surrounding environment, but also the size and shape of the nanoscaled building blocks [12, 13]. A variety of shapes has been employed: From simple spheres and ellipsoids to wires [14, 15], split-ring resonator (SRR) designs [5, 16], meshes [17, 18], meanders [19, 20], or swiss-rolls [5, 7]. Thus, in addition to exploiting the broad variety of materials provided by nature, researchers can now *engineer* new optical properties *by design*.

A wealth of features not found in nature has been proposed. For instance, a negative magnetic permeability  $\mu$  [5, 14–16, 21] along with a negative electric permittivity  $\epsilon$  [22] lead to metamaterials in which the refractive index can become negative [8, 10]. In terms of application, these astonishing properties could lead to novel devices such as optical cloaks rendering objects invisible e.g. to radar systems [23–26] or so-called perfect lenses beating the Abbe diffraction limit [27–29]. The strong spatial concentration of the electromagnetic radiation in the vicinity of the nanostructures allows for small volume sensing applications [30, 31] and improved data

storage [32]. Acting as nanoantennae, metamaterials can couple light to single molecules [33] or quantum dots [34, 35]. Nanostructures are also used in targeted cancer treatments [36] and solar catalysis to deliver high-yield photovoltaic panels [37, 38]. Similar to the electronic revolution of the last decades based on electronic components, metamaterials are promised a leading role in a broad panel of applications as the future building blocks of an optical revolution [39, 40]. Yet, despite the numerous applications and the control of the linear macroscopic optical properties, many applications will not triumph unless a deeper understanding of the microscopic effects is reached. In particular, the nonlinear optical responses are hardly understood so far, yet are essential to e.g. all-optical telecommunication networks [41, 42].

Nonlinear optics, in particular the lowest-order process of second harmonic generation (SHG) offers a variety of advantages in comparison to its linear counterpart. It constitutes an improved characterization tool [43–47]: Nonlinear optical processes reveal novel information about materials. Based on the involvement of more than a single light field, additional experimental degrees of freedom are available. New states become accessible by multiphoton transitions. Through its higher selectivity (in terms of photon energy, wavevector, and light polarization) nonlinear optical spectroscopy is a key for identifying the microscopic processes at play in a material. Also, the high intensity of the light fields involved in nonlinear optical excitations can lead to a modification of the optical properties of the material and thus result in new functionalities.

Hence, nonlinear optics is a powerful tool for the characterization as well as for the functional use of materials. Yet its application to the investigation of metamaterials remained quiescent for quite some time. No experimental reports or suggestions for a consistent microscopic theory of the nonlinear optical properties of metamaterials was reported before the work of Klein et al. [48, 49]. In this pioneering work, the nonlinear response of SRRs was experimentally investigated and a microscopic description based on a Lorentz force model was proposed. Since measurements were carried out at a fixed excitation frequency and limited to a single type of structure, the access to the microscopic mechanisms determining the nonlinear optical response of metamaterials remained limited. Aside from spectroscopy and shape variation, the interaction between the individual “meta-atoms” was not considered [50, 51]. Thus, the debate on the nonlinear optical performance of metamaterials remains a wide open field of research [52–58]. A variety of sources has been proposed to explain the optical nonlinearities, e.g. bulk and surface effects in the metal [59, 60] or plasmon-mediated field enhancement in the vicinity of the metamaterial [61]. As for the linear features, resonance effects and the nanostructures’ shape are expected to play an essential role [48].

It is the aim of this work to use SHG spectroscopy as a tool to investigate the nonlinear optical response of metamaterials in two complementary ways. On the one hand, the nonlinear optical performance is *characterized* by performing SHG spectroscopy on a variety of metamaterials differing in size, shape, and symmetry. On the other hand, the nonlinear optical performance is *applied* for manipulating the nonlinear optical response of the host system (substrate) onto which the metamaterials are deposited. Insights into the potential of metamaterials are gained in both cases, but a clear need to continue the experiments for obtaining a comprehensive picture of metamaterials as nonlinear medium is also acknowledged and guidelines are provided for a model system dissipating challenges encountered in this work.

Chapter 1 provides an introduction to the linear optics of metals at the nanometer scale. Starting with Maxwell's equations, it is shown how metamaterials differ from bulk gold and how a classical harmonic oscillator model suitably explains the main principles. Plasmon formation and decay are described, together with their relation to absorption and scattering properties.

Chapter 2 goes beyond the harmonic oscillator model and introduces the principles of SHG. The usual electric dipole approximation is extended to the first order expansion of the electromagnetic field, where magnetic dipole and electric quadrupole are present. The signature features of SHG are introduced, allowing other similar processes such as two photon photoluminescence to be differentiated from.

The focus of chapter 3 is to introduce the experimental methods used in this work. Both the samples and the setup are described. An insight into the electron beam lithography is given as a sample production method. For the metamaterial characterization, the design of the split ring resonator variations are justified and an SHG tensor component analysis is carried out based on their symmetry. For the application of metamaterials, the same is done for nanowires on a nonlinear crystal. Both host systems, hexagonal  $RMnO_3$  ( $R = Sc, Y, Dy-Lu$ ) and  $Cr_2O_3$ , are introduced together with their nonlinear features. Given its importance in allowing a proper characterization, the laser system is detailed, together with the normalization procedure.

Chapter 4 gathers the initial linear characterization and the SHG results. First, the SHG character of the measured light is verified and compared to that obtained from bulk gold. Then, the experimental results for the *characterization* and *application* of these metamaterials are discussed in section 4.2.3 and section 4.2.4, respectively.



# Chapter 1

## Linear Optics Principles for Metallic Nanostructures

In this section, the basic equations governing the electromagnetic response are recalled, based on the macroscopic Maxwell's equations. This is followed by an elementary description of the optical properties of metals via their plasmonic properties.

### 1.1 Maxwell's Equations in Matter

Maxwell's equations describe the evolution of electromagnetic fields in space and time in the presence of currents, charges, and matter. However, these equations are of limited use by themselves: Relations describing the response of the materials involved are needed. To do so, it is valuable to distinguish between external fields and fields induced by the material response when describing the interaction with matter. In the international unit system (SI), Maxwell's equations are expressed as follows.

$$\begin{aligned} (a) \quad \nabla \cdot \mathbf{D} &= \rho_{\text{ext}} & (b) \quad \nabla \cdot \mathbf{B} &= 0 \\ (c) \quad \nabla \times \mathbf{E} &= -\frac{\partial \mathbf{B}}{\partial t} & (d) \quad \nabla \times \mathbf{H} &= \frac{\partial \mathbf{D}}{\partial t} + \mathbf{J}_{\text{ext}} \end{aligned} \quad (1.1)$$

Here, the total electric charge density  $\rho$  and current density  $\mathbf{J}$  are separated into a driving set  $(\rho_{\text{ext}}, \mathbf{J}_{\text{ext}})$  external to the system being considered, and a responding internal set  $(\rho, \mathbf{J})$  [62].

$$\rho_{\text{tot}} = \rho + \rho_{\text{ext}} \quad \mathbf{J}_{\text{tot}} = \mathbf{J} + \mathbf{J}_{\text{ext}} \quad (1.2)$$

Then, a constitutive relation relates the electric displacement  $\mathbf{D}$  with the driving electric field  $\mathbf{E}$  and the local electric polarization  $\mathbf{P}$ . Similarly, the magnetic induction  $\mathbf{B}$  is related to the magnetic field  $\mathbf{H}$  and the local magnetization  $\mathbf{M}$ .

$$\mathbf{D} = \epsilon_0 \mathbf{E} + \mathbf{P} \quad \mathbf{B} = \mu_0 (\mathbf{H} + \mathbf{M}) \quad (1.3)$$

where the constants  $\varepsilon_0 = 8.8542 \times 10^{-12} \text{AsV}^{-1} \text{m}^{-1}$  and  $\mu_0 = 4\pi \times 10^{-7} \text{VsA}^{-1} \text{m}^{-1}$  are the permittivity and permeability of the vacuum, respectively.

The polarization  $\mathbf{P}$  describes the electric dipole moment per unit volume inside the material caused by the alignment of microscopic dipoles with the electric field.  $\mathbf{P}$  is related to the internal charge density and current densities via the charge conservation law  $\nabla \cdot \mathbf{J} = -\partial\rho/\partial t$ .

$$\rho = -\nabla \cdot \mathbf{P} \qquad \mathbf{J} = \frac{\partial \mathbf{P}}{\partial t} \qquad (1.4)$$

Last constitutive relation, the internal current density is related to the electric field, in a generalization of Ohm's law, introducing the conductivity  $\sigma$ .

$$\mathbf{J} = \sigma \mathbf{E} \qquad (1.5)$$

With this approach, the macroscopic electric field includes both the external and the induced field's polarization effects. This is shown in combining equation (1.1)(a) with the expression of the electric displacement in equation (1.3) leading to  $\nabla \cdot \mathbf{E} = \rho_{\text{tot}}/\varepsilon_0$ .

The material properties are phenomenologically introduced. In linear optics, the electric polarization is proportional to the electric field, and similarly with the magnetization being proportional to the magnetic field,

$$\mathbf{P} = \varepsilon_0 \chi \mathbf{E} \qquad \mathbf{M} = \chi_M \mathbf{H} \qquad (1.6)$$

where  $\chi$  and  $\chi_M$  are the linear electric susceptibility tensor and the linear magnetic susceptibility tensor of an instantaneously reacting medium, respectively. Therefore, the electric displacement and magnetic induction can be rewritten to account for the medium relative permittivity  $\varepsilon_r$ , also known as dielectric constant, and relative permeability  $\mu_r$ .

$$\mathbf{D} = \varepsilon_0 \varepsilon_r \mathbf{E} \qquad \mathbf{B} = \mu_0 \mu_r \mathbf{H} \qquad (1.7)$$

$\varepsilon_r = 1 + \chi$ , and  $\mu_r = 1 + \chi_M$  are generally tensors owing to the symmetry properties of the medium under consideration: They reduce to a scalar value in an isotropic medium only. Also, natural media never exhibit magnetic responses at optical frequency and hence present a unitary relative permeability,  $\mu_r = 1$ . For the sake of simplicity, only isotropic media with unit relative permeability are treated in this section.

Equations (1.5) and (1.7) are only valid for linear media that do not exhibit temporal or spatial dispersion. One has to account for the *non-locality* in time and space by generalizing the linear relationships. In other words,  $\mathbf{D}(t)$  at time  $t$  depends not only on the electric field  $\mathbf{E}$  at that moment, but also on the value of  $\mathbf{E}$  at all past times and similarly with space [63].

$$\mathbf{D}(\mathbf{r}, t) = \varepsilon_0 \iint \varepsilon_r(\mathbf{r} - \mathbf{r}', t - t') \mathbf{E}(\mathbf{r}', t') d\mathbf{r}' dt' \qquad (1.8)$$

$$\mathbf{J}(\mathbf{r}, t) = \iint \sigma(\mathbf{r} - \mathbf{r}', t - t') \mathbf{E}(\mathbf{r}', t') d\mathbf{r}' dt' \qquad (1.9)$$

$\varepsilon_r$  and  $\sigma$  describe the impulse response of the respective linear relationship. All length scales are assumed much larger than the lattice spacing. This ensures homogeneity, i.e. the impulse

response functions do not depend on the absolute spatial or temporal coordinate, but only on their differences.

The above equations simplify by taking the Fourier transform with respect to  $\int e^{i(\mathbf{k}\cdot\mathbf{r}-\omega t)} dt$ , turning convolutions into multiplications. Thus, the fields are decomposed into individual plane-waves of wave vector  $\mathbf{k}$  and angular frequency  $\omega$ . The resulting negative frequency components carry the same information as the positive ones and are left unaccounted for. The constitutive relations in the frequency domain follow:

$$\mathbf{D}(\mathbf{k}, \omega) = \varepsilon_0 \varepsilon_r(\mathbf{k}, \omega) \mathbf{E}(\mathbf{k}, \omega) \quad \mathbf{J}(\mathbf{k}, \omega) = \sigma(\mathbf{k}, \omega) \mathbf{E}(\mathbf{k}, \omega) \quad (1.10)$$

and one can show that the generally complex functions  $\varepsilon$  and  $\sigma$  are related by

$$\varepsilon_r(\mathbf{k}, \omega) = 1 + \frac{i\sigma(\mathbf{k}, \omega)}{\varepsilon_0 \omega} = \varepsilon_1(\omega) + i\varepsilon_2(\omega) \quad . \quad (1.11)$$

When considering the interaction of light with metallic nanostructures, the general form of the dielectric constant is simplified to the limit of a *spatially local* response,  $\varepsilon_r(\mathbf{k} = \mathbf{0}, \omega) = \varepsilon_r(\omega)$ . This simplification is valid with any material as long as the wavelength  $\lambda$  in the material is significantly longer than any characteristic dimension such as the size of the unit cell or the mean free path (MFP) of the electrons.

The complex values of  $\varepsilon_r(\omega)$  describe the amount of polarization and the energy dissipation of the material, respectively. They are related to the complex refractive index  $\tilde{n} = \sqrt{\varepsilon_r} = n + i\kappa$ .

$$n = \frac{1}{\sqrt{2}} \sqrt{\varepsilon_1 + \sqrt{\varepsilon_1^2 + \varepsilon_2^2}} \quad \kappa = \frac{\varepsilon_2}{2n} = \frac{1}{\sqrt{2}} \sqrt{-\varepsilon_1 + \sqrt{\varepsilon_1^2 + \varepsilon_2^2}} \quad (1.12)$$

Although not written explicitly, each term is frequency dependent.  $\kappa$  is the extinction coefficient that determines the optical absorption of an electromagnetic wave in a medium. Therefore it is linked to the absorption coefficient of Beer's law,  $\alpha = 2\kappa/c$ . Thus, from equation (1.11), the real (imaginary) part of the dielectric function,  $\varepsilon_1$  ( $\varepsilon_2$ ), is determined by the imaginary (real) part of the conductivity.  $\varepsilon_1$  and  $\varepsilon_2$  are dependent on each other and are related by the Kramers-Kronig relations, that are essential for the experimental measurement of the dielectric properties of a material.

Taking the curl of equation (1.1)(c) and making appropriate substitutions, one can derive the wave equation for linear optics

$$\nabla \times \nabla \times \mathbf{E} - \mu_0 \sigma \frac{\partial}{\partial t} \mathbf{E} - \frac{\tilde{n}^2}{c^2} \frac{\partial^2}{\partial t^2} \mathbf{E} = 0 \quad . \quad (1.13)$$

where the speed of light  $c = c_0/n$  and the complex refractive index  $\tilde{n} = \sqrt{\varepsilon_r \mu_r}$  are introduced, with the constant  $c_0 = 1/\sqrt{\varepsilon_0 \mu_0}$  as the vacuum speed of light. A standard textbook derivation indicates that in a metal, where  $\sigma \neq 0$ , an electromagnetic wave cannot propagate and vanishes exponentially [64]. This is of major importance for section 1.3 and the decay will be characterized in equation (1.22) later in this chapter.

Assuming now a dielectric medium without free charge carrier or current ( $\sigma$ ,  $\rho_{\text{tot}}$ , and  $J_{\text{tot}}$  all equal zero), equation (1.13) simplifies to

$$\nabla^2 \mathbf{E} - \frac{n^2}{c^2} \frac{\partial^2}{\partial t^2} \mathbf{E} = 0. \quad (1.14)$$

An elementary solution to equation (1.14) is a plane wave of the form  $\mathbf{E}(\mathbf{r}, t) = \mathbf{E}_0 e^{i(\mathbf{k}\cdot\mathbf{r} - \omega_0 t)}$ . While the direction of the electric field amplitude is also named polarization (of the electromagnetic wave), it should not be confused with the macroscopic polarization  $\mathbf{P}$  of the medium.  $\mathbf{k}$  is the wave vector pointing in the direction of propagation. The wave vector must satisfy the following relations to form a valid solution for Maxwell's equations:

$$\mathbf{k} \cdot \mathbf{E}_0 = 0 \qquad |\mathbf{k}| = \frac{\omega_0 n}{c} \qquad (1.15)$$

The former expression corresponds to a transversal wave solution, the latter is known as a dispersion relation. Numerical values in this thesis make use of the photon energy  $E = \hbar\omega_0$ , in electronvolt (eV), rather than the light frequency  $\omega_0$ , in terahertz (THz).  $\hbar$  is the reduced Planck constant and amounts to  $\hbar = 6.58211928 \times 10^{-16}$  eVs. Alternatively the wavelength in vacuum might be used,  $\lambda = 2\pi c_0/\omega_0$ , in nanometer (nm) or micrometer ( $\mu\text{m}$ ). The intensity of the electromagnetic wave is defined as the time average of the Poynting vector  $\mathbf{S} = \mathbf{E} \times \mathbf{B}$ . It is proportional to the square of the electric field amplitude yet independent of its phase:

$$I = \langle S \rangle = \frac{1}{2} \sqrt{\frac{\epsilon_0}{\mu_0}} n \mathbf{E}_0^2 \quad . \qquad (1.16)$$

Alternatively, following the derivation of equation (1.10), one might consider equation (1.14) in the frequency domain. Applying a Fourier transformation on Maxwell's equations (equation (1.1)) simplifies all time derivatives and equation (1.14) becomes

$$\nabla \times \nabla \times \mathbf{E}(\mathbf{k}, \omega) - \mathbf{k}^2 \epsilon_r(\mathbf{k}, \omega) \mathbf{E}(\mathbf{k}, \omega) = 0. \qquad (1.17)$$

Here, the material dielectric function  $\epsilon_r$  is explicitly frequency dependent and accounts for dispersive media. The following section provides a description for the dispersion in metals.

## 1.2 Dielectric Properties of Gold

Many properties of real metals, including optical properties, are suitably approximated by the Drude model [65]. In this model the interaction of metals with electromagnetic radiation is largely dictated by the free conduction electrons in the metal. One now demonstrates this with gold, which is the noble metal used for the nanostructures under investigation in this work.

In the Drude model, a metal is described by a free electron gas moving between heavier, stationary crystal ions. Essentially, this forms a plasma, i.e. a medium that possesses freely mobile charges. The model neglects interactions between the electrons and the ions and assumes that the electrons do not electromagnetically interfere with each other. The only possible interaction is an instantaneous kinetic collision between a free electron and another electron. This happens at a fixed rate, i.e. probability per unit time,  $\gamma$ , which corresponds to a phenomenological average relaxation time  $\tau = 2/\gamma$  for all the electrons. Each collision leads to a complete loss of directional information and results in a random orientation of the electron

velocity thereafter. This corresponds to Ohmic damping, and  $\gamma$  can be related to the electron mean free path (MFP)  $l_{\text{MFP}}$ :  $\gamma = v_{\text{F}}/l_{\text{MFP}}$ , where  $v_{\text{F}}$  is the Fermi velocity ( $\approx 1.4 \text{ nm fs}^{-1}$  in gold and silver [66]).  $l_{\text{MFP}}$  is an estimated 42 nm in gold.

Between collisions and in the presence of an external field, the free electrons, of mass  $m_e$  and charge  $-e$ , are accelerated. This results in a drift motion described by the equation of motion

$$\ddot{\mathbf{x}} + \gamma \dot{\mathbf{x}} = \frac{-e}{m_e} \mathbf{E} \quad , \quad (1.18)$$

where  $\mathbf{x}$  represents the electron displacement. Assuming a harmonic time dependence of the driving field  $\mathbf{E}(t) = \mathbf{E}_0 e^{-i\omega t}$ , a particular solution of this equation describing the oscillation of the electron is  $\mathbf{x}(t) = \mathbf{x}_0 e^{-i\omega t}$ . The drift of the charge carrier is described by

$$\mathbf{x} = \frac{1}{\omega^2 + i\gamma\omega} \frac{e}{m_e} \mathbf{E} \quad . \quad (1.19)$$

Electrons with density  $n_e$  sum up to a macroscopic polarization  $\mathbf{P} = n_e \mathbf{p} = -n_e e \mathbf{x}$ , with  $\mathbf{p}$  the dipole moment. Expressing the polarization as  $\mathbf{P} = \epsilon_0 (\epsilon_r - 1) \mathbf{E}$ , a relative permittivity can be defined as

$$\epsilon_r(\omega) = 1 + \chi = 1 - \frac{\omega_{\text{pl}}^2}{\omega^2 + i\gamma\omega} = \underbrace{1 - \frac{\omega_{\text{pl}}^2}{\omega^2 + \gamma^2}}_{\epsilon_1(\omega)} + i \underbrace{\frac{\omega_{\text{pl}}^2 \gamma}{\omega(\omega^2 + \gamma^2)}}_{\epsilon_2(\omega)} \quad , \quad (1.20)$$

where the bulk plasma frequency  $\omega_{\text{pl}} = \sqrt{(n_e e^2) / (\epsilon_0 m_e)}$  is the cut-off frequency for transverse electromagnetic waves. It describes a plasma oscillation in a bulk *unstructured* metal, i.e. a motion of the conduction electrons which act as a *relaxator* system. Here, the plasma frequency is *not* determined by the light excitation, which merely initiates the system perturbation.

In fact, two modifications are required to describe real metals. First, only electrons near the Fermi level contribute indeed, because the Pauli exclusion principle does not allow deeper lying electrons to change their electronic state. Second, one has to reflect the band-structure of matter. The first correction leads to the Drude-Sommerfeld model, also known as the free electron model. It becomes termed as quasi-free electron model after carrying out the second correction. Practically, this is accounted for by an effective mass of the electron  $m^*$  which generally differs from the free electron mass. However, the correction in the case of gold is minimal,  $m^*/m_e = 0.99 \pm 0.04$  [67].

Moreover, the ionic background has to be considered. This can be described away from the plasmon resonance by  $\epsilon_\infty$ . The dielectric function then reads

$$\epsilon_r(\omega) = \epsilon_\infty - \frac{\omega_{\text{pl}}^2}{\omega(\omega + i\gamma)} \approx \epsilon_\infty - \frac{\omega_{\text{pl}}^2}{\omega^2} + i \frac{\gamma \omega_{\text{pl}}^2}{\omega^3} \quad . \quad (1.21)$$

Figure 1.1 shows the real and imaginary part of the dielectric function of gold. The values measured on a vacuum-evaporated thin films at room temperature by Johnson and Christy [67] are fitted by the Drude function after equation (1.21). Fit parameter values are  $\hbar\omega_{\text{pl}} = 8.94 \text{ eV}$

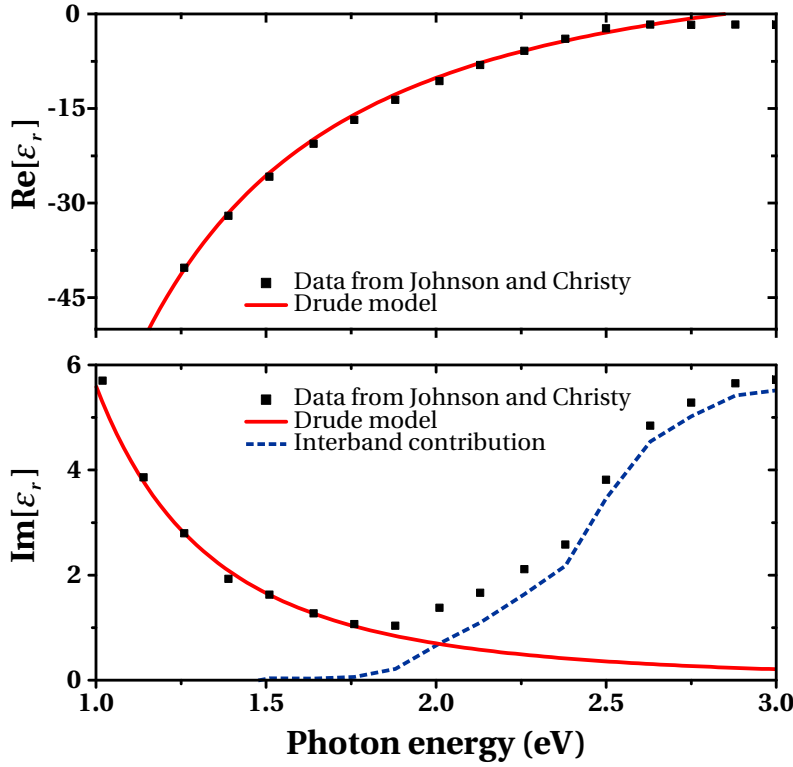


**Figure 1.1** – The relative permittivity of gold: Real (top) and imaginary part (bottom) of the dielectric function for gold as a function of the photon energy. Experimentally measured values taken from [67] (dots) with theoretical fits based on the Drude-Sommerfeld model (solid line,  $\hbar\omega_{\text{pl}} = 8.94$  eV,  $\epsilon_{\infty} = 9.84$ ,  $\hbar\gamma = 70$  meV). For photon energy higher than 1.80 eV the interband contribution (dashed line) is calculated from the difference of the experimental data to the quasi-free electron model.

for the plasma frequency,  $\epsilon_{\infty} = 9.84$  for the interband contribution, and  $\hbar\gamma = 70$  meV for the relaxation rate. Experiment and theory are in excellent agreement in the near-infrared spectral range of interest of this work.

In the visible spectral range ( $E > 1.80$  eV) large discrepancies occur with respect to the simple free electron model, in particular within the imaginary part of the dielectric function. The larger imaginary values, i.e. the higher absorption, are responsible for the characteristic color of the metal. The reason for this are the excitation of electrons from deeper bands into the conduction band, the so-called interband transitions, which are a manifestation of the density of states. This density of states is known from both experimental and theoretical results, e.g. via photoemission spectroscopy and relativistic band structure computation, respectively [68, 69].

Figure 1.2(a) shows a section of the band structure for gold [70]. The electronic configuration of the noble metal is such that all  $d$ -bands are located below the Fermi energy,  $E_{\text{F}}$ , and are fully occupied. Thus, the metallic properties originate from the  $sp$  conduction band. This band eventually crosses the Fermi level for  $\mathbf{k}$  vectors near the  $X$  and  $L$  symmetry points of the face-centered cubic (fcc) Brillouin zone (see figure 1.2(b)). There, interband excitations can occur in addition to intraband ones. Consequently, the intraband susceptibility described by equation (1.21) needs to be extended by a further interband term,  $\chi_{\text{IB}}(\omega)$ . The absorption of a photon of sufficiently high energy leads to the creation of an electron-hole pair. Most frequently, the resulting excitation relaxes non-radiatively in the solid and is ultimately converted into heat, see section 1.3.3. Nevertheless, after a rapid thermalization back to the Fermi energy, an electron in the  $sp$ -band can recombine with a hole in one of the flat  $d$ -bands. Figure 1.2(c)

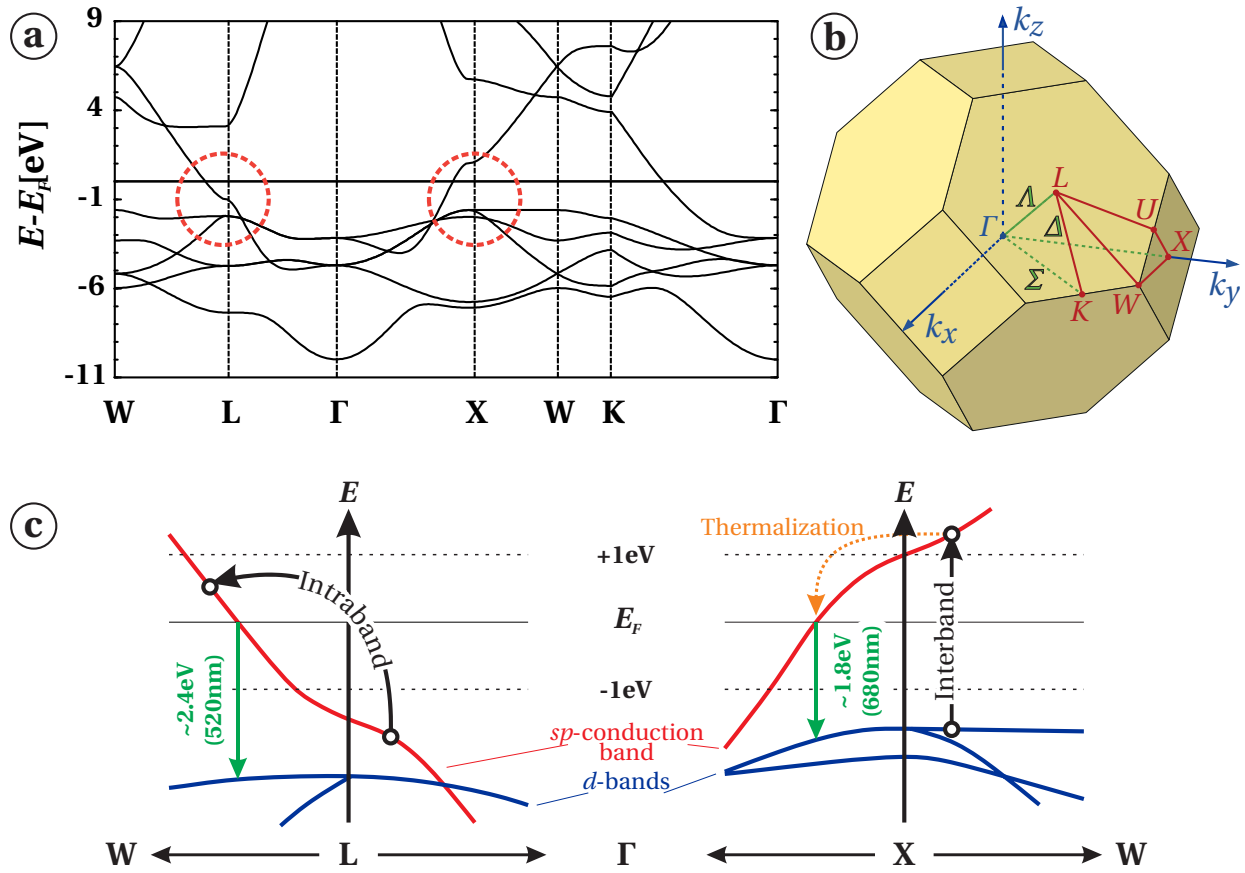


**Figure 1.2** – Low energy range band structure of gold. Energy bands (top left) plotted against the characteristic points of the first Brillouin zone of a face centered cubic lattice of the reciprocal space (top right). The band structure computation is based on plane waves [70]. Detailed reproductions (bottom) correspond to the circled regions near the  $L$  and  $X$  points where the  $sp$ -conduction band crosses the Fermi energy. Interband and intraband absorption processes are illustrated, which can result in photoluminescence peaked at 1.80 eV and 2.40 eV.

illustrates such a cycle. This is called photoluminescence and can also be triggered by multiple photon absorption. This process will be covered in section 2.2.

### 1.3 Optics of Metallic Nanostructures

Based on Maxwell's equations and the dielectric function of the material, one can compute the optical properties of nanostructures, i.e. absorption and scattering. However, given the complexity of the problem, an analytical solution is only accessible for a few simple particle geometries such as sphere and ellipsoids with dimensions of the order of magnitude of the wavelength of the incoming light. In the following, it is shown how these properties are correlated with so-called *plasmon resonances* and their dependence on particle features such as shape, material, and surrounding environment. Many characteristic properties of these

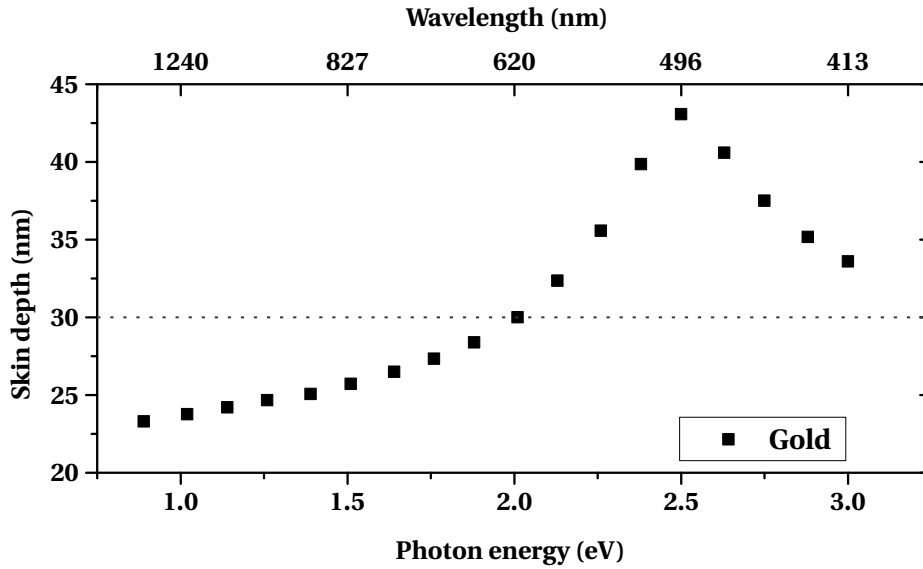


**Figure 1.3** – Skin depth for gold as a function of the photon energy. The depth at which the electric field decays to  $1/e$  of its surface value is calculated with equation (1.12) and (1.22) using the experimentally measured values taken from [67]. The horizontal dashed line provides an indication of the actual gold thickness of the nanostructures used in this work.

plasmon resonances can be approximated based on the classical harmonic oscillator model, described in the following section.

### 1.3.1 Particle Plasmon Classical Model

As an electromagnetic radiation hits a metal surface, its penetration depth in the metal is inversely proportional to the absorption:

$$\delta_p = \frac{c_0}{\omega\kappa} \quad , \quad (1.22)$$

where  $\kappa$  is the imaginary part of the complex refractive index, see section 1.2. The penetration depth, also known as skin depth, is defined as the depth at which the electric field decays to  $1/e$  of its surface value. Since the power of a wave in a particular medium is proportional to the square of a field quantity, the skin depth is twice the depth at which the intensity of the field decays to  $1/e$  of its surface value. The skin depth does not significantly vary over the photon energy spectrum used in this work and typically amounts to 24 nm at a wavelength of  $1.2\mu\text{m}$ , see figure 1.3. This is in the order of the thickness of the structures used in this work, see section 3.1. Thus, despite the large reflectivity of gold, the electromagnetic field penetrates to a considerable extent into the structure, and nearly all conduction electrons in the metal volume experience the electric field of light.

Furthermore, as one considers metallic nanoparticles rather than a plain film (in contrast to section 1.2), finite volumes and highly curved surfaces have to be accounted for. Thus, the mechanism described above leads to a polarization of the particles: The electric field of light shifts the conduction electrons with respect to the ionic background, where the ions

are considered to be immobile. In turn, the resulting surface charges of opposite sign on the opposite surface elements of the particle produce a restoring local field within the particle which rises with increasing shift of the electron gas relative to the ionic background. This depolarization field drives the electrons into a collective oscillation. The linear restoring force is a further contribution to equation (1.18) and determines the eigenfrequency of the system. Indeed, it is possible to describe the system as a harmonic Lorentz oscillator following the equation of motion:

$$\ddot{\mathbf{x}} + \gamma \dot{\mathbf{x}} + \omega_0^2 \mathbf{x} = \frac{-e}{m^*} \mathbf{E} \quad , \quad (1.23)$$

where  $\omega_0$  is the natural frequency of the oscillator, which is dependent on the structure being considered.  $\omega_0$  is used to define the damped eigenfrequency  $\Omega_{pp} = \sqrt{\omega_0^2 - \gamma^2}$ . Solving equation (1.23) leads to the expression of the electron displacement oscillation.

$$\mathbf{x} = \frac{1}{\omega_0^2 - \omega^2 + i\gamma\omega} \frac{e}{m_e} \mathbf{E} \quad . \quad (1.24)$$

Following the same method that led to equation (1.20) in bulk metal, one can now express the relative permittivity for nanostructured metal.

$$\varepsilon_r(\omega) = 1 + \chi = 1 + \frac{\omega_{pl}^2}{\omega_0^2 - \omega^2 + i\gamma\omega} = 1 + \underbrace{\frac{\omega_{pl}^2 (\omega_0^2 - \omega^2)}{(\omega_0^2 - \omega^2)^2 + \gamma^2 \omega^2}}_{\varepsilon_1(\omega)} + i \underbrace{\frac{\omega_{pl}^2 \gamma \omega}{(\omega_0^2 - \omega^2)^2 + \gamma^2 \omega^2}}_{\varepsilon_2(\omega)} \quad (1.25)$$

It is conceptually essential to understand that the modified expression of the oscillation induces a modification of the relative permittivity. In other words, departing from a bulk metal configuration, i.e. by *nanstructuring* a metal, it is possible to obtain tailored material responses. It is stressed that equation (1.23) deals with *free* electrons in a *nanostructure*: It is formally equivalent to the equation of motion of a *bound* electron oscillating around its equilibrium in an *atom*. Thus, an ensemble of nanostructures which size features are smaller than the wavelength of the impinging light can be seen as an effective material where each nanostructure acts as a *meta-atom* [71]. It is evident that the corresponding fundamental eigenfrequency of a nanostructure can only be lowered with respect to the free oscillation frequency set by the material via the plasma frequency,  $\omega_{pl}$ . This qualitative aspect is treated later in this section.

Equation (1.25) highlights the fact that the linear susceptibility  $\chi$  becomes large when  $\varepsilon_r$  is driven at a resonant  $\omega$ . Indeed, in contrast to the bulk behavior described in section 1.2, the restoring force formation makes the conduction electrons act like an *oscillator* system. If the excitation frequency is resonant to the eigenfrequency of the collective oscillation, even a small external field amplitude suffices to drive a strong plasmon oscillation. The eigenmodes of this oscillator correspond to a *collective* and *coherent* oscillation of the free electron gas within the particle. Most commonly, they are called Mie-plasmons, localized surface plasmons or, least ambiguously, particle plasmons. The term *localized surface plasmon* stems from the fact that, although all electrons are oscillating with respect to the ionic background, the

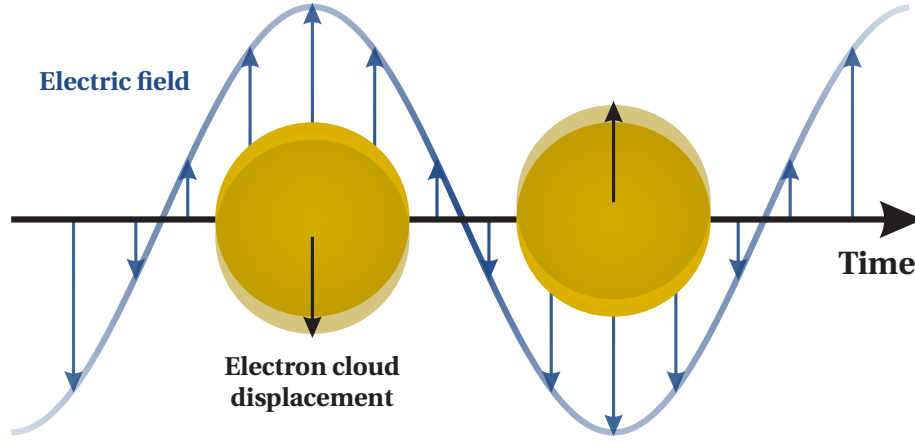


**Figure 1.4** – Schematic illustration of the localized surface plasmon resonance formation in a spherical nanosphere; adapted from [72]. Under excitation by an external electromagnetic plane wave, the conduction electron charge distribution is coherently shifted relative to the positive ionic background. Due to Coulomb interaction, a restoring force is induced and oscillates in antiphase with the electric field of the incoming light.

main effect producing the restoring force is the polarization due to electrons confined at the boundary, see figure 1.4. Particle plasmons differ from propagating (non-localized) surface plasmons at the interface between a metal and a dielectric, since there is no need for the excitation photon wave vectors to match: particle plasmons *directly* couple to the light field. This work deals exclusively with particle plasmons; section 3.1.4 and results thereof show how the localized aspect can be exploited.

In essence, the resonance frequency is mainly determined by the strength of the restoring force. The latter originates from the driving electric field of the light that induces a dipole moment proportional to the field. The ease with which a nanostructure is polarized is specified by the polarizability  $\alpha$ , introduced via

$$\mathbf{p} = \varepsilon_0 \varepsilon_m \alpha \mathbf{E}_{\text{eff}}, \quad (1.26)$$

where  $\varepsilon_m$  is the dielectric constant of the environment surrounding the particle. At low particle density,  $\mathbf{E}_{\text{eff}}$  identifies as the incident light electric field, for the near-field coupling from neighboring particles is negligible. For higher densities, screening terms must be included to get the effective local electric field resulting from the external source and from all nanoparticles within the sample except the one under consideration. In this work, particle spacing larger than the near field coupling range are considered. An analytical expression for  $\alpha$  is available only for particles with simple geometries, such as a sphere or an ellipsoid, and in the quasi-static limit with particle much smaller than the wavelength of light in the surrounding medium. In this case, the phase of the harmonically oscillating electromagnetic field is practically

constant over the particle volume, so that one can calculate the spatial field distribution by assuming the simplified problem of a particle in an electrostatic field. The harmonic time dependence can then be added to the solution once the field distributions are known. Then, the polarizability is expressed as [73]

$$\alpha_i = V \frac{\epsilon_r - \epsilon_m}{\epsilon_r - L_i (\epsilon_m - 1)}, \quad (1.27)$$

where  $V$  represents the volume of the structure. For an ellipsoid,  $i \in \{x, y, z\}$  corresponds to the principal axes, and  $L_i$  is the corresponding polarization factor for which the sum rule  $\sum_i L_i = 1$  holds. The longer the axis, the smaller the depolarization factor and in the special case of a sphere  $L_1 = L_2 = L_3 = 1/3$ . This approach can be extended to more complex structures with  $\alpha$  as a tensor determining the *eigenpolarizations*, i.e. modes, of a structure. The form of the tensor reflects the symmetry of the structure. The lower the symmetry the structure presents, the more non-degenerate modes it possesses [74]. Thereafter, a general expression for the eigenfrequency of a particle plasmon is expressed by the relation [75, 76]

$$\Omega_{pp} = \sqrt{L_i} \omega_{pl} \quad . \quad (1.28)$$

Equation (1.27) reveals the major parameters influencing the surface plasmon resonance position [72]: The particle shape, the dielectric function of the metal, and the dielectric function of the environment. The shape determines the distribution of the surface charges: A decreased surface charge density corresponds to a smaller restoring force which decreases the resonance frequency. The dielectric constant of the metal describes the intrinsic polarizability of the particle. This is shielded by the dielectric surrounding that partially compensates the polarization at the surface. In the case of a particle only partly in contact with a substrate, reasonably good results are obtained by considering this particle as fully *embedded* within a material presenting a weighted average of the dielectric function of air and of the substrate ( $\epsilon_m = 1$  in air or vacuum) [77].

The polarizability experiences a resonant enhancement under the condition that the denominator of in equation (1.27) vanishes, i.e.

$$\epsilon_r = \epsilon_m \left( 1 - \frac{1}{L_i} \right). \quad (1.29)$$

This relationship is called the *Fröhlich condition* and expresses the strong dependence of the resonance frequency on the dielectric environment. The associated mode (in an oscillating field) is the dipole particle plasmon of the metal nanostructure. To a good approximation, the electromagnetic field of the dipolar particle plasmon modes outside the particles can be analytically described by the electromagnetic field of an oscillating point dipole located in the center of the particle [63]. This approximation holds for dipolar particle plasmon resonances on arbitrarily shaped metal nanoparticles if the distance from the particle is much larger than the particle itself. The dipole approach is extended in section 1.3.2.

The resonance in  $\alpha$  implies a resonant enhancement of both the internal and dipolar fields. If excited resonantly, the amplitude of the induced plasmonic electric field can exceed the

exciting fields by several orders of magnitude. It is this field-enhancement at the plasmon resonance on which many applications of metal nanoparticles rely. Using the boundary conditions at the surface, it is possible to calculate the resulting electric fields  $\mathbf{E}_{\text{in}}$  and  $\mathbf{E}_{\text{out}}$ , respectively inside and outside of a sphere, due to the driving field  $\mathbf{E}$  [63, 73].

$$\mathbf{E}_{\text{in}} = \frac{3\varepsilon_m}{\varepsilon_r + 2\varepsilon_m} \mathbf{E} = f_e \mathbf{E} \quad (1.30)$$

$$\mathbf{E}_{\text{out}} = \frac{1}{4\pi\varepsilon_0} \left\{ k^2 (\mathbf{n} \times \mathbf{p}) \times \mathbf{n} \frac{e^{ikr}}{r} + [3\mathbf{n}(\mathbf{n} \cdot \mathbf{p}) - \mathbf{p}] \left( \frac{1}{r^3} - \frac{ik}{r^2} \right) e^{ikr} \right\}, \quad (1.31)$$

where  $f_e$  is the enhancement factor with respect to the incoming electric excitation,  $\mathbf{n}$  is the unit vector in the direction of the point of interest at a distance  $r$  from the dipole center. It is essential to notice that in equation (1.31) the term varying with the highest power of  $r$  dominates the near-field. Hence, since this work concentrates on the immediate vicinity of the metallic structure, one approximates  $\mathbf{E}_{\text{out}}$  with its near-field expression that moreover identifies with the electrostatic expression of an electric dipole:

$$\mathbf{E}_{\text{out}} \simeq \mathbf{E}_{\text{out,NF}} = \frac{3\mathbf{n}(\mathbf{n} \cdot \mathbf{p}) - \mathbf{p}}{4\pi\varepsilon_0} \frac{1}{r^3} \quad (1.32)$$

The metallic nanostructure acts as a far-field to near-field converter: It acts as an *optical antenna* with the capability of concentrating the light field strength in subwavelength volumes [78, 79], see section 3.1.4.

The qualitative features described in this section can be transposed to nanostructures of arbitrary shape, e.g. to the samples described in section 3.1. Thus, metal nanoparticles usually have more than a single oscillation mode that depends on the particle shape, the environment, and the metal used. The different modes differ in their charge and field distribution and set the linear optical properties of the metal nanostructures, presented in the following section.

### 1.3.2 Optical Manifestations: Scattering and Absorption

The resonantly enhanced polarization  $\alpha$  is associated with an enhancement in the efficiency with which a metal nanostructure scatters and absorbs light. In the simple model of an ellipsoid in the quasi-static regime, light scattering, absorption, and extinction are described by the frequency dependent cross-sections  $C_{\text{sca}}$ ,  $C_{\text{abs}}$ , and  $C_{\text{ext}}$ , respectively. Their relation to the polarizability is given by [80]:

$$\begin{aligned} C_{\text{abs}} &= |\mathbf{k}| \text{Im}[\alpha] = V |\mathbf{k}| \text{Im} \left[ \frac{\varepsilon_r - \varepsilon_m}{\varepsilon_r - L_i(\varepsilon_m - 1)} \right] \\ C_{\text{sca}} &= \frac{|\mathbf{k}|^4}{6\pi} |\alpha|^2 = V^2 \frac{|\mathbf{k}|^4}{6\pi} \left| \frac{\varepsilon_r - \varepsilon_m}{\varepsilon_r - L_i(\varepsilon_m - 1)} \right|^2 \\ C_{\text{ext}} &= C_{\text{abs}} + C_{\text{sca}}, \end{aligned} \quad (1.33)$$

where  $k$  is the wave vector. A figure of merit is defined as the ratio of scattered light to the extinction, also known as *radiative quantum yield*  $\eta$  and the cross-sections are related to their

corresponding spectrum according to

$$\eta = \frac{C_{\text{sca}}}{C_{\text{ext}}} \quad , \quad I_{\text{ext}}^{\text{sca}}(\omega) = \frac{I_0(\omega)}{A} C_{\text{sca}}^{\text{ext}}(\omega) \quad , \quad (1.34)$$

for a particle illuminated with the light intensity per area  $I_0(\omega)/A$ .  $\eta$  increases with particle diameter and varies from one structure design to another [81]. Equation (1.33) shows that for metal nanoparticles both absorption and scattering (and thus extinction) are resonantly enhanced at the particle plasmon resonance, i.e. where the Frölich condition is met [73].

The cross-section expressions above are valid for particles small compared to the local variations of the involved electromagnetic fields [73, 82]. This quasistatic approximation assumes the exciting field to be homogeneous and not retarded over the particle's volume: They are dominated by a dipole contribution. Mie's work overcomes these limits for spherical systems with dimensions of the order of magnitude of the wavelength of the incoming light [3]. For such nanoparticles, the extinction cross-sections are dominated by higher-order multipole absorption and scattering. An analytical expression for the extinction and scattering cross-sections is formulated in which the involved fields are decomposed into partial waves (spherical multipoles), and the scattered field is expressed as the superposition of these partial waves [80]:

$$C_{\text{ext}} = \frac{2\pi}{|\mathbf{k}|^2} \sum_{L=1}^{\infty} (2L+1) \text{Re}[a_L + b_L] \quad (1.35)$$

$$C_{\text{sca}} = \frac{2\pi}{|\mathbf{k}|^2} \sum_{L=1}^{\infty} (2L+1) (|a_L|^2 + |b_L|^2) \quad , \quad (1.36)$$

with

$$a_L = \frac{m\psi_L(mx)\psi'_L(x) - \psi'_L(mx)\psi_L(x)}{m\psi_L(mx)\xi'_L(x) - \psi'_L(mx)\xi_L(x)} \quad (1.37)$$

$$b_L = \frac{\psi_L(mx)\psi'_L(x) - m\psi'_L(mx)\psi_L(x)}{\psi_L(mx)\xi'_L(x) - m\psi'_L(mx)\xi_L(x)} \quad . \quad (1.38)$$

Here,  $m = \tilde{n}/n_m$ , where  $\tilde{n}$  denotes the complex refractive index of the particle and  $n_m$  the real refractive index of the *surrounding* medium.  $x = |\mathbf{k}|R = \frac{\omega}{c}R$  is the size parameter with  $R$  the sphere radius.  $\psi_L$  and  $\xi_L$  stand for Riccarti-Bessel functions. One recognizes the three key parameters determining the plasmon resonance: Structure size, and dielectric functions of both the structure material and of the surrounding medium. This is consistent with the model introduced previously, but it is only several decades after the seminal paper that Mie's framework was reinterpreted according to the modern concept of particle plasmons of different multipole order [12, 83].

The summation index  $L$  provides the order of the partial wave.  $L = 1$  corresponds to dipole fields,  $L = 2$  to quadrupole,  $L = 3$  to octupole, etc. The coefficients  $a_L$  and  $b_L$  are proportional to  $(|\mathbf{k}|R)^{2L+1}$ , so that the importance of higher order terms increases with larger structure size. The electric multipolar excitations are particle plasmon modes while their magnetic

counterparts consist of eddy currents. The magnetic multipoles are also due to electronic excitations and thus also depend on the dielectric function of the metal.

From there, it is possible to compute multipole spectral resonances featuring a Lorentzian profile with a photon energy at the resonance  $E_{\text{res},L} = \hbar\omega_L$  and linewidth, or full width at half maximum (FWHM),  $\Gamma = \hbar\Delta\omega$ . In the quasi-static limit of Mie theory, the positions of the Mie multipoles  $\omega_L$  and their resonance width  $\Gamma$  is given by [73, 84]:

$$\omega_L = \omega_{\text{pl}} \frac{1}{\sqrt{1 + \frac{L+1}{L} \varepsilon_m}} \quad , \quad \Gamma = \frac{2\varepsilon_2}{\sqrt{\left(\frac{d\varepsilon_1}{d\omega}\right)^2 + \left(\frac{d\varepsilon_2}{d\omega}\right)^2}} (1 + \beta) \quad . \quad (1.39)$$

Thus, the plasmon resonance increases in frequency with higher order, while a higher value for  $\varepsilon_m$  red-shifts it. For gold,  $\beta \ll 1$  and  $\left(\frac{d\varepsilon_2}{d\omega}\right)^2 \ll \left(\frac{d\varepsilon_1}{d\omega}\right)^2$  so that  $\Gamma$  becomes a linear function of  $\varepsilon_1$  and  $\varepsilon_2$ . Then, it consists of a dispersion and dissipative term. Practically, resonances get smeared out, eventually past recognition, for low  $\frac{d\varepsilon_1}{d\omega}$  and large  $\varepsilon_2$  values. For free-electron metals (section 1.2) where  $\gamma \ll \omega$ , a special case occurs with  $\Gamma = \gamma$ . However, in three-dimensionally confined samples additional processes lead to a broadening of  $\Gamma$ . These processes are discussed in section 1.3.3.

Thus, the framework of the Mie theory allows for the computation of far-field scattering cross-sections in a relatively straight-forward manner. However, analytical solutions are not readily available to address the problem for arbitrarily shaped structures. Excellent approximations exist for ellipsoidal shapes [80] and cylindrical rod [85], but for more complex structures one has to employ numerical methods. Among them are the finite difference time domain methods (FDTD) [86], the discrete dipole approximation (DDA) [87], the boundary element method (BEM) [88], and the scattering-matrix method (S-matrix) [89], to name a few. Numerical simulations, however, are not the topic of this work. Nevertheless, they represent a powerful guiding tool in the design stage, see section 3.1, and to get insight into the *near-field* distribution of the electric field. Specifically here in preliminary fabrication work, the output field is solved numerically by a S-matrix formalism based on a rigorous Fourier modal method [90, 91]. This allows to better quantify the parameter dependence introduced previously.

Thus, the qualitative features of the electronic resonances, and their correlated optical properties, are found again in larger, arbitrarily shaped particles. The appearance of retardation effects allows for higher order oscillation modes. Numerical simulations show that major differences appear in the radiative quantum yield of structures with similar resonance features, depending on their shape, see section 4.1.1. These differences are to be traced back to the promotion or weakening of different damping mechanisms, in function of the particle geometry. A description of these damping mechanisms is given in the following section.

### 1.3.3 Particle Plasmons Lifetime: Damping Mechanisms

As discussed in the previous sections, important plasmon properties such as the amplitude of the collective electron oscillation with respect to the driving amplitude and the width of the particle plasmon resonance  $\Gamma$  depend on the amount of damping. Generally, the application

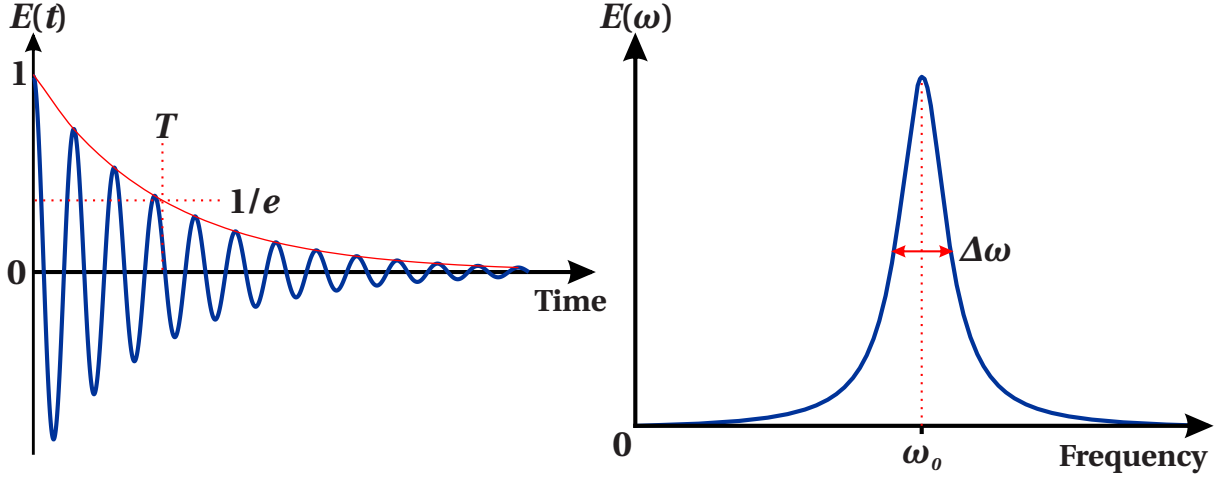


**Figure 1.5** – Related via the Fourier transformation, a damped oscillation in time (left) corresponds to a Lorentz-shaped peak in the frequency spectrum (right). Here, an oscillation with frequency  $\omega_0$  and damping time  $T$  is shown. The full width at half maximum  $\Delta\omega$  of the resonance in frequency space is  $2/T$ .

of particle plasmons benefits from reduced damping. Indeed, a fast decay (large damping) of the optically-induced polarization limits the time for coherent light-matter interaction.

Given an exponential decay with time constant  $T$ , and considering that time and frequency are related by the Fourier transformation, the spectral broadening of a Lorentz oscillator is given by  $\Gamma = \hbar\Delta\omega = 2\hbar/T$ , see figure 1.5. It is related to the figure of merit used to quantify the resonating feature of an oscillator, i.e. the quality factor,

$$Q = \frac{\omega_0}{\Delta\omega} = \frac{E_{\text{res}}}{\Gamma} . \quad (1.40)$$

The higher the plasmon damping, the larger the spectral broadening of the oscillating nanostructure and the lower is  $Q$ . For weakly damped oscillators,  $Q$  equals the local field enhancement factor  $f$  introduced in equation (1.30), i.e. the enhancement of the oscillation amplitude with respect to the driving amplitude.

To understand the underlying mechanism defining the spectral broadening, it is insightful to decompose a plasmon oscillation into the superposition of individual electrons oscillating in phase. Seen individually, each electron contributing to the plasmonic oscillation either releases its energy by inelastic dissipation processes on a  $T_{e^-}$  time scale, or loses its phase correlation to the other electrons by elastic dephasing processes on a  $T_{e^-}^*$  time scale [92, 93]. A phenomenological elastic plasmon relaxation time  $T_{e^-}^* = 30$  fs is given in [66]. Both decay channels add up and lead to the total plasmon decay time in a single structure  $T_{\text{hom}}$  according to

$$\frac{1}{T_{\text{hom}}} = \frac{1}{T_{e^-}} + \frac{1}{T_{e^-}^*} . \quad (1.41)$$

$T_{\text{hom}}$  describes the decay of the plasmonic *field* amplitude down to  $1/e$  of its maximum value. The oscillator's *energy* decays with a rate twice as fast, since it is related to the square of its

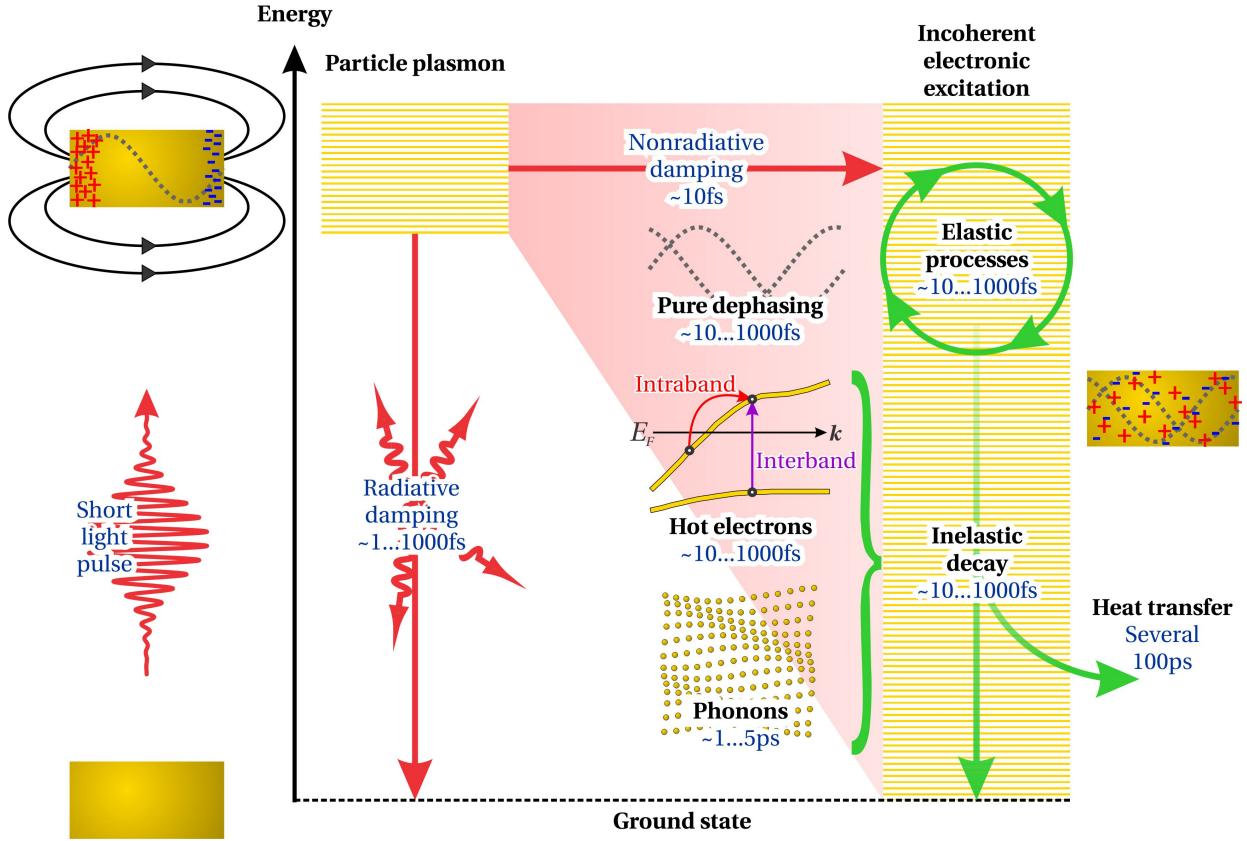


**Figure 1.6** – Schematic representation of the decay channels for a particle-plasmon excited by an ultra-short laser pulse. The contributions to the damping of localized plasmons can be separated into radiative and non-radiative processes. Inelastic damping, i.e. radiative damping (production of photons) as well as intra- and interband absorption (creation of electron-hole pairs), leads to the dissipation of energy on the time scale  $T_e^*$ . Elastic scattering leads to a pure dephasing with time constant  $T_e^*$ . The resulting energy bath then thermalizes with the environment.

amplitude. Ultimately, the electron population which non-radiatively stops to contribute to the coherent collective oscillation, supplies a system which consists of a reservoir of free kinetic energy modes, gold lattice vibration and phonon excitations. The latter bath then slowly decays to the ground state, i.e. it undergoes a thermalization back into a uniform Fermi-Dirac distribution across the nanostructure.

Separating and measuring the different contributions to the plasmon population decay is the topic of numerous theoretical as well as experimental publications, a selection of which is found in reference [93]. An intent in summarizing these is represented in a simplified diagram, see figure 1.6. The homogeneous linewidth  $\Gamma_{\text{hom}}$  of a plasmonic resonance can be decomposed into several contributions discussed below:

$$\frac{\Gamma_{\text{hom}}}{2\hbar} = \frac{1}{T_{\text{hom}}} = \sum_i \tau_i^{-1} = \tau_r^{-1} + \underbrace{\tau_{\text{cc}}^{-1} + \tau_{\text{surf}}^{-1} + \tau_{\text{e-h}}^{-1} + \dots}_{\tau_{\text{nr}}^{-1}} \quad (1.42)$$

Explicitly, the decay of a plasmon population follows either a radiative or non-radiative channel [92], corresponding to a relaxation time  $\tau_r$  and  $\tau_{\text{nr}}$ , respectively. Together with the total

decay time constant  $T_{\text{hom}}$  they are related to the cross-sections introduced in section 1.3.2, and hence to the radiative quantum yield as well:

$$T_{\text{hom}} \leftrightarrow C_{\text{ext}} \quad , \quad \tau_{\text{r}} \leftrightarrow C_{\text{sca}} \quad , \quad \tau_{\text{nr}} \leftrightarrow C_{\text{abs}} \quad , \quad \eta = \frac{\tau_{\text{r}}}{T_{\text{hom}}} \quad . \quad (1.43)$$

The radiative dissipation damps the plasmonic oscillation by emission of a photon at the resonance frequency. Based on Fermi's golden rule, it is possible to evaluate the time scale of radiative damping  $\tau_{\text{r}}$  for spherical particles and dipole modes as [94, 95]

$$\tau_{\text{r}}^{-1} = \frac{V \omega^4}{2\pi c^3} \quad , \quad (1.44)$$

with  $V$  the particle volume. Thus, the radiative relaxation rate  $\tau_{\text{r}}^{-1}$  is directly proportional to the *volume* of the particle, rather than its surface. Although equation (1.44) derives from simple models for spherical structures and dipolar modes, the qualitative aspects discussed below are conserved for other geometries [96].

Besides the radiative damping mechanism, several non-radiative processes can occur, corresponding to a relaxation time  $\tau_{\text{nr}}$ . Non-radiative processes regroup both elastic and inelastic electron damping mechanisms. A first damping mechanism consists of the creation of an electron-hole pair via an intra- or interband excitation. This process correlates to the frequency-dependent imaginary part of the dielectric function [97]. As such, it depends strongly on the central energy of the plasmonic excitation. Practically, the corresponding relaxation rate  $\tau_{\text{e-h}}^{-1}$  is negligible for gold for resonances below 1.80 eV, see section 1.2. Then, further non-radiative processes correspond to the mechanism described in section 1.2, where the electron collides with an unspecified collision center (lattice ion, core or conduction electron, phonon, defect, impurities, etc.). The combined influence of these processes sums up according to the Matthiessen's rule [98], at a scattering rate  $\tau_{\text{cc}}^{-1}$ . Finally, this is complemented by a further electron-surface scattering rate  $\tau_{\text{surf}}^{-1}$  due to the finite particle volume or e.g. to grain boundaries. Surface scattering results from additional collisions of the conduction electrons at the surface and is given empirically by [94, 99]:

$$\tau_{\text{surf}}^{-1} = A \frac{v_{\text{F}}}{R} \quad , \quad (1.45)$$

where  $R$  is the particle radius that reflects the ratio of the surface ( $\propto R^2$ ) to the number of electrons ( $\propto R^3$ ).  $A$  is an empirical parameter of the order of 1 describing the loss of coherence by the scattering event [100–102].

Based on equation (1.44) and equation (1.45), the size of a nanostructure determines the leading damping mechanism, see figure 1.7. Practically, for particles with a radius below 10 nm, radiative scattering corresponds to a relaxation time in the picosecond range. Therefore, this represents a negligible contribution being too slow with respect to other damping channels. However, for structures larger than 100 nm this corresponds to a relaxation time in the femtosecond range. Therewith, it becomes the dominating process for the plasmon relaxation of the largest structures. One should mention at that point another damping mechanism which occurs in large structures, namely retardation effects. During the plasmonic excitation, the

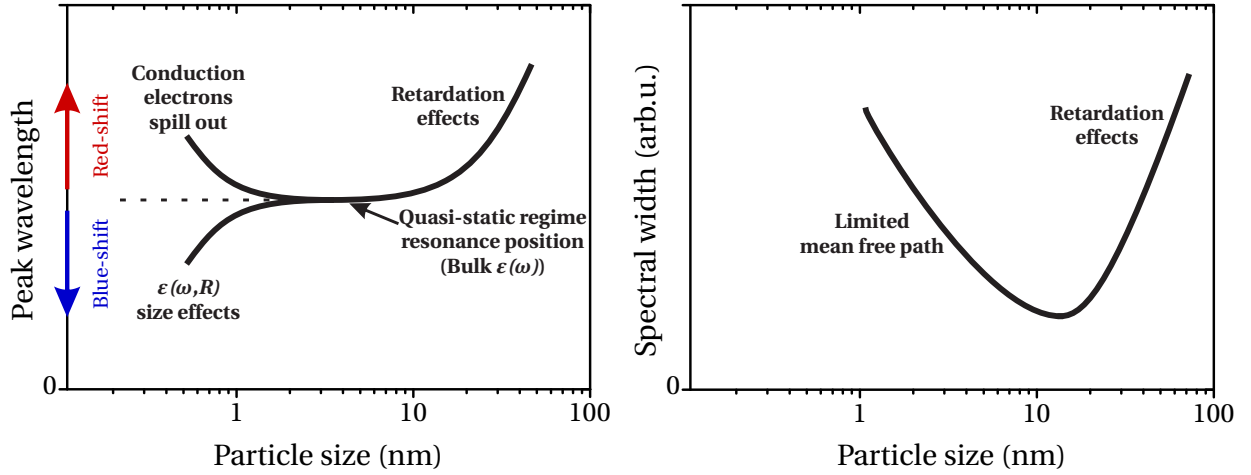


**Figure 1.7** – Qualitative dependence of the position (left) and linewidth (right) of the dipolar particle plasmon resonance in metallic nanostructures as a function of their size. Adapted from [73].

spatial extension of the particle leads to a phase difference of the electronic excitations across the particles. This weakens the restoring Coulomb force and therewith the quality factor of the structure. A further description of this process is given in references [103–106].

Inversely, surface scattering becomes relevant only for the smallest particles, typically for sizes below 20 nm. There, the effective electron mean free path (MFP) is smaller than the bulk mean free path. This alters the magnitude of the material dielectric functions  $\epsilon_1(\omega)$  and  $\epsilon_2(\omega)$ , which become size dependent:  $\epsilon(\omega) = \epsilon(\omega, R)$ . Also, as one further reduces a structure, the impact of the electronic *spill-out* at the boundary has to be accounted for. For large structures the electron charge density is assumed to drop sharply on the atomic scale from the value inside the metal to zero outside. However, owing to the wave nature of the electron, quantum-mechanical computation has shown that this change can take place over a distance of about the Fermi wavelength and thus can amount to several tenths of nanometer. Computation as well as experiments indicate a blue-shift effect on the resonance [107, 108].

The linewidth resulting from the above described processes corresponds to the linewidth of a *single* resonator. Therefore, we termed it as the *homogeneous* linewidth  $\Gamma_{\text{hom}}$ . However, our sample consists of an ensemble of hundreds of thousand of such unit blocks. Inevitably, the fabrication process leads to a non-monodisperse particle size distribution, see section 3.1. In consequence, the slightly different resonance wavelengths follow a stochastic distribution around an average value. Following a free-induction decay process, this is the source of an extra *inhomogeneous* broadening of the total linewidth of the resonances:

$$\Gamma = \Gamma_{\text{hom}} + \Gamma_{\text{inhom}} \quad , \quad \frac{1}{T} = \frac{1}{T_{\text{hom}}} + \frac{1}{T_{\text{inhom}}} \quad . \quad (1.46)$$

The more defects and deviations the particles present from one another, the more significant the inhomogeneous contribution becomes.

Finally, another effect needs be highlighted for regular, periodic arrangements of nanostructures. Two types of interaction can take place, namely near-field coupling and far-field interaction. On the one hand, near-field coupling between structures is relevant for nearly

touching particles due to the short range of the electromagnetic near fields. This effect is in the order of some tens of nanometers [109, 110] and thus will be ignored in our samples, owing to their periodicity length of several hundreds of nanometers, see section 3.1.1. On the other hand, far-field interaction is mediated by the nanostructures' scattered light fields. Indeed, dipolar interactions among particles on a regular array can occur, owing to the grating nature of the surface. At normal incidence, the diffraction angle is given by  $\theta_m = \arcsin(m\lambda/d)$ , where  $d$  is the nanostructure array period and  $m$  the diffractive order. Prohibited for an array period smaller than the wavelength, the light fields corresponding to a particular grating order become radiative at a grazing angle, at a critical nanostructure spacing  $d_c = \lambda$  [111, 112]. This is related to the so-called Wood anomaly [113] and leads to sharp dips or peaks in the extinction or reflection spectra, respectively [114]. For a larger grating constant, the light is scattered only at defined angles, due to coherent excitation and scattering of the individual nanoparticles in analogy to light diffraction from a grating. In consequence, the  $Q$  factor decreases due to enhanced radiation damping of the individual particle plasmons caused by an increase of the power radiated by the array.



# Chapter 2

## Perturbative Nonlinear Optics

In the preceding chapter, it was shown that the optical properties of a material, and consequently of nanostructures, result from the polarization of that material by the electric field of light. However, linear optics properly describe the interaction between an electromagnetic field and a medium only when the light field does not perturb the optical properties of the medium. This assumption is no longer valid in presence of high field strength, where the response of the illuminated medium depends nonlinearly on the applied field strength. In the following, the linear wave equation is extended to account for the anharmonic contributions which come into play in the nonlinear regime. The nonlinear effects relevant to the optical nonlinear spectroscopy method used in this work are presented. A more detailed treatment of nonlinear optics is found in references [44, 46, 47].

### 2.1 Second Harmonic Generation

Since the development of the laser [115], very high electric field strengths inaccessible to any other light source have become available. For pulsed lasers, values as high as  $E = 1 \times 10^{20} \text{ V m}^{-1}$  are possible (interatomic electric fields are of the order of  $1 \times 10^8 \text{ V m}^{-1}$ ). At high intensities, nonlinear terms in the electric polarization and magnetization have to be considered. Thus, equation (1.6) is generalized by expressing the polarization  $\mathbf{P}$  as a power series in the electric field  $\mathbf{E}$  [45]

$$P_i = \epsilon_0 \left( \chi_{ij}^{(1)} E_j + \chi_{ijk}^{(2)} E_j E_k + \chi_{ijkl}^{(3)} E_j E_k E_l + \dots \right) , \quad (2.1)$$

where the first term is the linear contribution of equation (1.6), and the  $n$ -th order susceptibilities  $\chi^{(n)}$  are  $(n+1)$ -th order tensors. In its general description, the nonlinear terms of the polarization lead to the excitation of a harmonic wave of frequency  $\omega_{\text{NL}} = \sum_{i=1}^n \pm \omega_i$  which is defined as an arbitrary linear combination of the incident light field frequencies  $\omega_i$ . The nonlinear processes are classified according to the number of incident fields, hence on the order  $n$  of the corresponding susceptibility. For instance, it is possible to carry out sum or difference frequency generation (SFG and DFG, respectively) with two photons or more. In the special case where all incident frequencies are equal, one speaks of second, third or higher

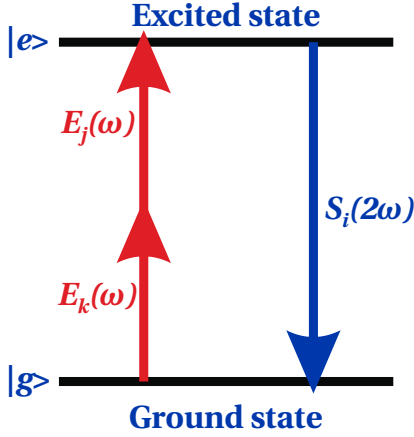


**Figure 2.1** – Schematic illustration of the SHG process: Energy-level diagram. The system is excited by the simultaneous absorption of two photons at frequency  $\omega$  of an intense light field, e.g. an ultra-short laser pulse. The system relaxes by emission of a photon with frequency  $2\omega$ . This nonlinear source term can originate from crystallographic and/or order-parameter related contributions.

harmonic generation (SHG, THG and HHG, respectively), as well as of optical rectification when a quasi-DC polarization is generated in the nonlinear medium (case  $\omega - \omega = 0$ ) [46]. The lowest order of these processes is the SHG, in which a material excited by a light source of frequency  $\omega$  generates a harmonic source oscillating at twice the excitation frequency,  $\omega_{\text{SHG}} = 2\omega$ . This effect was the first nonlinear process to be demonstrated experimentally [43] and is the workhorse of the present experiments. Here and in the following, the excitation frequency is termed the *fundamental* frequency, and its second harmonic the *SHG* frequency.

Based on equation (1.3) and equation (2.1), it is clear that the dielectric constant of the medium  $\epsilon_r$  now depends on the electric field strength. In a simplified picture where no assumption is made regarding the symmetry properties of the material, this corresponds to complementary terms in the restoring force of equation (1.23),

$$\ddot{x} + \gamma \dot{x} + \underbrace{\omega_0^2 x + C_3 x^2 + C_4 x^3 + \dots}_{\text{restoring force}} = \frac{-e}{m^*} E \quad , \quad (2.2)$$

where  $C_i$  represents the strength of the  $i$ -th power term in the resulting anharmonic potential. The corresponding second order nonlinear susceptibility is given classically by the product of the linear susceptibilities [46, 116]:

$$\chi^{(2)}(\omega_3 = \omega_1 + \omega_2, \omega_1, \omega_2) = \frac{C_3 m^*}{n_e^2 e^3} \chi^{(1)}(\omega_3) \chi^{(1)}(\omega_1) \chi^{(1)}(\omega_2) \quad , \quad (2.3)$$

with  $\omega_1 = \omega_2 = \omega$  and  $\omega_3 = 2\omega$  in the case of SHG. Hence, it is necessary, yet not sufficient, to have finite values of the linear susceptibilities at both the fundamental and SHG frequencies for SHG to take place. Consequently, the resonant feature of the linear susceptibility in nanostructures is expected to play a major role when characterizing the nonlinear response of nanostructures, see equation (1.3.1) and section 3.1.2.

This is best understood in describing the material system as a quantum mechanical system. Departing from the classical, wave-like description of light, the corresponding quantum mechanical picture describes the light-matter interaction in terms of photon absorption and emission processes. In this frame, linear optics processes involve a single photon of energy  $\hbar\omega$  being absorbed from a ground state  $|g\rangle$  to an excited state  $|e\rangle$ , and relaxing back to  $|g\rangle$

by emission of a photon of the same energy  $\hbar\omega = \Delta E_{eg}$ . In contrast, as mentioned above, nonlinear optics effects require more than one photon to initiate such transitions. For SHG, the transition from  $|g\rangle$  to  $|e\rangle$  is carried out by *simultaneous* absorption of two photons of energy  $\hbar\omega$  via an intermediate state  $|i\rangle$ . The transition back to the ground state is achieved *instantaneously* by emission of a photon with energy  $\Delta E_{eg} = \hbar\omega_{\text{SHG}} = 2\hbar\omega$ , see figure 2.1.

The regime described above belongs to perturbative nonlinear optics: The term amplitudes of the Taylor expansion in equation (2.1) decline with higher order, and the ground and excited quantum states of the nonlinear material are unchanged by the interaction with the optical field. One speaks of a *parametric* nonlinearity for which energy and momentum conservation of the optical field is observed. The system returns to the same *real* ground state after excitation, whereas both the excited and the intermediate states can be real or *virtual*. So-called virtual states really are real states excited highly non-resonantly. Indeed, the conversion process is characterized as instantaneous: A parametric process population can be removed from the ground state only for the brief interval of time when it resides in a virtual level. According to the uncertainty principle, a population can reside in a virtual level for a time interval of the order of  $\hbar/\Delta E$ , where  $\Delta E$  is the energy difference between the intermediate level energy  $E_{|i\rangle}$  and  $\hbar\omega$ . As a direct consequence, the probability of absorption of the two photons is enhanced when the intermediate state (and/or excited) state is real, i.e. when  $|i\rangle$  (and/or  $|e\rangle$ ) possesses a finite lifetime. For nanostructures, the intermediate state corresponds to the plasmonic excitation and the link with equation (2.3) is straightforward:  $\chi^{(1)}(\omega)$  takes large values only for those values of  $\omega$  where a plasmon is excited with lifetime as discussed in section 1.3.3.

The nonlinear terms of equation (2.1) lead to an excitation of frequency  $2\omega$ , and equation (1.14) evolves into the nonlinear optical wave equation [46]:

$$\nabla^2 \mathbf{E} + \frac{\varepsilon}{c_0^2} \frac{\partial^2}{\partial t^2} \mathbf{E} = \mathbf{S} \quad , \quad (2.4)$$

where  $\mathbf{S}$  is a source term driving the nonlinear optical wave. For instance, when light with frequency  $\omega$  and electric field  $\mathbf{E}(\omega)$  is incident on a material, harmonic generation can lead to an electromagnetic polarization at frequency  $2\omega$ . This acts as source term  $\mathbf{S}(2\omega)$  for an SHG light wave [43]. It is possible to express the source term by the multipole expansion [45],

$$\mathbf{S} = \mu_0 \frac{\partial^2 \mathbf{P}^{\text{NL}}}{\partial t^2} + \mu_0 \left( \nabla \times \frac{\partial \mathbf{M}^{\text{NL}}}{\partial t} \right) - \mu_0 \left( \nabla \cdot \frac{\partial^2 \mathbf{Q}^{\text{NL}}}{\partial t^2} \right) \quad , \quad (2.5)$$

where  $\mathbf{P}^{\text{NL}}$ ,  $\mathbf{M}^{\text{NL}}$ , and  $\mathbf{Q}^{\text{NL}}$  are the electric dipole (ED), magnetic dipole (MD), and electric quadrupole (EQ) moments, respectively. This expansion is valid when volume elements whose dimensions are small compared to the field wavelength are used in averaging to obtain such macroscopic quantities. Taking terms of the order 0 and 1 in the expansion of the electromagnetic field into account, the following contributions, associated with the ED, MD, and EQ, are obtained [117–119]:

**0<sup>th</sup> order:**

$$\mathbf{P}_i^{\text{NL}} \propto \chi_{ijk}^{eee} : \mathbf{E}_j \mathbf{E}_k \quad (2.6)$$

1<sup>st</sup> order:

$$\mathbf{P}_i^{\text{NL}} \propto \chi_{ijkl}^{em,q} : \mathbf{E}_j \nabla_k \mathbf{E}_l \quad (2.7)$$

$$\mathbf{M}_i^{\text{NL}} \propto \chi_{ijk}^{mee} : \mathbf{E}_j \mathbf{E}_k \quad (2.8)$$

$$\mathbf{Q}_{ij}^{\text{NL}} \propto \chi_{ijkl}^{qee} : \mathbf{E}_k \mathbf{E}_l \quad (2.9)$$

The  $\chi$  tensors above denote nonlinear susceptibilities and describe the response of any system in the presence of intense light field. The subscripts  $i, j, k$ , and  $l$  refer to Cartesian coordinates ( $i, j, k, l \in \{x, y, z\}$ ), and summation over repeating indices is implied. The superscripts refer to electric-dipole (e), magnetic-dipole (m), and electric quadrupole (q) interactions. Thus, the meaning of the subscripts applies to the electric field or magnetic field accordingly. For instance, in  $\chi_{ijk}^{eee}$  the indices  $j, k$  express the polarization direction of the incident light fields, while  $i$  determines the direction of the induced electric-dipole oscillation. Equation (2.7) involves MD and EQ coupling at the fundamental frequency  $\omega$  while in equation (2.8) and (2.9) the magnetization and quadrupolarization at  $2\omega$  is considered. Each term contributes linearly to the SHG process.

The tensor components  $\chi_{ijk}^{eee}$  and  $\chi_{ijk}^{mee}$  obey intrinsic permutation symmetry on the indices  $j$  and  $k$  because the components of the electric field of the fundamental wave are indistinguishable. As for the EQ tensors, due to the rotational symmetry and zero-trace property of the polar quadrupole moment tensor,  $\chi_{ijkl}^{qee} = \chi_{jikl}^{qee} = \chi_{jilk}^{qee} = \chi_{ijlk}^{qee}$  holds. Additionally, emission from the quadrupolarization involves a gradient of the source with respect to the direction of propagation  $\nabla_i \mathbf{Q}_{ij}$ .

In crystalline solids, the magnetic dipole and electric quadrupole contributions are smaller than the electric dipole by a factor  $\lambda/a \sim 10^3$ , where  $\lambda$  is the radiation wavelength and  $a$  is the lattice constant of the crystal. Therefore, they can often be neglected which is termed as electric-dipole approximation. However, nanostructures typically present a much smaller ratio  $\lambda/a \leq 10$ , for which the SHG contributions of MD and EQ terms may become relevant.

Neumann's principle states that "any type of symmetry which is exhibited by the point group of the crystal is possessed by every physical property of the crystal". Hence, the magnetic and crystallographic symmetry operations of a sample uniquely determine the set of nonzero tensor components  $\chi_{ijk}, \chi_{ijkl} \neq 0$ , see sections 3.1.3 and 3.1.5. In turn, observation of a vanishing component allows one to derive information about the structure. Tensors are classified according to their transformation behavior under the two fundamental parity operations, i.e. space inversion and time inversion, both having eigenvalues  $\pm 1$ . For tensors, the corresponding operators are typically denoted by  $\hat{I}(r \rightarrow -r)$  and  $\hat{T}(t \rightarrow -t)$ , respectively.

**Polar and axial tensors:** Polar and axial tensors distinguish themselves with respect to spatial inversion. A tensor  $\Xi^{(n)}$  of rank  $n$  is classified according to which of the following equation holds:

$$\text{polar:} \quad \hat{I}\Xi^{(n)}(\mathbf{r}, t) = (-1)^n \Xi^{(n)}(-\mathbf{r}, t) \quad (2.10)$$

$$\text{axial:} \quad \hat{I}\Xi^{(n)}(\mathbf{r}, t) = (-1)^{n+1} \Xi^{(n)}(-\mathbf{r}, t) \quad (2.11)$$

This definition has important general consequences: In a centrosymmetric crystal, all axial tensors of even rank and all polar tensors of odd rank have to vanish identically. Moreover, the product of two polar or two axial tensors transforms like a polar tensor, whereas the product of one polar and one axial tensor behaves like an axial tensor.

**Tensors of i- and c-type:** The classification as i- or c-tensor reflects either the invariance (i-) or the change (c-) of the sign of a tensor under time reversal:

$$\text{i-tensor:} \quad \hat{T}\Xi^{(n)}(\mathbf{r}, t) = +\Xi^{(n)}(\mathbf{r}, -t) \quad (2.12)$$

$$\text{c-tensor:} \quad \hat{T}\Xi^{(n)}(\mathbf{r}, t) = -\Xi^{(n)}(\mathbf{r}, -t) \quad (2.13)$$

A product of two i- or two c- tensors always transforms like an i-tensor (is invariant under  $\hat{T}$ ), whereas the product of an i- and a c-tensor changes sign under the time-reversal operation. The concept of i- and c-tensors is important for magnetically ordered systems, see section 3.1.4. The onset of magnetic ordering generally violates the time-inversion symmetry of a crystal, allowing for nonzero c-tensors.

According to these definitions, the electric dipole tensor  $\chi^{eee}$  is a third-rank polar tensor. All indices are associated with a polar vector. The magnetic dipole tensor  $\chi^{mee}$  is an axial third-rank tensor. The last two indices are associated with a polar vector (electric quantities), whereas the first index is associated with an axial vector (magnetic quantity). The electric quadrupole tensors  $\chi^{eem,q}$  and  $\chi^{qee}$  are polar fourth-rank tensors. All indices are associated with polar vectors. Consequently, any improper transformation (reflection or inversion) leads to a different sign between the respective components of  $\chi^{eee}$  and the MD and EQ tensors. A direct conclusion is that the magnetic-dipole and the electric-quadrupole contributions are allowed when a center of inversion is present. In contrast, electric-dipole contributions to an SHG signal are only allowed in noncentrosymmetric crystals: An electromagnetic wave incident on a centrosymmetric structure such as an isotropic continuous metal surface at normal incidence (or oblique to this surface in s-polarization) cannot create an ED-SHG wave according to equation (2.6) for it implies  $\chi_{ijk}^{eee} = -\chi_{ijk}^{eee}$  [120, 121]. However, in centrosymmetric material a break of symmetry occurs at an interface at other incidences and polarization. Then, symmetry is disrupted in the first few atomic or molecular layers of a system, so that the properties of the surface SHG signal provides information about the interface only. Surface SHG is possible even for materials which do not exhibit bulk SHG and is an important characterization method in surface science.

The sensitivity to structure and symmetry makes SHG a key technique for investigating the effects of shape, structure, and symmetry. The polarization dependence mentioned above is the first of three features that are signatures for SHG signals. Second feature, the intensity of the nonlinear signal is proportional to the square of the nonlinear source term, hence to the square of the fundamental intensity  $I_\omega$  and to the power four of the incoming light electric field, see equation (1.16):

$$I_{2\omega} \propto |\mathbf{S}|^2 \propto I_\omega^2 \propto E_\omega^4 \quad . \quad (2.14)$$

Together with equation (1.30), this relation is key when employing nanostructures as optical catalyst. The process description is developed in section 3.1.4. The third and last feature has

already been mentioned in providing the parametric quantum mechanical picture for SHG emission: A photon of frequency  $2\omega$  is emitted under excitation at  $\omega$ . In other words, the SHG emission is spectrally sharp when excited monochromatically. These criteria are unique signatures distinguishing SHG signals from other optical processes such as photoluminescence, which is treated in the following section.

## 2.2 Two-Photon Photoluminescence

The nonlinear mechanisms described above are parametric processes which are described by a real susceptibility. Yet, transition from a ground state energy level to a real excited state can occur via non-parametric processes of order  $n$ . Here, the energy need not be conserved because energy can be transferred to or from the material medium. These processes of order  $n$  are described by the imaginary part of the susceptibilities  $\chi^{(n)}$ . Multiphoton absorption belongs to such non-parametric mechanisms: A transition to a higher energy level is obtained by simultaneous absorption of  $n$  photons via  $n-1$  virtual states. The total absorption cross-section  $\sigma$  is determined as the sum of all order cross-sections:  $\sigma_{\text{abs}} = \sum_n \sigma_{\text{abs}}^{(n)} I_\omega^{n-1}$ . In particular, while the linear cross-section does not depend on the laser intensity  $I_\omega$ , the two-photon absorption depends linearly on it. Consequently, the transition rate  $R^{(2)}$  due to two-photon absorption scales as the square of the laser intensity:

$$R^{(2)} = \frac{\sigma_{\text{abs}}^{(2)} I_\omega^2}{\hbar\omega}. \quad (2.15)$$

For high field strength, the multiphoton absorption processes lead to absorption even in the case where the electric dipole transition is forbidden by the selection rule for the linear absorption, or if the fundamental frequency is not resonant with the investigated system. The two-photon absorption process was first described theoretically in 1931 and demonstrated experimentally shortly after the invention of the laser in 1961 [122, 123].

The process is relevant for this work, for it can lead to luminescence of the gold nanostructures. One then speaks of two-photon photoluminescence (TPPL, also found as 2PPL in literature). For gold, it has been experimentally demonstrated that TPPL is the result of two sequential single-photon absorption steps mediated by a real state [124]. In detail, the first photon excites an electron via an intraband transition within the  $sp$  conduction band, while the second photon excites an electron from the  $d$  band to recombine with an  $sp$  hole in the conduction band. The dynamics of the TPPL signal, caused by the radiative recombination of  $d$  holes, is ruled by the relaxation time of the transient distribution excited in the  $sp$  conduction band after the first absorption event [125, 126]. Thus, the TPPL yield depends on the laser pulse width  $\delta$ , hence on the laser-pulse peak power. Indeed, in the  $\delta > 1$  ps regime, the TPPL yield decreases as  $\delta$  is increased. The process saturates for shorter pulse widths and becomes independent of  $\delta$  [124]. Because of the increased density of states, interband radiative recombination in TPPL occurs close to the  $L$  and  $X$  points in the reciprocal space, see figure 1.2. This leads to broad emission bands located in the green and red spectral regions, respectively [126].

The band structure details in figure 1.2 show that a minimal fundamental photon energy of 0.90 eV is necessary to excite charge carriers above the Fermi level via two-photon absorption near the  $X$  point (1.20 eV near the  $L$  point). This corresponds to the spectral range of interest of this work, and caution in separating TPPL from SHG signals should be taken. In doing so, the quadratic dependence on the fundamental beam electric field is shared between the TPPL and SHG signal, see equation (2.15). Thus it is not an appropriate criterion in differentiating the two signals. The *incoming* polarization dependence is not relevant either, for nanostructuring leads to polarization-dependent inhomogeneous field distributions and therewith anisotropic TPPL yield. In consequence, only the *emission* polarization and/or the spectral bandwidth of the signals differ: isotropic and spectrally broad for TPPL, respectively, but anisotropic and nearly monochromatic, respectively, for SHG.



# Chapter 3

## Experimental Methods

This section introduces the experimental methods used in this work. First, the electron beam lithography (EBL) sample fabrication process is summarized in section 3.1.1. Two kinds of samples are produced depending on the investigation: Metamaterial characterization, or application thereof, for nonlinear amplification. The rationales for the corresponding building block geometries are presented in section 3.1.2 and 3.1.4, respectively. The resulting tensor components allowed for SHG investigation are explained and listed in section 3.1.3 and 3.1.5, respectively. After the fabrication, a preliminary measurement of the linear-optical properties of the samples is carried out to experimentally verify the plasmonic resonance positions. The setup for measuring the linear spectra is described in section 3.2. The core work consists of nonlinear spectroscopy investigations: The tunable high-intensity laser source is presented in section 3.3. The optical setup for measurement of SHG is explained in section 3.4. The chapter ends with specific aspects regarding the signal normalization and sample destruction limit in section 3.6 and 3.7, respectively.

### 3.1 Samples

#### 3.1.1 Fabrication: Electron Beam Lithography

EBL is a versatile method to define a nanoscale 2D mask pattern [127]. 3D samples can be obtained by stacking [128], yet this work concentrates on *monolayer* structured samples. The method is based on a scanning-electron microscope (SEM) of which the electron beam deflection unit is controlled by a computer providing the pattern from a CAD software. The beam is switched on and off while rastering specific locations on the sample substrate: Exposure dose and dwell time is assigned in the software. The rastering path need not be a regular grid but is optimized for shortest overall fabrication time and minimization of charge build-up effects. EBL is applicable to non-conductive substrates with the help of a thin conductive layer deposition, typically indium tin oxide (ITO,  $\text{In}_2\text{O}_3:\text{SnO}_2$ ) or, as in this case, chromium with a nominal thickness of 3 nm. The function of such a layer is to drain the electrons of the writing beam and avoids local charging of the sample.

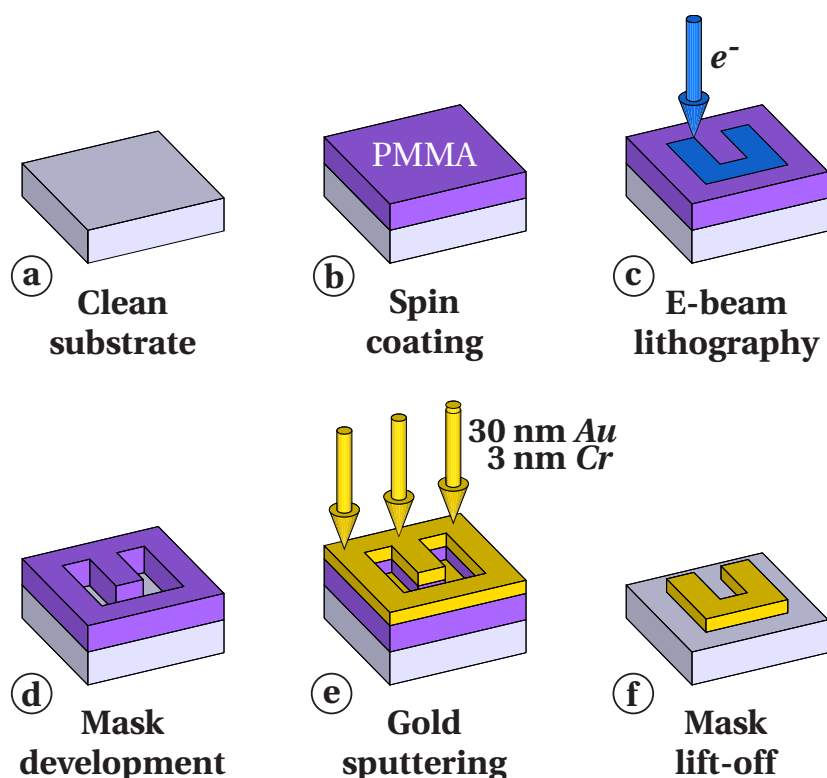


**Figure 3.1** – Main fabrication steps of plasmonic nanostructures by means of electron beam lithography. For sake of simplicity, the diagram shows neither the second PMMA layer nor the uppermost conductive layer, but their actual presence is herewith explicitly mentioned. The deposition of a thin 3 nm chrome layer, used for the adhesion of gold on glass, is stressed in (e).

The samples used in this work were produced in the group of Harald Giessen at the University of Stuttgart. The EBL system (e\_Line, Raith GmbH) at the Max-Planck-Institute for Solid State Research Stuttgart was used. Typical values for SEM operation include an acceleration voltage of 20 kV and an aperture of 20  $\mu\text{m}$  resulting in an average beam current of 135 pA. The patterning procedure is summarized in figure 3.1. The substrate in (a) is covered by a 120 nm layer of the standard positive resist poly(methyl-methacrylate) (PMMA). This is deposited from solution by spin-coating at 3000 rpm for 5 s followed by a 5 min post-bake at 160  $^{\circ}\text{C}$  for polymerization, (b). A second PMMA layer is deposited (not shown): Slightly less sensitive due to a higher molecular weight, it improves the quality of the end structure's edges. Here, spin-coating occurs at 8000 rpm for 30 s, followed by a 5 min post-bake at 160  $^{\circ}\text{C}$  for polymerization: A 50 nm layer results. The above mentioned conductive layer is deposited on top of the PMMA and is removed during processing (not shown). The organic resist is sensitive to irradiation with electrons: Upon exposure with high-energy electrons, chemical bonds of the long polymer chains break up, (c). Subsequently, the resist is removed in all areas where the local charge dose exceeded the sensitivity threshold of 325  $\mu\text{C cm}^{-2}$ : The development occurs during a 90 s bath in a wet solution (mixture of methyl-isobutyl-ketone (MIBK) and isopropanol in a volume ratio of 1:3). The result is a nanostructured polymer mask with precisely located holes at the exposed areas, (d).

The resolution is not primarily determined by the beam spot size, but rather limited by scattered secondary electrons, effectively exposing nearby regions as well (proximity effect). However, electron-beam lithography yields reproducible and accurate results. Shapes with feature sizes around 20 nm and accuracy of the order of a few nanometers is common nowadays [129, 130]. The magnification of the SEM determines both the scanning resolution and

the write-field size, i.e. the area that can be addressed by deflecting the electron beam alone, without moving the motorized sample stage. A  $\times 1000$  magnification results in a scanning resolution of about 5 nm and a write-field size of  $100 \times 100 \mu\text{m}^2$ . Larger fields are exposed piece-wise through shifting the substrate on a motorized stage. This is a potential issue for reproducibility: Perfect focus needs to be maintained. Thus, a basic design, or building block, is reproduced over a large area: For the present samples, the distribution of the unit blocks corresponds to a 2D Shah function, i.e. a regular quadratic array with identical periods in both directions. The major drawback of this method is the sequential processing (one unit block is exposed after another) leading to lengthy exposure times of several hours for patterning a large nanostructures field. During this process, absolute mechanical and electrical stability needs to be assured.

After the mask patterning, a first 3 nm layer of chromium is evaporated. Chromium serves as an adhesion promoter for gold, which sticks poorly to the substrates used. Owing to its reduced thickness, the chromium layer does not impair the optical properties of the samples. Sputtering of a gold layer follows with a typical thickness of 30 nm, (e). Most of the gold remains on top of the resist: Only the gold volume deposited through the holes in the resist contributes to the formation of the gold nanostructures. Then, the resist and the gold on top of it are removed by a lift-off process in a hot acetone bath at  $50^\circ\text{C}$  for 2 min and subsequent rinsing in acetone, (f). The end result is a sample with several fields consisting each of an array of identical gold nanoparticles of a specific design on top of a dielectric substrate.

Contaminations or failure of one of the above processes can render a sample useless. Deviation from a perfect nominal design can occur on different scale levels: In this work, defects are called *macroscopic* on the millimeter scale of the substrate, *microscopic* across the hundred micrometer span of a field, *mesoscopic* across the hundred nanometer length of a unit block, and *nanoscopic* for the finest features of the nanostructures. After each production batch, the macroscopic and microscopic homogeneity of the gold particle arrays and the cleanliness are checked under an optical microscope. Defective samples are discarded. Smaller scale inspection is verified under a field emission scanning electron microscope (S-4800, Hitachi Ltd.) to check the actual geometry of the gold structures and their surface and edge quality. Minimal deviations of a couple of nanometers from the nominal design are observed. The linear-optical properties are not significantly altered, but the impact is potentially critical in nonlinear-optical experiments since this reduces the symmetry of the structures. Thus, mesoscopically, oblique-view SEM pictures reveal that the corners and edges of the fabricated gold structures are actually not straight, but rounded off. Also, each single structure displays its own shape variation analogous to bending, twisting, shearing, or asymmetrical scaling. This is due to surface tension, to the EBL smallest mechanical or electrical instabilities (vibrations, electron-beam astigmatism), and to the lift-off process. On a nanometer scale, each structure always displays rough surfaces and edges. Such extra features originate from the lift-off process and from the polycrystalline nature of the sputtered gold composing the nanostructures. These 3D structures constitute hot spots of extremely high electromagnetic fields (lightning-rod effect). They can result in systematic errors and misinterpretations.

Gold is the metal of choice since it is a very good conductor up to optical frequencies. It does not degrade when exposed to air so that optical experiments should be highly reproducible

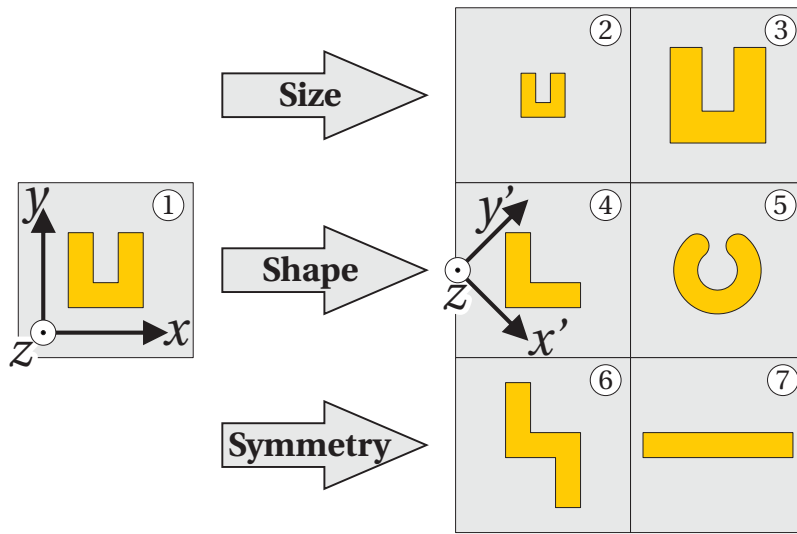


**Figure 3.2** – Schematic geometry of the building blocks for the metamaterials fabricated as two-dimensional periodic arrays of gold on glass. The geometries were selected to investigate the effects of size, shape, and symmetry on the nonlinear optical performance. The Cartesian coordinate system is oriented according to [120]. The L-shaped structures require a 45° rotation of their coordinate system along the  $z$ -axis to match the nomenclature and symmetry operations used for the description of the other structures.

with a given sample over a long period of time of several months. Resistance to oxidation is the reason why gold is preferred over e.g. aluminum or silver, although they present sharper and higher energy plasmon resonance for equivalent shape. A trade-off is also made for the choice of the supporting transparent substrate in the following section. Alternative to glass are e.g. ITO (no need for an extra conductive layer during patterning) and sapphire (higher thermal conductivity for energy dissipation) but for both the refractive index is too high and red-shifts the resonances above the detection spectral range of the setup, see section 3.4. The choice of a structure geometry is explained in the following section.

### 3.1.2 Nonlinear Characterization: Nanostructured Gold on Glass

In this section, the substrate consists of an amorphous  $10 \times 10 \text{ mm}^2$  quartz glass substrate (Suprasil 1, Heraeus GmbH). Being centrosymmetric, it is inactive for SHG, and detection of SHG signals is traced back to the nanostructures lithographed on its surface by EBL, see previous section. Here, the goal is to deepen the understanding of the link between the nanostructures morphology and their nonlinear optical properties. U-shaped sub-wavelength building-blocks are selected as the reference structure for this investigation since they are most commonly studied [48, 49]. Furthermore, this shape is easily scalable, and basic design variations in size, symmetry and shape complexity allow for investigating the effects these parameters have on the SHG performance. Figure 3.2 depicts the seven design variations that are measured:

- i **Reference design:** The reference building block consists of a classical U-shaped SRR of approximately 215nm base length with an arm-to-base length ratio close to one. Base and arm width amounts to 70nm. For an excitation parallel to the arms, a linear resonance at 1.25eV with a 0.50eV FWHM is observed.
- ii **Size effect:** The effect of size scaling is investigated with the second and third designs. The former increases both the base and arm lengths to achieve a linear resonance at

lower energy (0.90 eV with 225 nm base length), while the later reduces them to obtain a linear resonance at higher energy (1.30 eV with 200 nm base length). Note that the effects of scaling and spectroscopy are directly compared in the present approach: In contrast, Klein et al. substituted spectroscopy by geometric scaling in their experiments (wavelength scaling instead of structural scaling) [48, 49].

- iii **Shape effect:** All further shape variations are adapted to ensure a linear resonance matched to the first design. Designs number 4 and 5 give insight into the effect of shape complexity. The basic shape of an SRR is retained, but the number of corners is reduced in the design. Corners are associated with local field peaks and may favor higher-order nonlinear contributions, e.g. according to equation (2.5). The elementary unit in configuration 4 has no base and consequently presents one pair of corners less in an L-shaped geometry [116, 131–133]. Both arms share the same nominal length and width, about 295 nm and 80 nm, respectively. Design 5 avoids corners altogether with its round C-shaped geometry. Nominal dimensions are a 345 nm diameter, 80 nm width, and 45° opening angle. Noticeably, both structures share the same symmetry class and therewith the allowed SHG contributions as the U-shaped one, see section 3.1.3.
- iv **Symmetry effect:** Centrosymmetric structures are produced in the form of the last two layouts. For these structures any SHG emission is forbidden in the electric dipole approximation so that higher-multipole or local contributions according to section 2 become observable. Pattern number 6 differs from the original design only in that one arm is flipped respectively to the base. Thus, only the symmetry is changed while retaining the shape complexity. Base and arm length amount to 235 nm, with a width of 85 nm. The last design, number 7, represents a simple cut-wire geometry, i.e. a U-shaped structure with unfolded arms. Total length amounts to 385 nm with a width of 60 nm. Symmetrical features are clearly visualized later in figure 3.4. Their consequences in terms of expected allowed tensor components is discussed in the next section.
- v **Bulk material effect:** As a bulk material reference, a sample consisting of a bare gold film is produced, covering half the area of the substrate (not shown). Its use in the evaluation for the damage threshold for laser irradiation is discussed in section 3.7. It is also employed to measure the surface-induced SHG from gold, see section 4.2.2.

Electron micrographs of the fabricated structures are shown in figure 3.3. It shows normal-incidence images of some of the structures investigated in this work. The structures are mechanically very stable and withstand aggressive cleaning steps such as pressured air flow and ultrasound bath of acetone where required. Further SEM acquisitions are shown later in figure 4.3.

A substrate is patterned with different fields, at least one for each design, each comprising an array of thousands of building blocks. The lateral size of each array is  $250 \times 250 \mu\text{m}^2$  with equivalent field-to-field distances in the order of  $250 \mu\text{m}$ . The period within each field is 550 nm so that both the near-field and far-field coupling of the structures is negligible, see end of section 1.3.3. As mentioned in section 1.3.1, such an ensemble of nanostructures with size features smaller than the wavelength of the impinging light is considered as an effective

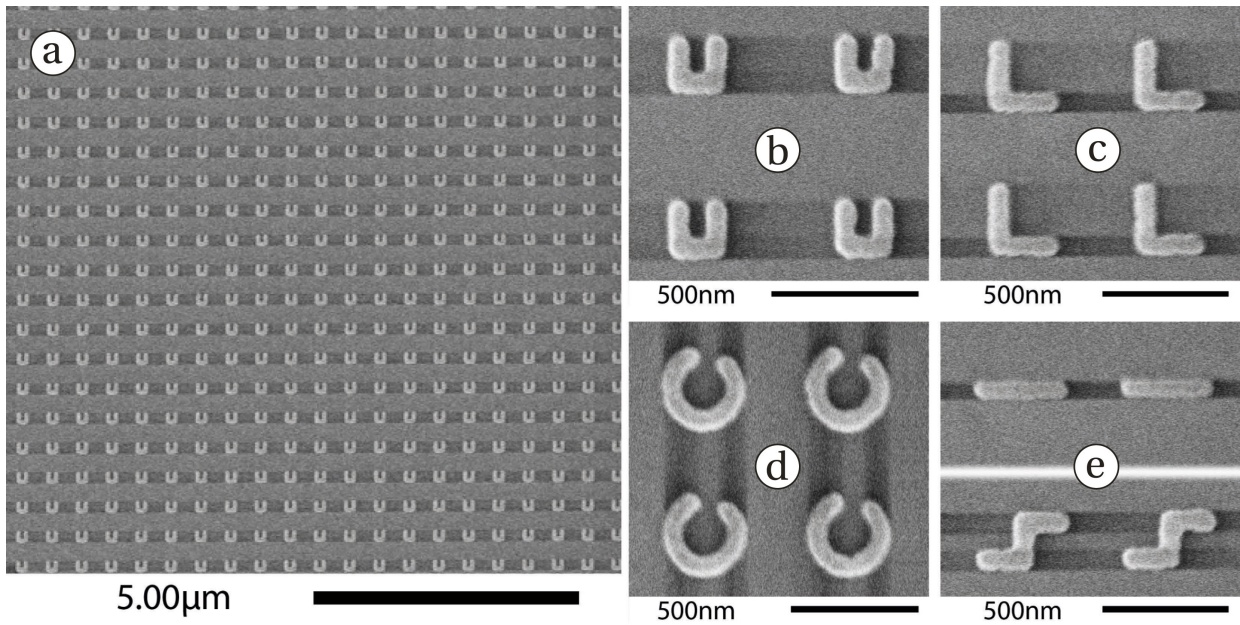


**Figure 3.3** – Normal incidence SEM micrographs of gold structures (light gray) written on a glass substrate (dark gray). Image (a) demonstrates the uniformity of the structures over a large area. The shadows between the nanostructures are caused by the screening of secondary electrons by the metal.

material in this work: Each nanostructure acts as a meta-atom, or rather meta-molecule whose shape defines eigen-polarization axes. As a consequence, the symmetry features impose a reduction on the number of non-vanishing tensor components, as explained in section 2.1. The allowed tensor components are determined in the following section.

### 3.1.3 Gold Nanostructures: SHG Tensor Components

Here and in section 3.1.5, an effective SHG susceptibility is considered, describing the global symmetry of a periodic arrangement of *ideal* gold nanostructures. Therewith, the local mesoscopic and nanoscopic deviations mentioned in section 3.1 are neglected in the individual structures. It is one purpose of this work to verify the validity of this approach, see section 4.2.3. The symmetry features for each design are illustrated in figure 3.4. The designs 1 to 5 in figure 3.2 all share the same symmetry. At normal incidence, the substrate's role in the nonlinear response is commonly ignored in SHG studies. Accordingly, only the gold structure symmetry should be considered. However, the strong gradients in charge distribution in plasmonic structures hint at a possible effect of the glass substrate. Its presence is a further reduction in sample symmetry. Therefore, both analyses with or without substrate are carried out. A distinction in symmetry class appears for the same design: Where the substrate is taken into consideration, the red symmetry planes in figure 3.4 are irrelevant. For simplicity, designs 6 and 7 may be called centrosymmetric structures even when the substrate is considered.

Table 3.1 regroups all information related to the symmetry class and allowed tensor components as related to equation (2.6) to (2.9). Here, following the international notation, the point group depends on the symmetry operations that leave the structures invariant. Based on

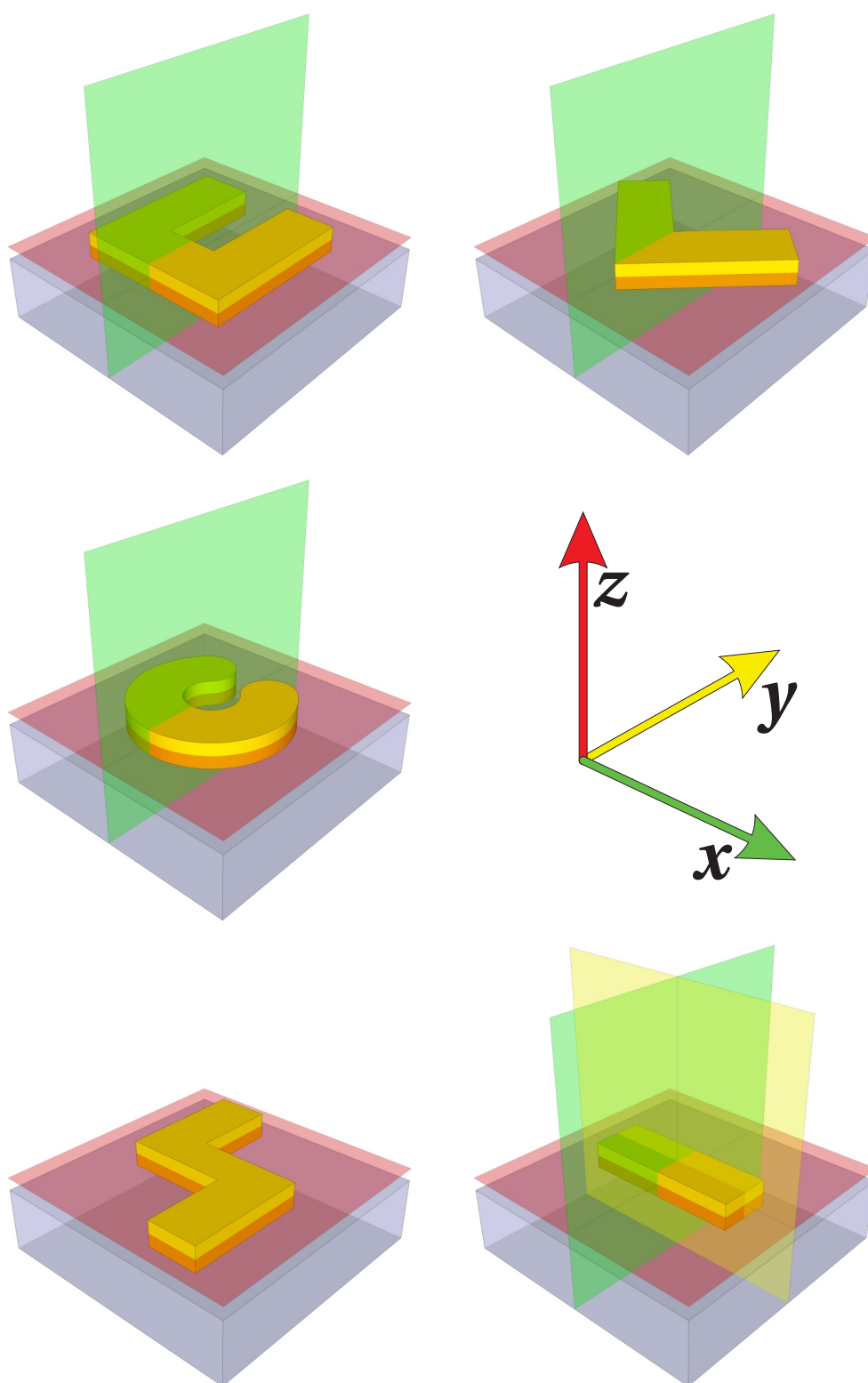


**Figure 3.4** – Symmetry elements of the investigated nanostructures. The represented surfaces are symmetry planes for the gold nanostructures. The red plane ceases to be a symmetry element when the glass substrate is considered in addition to the gold volume. The U-, L-, and C-shaped structures are equivalent from a symmetry point of view.

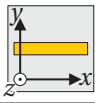
**Table 3.1** – Symmetry operations, point group, and allowed tensor components for the investigated nanostructures. The symmetry analysis is carried out up to the first order expansion of the electromagnetic field. Simplification is available based on the setup configuration and considering a *plane-wave* excitation and outgoing emission. All measurements are carried out at normal incidence ( $\mathbf{k} = (0, 0, 2\pi/\lambda)$ ). Non-contributing components according to this configuration are crossed out.

	without substrate	with substrate
<b>Symmetry operations</b>	$1, 2_y, \bar{2}_x, \bar{2}_z$	$1, \bar{2}_x$
<b>Point group</b>	<b>m2m</b>	<b>m</b>
<b>Tensor components</b>	Non-vanishing elements indices ( $ijkl \equiv \chi_{ijkl}$ )	
$\chi_{ijk}^{eee}$	$xyx = xyx, yxx, yyj, yzz,$ <del><math>zyz = zzy</math></del>	$xyx = xyx, yxx, yyj,$ <del><math>xxz = xzx, yyz = yzy, yzz,</math></del> <del><math>zxx, zyy, zyz = zzy, zzz</math></del>
$\chi_{ijk}^{mee}$	<del><math>xyz = xzy, yxz = yzx,</math></del> <del><math>zxy = zyx</math></del>	$xxx, xyj, yxy = yyx,$ <del><math>xyz = xzy, xzz, yxz = yzx,</math></del> <del><math>zxy = zyx, zxx = zzx</math></del>
$\chi_{ijkl}^{qee}$	<del><math>xxxx, xxyy, xxzz,</math></del> <del><math>xyxy = xyyx = yxxy = yxyx,</math></del> <del><math>xzxx = xzzx = zxxx = zxxz,</math></del> <del><math>yyxx, yyyy, yyzz,</math></del> <del><math>yzyz = yzzy = zyyz = zyzy,</math></del> <del><math>zzxx, zzyy, zzzz</math></del>	<del><math>zxxj = zxyx = xzxy = xzyx,</math></del> <del><math>zyxx = yzxx, zyjj = yzyy,</math></del> <del><math>xxxx, xxyy, xxyz = xxzy,</math></del> <del><math>xyxy = xyyx = yxxy = yxyx,</math></del> <del><math>xyxz = xyzx = yxxx = yxxz,</math></del> <del><math>xzxx = xzzx = zxxx = zxxz,</math></del> <del><math>yyxx, yyyy, yyyz = yyzy,</math></del> <del><math>yyzz, yzyz = yzzy,</math></del> <del><math>yzzz = zyzz, zyyz = zyzy,</math></del> <del><math>zxxx, zzyy, zzyz = zzzj,</math></del> <del><math>zzzz, xxxz</math></del>
$\chi_{ijkl}^{eem,q}$	<del><math>xxxx, xxyy, xxzz, xyxy,</math></del> <del><math>xyyx, xzxx, xzzx, yxxy,</math></del> <del><math>yxyx, yyxx, yyyj, yyzz,</math></del> <del><math>yzyz, yzzy, zxxx, zxxz,</math></del> <del><math>zyyz, zyzy, zxxx, zzyy,</math></del> <del><math>zzzz</math></del>	<del><math>xxzy, xyzx, yxxz, yyzy,</math></del> <del><math>xxxx, xxyy, xxyz, xxzz,</math></del> <del><math>xyxy, xyyx, yxxz, xzxy,</math></del> <del><math>xzyx, xzxx, xzzx, yxxy,</math></del> <del><math>yxyx, yxxx, yyxx, yyyj,</math></del> <del><math>yyyz, yyzz, yzxx, yzyy,</math></del> <del><math>yzyz, yzzy, yzzz, zxxx,</math></del> <del><math>zxyx, zxxx, zxxz, zyxx,</math></del> <del><math>zyyy, zyyz, zyzy, zyzz,</math></del> <del><math>zxxx, zzyy, zzyz, zzzj,</math></del> <del><math>zzzz</math></del>

Table 3.1 – (continued)

	without substrate	with substrate
<b>Symmetry operations</b>	$1, \bar{1}, 2_z, \bar{2}_z$	$1, 2_z$
<b>Point group</b>	<b>2/m</b>	<b>2</b>
<b>Tensor components</b>	Non-vanishing elements indices ( $ijkl \equiv \chi_{ijkl}$ )	
$\chi_{ijk}^{eee}$	–	<del><math>xxz = xzx, xyz = xzy,</math></del> <del><math>yxz = yzx, yyz = yzy, zxx,</math></del> <del><math>zxy = zyx, zyy, zzz</math></del>
$\chi_{ijk}^{mee}$	<del><math>xxz = xzx, xyz = xzy,</math></del> <del><math>yxz = yzx, yyz = yzy, zxx,</math></del> <del><math>zxy = zyx, zyy, zzz</math></del>	<del><math>xxz = xzx, xyz = xzy,</math></del> <del><math>yxz = yzx, yyz = yzy, zxx,</math></del> <del><math>zxy = zyx, zyy, zzz</math></del>
$\chi_{ijkl}^{gee}$	<del><math>xxxx, xxxy = xxyx, xxyy,</math></del> <del><math>xxzz, xyxx = yxxx,</math></del> <del><math>xyxy = xyyx = yxxy = yxyx,</math></del> <del><math>xyyy = yxyy, xyzx, yxzz,</math></del> <del><math>xzxx = xzzx, xzyz = xzzy,</math></del> <del><math>yyxx, yyxy = yyyx, yyyy,</math></del> <del><math>yyzz,</math></del> <del><math>yzxz = yzzx = zyxx = yzxx,</math></del> <del><math>yzyz = yzzy = zyyz = zyzy,</math></del> <del><math>zxxx = zxxz = zxyx = zxxz,</math></del> <del><math>zzxx, zzxy = zzyx, zzyy,</math></del> <del><math>zzzz</math></del>	<del><math>xxxx, xxxy = xxyx, xxyy,</math></del> <del><math>xxzz, xyxx = yxxx,</math></del> <del><math>xyxy = xyyx = yxxy = yxyx,</math></del> <del><math>xyyy = yxyy, xyzx, yxzz,</math></del> <del><math>xzxx = xzzx, xzyz = xzzy,</math></del> <del><math>yyxx, yyxy = yyyx, yyyy,</math></del> <del><math>yyzz,</math></del> <del><math>yzxz = yzzx = zyxx = yzxx,</math></del> <del><math>yzyz = yzzy = zyyz = zyzy,</math></del> <del><math>zxxx = zxxz = zxyx = zxxz,</math></del> <del><math>zzxx, zzxy = zzyx, zzyy,</math></del> <del><math>zzzz</math></del>
$\chi_{ijkl}^{eem,q}$	<del><math>xxxx, xxxy, xxyx, xxyy,</math></del> <del><math>xxzz, xyxx, xyxy, xyyx,</math></del> <del><math>xyyy, xyzx, xzxx, xzzx,</math></del> <del><math>xzyz, xzzy, yxxx, yxxy,</math></del> <del><math>yxyx, yxyy, yxzz, yyxx,</math></del> <del><math>yyxy, yyyx, yyyy, yyzz,</math></del> <del><math>yzxz, yzzx, yzyz, yzzy,</math></del> <del><math>zxxx, zxxz, zxyx, zxxz,</math></del> <del><math>zyxz, yzxx, zyyz, zyzy,</math></del> <del><math>zzxx, zzxy, zzyx, zzyy,</math></del> <del><math>zzzz</math></del>	<del><math>xxxx, xxxy, xxyx, xxyy,</math></del> <del><math>xxzz, xyxx, xyxy, xyyx,</math></del> <del><math>xyyy, xyzx, xzxx, xzzx,</math></del> <del><math>xzyz, xzzy, yxxx, yxxy,</math></del> <del><math>yxyx, yxyy, yxzz, yyxx,</math></del> <del><math>yyxy, yyyx, yyyy, yyzz,</math></del> <del><math>yzxz, yzzx, yzyz, yzzy,</math></del> <del><math>zxxx, zxxz, zxyx, zxxz,</math></del> <del><math>zyxz, yzxx, zyyz, zyzy,</math></del> <del><math>zzxx, zzxy, zzyx, zzyy,</math></del> <del><math>zzzz</math></del>

Table 3.1 – (continued)

	without substrate	with substrate
<b>Symmetry operations</b>	$1, \bar{1}, 2_x, 2_y, 2_z, \bar{2}_x, \bar{2}_y, \bar{2}_z$	$1, 2_z, \bar{2}_x, \bar{2}_y$
<b>Point group</b>	<b>mmm</b>	<b>mm2</b>
<b>Tensor components</b>	Non-vanishing elements indices ( $ijkl \equiv \chi_{ijkl}$ )	
$\chi_{ijk}^{eee}$	–	<del><math>xxz = xzx, yyz = yzy, zxx,</math></del> <del><math>zyy, zzz</math></del>
$\chi_{ijk}^{mee}$	<del><math>xyz = xzy, yxz = yzx,</math></del> <del><math>zxy = zyx</math></del>	<del><math>xyz = xzy, yxz = yzx,</math></del> <del><math>zxy = zyx</math></del>
$\chi_{ijkl}^{qee}$	<del><math>xxxx, xxyy, xxzz,</math></del> <del><math>xyxy = xyyx = yxxy = yxyx,</math></del> <del><math>xzzz = xzzx = zxxz = zxxz,</math></del> <del><math>yyxx, yyyy, yyzz,</math></del> <del><math>yzyz = yzzy = zyyz = zyyz,</math></del> <del><math>zzxx, zzyy, zzzz</math></del>	<del><math>xxxx, xxyy, xxzz,</math></del> <del><math>xyxy = xyyx = yxxy = yxyx,</math></del> <del><math>xzzz = xzzx = zxxz = zxxz,</math></del> <del><math>yyxx, yyyy, yyzz,</math></del> <del><math>yzyz = yzzy = zyyz = zyyz,</math></del> <del><math>zzxx, zzyy, zzzz</math></del>
$\chi_{ijkl}^{eem,q}$	<del><math>xxxx, xxyy, xxzz, xyxy,</math></del> <del><math>xyyx, xzzz, xzzx, yxxy,</math></del> <del><math>yxxy, yyxx, yyyy, yyzz,</math></del> <del><math>yzyz, yzzy, zxxz, zxxz,</math></del> <del><math>zyyz, zyzy, zzzx, zzyy,</math></del> <del><math>zzzz</math></del>	<del><math>xxxx, xxyy, xxzz, xyxy,</math></del> <del><math>xyyx, xzzz, xzzx, yxxy,</math></del> <del><math>yxxy, yyxx, yyyy, yyzz,</math></del> <del><math>yzyz, yzzy, zxxz, zxxz,</math></del> <del><math>zyyz, zyzy, zzzx, zzyy,</math></del> <del><math>zzzz</math></del>

the point group and the SHG channel under consideration, one derives the non vanishing tensor components [120]. For the centrosymmetric structures (Z- and I-shaped, design 6 and 7), the coordinate system is oriented according to [120], with  $z$  representing the axis of highest symmetry. However, this referential is adapted for non-centrosymmetric geometries (U-, L-, and C-shaped, design 1 to 5) for homogeneity in the nomenclature.

Not all non-vanishing tensor component can be excited and/or analyzed. This is due to the experimental configuration imposed by the setup and leads to a drastic simplification of the list of components potentially contributing to the SHG signal. Non-participating contributions are crossed out in table 3.1. Their exclusion from contributing to the signal is related to the normal incidence of the light beam. With a light beam propagating along the  $z$ -axis, i.e.  $\mathbf{k} \parallel \hat{z}$ , all the susceptibilities involving excitations and signals along  $\hat{z}$  are inaccessible. For  $\chi_{ijk}^{eee}$ , any tensor component with one or more indices  $z$  is impracticable because of the transverse nature of light:  $\mathbf{k} \cdot \mathbf{E} = 0$  and  $\mathbf{k} \cdot \mathbf{B} = 0$ , so that  $E_z$  and  $B_z$  are always zero. The analysis is similar for  $\chi_{ijk}^{mee}$ ,  $\chi_{ijkl}^{qee}$ , and  $\chi_{ijkl}^{eem,q}$ , though interacting with the  $\nabla$  operator, to contribute to the nonlinear source via  $\nabla \times \mathbf{M}_{NL}$ ,  $\nabla_k \mathbf{E}_l$ , and  $\nabla \cdot \hat{\mathbf{Q}}_{NL}$ , respectively, see equation (2.5) to (2.9).

**Table 3.2** – Polarizing optics configurations for all potentially non-zero SHG tensor components. Polarization orientations are denoted by  $h$  (horizontal polarization, i.e. parallel to the  $x$ -axis in the chosen referential),  $v$  (vertical polarization, i.e. parallel to the  $y$ -axis in the chosen referential), and  $d$  (diagonal at  $45^\circ$  between the  $h$  and  $v$  polarizations).

		$\chi_{ijk}^{eee}$	$\chi_{ijk}^{mee}$	$\chi_{ijkl}^{qee}$	$\chi_{ijkl}^{eem,q}$
<b>Pol</b>	<b>Ana</b>	Non-vanishing elements indices ( $ijkl \equiv \chi_{ijkl}$ )			
$v$	$v$	$yyy$	$xyy$	$zyyy$	$yyzy$
$h$	$v$	$yxx$	$xxx$	$zyxx$	$yxzx$
$d$	$h$	$xyy = yxx$	$yxy = yyx$	$zxyy = zyxx$	$xxzy, xyzx$

The  $\nabla$  operator identifies with the propagation vector  $\mathbf{k}$  as one considers the propagation of plane waves of the form  $\mathbf{E} = \mathbf{E}_0 \exp[i(\mathbf{k} \cdot \mathbf{r} - \omega t)]$ .

The resulting analyzer-polarizer configurations are summarized in table 3.2 for all accessible tensor components.  $h$ -,  $v$ -, and  $d$ -polarization are polarizations along  $x$ ,  $y$ , and diagonal thereof, respectively. The three configurations are later mentioned as  $vv$ ,  $hv$ , and  $dh$ , respectively. Similarly,  $hh$ ,  $vh$ , and  $dv$  might be used. It is stressed that for diagonal excitation, both  $h$ -only and  $v$ -only excited contributions are also analyzed simultaneously.

### 3.1.4 Nonlinear Optical Catalyst: Gold Nanowires on SHG Active Crystals

Here, the substrate consists of a non-centrosymmetric crystal, hence SHG active. In contrast to section 3.1.2, it is now the nanostructures patterned at its surface which are centrosymmetric and expected not to deliver an SHG signal of their own: Detection of SHG signals is traced back to the underlying crystal.

The gold nanostructures consist of simple nanowires spanning the whole length of a nanostructured field. As described in section 1.3.1, the electric field of a light wave polarized perpendicular to the wires drives a collective electron oscillation leading to a strong electric field enhancement localized at the edge of the wires. Thus, the wires can act as an optical field enhancement device. The quadratic dependence expressed by equation (2.14) then leads to a several orders of magnitude increase of the SHG efficiency. The SHG yield of the crystals is enhanced by tailoring the electromagnetic light field within the sample. However, it is stressed that the amplification can only take place in the volume of the crystal *immediately below* the surfaces, for the amplified field penetrates the crystal only a few tenths of nanometers. Furthermore, while measuring in reflection, any SHG produced below the gold structure cannot be extracted, for it is absorbed in the gold volume, see figure 1.3. Thus, one can measure an amplified signal only in the case where the enhanced SHG produced at the edge of the nanostructure overcompensates the loss of SHG signal due to the surface of the crystal being partially covered with gold. Figure 3.5 summarizes these features, the model used is presented in section 4.2.4, the corresponding Mathematica code is reported in code B.2. It is stressed that the amplified response should then depend on the wire orientation with respect to the crystal axes, see section 3.1.5.

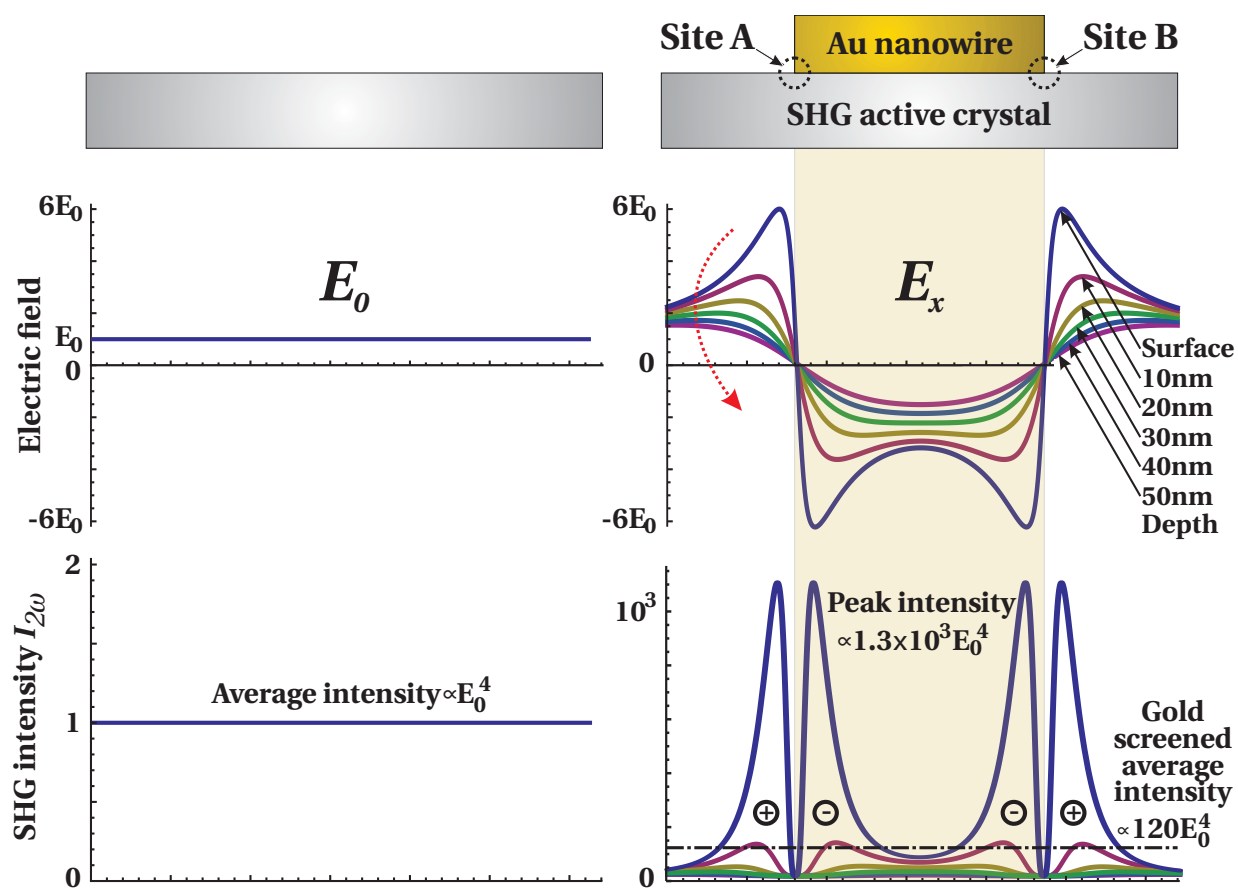


**Figure 3.5** – Illustration of the electric field amplification mediated by a plasmonic gold nanowire: Predominance of the nanostructures’ boundary in the SHG signal strength. SHG without and with wire mediation is illustrated in the left and right column, respectively. The system excitation consists of a plane wave at normal incidence from above with amplitude  $E_0$  (not depicted). For each case, a cross section of the system is shown (top). The spatial distribution of the transversal electric field strength  $E_x$  is shown starting at the crystal surface (middle). Further curves show the evolution in 10nm depth steps within the crystal, as indicated by the dotted red arrow. The resulting SHG strength distribution is shown with an indication about the phase ( $\oplus$  or  $\ominus$ ) of the generated signal (bottom). For the illustration, the amplification factor is arbitrarily set to a conservative value of 6. Figures of merit are provided, taking into consideration that measurements are carried out in reflection.

The described method is general enough to be applied to *any* kind of material. However, a model compound is required to study both the *mechanism* and the *functionality* of the SHG enhancement. For this, crystals from the hexagonal rare-earth manganites and chromium(III) oxide families were selected as model systems. Both crystals type are described below; corresponding reference spectra are provided in annex A.

**$RMnO_3$ :** *c*-cut hexagonal crystals from the multiferroic  $RMnO_3$  family are considered, grown either by the flux [134] or the floating-zone technique, also known as melting-zone process [135]. The corresponding crystals are labeled FG and FZ, respectively. The floating-zone melting process melts  $RMnO_3$  pressed pellets into large single-crystal rods of up to 3 cm in length and 0.5 cm diameter [136]. The flux method delivers much smaller platelets with a thickness of typically about hundred micrometers and a diameter of a

few millimeters [137]. Furthermore, this method may come to the formation of surface layers with a high proportion of bismuth in the thickness range of several micrometers. In particular, this may lead to a change in the ferroelectric properties of the crystals [138].

The isomorphous hexagonal  $RMnO_3$  crystals ( $R=Sc, Y, Dy-Lu$ ) belong to the family of multiferroics, i.e. compounds displaying simultaneous long-range electric and magnetic order [139]. SHG is particularly suited for the simultaneous investigation of the two forms of ordering and thus their interaction [139]. The SHG spectral, polarization, spatial, and temperature dependencies are very well known for both the ferroelectric (FEL) and the antiferromagnetic (AFM) order of the hexagonal  $RMnO_3$  system [140, 141].  $RMnO_3$  crystals possess a hexagonal unit cell and a fivefold coordination of the central  $Mn^{3+}$  ion [140]. Above the Curie temperature  $T_C = 570\text{ K}$  to  $995\text{ K}$ , the compound is paraelectric and paramagnetic, possessing the space symmetry  $P6_3/mmc$  (point group  $6/mmm$ ) [120]. At  $T_C$ , a FEL distortion leads to a spontaneous polarization  $P$  along the hexagonal axis.  $P$  is the ferroelectric order parameter which transforms like a time-invariant ( $i$ -type) scalar [120, 142]. The ferroelectric ordering breaks the inversion symmetry and reduces the symmetry to  $P6_3cm$  (point group  $6mm$ ). At the Néel temperature  $T_N = 75\text{ K}$  to  $130\text{ K}$ , AFM ordering of the  $Mn^{3+}$  spins occurs in the basal plane perpendicular to the sixfold  $z$ -axis and breaks the time-reversal symmetry of the crystal [143]. The AFM order parameter of the triangular spin lattice is  $\mathbf{l}$ , that transforms like the component of a third-rank axial time-noninvariant ( $c$ -type) tensor [120, 142]. It reduces the symmetry of the simultaneously FEL and AFM lattice to  $P\bar{6}_3/cm$  or  $P\bar{6}_3/\bar{c}m$  (point group  $\bar{6}mm$  or  $6\bar{m}m$ ) depending on the orientation of the spins along the  $x$ - or  $y$ -axis, respectively. This corresponds to the  $\alpha_x$  and  $\alpha_y$  models in reference [143], where an extensive investigation of these substances by SHG is to be found.

In the present work, FG  $HoMnO_3$  ( $T_C = 875\text{ K}$ ,  $T_N = 76\text{ K}$ ) and FZ  $YbMnO_3$  ( $T_C = 995\text{ K}$ ,  $T_N = 87\text{ K}$ ) crystals are used.  $YbMnO_3$  follows the  $\alpha_y$  model for all temperatures below  $T_N$ . For  $HoMnO_3$  however, a collective  $90^\circ$  rotation of the  $Mn^{3+}$  spins from  $y$ - to  $x$ -axis changes the magnetic symmetry from  $\alpha_y$  configuration below  $T_N$  to  $\alpha_x$  below a phase transition occurring around  $40\text{ K}$ . Both the FEL and the AFM contribution to the SHG signal are employed. Under ambient conditions, the broad spectral range of FEL SHG allows for investigation of the basic mechanism of the SHG enhancement. The functionality of the SHG enhancement is investigated by monitoring the response of the AFM domains to the metamaterial on the  $RMnO_3$  samples. AFM experiments are carried out at cryogenic conditions below the Néel temperature  $T_N$ . An SHG signal of FEL origin is observable in the broad  $1.20\text{ eV}$  to  $3.00\text{ eV}$  range, see figure A.12. The usable range for AFM SHG contributions across the  $RMnO_3$  family is restricted to the much narrower  $2.30\text{ eV}$  to  $2.80\text{ eV}$  range. Note that the maximum yield of the AFM SHG signal is obtained at  $2.40\text{ eV}$ , see figure A.13.

**Cr<sub>2</sub>O<sub>3</sub>:**  $c$ -cut trigonal crystals of  $Cr_2O_3$  are used, all cut from the same boule grown by the Verneuil method [144]. Above the Néel temperature  $T_N = 307.6\text{ K}$ , paramagnetic  $Cr_2O_3$  crystallizes in the centrosymmetric point group  $\bar{3}m$  [120, 145, 146]: Nonlinear electric-dipole effects due to  $\chi_{ijk}^{eee}$  (polar  $i$  tensor of third rank) are forbidden, but MD effects

due to  $\chi^{mee}$  (axial  $i$  tensor of third rank) and EQ contributions  $\chi^{qee}$  (polar  $i$  tensor of fourth rank) are allowed in this point group [120, 147]. Without nanostructuring of the crystal surface, quadrupole contributions to the SHG signal due to  $\chi^{qee}(i)$  are neglected since they have not been observed in  $\text{Cr}_2\text{O}_3$ . Thus, SHG is measured from a magnetic dipole contribution due to  $\chi_{ijk}^{mee}(i)$  above  $T_N$ .

Below  $T_N$ , four spins in the unit cell order along the optical axis in a non-centrosymmetric antiferromagnetic structure [145, 146, 148]. The arising antiferromagnetic vector  $\mathbf{l}$  is also oriented along the optical axis. The positive or negative orientation of the magnetic moments in the unit cell defines the two types of magnetic domains, so-called  $180^\circ$  domains. Both space- and time-reversal symmetry operations are simultaneously broken, but the combined space-time-reversal operation  $\bar{1}$  remains a symmetry element. The resulting magnetic point group of  $\text{Cr}_2\text{O}_3$  is  $\bar{3}m$ . In this point group new phenomena described by polar  $c$  tensors of odd rank (ED) and axial  $c$  tensors of even rank are allowed. Thus, in addition to the crystallographic SHG due to  $\chi_{ijk}^{mee}$  (axial  $i$  tensor) electric dipole effects due to  $\chi_{ijk}^{eee}$  (polar  $c$  tensor of third rank) are allowed below  $T_N$  [120, 147]. Besides, the existence of an axial  $c$  tensor of second rank leads to the static magnetoelectric effect in  $\text{Cr}_2\text{O}_3$  [146, 149].

The magnetoelectric effect can be exploited to reorient antiferromagnetic domains in a controlled fashion [149, 150]. For this purpose, the sample is cooled from the paramagnetic to the antiferromagnetic phase in presence of both an electric and a magnetic field applied along the crystallographic  $c$ -axis [151]. As the crystal crosses the Néel temperature, the electric field induces a magnetic moment aligned with the magnetic field, via the magnetoelectric effect. Varying the strength of both fields allows for varying the ratio of both domains thus altering the position of domain boundaries across a sample. The domain topography is accessible in spatially resolved SHG experiments, see section 4.2.4. The domain orientation results in either constructive or destructive interference between the reciprocal and non-reciprocal SHG contributions [152]. Thus, a contrast is observed between two  $180^\circ$  domains, that transform into each other by the time reversal operation, i.e. employing right or left circularly polarized light. The domains are often pinned by intrinsic defects and typically span across several square millimeters.

SHG contributions from  $\text{Cr}_2\text{O}_3$ , be it of crystallographic or magnetic origin, extend in the 1.80 eV to 3.00 eV range. Maximum yield of the SHG signal is obtained around 2.10 eV, see annex A.3. An extensive description of the substance and its investigation by SHG is found in reference [151].

The sample preparation steps are identical for both material families. First, Laue diffraction allows for precise orientation ( $\leq 2^\circ$ ) of the crystal axes. Then the crystal is mechanically ground and lapped in the plane normal to the  $c$ -axis.  $3\mu\text{m}$  abrasive  $\text{Al}_2\text{O}_3$  and SiC particles are used for  $\text{RMnO}_3$  and  $\text{Cr}_2\text{O}_3$ , respectively. The wedge allowing, this step is potentially bypassed for FG  $\text{RMnO}_3$  samples, many of them offering an excellent planar surface to start with. Then, optical polishing is chemo-mechanically achieved. Silica slurry and diamond suspension solutions are used for  $\text{RMnO}_3$  and  $\text{Cr}_2\text{O}_3$ , respectively, with a 1:5 volume addition

of hydrogen peroxide ( $\text{H}_2\text{O}_2$ ). In the silica slurry, silica particles ( $\text{SiO}_2$ ) form a colloid with sodium hydroxide ( $\text{NaOH}$ ) with a pH-value of 10. Particle sizes amount to  $100\text{\AA}$  and  $1\mu\text{m}$  for  $\text{SiO}_2$  and diamond, respectively. SiC and diamond are required when handling  $\text{Cr}_2\text{O}_3$ , for it features a very high Mohs hardness value of 9.5 (9.8 for SiC, 10 for diamond). Best results are achieved in balancing the rates of chemical and mechanical polishing, the former controlled by the rate of fluid flow and the latter by the polishing plate rotation speed [153]. In reflection measurements, the back face is left rough to prevent interference via back reflections and Fabry-Perot effects. The back surface is polished only for the domain topography experiment described in section 4.2.4, carried out in transmission. Then, the back surface polishing plane is arbitrarily chosen at a slight angle with respect to the front face, again to prevent Fabry Perot effects. Depending on the crystal used, the thickness varies from  $100\mu\text{m}$  to  $1500\mu\text{m}$ . For such large values, the absolute crystal thickness is of no relevance for this work other than mechanical stability during EBL processing.

Thereafter, a set of wire field pairs are fabricated. Each pair corresponds to a wire design, i.e. the linear resonance energy is shared between the two fields within the reproducibility limit of the fabrication process. The two fields present a relative orthogonal wire orientation, namely parallel and perpendicular to the crystallographic  $a$ -axis. The wires form gratings with an extension of  $200 \times 200\mu\text{m}^2$  to  $500 \times 500\mu\text{m}^2$ , depending on the available area on the sample. The wire width varies between  $100\text{nm}$  and  $300\text{nm}$ , with a typical periodicity of  $450\text{nm}$ . For  $\text{RMnO}_3$ , the linear resonance of the wires is tuned in the range from  $0.80\text{eV}$  up to  $1.45\text{eV}$ . Similarly for  $\text{Cr}_2\text{O}_3$ , the linear resonance of the wires is tuned in the range from  $0.87\text{eV}$  up to  $1.33\text{eV}$ . In both cases the tunability is obtained in varying the width only, *not* their height, so that the penetration of the electromagnetic field of light is the same for all samples.

#### 3.1.5 $\text{RMnO}_3$ and $\text{Cr}_2\text{O}_3$ : SHG Tensor Components

The space symmetry of the crystals used in this work are described in a Cartesian coordinate system which is related to the hexagonal unit-cell axes by  $z = c$  and  $x = a$ . With respect to this referential, the wires are designated as  $x$ - or  $y$ -wires, depending on the orientation of their long axis along  $x$  or  $y$ , respectively. In the following, ( $i$ ) and ( $c$ ) refer to the reciprocal and not reciprocal behavior of the  $\chi$ -tensor under time inversion.

For hexagonal  $\text{RMnO}_3$ , all SHG contributions allowed by symmetry analysis are listed in table 3.3. However, not all allowed tensor components actually contribute to a measured signal and the analysis is substantially simplified based on an appropriate setup configuration. On the one hand, leading order AFM contributions to SHG involve  $x$ -polarized and  $y$ -polarized light only. On the other hand, all FEL contributions involve the participation of  $z$ -polarized fundamental or SHG light. Hence, the AFM order is best observed with light incident along the  $z$ -axis where purely ferroelectric SHG contributions cannot be excited for the projection of the light field is zero along  $\hat{z}$ . In turn, an investigation of the FEL order is only possible with light *not* incident along the  $z$ -axis. Given that only crystals cut normal to the  $z$ -axis were available for this work, a  $45^\circ$  incidence configuration is employed to project the exciting field along  $\hat{z}$ . This also provides access to the SHG contributions along the  $z$ -axis. Mixing with AFM contributions to SHG is avoided by performing the experiment at  $T > T_N$  where

**Table 3.3** – Symmetry operations, point group, and allowed tensor components in  $RMnO_3$  crystals. Below the Néel temperature, tensor components are given only for crystals obeying the  $\alpha_y$  spin order. The symmetry analysis is carried out up to the first order expansion of the electromagnetic field. Simplification is available based on the setup configuration and considering a *plane-wave* excitation and outgoing emission. Measurements are carried out at  $45^\circ$  incidence for the FEL signal ( $\mathbf{k} = 1/\sqrt{2}(1, 0, 1)$ ) and normal incidence for the AFM one ( $\mathbf{k} = (0, 0, 1)$ ). Non-contributing components according to these configurations are crossed out.

$RMnO_3$	$T < T_C$	$T < T_N$
<b>Symmetry operations</b>	$1, 2_z, 6(\bar{2}_\perp), \pm 3_z, \pm 6_z$ $\underline{1}, \underline{2}_z, 6(\underline{2}_\perp), \pm \underline{3}_z, \pm \underline{6}_z$	$1, 3(\bar{2}_\perp), \pm 3_z, \underline{2}_z, 3(\underline{2}_\perp), \pm \underline{6}_z$
<b>Point group</b>	<b>6mm</b>	<b>6mm</b>
<b>Tensor components</b>	Non-vanishing elements indices ( $ijkl \equiv \chi_{ijkl}$ )	
	(i)-type	(c)-type
$\chi_{ijk}^{eee}$	$xxz = xzx = yyz = yzy,$ $zxx = zyy, zzz$	$xxx = -xyy = -yxy = -yyx$
$\chi_{ijk}^{mee}$	$xyz = xzy = -yxz = -yzx$	$yyy = -yxx = -xxy = -xyx$
$\chi_{ijkl}^{qee}$	$xxxx = yyxx + xyyx + yxyx$ $= yyyy, xxyy = yyxx,$ $xxzz = yyzz,$ $xyxy = xyyx = yxyx = yxxxy,$ $xzxx = xzzx = yzyz = yzzz,$ $zxzx = zxxz = zyyz = zyzzy,$ $zzxx = zzyy, zzzz$	$zxxx = -zxyy = -zyxy = -zyyx$ <del><math>xxxz = xxzx = -xyyz = -xyzy =</math></del> <del><math>-yxyz = -yxzy = -yyxz = -yyzx,</math></del> <del><math>xzxx = -xzyy = -yzxy = -yzyx,</math></del>
$\chi_{ijkl}^{eem,q}$	$xxxx = yyxx + xyyx + yxyx$ $= yyyy, xxyy = yyxx,$ $xxzz = yyzz, xyxy = yxyx,$ $xyyx = yxxxy, xzxx = yzyz,$ $xzzx = yzzz, zxxx = zyyz,$ $zxzx = zyzzy, zzxx = zzyy,$ $zzzz$	$xxzx = -xyzy = -yxzy = -yyzx,$ <del><math>xxxz = -xyyz = -yxyz = -yyxz,</math></del> <del><math>xzxx = -xzyy = -yzxy = -zyxy,</math></del> <del><math>zxxx = -zyyx = -zyxy = -zxyy</math></del>

the AFM SHG contribution is inexistent. Thus, many allowed terms do not contribute when the measurements are performed according to the above observations, assuming a plane wave excitation. These terms are crossed out in table 3.3. Although the expressions for the FEL quadrupole excitations remain intricate under  $45^\circ$  incidence, their effect is negligible with respect to leading order contributions. A detailed discussion of SHG spectroscopy on the  $RMnO_3$  system is found in references [139, 140]. In the absence of nanostructure and with plane waves for the incoming laser fields, one derives the time-invariant and time-

### 3.1. SAMPLES

**Table 3.4** – Symmetry operations, point group, and allowed tensor components in  $\text{Cr}_2\text{O}_3$  crystals. The symmetry analysis is carried out up to the first order expansion of the electromagnetic field. Simplification is available based on the setup configuration and considering a *plane-wave* excitation and outgoing emission. All measurements are carried out at normal incidence ( $\mathbf{k} = (0, 0, 1)$ ). Non-contributing components according to this configuration are crossed out.

$\text{Cr}_2\text{O}_3$	$T < T_C$	$T < T_N$
<b>Symmetry operations</b>	$1, \bar{1}, 3(2_\perp), 3(\bar{2}_\perp), \pm 3_z, \pm \bar{3}_z$	$1, \bar{1}, 3(2_\perp), 3(\bar{2}_\perp), \pm 3_z, \pm \bar{3}_z$
<b>Point group</b>	$\bar{3}m$	$\bar{3}m$
<b>Tensor components</b>	Non-vanishing elements indices ( $ijkl \equiv \chi_{ijkl}$ )	
$\chi_{ijk}^{eee}(c)$	–	$yyy = -xxy = -xyx = -yxx,$ $xyz = xzy = -yxz = -yzx$
$\chi_{ijk}^{mee}(i)$	$yyy = -xxy = -xyx = -yxx,$ <del><math>xyz = xzy = -yxz = -yzx</math></del>	
$\chi_{ijkl}^{qee}(i)$	$xzxx = -xzyy = -yzyx = -yzxy$ $= zxzx = -zyyx = -zyxy = -zxyy,$ $xxxx = yyxx + xyyx + yxyx = yyyy,$ <del><math>xxxz = -yyxz = -yxyz = -xyyz</math></del> <del><math>= xxzx = -yxzy = -xyzy = -yzzx, xxxy = yyxx,</math></del> <del><math>xxxz = yyzz, xyxy = yxyx = xyyx = yxxy,</math></del> <del><math>xzxz = yzyz = xzzx = yzzz = zxxx = zyyz = zxxz = zyzy,</math></del> <del><math>zxxx = zzyy, zzzz</math></del>	
$\chi_{ijkl}^{em,q}(i)$	$xxzx = -yxzy = -xyzy = -yyzx,$ $xxxx = yyxx + xyyx + yxyx = yyyy,$ <del><math>xxxz = -yyxz = -yxyz = -xyyz, xxxy = yyxx, xxxz = yyzz,</math></del> <del><math>xyxy = yxyx, xyyx = yxxy, xzxz = -xzyy = -yzyx = -yzxy,</math></del> <del><math>xzxz = yzyz, xzzx = yzzz, zxxx = -zyyx = -zyxy = -zxyy,</math></del> <del><math>zxxx = zyyz, zxxx = zyzy, zxxx = zzyy, zzzz</math></del>	

noninvariant contributions of the leading order ED contributions:

$$\mathbf{P}^{\text{NL}}(i) = \varepsilon_0 \begin{pmatrix} 2\chi_{xxz}^{(i)} E_x E_z \\ 2\chi_{xxz}^{(i)} E_y E_z \\ \chi_{zxx}^{(i)} (E_x^2 + E_y^2) + \chi_{zzz}^{(i)} E_z^2 \end{pmatrix} \quad \mathbf{P}^{\text{NL}}(c) = \varepsilon_0 \begin{pmatrix} \chi_{xxx}^{(c)} (E_x^2 - E_y^2) \\ -2\chi_{xxx}^{(c)} E_x E_y \\ 0 \end{pmatrix}, \quad (3.1)$$

where  $E_x$ ,  $E_y$ , and  $E_z$  are the electric field components along the  $x$ -,  $y$ -, and  $z$ -axis, respectively.

For  $\text{Cr}_2\text{O}_3$ , all SHG contributions allowed by symmetry analysis are listed in table 3.4. The analysis is restricted to light propagating along the optical  $z$ -axis, for which both the crystallographic and magnetic SHG processes can be excited and analyzed. Above  $T_N$  and in the absence of gold nanostructures, only one independent component  $\chi_m(i) \equiv \chi_{yyy}^{mee}(i) = -\chi_{yxx}^{mee}(i) = -\chi_{xyx}^{mee}(i) = -\chi_{xxy}^{mee}(i)$  of the nonlinear susceptibility contributes to the nonlinear magnetization [120]. In fact, this tensor combines time invariant contributions, both of magnetic and quadrupole origin, yet whereas electric quadrupole contributions are allowed, they

are mix inseparably with the MD contributions. In the wave equation, the magnetic-dipole contribution leads to a source term  $\mu_0 \nabla \times \partial \mathbf{M}^{\text{NL}}(i) / \partial t$  for SHG [117, 147], see equation (2.8). This source term is allowed above and below  $T_N$  and does not induce any anomalous change of the SHG when going from the paramagnetic to the antiferromagnetic state. Below  $T_N$ , an additional source term occurs which is due to the breaking of space-inversion symmetry. Since this breaking is due to magnetic ordering, the relevant tensor  $\chi_{ijk}^{eee}(c)$  is of  $c$  type [120] and depends linearly on the order parameter. This leads to a nonlinear polarization  $P^{\text{NL}}(c)$ . For light propagating along the  $z$  axis,  $P^{\text{NL}}(c)$  is given by one independent component  $\chi_e(c) \equiv \chi_{yyy}^{eee}(c) = -\chi_{yxx}^{eee}(c) = -\chi_{xyx}^{eee}(c) = -\chi_{xxy}^{eee}(c)$  of the nonlinear susceptibility [120]. In the wave equation, the electric-dipole contribution leads to the source term  $\mu_0 (\partial^2 \mathbf{P}^{\text{NL}}(c) / \partial t^2)$  for SHG, see equation (2.6). With plane waves for the incoming laser fields and neglecting contributions like  $\chi^{em,q}$ , one derives the total source term:

$$\mathbf{S} = \mu_0 \left( \nabla \times \frac{\partial \mathbf{M}^{\text{NL}}(i)}{\partial t} + \frac{\partial^2 \mathbf{P}^{\text{NL}}(c)}{\partial t^2} \right) \quad (3.2)$$

$$\begin{pmatrix} S_x \\ S_y \\ S_z \end{pmatrix} = 4 \frac{\omega^2}{c^2} \begin{pmatrix} \chi_m(i) (E_x^2 - E_y^2) + 2\chi_e(c) E_x E_y \\ -2\chi_m(i) E_x E_y + \chi_e(c) (E_x^2 - E_y^2) \\ 0 \end{pmatrix}, \quad (3.3)$$

where  $E_x$  and  $E_y$  are the electric field components along the  $x$ - and  $y$ -axis, respectively. Given there is no projection of the light field along the  $\mathbf{z} \parallel \mathbf{k}$  axis,  $z$ -polarized light cannot be analyzed.

It is also convenient to define a circular basis for right- and left-handed circular polarized light, indicated by a  $+$  or  $-$  index, respectively. The unit vectors are then  $\hat{\mathbf{e}}_+ = -(\hat{\mathbf{e}}_x + i\hat{\mathbf{e}}_y) / \sqrt{2}$  and  $\hat{\mathbf{e}}_- = (\hat{\mathbf{e}}_x - i\hat{\mathbf{e}}_y) / \sqrt{2}$ , with  $\hat{\mathbf{e}}_z$  being left unchanged. Then, the source term becomes

$$\mathbf{S} = \begin{pmatrix} S_+ \\ S_- \\ S_z \end{pmatrix} = 4\sqrt{2} \frac{\omega^2}{c^2} \begin{pmatrix} (-\chi_m(i) + i\chi_e(c)) E_-^2 \\ (+\chi_m(i) + i\chi_e(c)) E_+^2 \\ 0 \end{pmatrix}. \quad (3.4)$$

Considering complex susceptibilities at the resonance,  $\chi = \chi' + i\chi''$ , and circularly polarized light of intensity  $I_0$ , one constructs the abbreviations  $C$  and  $\Delta$  to express the resulting SHG intensity  $I$  as a function of the orientation of the order parameter  $l = \pm 1$  and of the circular polarization  $\sigma = \pm 1$ :

$$\begin{aligned} C &= |\chi_m(i)|^2 + |\chi_e(c)|^2 \\ \Delta &= 2l \left( \chi'_m(i) \chi''_e(c) - \chi''_m(i) \chi'_e(c) \right) \\ \frac{I}{I_0^2}(l, \sigma) &= C - \text{sgn}(l) \text{sgn}(\sigma) \cdot \Delta \quad . \end{aligned} \quad (3.5)$$

Experimentally, space-inversion corresponds to changing the circular polarization of the incident light, while time-reversal equals a change in the domain orientation where the SHG signal is generated. After equation (3.5), both actions lead to a relative change in the SHG

intensity by a value  $2\Delta$  and thereby allow the optical identification of AFM domains. This feature is exploited in section 4.2.4 to demonstrate that the nanopatterning of the crystal surface with gold does not alter the crystal features. Further theoretical and experimental details are provided in reference [151].

## 3.2 Linear Characterization

The linear spectra are experimentally determined using a Fourier transform infrared spectrometer (Bruker Vertex 80, Bruker Optik GmbH) with an attached microscope (Bruker Hyperion, Bruker Optik GmbH). The system provides transmission and reflection capabilities at normal incidence. It operates for shorter wavelengths ( $0.4\mu\text{m}$  to  $1.2\mu\text{m}$ ) with a quartz beam splitter and a silicon detector, and for longer wavelengths ( $0.9\mu\text{m}$  to  $2.5\mu\text{m}$ ) with a calcium-fluoride beam splitter and a mercury-cadmium-telluride (MCT) detector cooled by liquid nitrogen. Small sample areas ranging from  $8\mu\text{m}$  to  $100\mu\text{m}$  in diameter can be investigated. A polarizer allows to excite the nanostructures with light of a defined linear polarization. Importantly, with respect to the FWHM, the light is focused and collected with Cassegrain lenses (15x reflective microscope objectives) with a numerical aperture of 0.4, or more precisely, the sample is illuminated and light is collected from all directions between  $25^\circ$  off the substrate normal.

Alternatively, a conventional infrared spectrometer with an attached microscope (MSV-370, Jasco Ltd.) is used with similar capabilities in the  $0.2\mu\text{m}$  to  $2.5\mu\text{m}$  range. Operating principle aside, differences include a lead-sulfide (PbS) detector for longer wavelength ( $0.8\mu\text{m}$  to  $2.5\mu\text{m}$ ), and square sample areas ranging from  $30\mu\text{m}$  to  $500\mu\text{m}$  in side length. Here too, the light is focused and collected with Cassegrain lenses (10x reflective microscope objectives) with a numerical aperture of 0.5, or more precisely, the sample is illuminated from all directions between  $30^\circ$  off the substrate normal.

Since the resonant phenomena investigated in this thesis are angle-sensitive, the use of Cassegrain lenses results in transmittance spectra with broadened and less pronounced peaks and dips [154]. Nevertheless, although an exact determination of the spectral width of a nanostructure resonance cannot be achieved, the spectral peak positions remain accurate. These linear characterization systems are used equivalently for the linear-optical measurements presented in section 4.1.

## 3.3 Laser System

The optical setup used in this work is sourced with intense femtosecond laser pulses. To generate such high intensity pulses, one employs the state-of-the-art technique of chirped pulse amplification (CPA, [155]) in a regenerative amplifier to avoid damage in the optics and nonlinear distortion of the spatial and temporal profile of the laser beam. The process is reviewed in reference [156] and is summarized below. The effective ultrashort pulse length is determined by means of an autocorrelator, and the central wavelength is tuned using optical

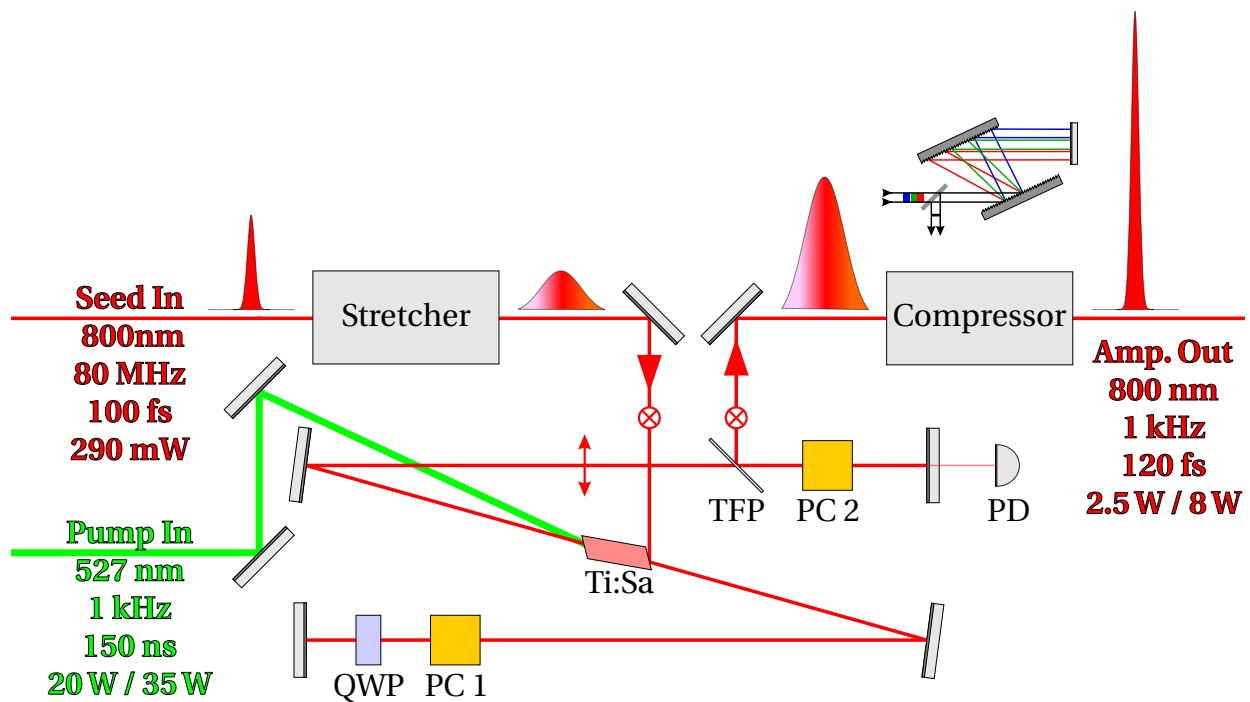


**Figure 3.6** – Optical layout and evolution of the temporal pulse shape in a chirped-pulse amplifier. The main steps of the process consist successively of stretching, amplification, and recompression of the light pulse. Stretcher and compressor are similar in their operating principle: Both rely on an optical path difference for different wavelength. An inset provides details for the latter. The amplification takes place in the Ti:Sa crystal placed at the center of the optical cavity and is controlled by a photodiode (PD). Incoupling and outcoupling within the cavity is ensured by polarization optics: Two Pockel cells (PC), a quarter wave plate (QWP) and a thin film plate (TFP).

parametric amplification (OPA) to allow for spectroscopy. The different parts are introduced in the following.

### 3.3.1 Regenerative Amplifier (RGA)

To generate femtosecond pulses, a turn-key mode-locked Ti:Sa oscillator (Vitesse, Coherent) is used, combined with an integrated diode-pumped solid-state laser (Verdi, Coherent,  $\approx 1.5$  W CW power). The lowest noise commercially available ( $< 0.02\%$  rms) of the Verdi, provides the oscillator with optimal peak-to-peak as well as long term stability laser output. This seed laser delivers 290 mW of 100 fs pulses linearly polarized with a central wavelength of 800 nm at 80 MHz repetition rate. This represents 3.625 nJ per pulse.

For the RGA pump source, an intra cavity doubled, Q-switched neodymium-doped yttrium lithium fluoride laser (Nd:YLF, Evolution, Coherent) is used, providing 20 W of about 150 ns pulses centered at 527 nm, with a 1 kHz repetition rate.

In the RGA (Legend Elite, Coherent), see figure 3.6, the seed pulse coming from the laser oscillator is first stretched out temporally and spectrally prior to amplification. To do so, a quad pass grating scheme (not shown) is used to stretch the pulse in time by three to four orders

of magnitude. The pulse is then injected into a 1.5m long optical cavity (10ns round-trip time). This is done by controlling the polarization using an electro-optical modulator (Pockels cell PC1), switched at proper timing, together with a quarter wave-plate (QWP). Closed with concave confocal end mirrors, the optical resonator is built in a z-fold scheme to account for astigmatic compensation. The light pulse is amplified in a 1/4" × 1" Ti:Sa rod gain medium during approximately 10 round trips (30m total propagation length) leading to a maximal gain to loss ratio. The amplification build-up is monitored using leakage power detection by a photodiode (PD) placed behind an end mirror. Ti:Sa crystals are ideally suited for high-power ultra short pulse amplification since they provide a broad gain bandwidth peaked at 800nm and high thermal conductivity. During operation, the crystal is thermo-electrically (TE) stabilized at 0°C, and its environment is kept dry to prevent ice and condensation build-up susceptible to lead to crystal damage or higher loss. After amplification, the pulse is then coupled out of the cavity using another Pockels cell (PC2) in combination with a reflective plate at Brewster angle, or thin film polarizer (TFP).

Finally, the pulses are recompressed in a similar grating arrangement as for the stretcher resulting in 2.5W of 120fs pulses linearly polarized with a central wavelength of 800nm at 1kHz repetition rate. Thus, with 2.5mJ per pulse, this represents an overall amplification of  $6.9 \times 10^5$ . To reach the highest possible amplification, it is important to keep the energy of any satellite pulses very low, i.e. to achieve a high pulse contrast. Such satellite pulses can occur in various ways, e.g. via imperfect switching of the Pockels cell or parasitic reflections in the amplifier. Also, the duration of the amplified pulse is slightly increased with respect to the pulse delivered by the seed laser. This is due to the limited gain bandwidth of the amplifier medium which reduces the pulse bandwidth, together with limited clipping on mirrors and gratings in the stretcher and compressor regions. The very long propagation length mentioned above renders the device sensitive to the slightest local parameter variation within the cavity, most notably temperature fluctuations, air turbulences or dust. When properly operated, the beam profile is close to a pure Gaussian TEM<sub>00</sub> mode (beam quality factor  $M^2 < 1.5$ ).

Alternatively, a laser system presenting upgraded specifications was available (Legend Elite Duo, Coherent). Virtually identical in its operating principles, it presents a higher power RGA pump source (35W) and an additional single-pass power amplifier (SPA) before the compressor. While the first RGA Ti:Sa crystal also gets pumped harder, most of the added power is used in the SPA. Similar to the gain medium mentioned above, this additional amplifier stage consists of a TE-cooled, environment-controlled Ti:Sa crystal. The main difference resides in that the amplification takes place in a single pass, hence the name. During this single pass, the light pulse's power is roughly doubled up to 8W. Here, the overall amplification is about  $2.2 \times 10^6$  with 8mJ per pulse.

#### 3.3.2 Auto-Correlation Measurement

The generation, control, and use of ultra short laser pulses requires a precise characterization. For a measurement of the time-dependent envelope of an ultrashort laser pulse, dedicated methods are required. Direct electronic techniques for temporal pulse-width measurements, consisting of fast photodiodes and high-bandwidth oscilloscopes, are limited to the several

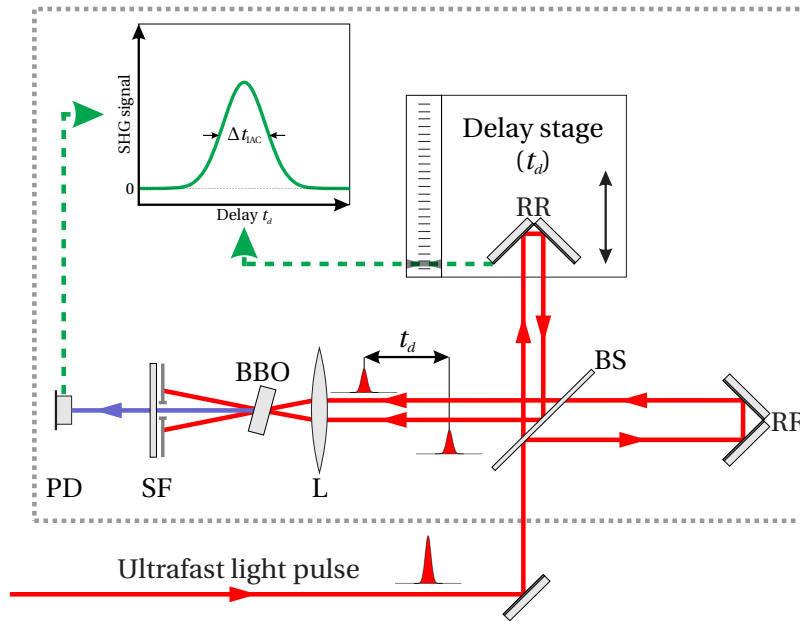


**Figure 3.7** – Optical layout for the autocorrelator. A light beam is split in two by a beam splitter (BS). After propagating through two optical arms whose respective length is set by retro-reflectors (RR), both beams are separated by a delay  $t_d$ . They are then focused by a lens (L) onto a BBO nonlinear crystal. The resulting SHG signal is transmitted through spatial and spectral filters (SF) and recorded by a photodetector (PD) as a function of  $t_d$ . The FWHM of the resulting signal  $\Delta t_{AC}$  is correlated to the light pulse's temporal width.

picosecond regime. The only detector that reaches time resolution below 1 ps is the so-called *streak camera*, quoted with temporal resolution  $< 200$  fs [157, 158], and recently used to image the propagation of repeated femtosecond light pulses [159]. Electronic methods are therefore not suited to record the temporal profile of an ultrashort laser pulse. Such a characterization requires optical correlation techniques.

A widely used technique to estimate the pulse duration is used here, the so-called intensity autocorrelation (IAC) [160]), described by the following equation:

$$I_{IAC}^{SHG}(t_d) = \int_{-\infty}^{+\infty} |E(t)E(t-t_d)|^2 dt = \int_{-\infty}^{+\infty} I(t)I(t-t_d) dt \quad . \quad (3.6)$$

This is the time integral of one pulse intensity multiplied by the intensity of a time-shifted replica of the same pulse as a function of time shift,  $t_d$ . The IAC has its maximum at  $t_d = 0$  and is always symmetrical [161].

The required experimental setup for its measurement is shown in figure 3.7. In our setup, it consists of a compact commercially available autocorrelator device (Pulse check & Mini, APE GmbH). In this fundamental configuration, one pulse serves as a gate to scan the other. It can be realized with any interferometer that splits the pulse into two pulses and recombines them with an adjustable time delay between them. For example, a 100 fs pulse duration corresponds to a spatial extend of  $30 \mu\text{m}$ , a dimension readily measurable with standard translation stages. Measuring the spatial overlap of the two pulses requires a nonlinear process to generate a detection signal proportional to the intensity product of the two pulses. Here, second-harmonic generation is used in a thin beta-barium borate (BBO,  $\text{BaB}_2\text{O}_4$ ) crystal. A thin crystal has to be used to ensure that the ratio of the crystal phase-matching bandwidth to the pulse spectral bandwidth is large. For 100 fs pulses at 800 nm the BBO crystal thickness should be no thicker than about  $100 \mu\text{m}$ .

The intensity autocorrelation is obtained directly when the two time-delayed laser pulses are recombined non-collinearly into the thin nonlinear crystal. This leads to the so-called *background free intensity autocorrelation*. In the collinear case a constant background appears with a signal to background ratio of 3:1.

The IAC provides only limited information on the pulse shape because there are an infinite number of symmetric (and asymmetric) pulse shapes that lead to the same autocorrelation trace. The procedure to estimate the pulse duration from the IAC is to assume a pulse shape and then to calculate the FWHM pulse duration  $\Delta t$  from a tabulated ratio with respect to the measured IAC FWHM,  $\Delta t_{\text{IAC}}$ : For a Gaussian pulse  $\Delta t_{\text{IAC}}/\Delta t = 1.414$  [162].

It is important to notice that using IAC, the exact field amplitude and phase information is lost: One only gets insight into the envelope function of the pulse. Applications that require complete characterization of arbitrarily-shaped ultrashort laser pulses with respect to their temporal amplitude and phase function (or their frequency-domain counterparts) make use of methods operating in the joint time-frequency domain. The most common method is the so-called *frequency-resolved optical gating* (FROG), described in great detail in references [163, 164] and references therein. The basic optical layout is the same as for IAC, the detector being replaced by a spectrometer and camera to spectrally resolve the gated pulse.

Since an extensive FROG measurement was not available in the time frame of this work, the IAC measured pulses were considered to be transform-limited Gaussian pulses. Thus, for monitoring purposes, approximately 0.4% of the RGA output is split and sent into the autocorrelator. A value of  $\Delta t = 120$  fs (FWHM, data not shown) is determined for both systems. These pulses are then used to seed an optical parametric amplifier (OPA) to allow for spectral tunability.

#### 3.3.3 Optical Parametric Amplifier (OPA)

For spectroscopy, it is required to extend the tuning capability of the RGA, fixed at 800 nm, into a broad range of wavelength. This operation is carried out by means of a fully integrated, computer-controlled femtosecond OPA (TOPAS-C, Light Conversion Ltd, downstream the Legend Elite system; OPerA Solo, Coherent, downstream the Legend Elite) [165, 166]. Both OPA systems are virtually identical except for their pump power and polarization orientation in the SH signal range, see table 3.5.

The operating principle of the OPA is shown in figure 3.8. Its input is split into three parts: About 4% is used for the generation of a white light continuum (WLC) in a sapphire plate (SP), and 17% (83%) of the remainder yield the first (second) pass amplification light. The white light continuum is stretched spatially in a highly dispersive element (DE) to allow for spatial selection of the seed wavelength. Then, it propagates through a first BBO crystal (type II, BBO 1), which selects the seed wavelength to be amplified into the second BBO crystal (type II, BBO 2). The selection and amplification of this wavelength employs an optical parametric generation (OPG) process. In such a process, *signal* photons are generated by temporal and spatial overlap (retroreflectors RR 1 and RR 2) with a proper phase matching angle within the crystals placed on rotating stages. It should be noted that the *idler* photons are a free

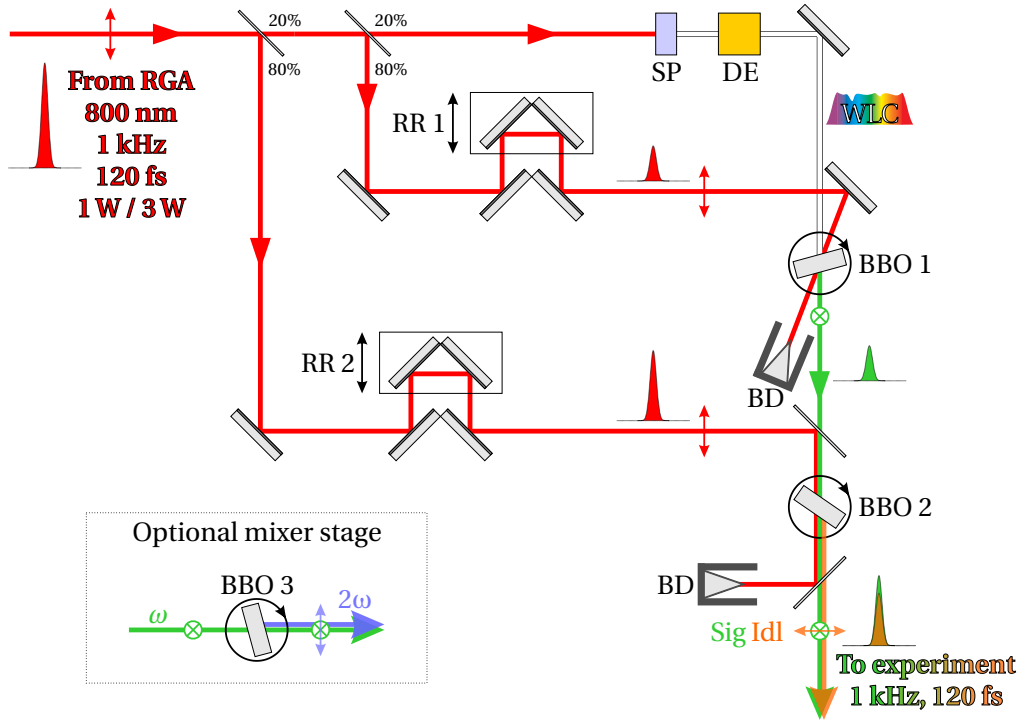


**Figure 3.8** – Optical layout for the optical parametric amplifier. The operating principle relies on several nonlinear stages following the generation of a white light continuum (WLC) in a sapphire plate (SP) followed by a dispersive element (DE). Wavelength selection and light amplification is ensured by setting proper phase matching conditions. This is obtained by rotating the BBO crystal used in each nonlinear and ensuring temporal overlap via motorized retro-reflectors (RR). (BD = Beam dump)

by-product of this operation. They allow to further extend the tunable range according to:

$$\omega_p = \omega_s + \omega_i \quad , \quad (3.7)$$

where  $\omega_p$ ,  $\omega_s$  and  $\omega_i$  are the input pump, the signal and idler frequency, respectively (the wave with higher frequency is called signal, for historic reasons). In total, an amplification factor of about  $1 \times 10^6$  is achieved. Thus, the wavelength tuning of the OPA is done by selecting the phase matching angle of the BBO crystals, thereby ensuring that the wavevectors follow  $k_{\text{pump}} = k_{\text{sig}} + k_{\text{idl}}$  together with a proper time delay of the retroreflectors. In addition, it is possible to extend the accessible wavelength range by placing an additional mixer stage at the OPA output port. The mixer stage consists of a second harmonic generator setup based on an additional BBO crystal (BBO3). Again, phase matching is used to produce either the second harmonic signal (SHsig) or second harmonic idler (SHidl), depending on the orientation, vertical or horizontal, of the BBO rotation axis. Signal and idler waves as well as SHsig and SHidl ones are cross-polarized one to the other, respectively. This allows for simple separation using polarization optics (Glan-Taylor or Glan-laser prisma). The SHidl or SHsig beams share the same light polarization as the signal and idler beams, respectively. For that reason, it is simplest to place a polarization optics upstream from the mixer stage to remove the beam like-polarized with the beam of interest.

For sake of completeness, if, as in the OPerA units, the output beam power is high enough, a further crystal can be added to reach even higher photon energy via the fourth harmonic

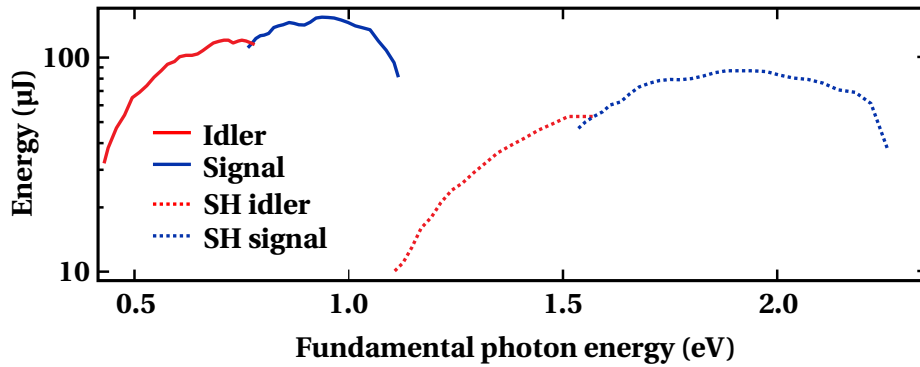


**Figure 3.9** – Energy spectrum of the optical parametric amplifier (TOPAS-C unit; OPerA Solo units about three times as high). The spectrum is split into four ranges depending on the process used to obtain the corresponding photon energy: The idler (0.47 eV to 0.78 eV) is represented by a continuous red line, the signal (0.76 eV to 1.11 eV) is represented by a continuous blue line, the SH-idler (1.06 eV to 1.55 eV) is represented by a dotted red line, the SH-signal (1.51 eV to 2.21 eV) is represented by a dotted blue line.

**Table 3.5** – Spectral output ranges and polarizations of the OPAs and corresponding filters. H and V stands for horizontal and vertical, respectively. For the end-user, the two OPAs used in this work differ only in their output power and SH signal polarization. Filters F1 and F2 are placed immediately upstream and downstream from the sample, respectively. Filter values are given only for the measurements carried out in this work: They are not suitable at the very edges of the spectrum covered by the idler and SH signal ranges. Note that F2 is complemented by the monochromator before SHG light reaches the detector.

	<b>Idler</b>	<b>Signal</b>		<b>SH idler</b>	<b>SH signal</b>
<b>Range (nm)</b>	1600-2340	1120-1400	1400-1630	800-1170	560-820
<b>Range (eV)</b>	0.53-0.78	0.76-0.89	0.89-1.11	1.06-1.55	1.51-2.21
<b>TOPAS-C</b>	H	V	V	V	H
<b>OPerA Solo</b>	H	V	V	V	V
<b>Filter F1</b>	Silicon	Silicon	Silicon	RG850/3	RG695/3
<b>Filter F2</b>	RG9/9	Water	KG5/3	BG39/3	BG39/3

generation (FHG: FHsig and FHidl). Similarly, using another OPG process, namely difference frequency generation (DFG), it is possible to extend the tunable range into the infrared (IR) range up to 16  $\mu\text{m}$ . However, neither the FHG nor the IR ranges have been used in this work, which concentrates on the signal and SHidl ranges. This represents near-IR fundamental frequencies, delivering a signal in the optical range. Figure 3.9 shows the typical spectra form of both OPA units (with OPerA Solo units having about three times as high an output energy as the TOPAS-C units). Their tuning range is detailed in table 3.5. Depending on the photon energy and the laser system used, the laser pulses emitted by the OPA have a fluence of 30 to 300  $\text{mJ cm}^{-2}$ . This corresponds to the 1100 nm SHsig configuration with the Legend Elite and 1300 nm signal configuration with the Legend Elite Duo. However, the fluence is reduced to 2.3  $\text{mJ cm}^{-2}$  across the whole spectral range to protect the samples from destruction, see section 3.7. Hence, light pulses of 0.7  $\mu\text{J}$  with a photon energy of 0.76 eV to 1.57 eV are focused

on a spot with a diameter of about 200  $\mu\text{m}$ .

The Heisenberg uncertainty principle  $\Delta E \Delta t \geq \hbar/2$  provides a theoretically highest achievable spectral resolution limit of 3 meV when applied to 120 fs pulses. In fact, the experimental verification delivers a value of 25 meV [167], therewith limiting the smallest spectral step width in the spectroscopy measurements. A finer spectral resolution would be obtained e.g. with a neodymium-doped yttrium aluminum garnet laser (Nd:YAG short for Nd:Y<sub>3</sub>Al<sub>5</sub>O<sub>12</sub>) emitting nanosecond laser pulses. However, no detectable SHG is obtained with such a laser system due to much lower peak intensities and shorter coherent interaction time with the ultrafast plasmonic process, see section 1.3.3. On the other end in terms of pulse width, much faster systems delivering pulses of only a few femtoseconds are spectrally too wide to carry out proper SHG spectroscopy. For instance, it is no longer possible to distinguish between SFG and its special case SHG.

Also, the spectral tunability offered by an OPA is achieved only with the high intensities offered by a regenerative amplifier laser system. One has to deplore that such systems are currently limited to the few-kilohertz range for the repetition rate. Increasing the repetition rate towards the 100 kHz regime or above would improve the signal acquisition in terms of signal-to-noise ratio and/or acquisition time due to a higher photon flux. While *non-amplified* laser system designs exist that reach the megahertz regime, they lack the required peak intensities to allow for subsequent spectral tunability as well as reasonably long exposure time. Thus, one has to stick to amplified systems: All requirements considered, an amplified system with picojoule to microjoule pulses with a repetition rate in the 100 kHz range is the best suitable for investigating plasmonic nanostructures with currently commercially available products.

### 3.4 Optical Setup for SHG Spectroscopy

The experimental setup is shown in figure 3.10. Since the OPA delivers two linearly crossed-polarized light beams (signal & idler or signal & SHidl), a calcite Glan-polarizing prism is used to select the beam of interest and ensure a linear polarization at the entrance of the setup (1 : 10<sup>6</sup> contrast, 4° field of view, PGH-10, Bernhard Halle GmbH). Then, a computer-controlled rotating half-wave plate (quartz/MgF<sub>2</sub>, RAC 6.2.10, Bernhard Halle GmbH) adjusts the polarization of the light pulses without changing the following beam path. For measurements involving circularly polarized light, the half-wave plate is replaced by a quarter-wave plate (quartz/MgF<sub>2</sub>, RSU 1.4.10, Bernhard Halle GmbH). The light transmitted through the wave plate then passes an oblique glass plate (not shown). The reflection of the incident light is focused onto a pyroelectric detector (flat spectral response J3-05, Molectron Inc.) to measure the linear intensity for reference. At low incidence angles, the reflection from the glass plate is essentially independent of the laser polarization. Two further optics are on the optical path before the pulse train impinges on the sample. First, a borosilicate lens (BK7,  $f = 300$  mm) is used to focus onto the sample. Using a long focal length lens allows for neglecting the coupling of the incident light to the normal component of the sample. The sensitivity to chromatic aberration of the peak intensity is also reduced due to the long Rayleigh length.

### 3.4. OPTICAL SETUP FOR SHG SPECTROSCOPY

Second, a long-pass glass filter is used to block SHG spectral contributions from elements preceding the sample.

Before the light beam impinges on the sample, it propagates through less than 30mm of optical components with group delay dispersion (GDD) lower than  $60\text{fs}^2\text{mm}^{-1}$  [162, 168]. Hence, a conservative higher limit in the effective pulse length impinging on the sample is about 130fs, i.e. a  $< 10\%$  increase from the pulse length delivered after the OPA. This validates the choice of common transmission optics over GDD-free but alienating reflective ones such as parabolic mirrors for focusing.

The typical beam waist is  $150\mu\text{m}$ , the Rayleigh length is of the order of 25 mm [169], and the numerical aperture is 0.004, as measured with a knife-edge technique [170, 171]. For 1 mW excitation power, the pulse peak intensity and electric field strength on the sample are an estimated  $8.2 \times 10^{10}\text{Wcm}^{-2}$  and  $4.0 \times 10^8\text{Vm}^{-1}$ , respectively.

The sample position is adjusted by a 3D micrometer translation stage. This allows to target a

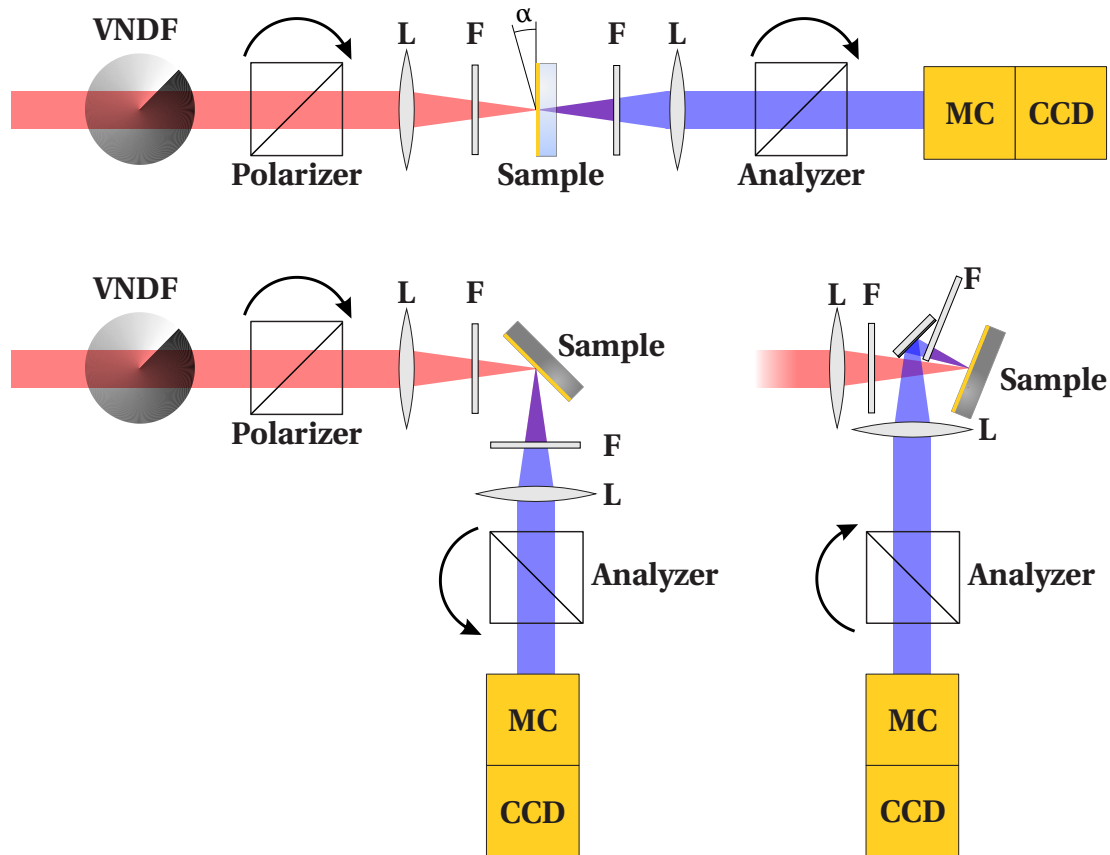


**Figure 3.10** – Optical layout for nonlinear spectroscopy. The operating principle remains the same whether the measurement is carried out in transmission (top,  $\alpha = 0^\circ$ ) or in reflection (bottom left,  $\alpha = 45^\circ$ , and right,  $\alpha \leq 2^\circ$ ). Where required, the sample is cooled using a cryostat or cold nitrogen vapors (not shown). The beam intensity is set by a variable neutral density filter (VNDF). Selected tensor components are determined by polarization optics, i.e. a polarizer ( $\lambda/2$ - or  $\lambda/4$ -wave-plate) and an analyzer (Glan-Taylor prism). Light is focused and collected by lenses (L) and spectrally filtered before and after the sample by colored glass filters (F). The signal is ultimately collected and integrated by a charge coupled detector camera (CCD).

specific field on a given sample by centering the focus beam waist on a nanostructure field. The nanostructure fields have areas ranging from  $100 \times 100 \mu\text{m}^2$  to  $500 \times 500 \mu\text{m}^2$  depending of the sample batch, see section 3.1. For the smaller fields, the beam diameter is reduced to be fully encompassed by the nanostructured field, and the peak pulse intensity is matched. For all samples, the beam covers about one fourth of the total field surface even under  $45^\circ$  incidence angle.

The angle of incidence varies depending on the sample used and on the origin of the signal under investigation. For gold structures on glass, the incidence is normal and the transparency of the sample allows for transmission measurements. With the opaque  $\text{RMnO}_3$  and  $\text{Cr}_2\text{O}_3$  samples, measurements need be carried out in reflection. Such a configuration also makes sure that SHG occurs only near the surface where the plasmonic structure are expected to interact. For  $\text{RMnO}_3$ , the SHG signals of FEL origin are obtained with light incident at  $45^\circ$  to the sample surface to access the  $z$  component, which is present in all the tensor components contributing to FEL SHG, see section 3.1.5. The SHG signals of AFM origin are measured at near-normal incidence ( $\leq 2^\circ$ ) to suppress any FEL SHG. Because of their cryogenic Néel temperature, the  $\text{RMnO}_3$  samples are mounted in an optical cryostat operated with liquid helium (ST-500-UC, Janis Research Company LLC). For  $\text{Cr}_2\text{O}_3$  samples, the incidence is also near-normal ( $\leq 2^\circ$ ) and the sample temperature control is eased by a much higher Néel temperature: Controlled blazing of cold vapors from liquid nitrogen is sufficient to gain access to the AFM signal [172].

In the sample, the incident pulse train generates optical second harmonic and/or third harmonic. Depending on the sample being transparent or opaque, either the SHG light radiated into the forward direction or the reflected SHG beam is collected. A spectral selection is made right after the sample by means of optical glass filters to block the fundamental beam and prevent SHG light to be generated in the following optics. Only harmonics of the fundamental light are transmitted by this short-pass filter. The SHG light represents the signal of interest, not to be confused with the fundamental signal beam. Then, the transmitted light reaches a small aperture iris: Omni-directional signals resulting from incoherent processes such as photoluminescence are excluded by spatial filtering, see section 2.2. Thus, only the SHG signal is transmitted to a second Glan-polarizing prism together with no detectable traces of luminescence. This takes the role of a computer-controlled rotating analyzer and selects the output polarization of the SHG signal being transmitted to the detector. A single achromatic lens ( $f = 200 \text{ mm}$ ) with antireflection coating is used to project the SHG light onto the entrance port of an imaging spectrograph (Triax 190, Horiba Jobin Yvon). The exit port bears a liquid-nitrogen-cooled digital camera ( $\times 1.75$  effective magnification). Using a single coated lens rather than e.g. an aberration corrected camera lens allows for reduction of reflective losses (4% at each air-glass interface) while providing a satisfying light collection. The grating monochromator ensures that higher harmonics than SHG are blocked and allows for spectral analysis. Also, it allows for the reduction of background environmental light not related to the signal of interest. Where the spectral analysis is not required, the monochromator can be replaced by an additional THG filter. All optical filters are reported in table 3.5. The SHG photons reaching the charge-coupled device (CCD) chip are integrated in spectroscopic experiments or spatially resolved for a precise alignment of the laser beam with respect to the metamaterial array. Considering the low excitation density, the low conversion efficiency of

the nonlinear optical process and the monolayer thickness of the material contributing to SHG, the very low dark current of the camera (four electrons per pixel and hour) and its high average quantum efficiency ( $\sim 50\%$ ) are a key for obtaining a detectable SHG signal.

## 3.5 Optical Setup for AFM Domain Topography

The back-illuminated deep-depletion LN<sub>2</sub>-cooled CCD camera offers a  $1024 \times 256$  px<sup>2</sup> resolution, each pixel  $26 \times 26 \mu\text{m}^2$  in size. This enables the acquisition of spatially resolved SHG: Getting access to the topography of the  $180^\circ$  domains in Cr<sub>2</sub>O<sub>3</sub>, see section 3.1.4, allows one to evaluate whether the surface nano-patterned crystals are perturbed by nanostructures lying on their surface. For this measurement only, the laser system is replaced by a nanosecond Nd:YAG laser system (Powerlite Precision II 8000, Continuum Ltd). In this system, an optical medium pumped by flash lamps at 10 Hz delivers 6 ns light pulses. The 1064 nm output is frequency tripled down to 355 nm using a type II followed by a type I BBO doubler. The resulting beam is used to pump an optical parametric oscillator (OPO, VersaScan, GWU-Lasertechnik) to tune the central wavelength to the desired photon energy. A detailed description is available in reference [173]. The setup layout is identical in its principles to the transmission setup shown in figure 3.10. The polarizer consists of a quarter wave plate used to produce circular-polarized light. The analyzer is removed altogether, for circularly polarized light is produced. A single fundamental photon energy of 1.05 eV is used where the SHG signal is maximum, see annex A.3. For this reason and provided vertical and horizontal spatial resolution is required, the monochromator is replaced by a THG filter. The domain contrast inversion with left- or right-circularly polarized light is employed to establish the magnetic origin of the signal, see section 3.1.4.

It is stressed that in such a measurement the domain topography under physical perturbation is being investigated, *not* the amplification of their signal via the nanowires. Indeed with nanosecond pulses, the coherent interaction with particle plasmons is negligible, see section 1.3.3. The reason in using this nanosecond laser system is two-fold. First, the large flat-top beam profile presents a constant homogeneous intensity across the whole beam diameter, focused to 1 cm diameter on the sample. Therewith, the excitation is homogeneous across the entire sample area and the SHG intensity of any point within the beam can be directly compared to any other point. Second, the peak intensity is much lower than in the femtosecond laser system and ensures the structures are not getting damaged as one investigates their effects on the crystal. Nevertheless, it is clear that observing the actual amplification of SHG on different domains via nanopatterning of the crystal surface needs be carried out with a femtosecond system and in a reflection configuration.

## 3.6 Signal Normalization

Nonlinear spectroscopy with femtosecond laser pulses depends critically on the normalization procedure applied to the data. There are two ways to perform intensity normalization. The

two methods described below are virtually identical when the beam profile is constant and unchanged across the spectrum.

Most commonly, the spectral response function  $f(\omega)$  including the transmission of the optical filters and of the monochromator grating and the quantum efficiency of the camera is calculated by referring to the respective lookup tables. When measuring the pulse energy of the fundamental light with a flat-response Joulemeter one can normalize the SHG data to the intensity of the incident light according to:

$$I_{2\omega}^{\text{norm.}} = \frac{I_{2\omega}^{\text{meas.}}}{f(\omega) \cdot I_{\omega}^2}, \quad (3.8)$$

with  $I_{2\omega}^{\text{norm.}}$  the normalized SHG intensity,  $I_{2\omega}^{\text{meas.}}$  the measured SHG intensity, and  $I_{\omega}$  the intensity of the fundamental wave. However, this approach does not account for the spectral or temporal variations of the pulse length or the beam profile.

Therefore, in a refined normalization procedure, the sample is replaced by a reference SHG source with spectrally flat SHG response such as the surface of a silver or aluminum mirror in our case. This leads to a normalized SHG intensity according to

$$I_{2\omega}^{\text{norm.}} = \frac{I_{2\omega}^{\text{meas.}}}{I_{2\omega}^{\text{ref.}}}, \quad (3.9)$$

with  $I_{2\omega}^{\text{ref.}}$  the reference SHG intensity. Note that with this approach the spectral response function of the setup  $f(\omega)$  is automatically included in the normalization. Since the setup responds differently to  $s$ - and  $p$ -polarized light due to the monochromator grating, both reference configurations have to be measured. Thus, any measurement is normalized depending on the polarizer orientation: The normalization function is a linear combination of the latter two orthogonal measurements. A precise positioning of the reference metal surface in the

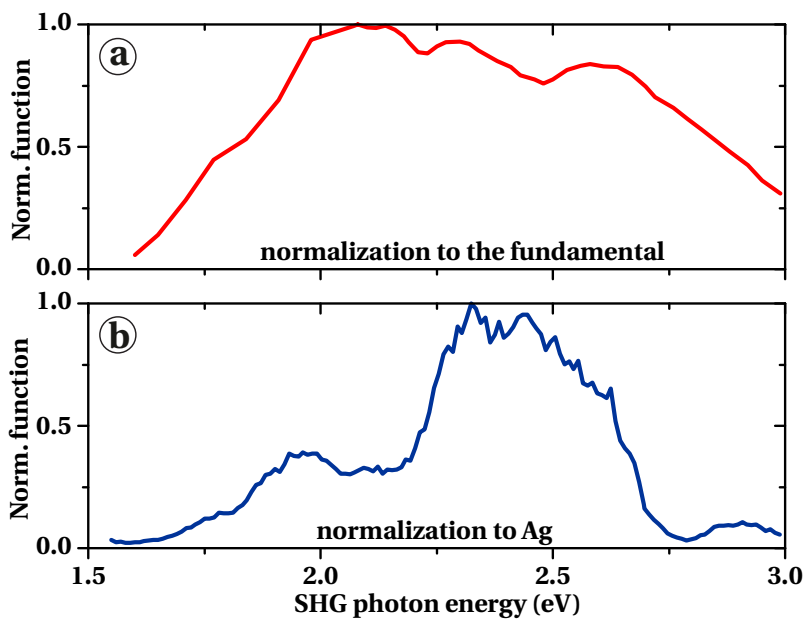


**Figure 3.11** – Normalization functions: (a) Normalization to the spectral transmission of the optical setup and the intensity of the incident fundamental light ( $f(\omega) \cdot I_{\omega}^2$ ) or (b) to the SHG signal obtained on a reference sample with a spectrally broad and flat SHG response, here a silver mirror ( $I_{2\omega}^{\text{ref.}}$ ). The comparison reveals discrepancies due mainly to the beam profile quality so that the normalization procedure to a sample reference should be preferred.

exact same focus plane as for the metamaterial sample is required. Figure 3.11 clearly demonstrates that application of the refined procedure is indispensable for proper normalization as it reveals a pronounced discrepancy between the results of the two normalizing procedures. This difference originates from an evolution of the beam profile across the spectrum via e.g. depletion of the pump within the OPA. These variations evolve in time or as the light path changes (different sample position, focusing, etc.) so that reference acquisitions should be carried out regularly based on the laser system evolution under external perturbation, e.g. temperature variations. Using equation (3.8) is sufficient when the beam profile diameter and quality is constant across the whole spectrum. Ideally, a reference should be measured parallel to every measurement [58], equipment and fundamental beam intensity allowing. The evolution and quality of the beam profile also plays a major role for the peak intensity and therefore for the sample damage threshold evaluated in the following section.

## 3.7 Sample Damage

Illumination of the samples with intense femtosecond laser radiation can lead to alterations or, in the worst case, to the complete destruction of the metamaterials. Therefore, a procedure is needed for maximizing the SHG signal without destroying the samples, and it is essential to estimate the damage threshold of the samples. For this purpose, the reference sample with the half-coated continuous gold film is used. The metamaterial arrays do not consist of a closed layer of gold, but of nanostructures with numerous gold-substrate transitions. Therefore, the reference sample is positioned such that the focused beam hits the edge of the coated area. This is based on the assumption that the threshold for damage at the edges is lower than in the center of a continuous layer. Damage mechanisms are a complex issue and have been discussed in reference [174]. Among other aspects, the confinement of the area covered with the gold results in a reduced heat dissipation from the illuminated region. This effect is worsened by the low thermal conductivity of the glass substrate. The test pulse energy is increased gradually as long as an exposure time of 15 min leaves the sample edges unharmed. The maximum intensity applied to the metamaterial fields is then arbitrarily fixed at one-eighth of the damage threshold. This corresponds to a value of  $2.3 \text{ mJ cm}^{-2}$ . This is a trade-off meant to preserve the sample while allowing proper signal-to-noise ratio. On the one hand, further reducing the fundamental intensity is unpractical since the CCD camera detector does not accommodate extended acquisition times due to its sensitivity to cosmic ray and stray light. On the other hand, having the fundamental intensity just below the destruction threshold means being critically sensitive on laser beam profile variations over the spectrum and/or time. In practice, the output spectrum of the OPA was controlled regularly to audit both spectral gradients and the peak intensity photon energy. Pronounced spectral gradients of the OPA, particularly around the 1.10 eV range, required splitting SHG spectra acquisition in sub-ranges for which the beam intensity was set at the maximum value at the peak intensity photon energy. When the peak intensity photon energy matched a nanostructure's plasmonic resonance, an extra safety measure was taken and the maximum intensity applied to the metamaterial was about halved down to  $1 \text{ mJ cm}^{-2}$ .

At fixed focus size, the above-mentioned intensity represents only a few percent of the capa-

bility of the laser system across the whole spectrum. Still, the high pulse intensities obtained at a repetition rate of 1 kHz deposit a considerable amount of energy into the sample with the potential to cause damage. However, a better suited laser system with a higher repetition rate, as discussed in section 3.3.3, was not available in the time-frame of this work. Only repetition rate improvements of amplified laser systems could trade high peak intensities for higher photon flux to avoid excessively long exposure time.

# Chapter 4

## Results and Discussion

This section provides an initial linear characterization of the metamaterials used in this work. This is done to verify the hypothesis proposed in section 2.1 that any plasmonic effects at  $\omega$  are reflected in SHG processes at  $2\omega$ . Then, one first focuses on the nonlinear characterization by investigating size, shape, and symmetry effects. Following this initial characterization, metamaterials are employed as a potential optical catalyst in an attempt to improve SHG of nonlinear crystals.

### 4.1 Linear Characterization

The linear extinction spectra of the gold structures on glass described in section 3.1.2 are presented in section 4.1.1. Those of gold wires on a nonlinear crystal, described in section 3.1.4, follow in section 4.1.2. Spectra acquisition is carried out at normal incidence after verification that the investigated fields are free of macroscopic and microscopic damages and preceding any femtosecond laser pulse illumination.

#### 4.1.1 Nanostructures on Glass

The linear spectra shown in figure 4.1 reveal several resonances related to different plasmonic oscillation modes, see section 1.3.2. The resonances depend on the incoming light polarization: Each sample field is strongly dichroic with the orientation of the eigenpolarizations depending on the nanostructure geometry [175]. This is demonstrated when continuously varying the incident polarization angle, see annex A.1. The eigenpolarizations correspond to the  $x$ - and  $y$ - symmetry axes of the structures, see figure 3.4. The dichroic structures possess a fundamental linear resonance near 0.70 eV and a cross-polarized higher energy resonance at about 1.15 eV.

This agrees well with numerical simulations carried out specifically for our structures by Richard Taubert in Stuttgart (collaboration group of Prof. Giessen for structure production and linear simulations). The software used is CST Studio Suite developed by Computer Simulation

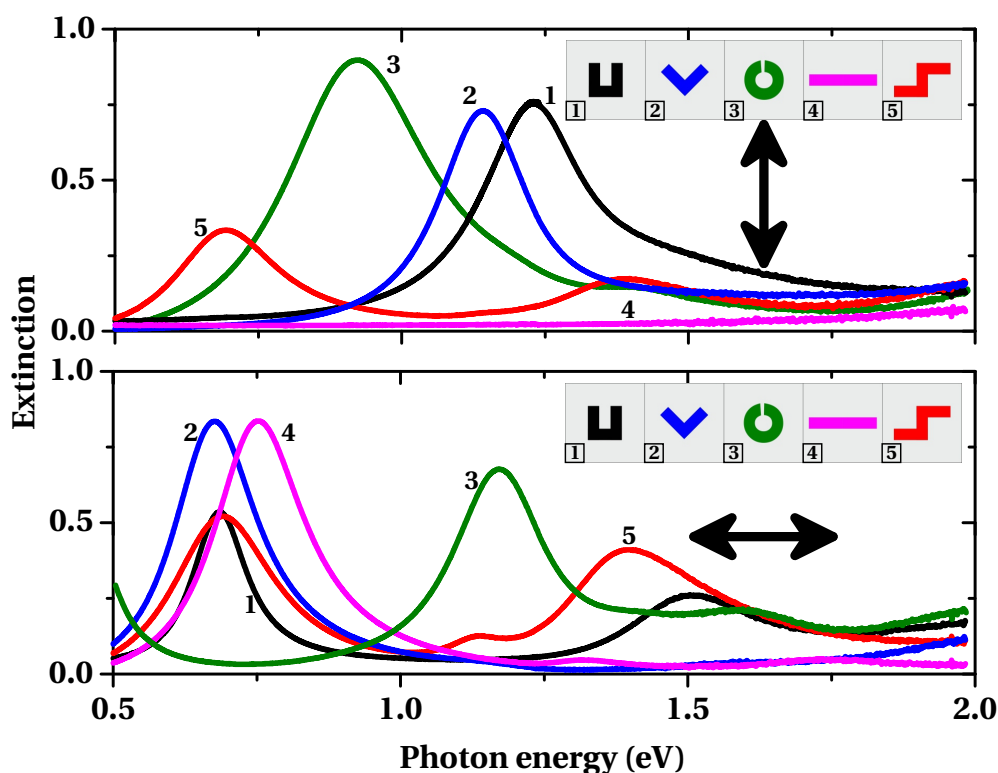


**Figure 4.1** – Linear plasmonic resonances for gold nanostructures on glass. All samples present a fundamental linear resonance with a width of 0.20 eV to 0.35 eV, centered around 0.70 eV, as well as a higher resonance at about 1.15 eV. The polarization of the incident light is indicated by the arrows. The output polarization is not analyzed. The linewidth is indicative only, due to the large aperture angle of the linear spectrometer.

Technology (CST AG). Carried out at the corresponding resonance frequency, these simulations stress the predominance of the structures corners and, to a lesser extent, the edges of the nanostructures for the electric field strength distribution, see figure 4.2. In this figure, the normal component of the electric field is chosen as it reveals most clearly the number of nodes, i.e. the order of the plasmonic resonance. Modes with an odd number of nodes are excited if the incident field is polarized parallel to the gap of a split ring resonator, whereas modes with an even number of nodes are excited for polarization perpendicular to the gap.

In contrast to the numerical model, real nanostructures present rounded edges and corners, a challenging configuration for simulations. Hence, although the qualitative behavior, i.e. the peak wavelength and linewidth, is properly described by the model, one should be very cautious in drawing quantitative conclusions from computational models. The actual shape of the structures is shown in the oblique SEM acquisitions of figure 4.3. The pictures further demonstrate the good uniformity of the EBL-written structures as seen in figure 3.3. The nearly inexistent deviation from a single building block to the others hints at the negligible character of inhomogeneous broadening. The total linewidth of the resonances for an ensemble of nanostructures of the same shape is then essentially that of a single of these nanostructures.

Thus, in accordance with section 1.3, the linear optical behavior is traced back to the symmetrical distribution of the electric charges and hence of the near-field electric field, i.e. the field within and in the immediate vicinity of the structure under optical excitation. This

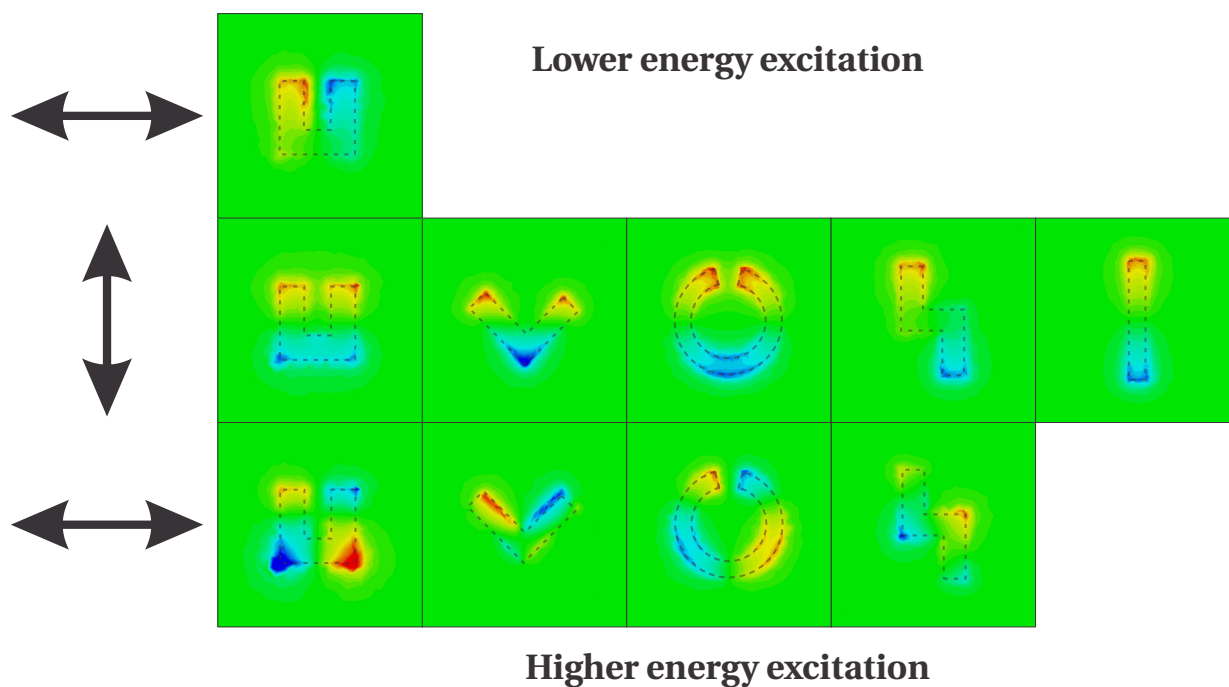


**Figure 4.2** – Normalized simulated electric field distribution within and around the nanostructures: Normal component of the electric field for the first three plasmon modes. The orientation of the fundamental electric field is indicated by an arrow and the resonance energy increases with each row. The first order horizontal polarization resonance is shown only for the U-shaped structure since no other design presents it in the spectral range studied in this work. The predominance of the structures’ corners and edges for processes driven by the electric field is demonstrated. Computation performed using the commercial tool CST Microwave Studio (Computer Simulation Technology GmbH).

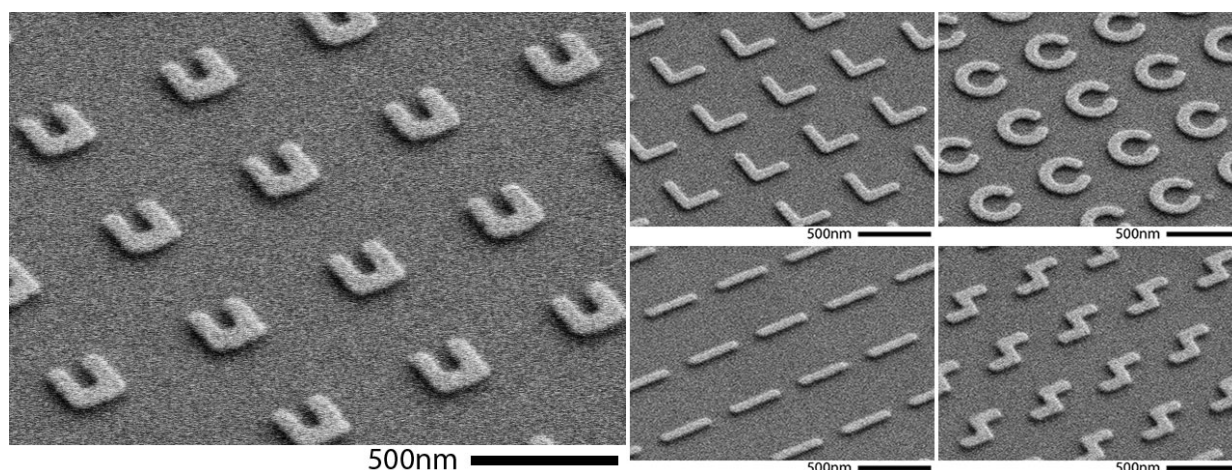


**Figure 4.3** – Oblique incidence SEM micrographs of the gold structures used in this work (light gray) written on a glass substrate (dark gray). All images confirm the homogeneity of the structures and reveal smooth edges and corners regardless of the symmetry design.

supports a potential role of the structures' mesoscopic symmetry in symmetry-sensitive SHG measurements, rather than a determination of the nonlinear optical properties by the bulk gold material properties.

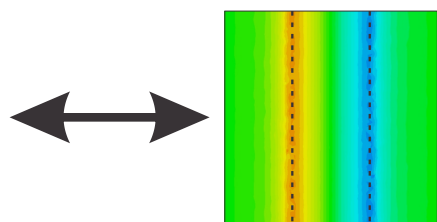
A plasmonic effect at the excitation frequency  $\omega$  should be noticeable at  $2\omega$  via SHG processes, see section 2.1. Thus, in the following SHG spectra, the peak resonance frequency is indicated by vertical dashed lines centered at  $\omega$  and  $2\omega$ . This allows for checking correlations between the linear properties of the nanostructures and their SHG spectra.

### 4.1.2 Nanowires on Nonlinear Crystals and Glass

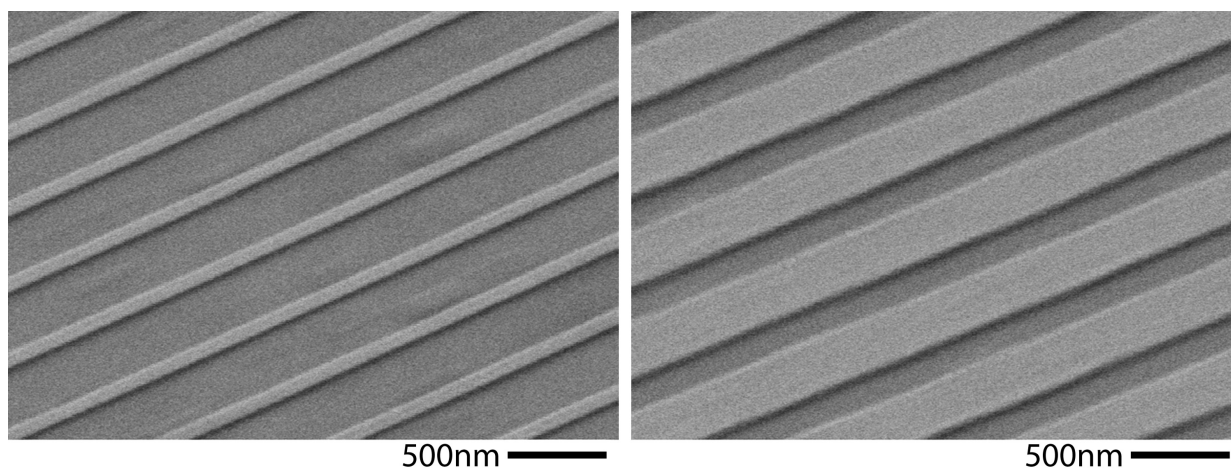
The qualitative observations made above for the metamaterial building blocks on glass hold for the gold wires at the surface of a nonlinear crystal. This is sensible since the processes at play are identical: Changing the gold volume geometry and the nature of the underlying material only tunes the resonance energy and linewidth, see section 1.3. A computer simulation is shown in figure 4.4 that again demonstrates the preponderance of the edges in the electric field amplification process. Here too, oblique SEM perspectives in figure 4.5 display the smooth character of the edges. This results from the fabrication process and contrasts with the model used in the computer simulation without affecting the qualitative observations made on the charge distribution. As shown in figure 4.6, the linear resonances can be tuned across the 0.50 eV to 1.50 eV range, with a typical 0.45 eV FWHM linewidth. Following the same convention as for the nanostructures on glass, the linear resonance is later indicated by vertical dashed lines at  $\omega$  and  $2\omega$  in the following SHG graphs.

Figure 4.7 displays the linear resonance features of metamaterial fields written on  $\text{Cr}_2\text{O}_3$  in a single batch. These are discussed in section 4.2.4. Figure 4.8 displays the same features for similar nanostructures *on glass*. Being amorphous, the glass substrate does not offer any preferred direction with respect to its electromagnetic features. Neither does fused silica have remarkable optical features in the resonance range covered by the nanowires. As a consequence, all plasmonic features vary roughly linearly as the nanowires' width shrinks with increasing field number. In particular the quality factor  $Q$  increases with field number. The comparison with the former graph with structures on a nonlinear crystal is essential to understand the subtleties of metamaterials. The  $\text{Cr}_2\text{O}_3$  sample features a peak in the quality factor for metamaterial fields with a plasmonic resonance around 1.05 eV, a region of high optical density for  $\text{Cr}_2\text{O}_3$ . In other words, it is experimentally verified that the linear spectra are related to their environment, as described in section 1.3. The point is cardinal: A given batch of nanowire geometries on glass can hardly be compared to the same nanowire geometries on a crystal. Not only is the central resonance peak shifted, but also the quality factor is altered. Any comparison is to be carried out with great caution. Nanowires on glass are discussed later in section 4.2.4.

#### 4.1. LINEAR CHARACTERIZATION



**Figure 4.4** – Normalized simulated electric field distribution within and around a gold nanowire: Normal component of the electric field for the first plasmon mode. The incident field is polarized perpendicular to the wire axis, as indicated by the arrow. The gold section in the middle is delimited by dashed lines. The predominance of the structures corners and edges for processes driven by the electric field is verified. Computation performed using the commercial tool CST Microwave Studio (Computer Simulation Technology GmbH).



**Figure 4.5** – Oblique incidence SEM micrographs of gold structures (light gray) written on a  $\text{Cr}_2\text{O}_3$  crystal (dark gray). The images show the smallest (left) and largest (right) gold widths and reveal the smooth edges of the wires.

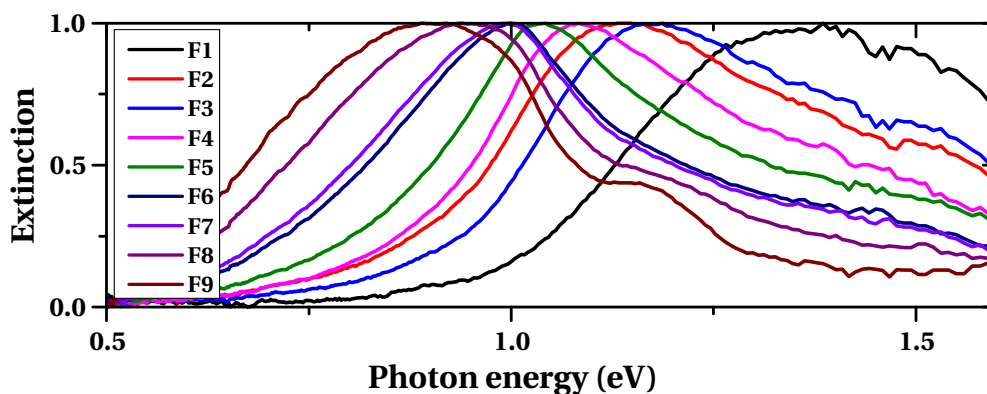


**Figure 4.6** – Typical linear plasmonic resonances for gold nanowires on a nonlinear crystal. All samples present a fundamental linear resonance with a linewidth of about 0.45 eV for a polarization of the incident light normal to the wire orientation. No resonance is present for an incident light polarization along the wires. The output polarization is not analyzed. The linewidth is indicative only, due to the large aperture angle of the linear spectrometer.

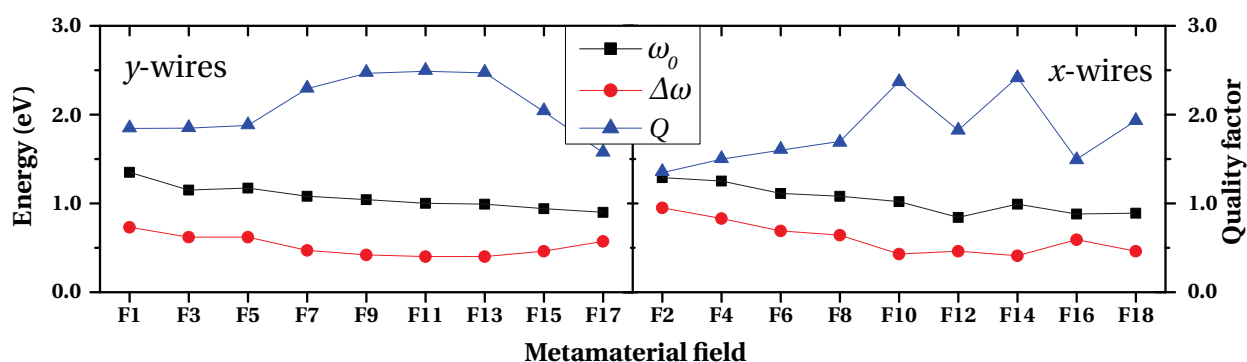


**Figure 4.7** – Resonance features of nanowire field pairs on  $\text{Cr}_2\text{O}_3$  (sample DMF18). The resonance peak energy  $\omega_0$ , the linewidth  $\Delta\omega$ , and the quality factor  $Q = \omega_0/\Delta\omega$  are reported. For each  $y$ -wire field design  $F_i$  corresponds a  $x$ -wire field  $F_{i+1}$  with similar resonance features. Globally,  $x$ -wires present a broader linewidth (up by maximum of 0.20 eV), reflected in a lower quality factor.  $y$ -wires' features display a continuous trend, as targeted during production. On the contrary,  $x$ -wires appear much noisier in their resonance features, despite sharing the same fabrication process. Lines are drawn to guide the eye.

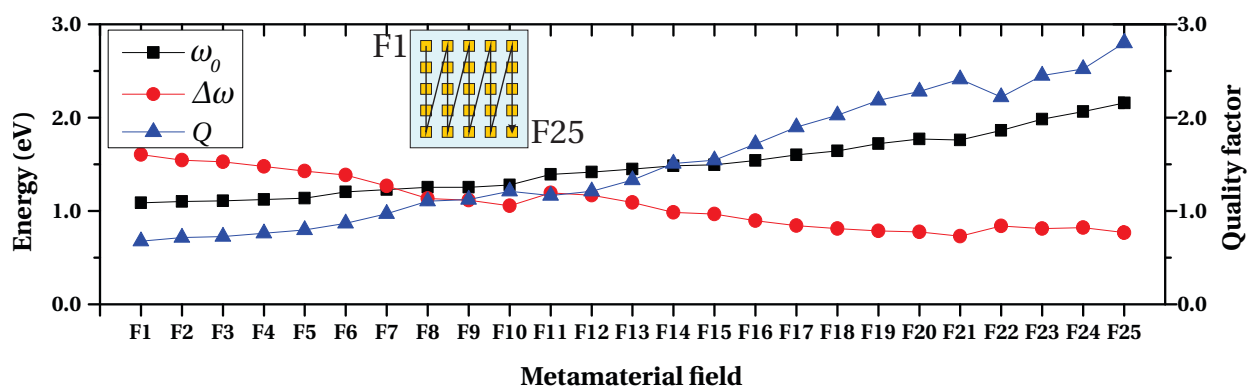


**Figure 4.8** – Resonance features of nanowire fields on glass. The resonance peak energy  $\omega_0$ , the linewidth  $\Delta\omega$ , and the quality factor  $Q = \omega_0/\Delta\omega$  are reported. All nanowire fields are oriented in the same way since the substrate is isotropic. Lines are drawn to guide the eye.

## 4.2 Nonlinear Measurements

Nonlinear SHG measurements are described and discussed in this section. The SHG character of the emitted light is first verified. Then, the SHG spectrum from bulk gold is investigated for reference with respect to nanostructured gold samples. Two sections follow: First SHG from different metamaterial designs are discussed. The aim is to characterize the SHG generation process in metamaterials. Second, the local field enhancement feature of metamaterials is investigated to validate nanowires as optical catalysts for SHG generation.

### 4.2.1 SHG Character of the Emitted Light

As highlighted in section 2.2, caution in separating TPPL from SHG signals should be taken. This is carried out based on the signature features of SHG signals as detailed at the end of section 2.1: Quadratic electric field dependence, narrow spectral width, and polarization

## 4.2. NONLINEAR MEASUREMENTS

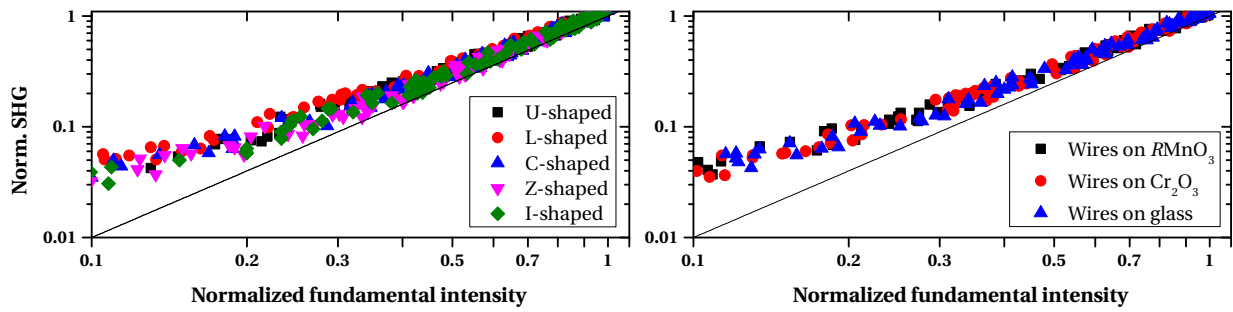


**Figure 4.9** – Typical signal intensity versus fundamental intensity for the nanostructures on glass (left), and for the nanowires on a nonlinear crystal (right). The signals exhibit the SHG characteristic square power dependence on incident power, indicated by a continuous line. At lower intensity, a deviation is observed due to noise contributions.

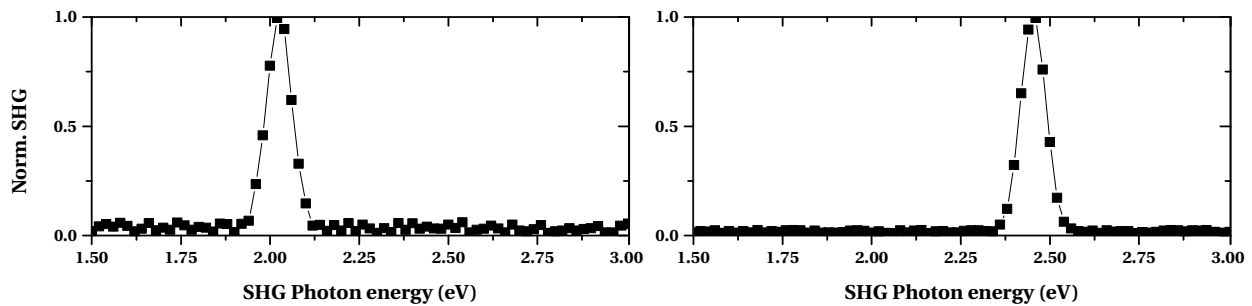


**Figure 4.10** – Typical signal intensity versus monochromator-transmitted photon energy for the nanostructures on glass (left) and for the nanowires on a nonlinear crystal (right). The signals exhibit the SHG characteristic of near-monochromaticity, indicated here by a narrow 0.07 eV linewidth centered on twice the energy of the 1.00 eV and 1.23 eV fundamental, respectively. The continuous lines are used to guide the eye.

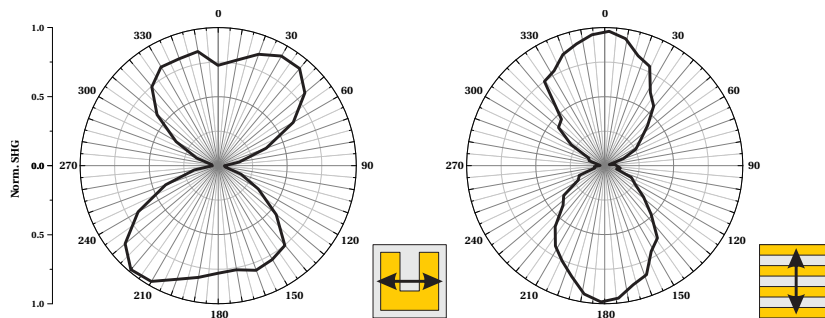


**Figure 4.11** – Typical emission polarization anisotropy of the measured signals for nanostructures on glass (U-shaped, left) and for the nanowires on a nonlinear crystal (right) excited in their lowest order resonance. For each structure, the excitation polarization is indicated by an arrow. The anisotropic form of the signals excludes a TPPL process as the signal source.

anisotropy of the SHG signal. Although all three features must be present to ascertain the presence of SHG, only the last two are decisive in separating SHG from TPPL. In particular, the *output* polarization anisotropy is key, since a broad SHG spectrum could be related to spectrally broad plasmonic resonances, see section 1.3.3. For the same reason, one would prefer a system providing rather long, i.e. spectrally narrow, 100 fs light pulses rather than ultrashort, but spectrally wide, 8 fs pulses.

One verifies with figure 4.9 that the measured signals are quadratically dependent on the fundamental electric field. This is verified for all types of nanostructures investigated in this

work, independently of the design (U-, L-, C-, Z-, I-, or wire-shaped) or the substrate used (glass or nonlinear crystal). A low-intensity deviation is observed that cannot be related e.g. to TPPL since TPPL is also quadratically dependent on the electric field, see equation (2.15). Rather, this is attributed to background and read-out noise at the level of the CCD camera. Indeed, subtracting a constant level, as measured with the laser beam blocked, leads back to a near perfect square power dependence.

Figure 4.10 displays the narrow 0.07 eV linewidth of the measured signals. Therewith, the possibility of being in presence of TPPL is already discarded, since it is known to present broader luminescence lines on gold [125]. This is confirmed with figure 4.11 where a clear anisotropy in the output polarization is visible. The anisotropic form of the signals excludes a TPPL process as the signal source. Hence, one concludes that the measured signals discussed in the following sections result from an SHG process. It is stressed for the following discussion that analyzer measurements carried out on horizontal nanowires deliver a  $\cos^2 \theta$  signal form ( $\sin^2 \theta$  for vertical nanowires).

## 4.2.2 Bulk Material Nonlinear Spectroscopy

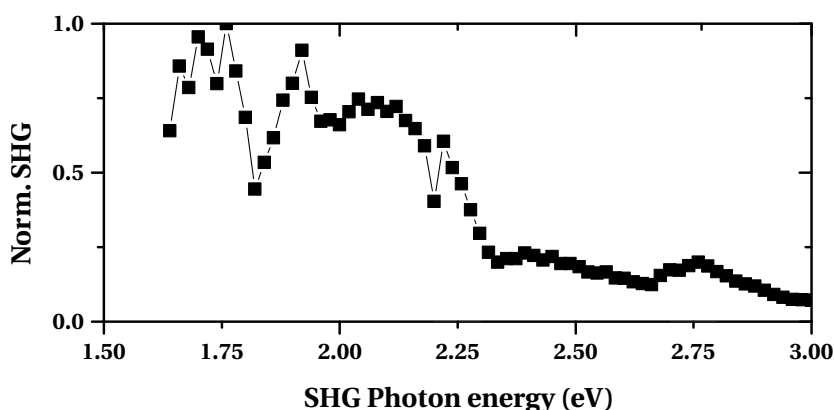


**Figure 4.12** – Normalized SHG spectrum of a plain gold film illuminated by  $p$ -polarized light at an angle of incidence of  $45^\circ$ . The spectrum lacks spectral features that could explain the nanostructures' nonlinear spectra.

The previous section established the measured signals result from an SHG process. However, no insight was provided into its mechanism. The non-predominance of the bulk material in the linear optical features of the nanostructures does not indubitably rule out the role of gold in nonlinear measurements. Though the amorphous gold used in the nanostructures is centrosymmetric, surface SHG is always possible and has been readily reported for metallic surfaces and gold in particular [176, 177]. Since the nanostructures present a finite volume and are imperfectly flat, as shown in the SEM acquisitions above, surface SHG is likely to occur even at normal incidence. Thus, the strength of the surface-induced SHG *material* response in SHG measurements constitutes a first reference measurement. The gold film mentioned in section 3.1.2 is measured at  $45^\circ$  incidence in  $p$ -polarized incoming and outgoing polarizations. Indeed, surface SHG cannot take place and no SHG is recorded on a gold film at normal incidence. The resulting spectrum is shown in figure 4.12. Neither does it display clear spectral features, nor does the comparison of this measurement with all following SHG spectral acquisitions from nanostructures show direct correlations. One concludes that the

measured SHG spectrum for any given meta-atom geometry truly reflects the nonlinear optical properties of the metamaterial: In other words, the building-block geometrical features seem to predominate over the material.

### 4.2.3 SHG Characterization

It has been verified in the previous sections that the measured SHG signals cannot be explained as a mere material, i.e. gold, feature. Thus, they must be determined by the design features of the metallic nanostructures. In this section, one now concentrates on the effect of size, shape, and symmetry. To do so, the process of SHG on metamaterials is characterized by polarization-dependent SHG spectroscopy measurements on the SRR structures shown in figure 3.2.

As detailed in section 3.1.2, different nanostructures can share a given symmetry and/or particular features such as the number of corners. Remarkably, sharing a symmetry does not necessarily involve exhibiting the same features and vice-versa. For instance, U- and Z-shaped metamaterials possess the same number of arm-to-base corners, yet fundamentally differ in their symmetry group. On the contrary, C-shaped structures lack corners completely (even the arm ends are rounded), yet follow exactly the U-shaped structures with respect to the transformations leaving the structures invariant. On the one hand, any correlation between different geometry patterns provides information about the *mechanism* at play for SHG in metamaterials. On the other hand, employing the exact same structure up- or downscaled to red- or blue-shift the linear resonance, respectively, provides information about the *spectral dependence* of the mechanism. In other words, one investigates to which extent the spectral dependence of the SHG signal is related to the nonlinear susceptibility  $\chi^{(2)}$  and to which extent it is due to linear modifications of the incident light at  $\omega$  and the emitted light at  $2\omega$ .

It is stressed that reproducibility issues recurrently occurred with all measurements related to nanostructures on glass. This is discussed at the end of this section.

#### Size Effects: Spectral Dependence

The spectral dependence is considered first. Figure 4.13 compares the SHG signal strength of three similar U-shaped nanostructures differing only in the position and strength of their respective linear resonance, i.e. the arm and base lengths. The  $h\nu$  configuration is investigated, see table 3.2. In the ED approximation, this corresponds to the  $\chi_{yxx}^{eee}$  tensor component. Under  $x$ -polarized excitation, the lowest-energy linear resonance corresponds to the fundamental plasmon mode.

For each structure size, the spectral dependence of this tensor component is put in perspective to the linear extinction spectrum. The scale of the linear spectra is chosen such that any correlation to the SHG signal may be seen more easily at the fundamental frequency  $\omega$ . No interesting linear spectral features are present at the harmonic frequency (not shown, for sake of clarity). All three samples lack a correlation of their nonlinear signal strength with the linear resonance. This behavior is observed in all other samples, too.

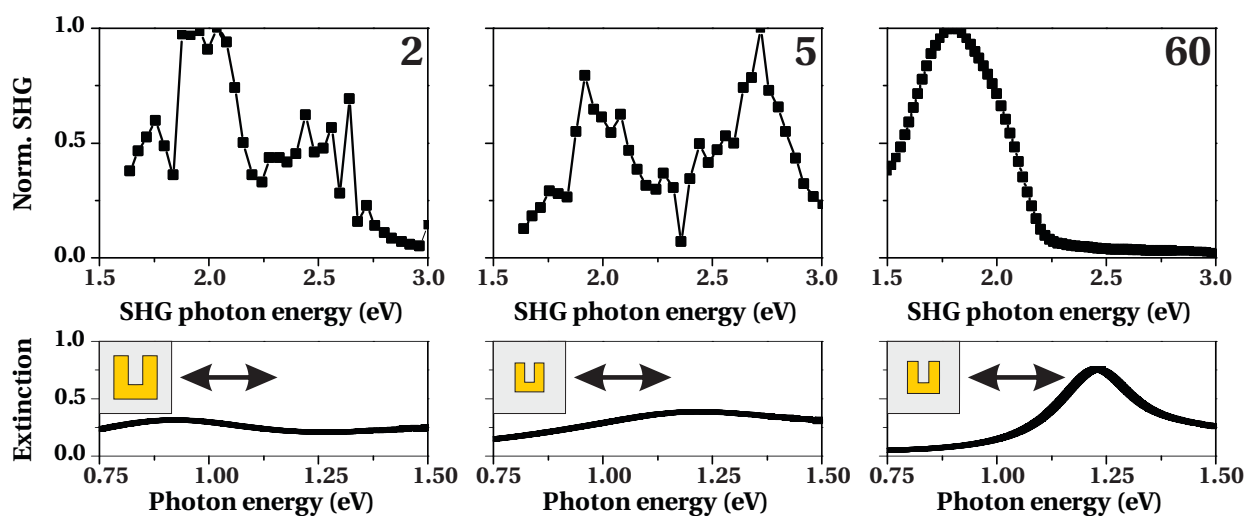


**Figure 4.13** – Spectral comparison of normalized SHG signals for three similar U-shaped metamaterials. The nanostructures differ only in their arm and base lengths, i.e. the position and strength of their respective linear resonance. The fundamental beam is polarized horizontally along the base or  $x$ -axis, SHG is analyzed vertically along the arms or  $y$ -axis. The corresponding linear resonances are displayed below each graph. The last column sample field is more recent than the first two samples: It features a higher resolution geometry and consequently displays sharper resonance features. The excitation polarization is indicated in inset beside a not-to-scale indication of the relative size of the unit-block geometries.

Also, the spectra and their relative amplitudes are strongly altered. Although the modification of the base design is minimal and maintains the overall geometry, there is no obvious trend in the evolution of the SHG spectra with respect to their linear counterparts. It follows that the spectral dependence of SHG in metamaterials does not match a straightforward projection of their linear response. A more complex process must be at play than the correlation initially suggested in reference [58], in which the spectral range being considered is much narrower.

### Shape Effects: Geometrical Feature Dependence

Further insight into the complex mechanism is researched by investigating different sample shapes. Figure 4.14 offers a structured overview of the relative SHG intensity gained from the variety of designs in figure 3.2. The corresponding linear resonances' maxima and FWHM are represented by a vertical dashed line and a grey area on each spectrum, respectively. The complete linear spectra are displayed in annex A.1.

Many striking features are observed in the SHG spectra. In some cases, like for the  $\chi_{yxx}$  components of the non-centrosymmetric structures, the SHG spectra appear not to be correlated to the corresponding horizontally polarized linear spectra. In other cases, such as the  $\chi_{yyy}$  components with the vertically polarized linear spectra, such a correlation seems present, at least for the U- and L-shaped structures, less so for the C-shaped one. Here too, it is not possible to confirm a systematic correlation between the spectra at  $\omega$  and  $2\omega$ . In addition, the nonlinear spectra do not display a narrowing of their FWHM with respect to that of the linear spectra as one would expect through the SHG process. This confirms that a more subtle

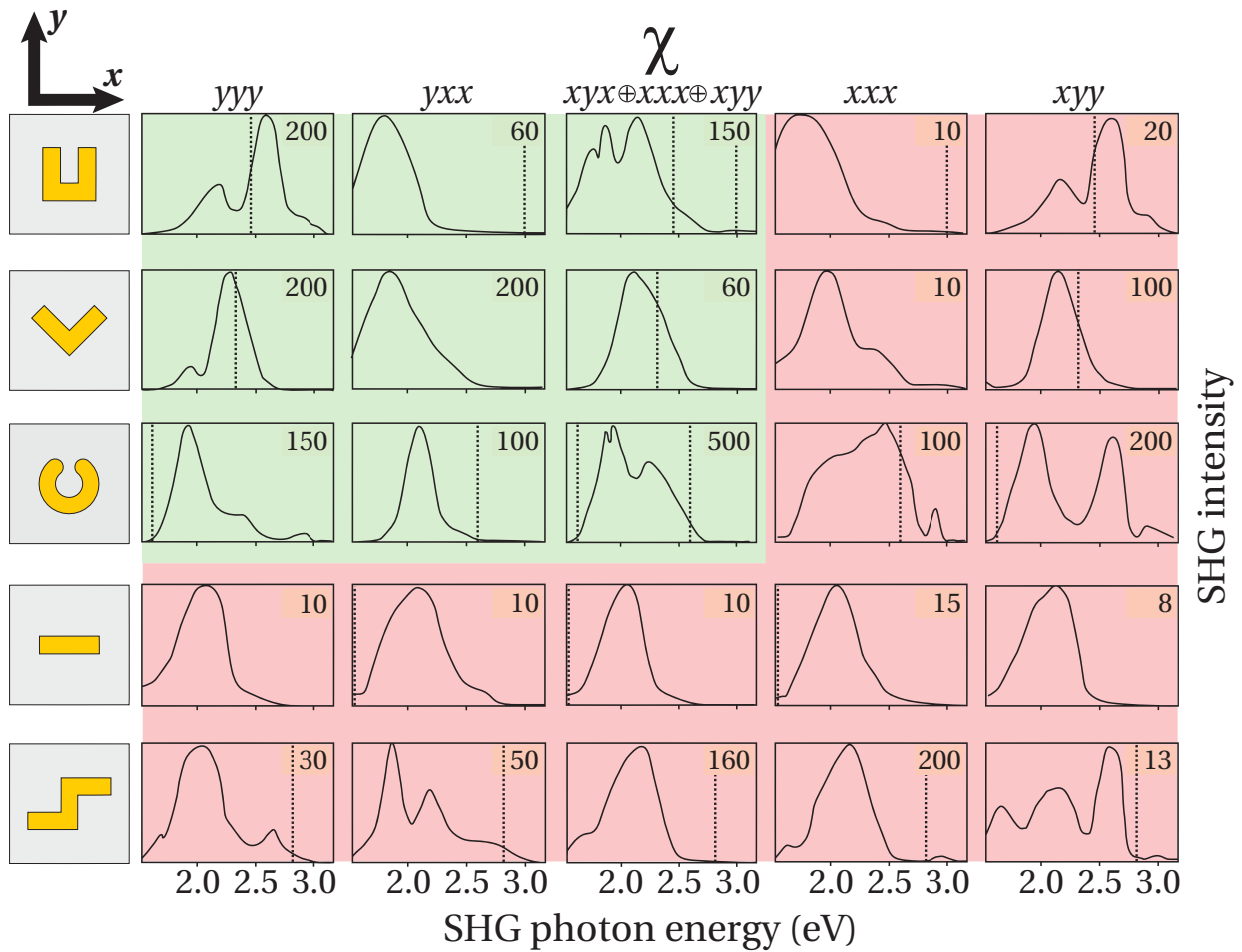


**Figure 4.14** – SHG spectra for metamaterials featuring a variety of designs. Diagrams with a green or red background are allowed or forbidden by symmetry analysis, respectively. The inset values represent the peak value of each spectrum on a common arbitrary scale. The spectra in the center column represent a convolution of contributions from three independent SHG tensor components. The second harmonic of the nanostructures’s excited linear resonance is indicated by a vertical dotted line.

process is responsible for the spectral dependence of the SHG signal than the linear plasmonic resonances alone, as shown above through size effects.

Interestingly, one observes that both  $x$ - and  $y$ -polarized excitations can lead to SHG signals of equal order of amplitude. On the one hand, the *magnetic* metamaterial aspect in reference [48] may not be a suitable interpretation, as the same authors later suggested in reference [55]. On the other hand, this is consistent with the plasmonic excitation description in reference [178], which is used in this work. Thus, it is sufficient to define optical metamaterials according to a metal nanostructure nomenclature, i.e. using a plasmon picture. Therewith, one departs from the historical LC-model used for larger metamaterial structures with resonances in the infrared [179, 180].

One now compares the SHG spectra of the top three SRR structures in figure 4.14. They differ from one another in their structural complexity, see section 3.1.2iii. Although they share the same  $mm2$  geometry, the spectra of corresponding SHG susceptibilities exhibit pronounced

differences. However, understanding the underlying processes is not trivial. The approach in this work is to investigate the role of surface curvature and find possible evidence for local field enhancement at corners, see section 3.1.2. Indeed, the peak signal between the U-, L-, and C-shaped structures varies, but a systematic relation to the number of corners in the SRR design is not obvious. In several of the spectra ( $\chi_{yyy}$ ,  $\chi_{xxx}$ ,  $\chi_{xyy}$ ) one observes double peaks whose relative amplitude varies with the design. In addition, the change of design is accompanied by red shifts ( $\chi_{yxx}$ ,  $\chi_{xxx}$ ) and blue shifts ( $\chi_{yyy}$ ) of the spectra. The reasons for all these features are not yet understood.

Noticeably, the strongest signal is measured for the round SRRs in the  $\chi_{yzy}$  configuration. With a peak value of 500, it is more than twice as large as any other signal. For the C-shaped SRR, the energy difference between the two resonances at 0.90 eV and 1.15 eV is the smallest of the SRRs shown here. Therefore, the high SHG intensity may be the result of a constructive interference of the SHG contributions from the two resonances. Indeed, these two resonances are simultaneously present under  $d$ -excitation and correspond to a vertical and horizontal excitation, respectively.

### Symmetry Effects: Interferences Dependence

This part focuses on the two centrosymmetric structures shown at the bottom of figure 4.14 to verify the presence of any SHG contributions that are not due to the leading-order ED type, see section 3.1.2iv. The SHG signal observed on the cut-wire structures is approximately zero. For this structure, the point symmetry analysis and the ED approach are therefore the appropriate way to describe the structure. However, the centrosymmetric Z-shaped nanostructures exhibit a SHG signal with an intensity comparable to that measured on the non-centrosymmetric structures. This is corroborated by the observations of other SHG contributions expected to be forbidden by the symmetry (i.e.  $\chi_{yyy}$ ,  $\chi_{yzz}$ ) even on the non-centrosymmetric designs.

These striking observations show that the description of the metamaterials by an effective SHG susceptibility describing only the global symmetry of the periodic arrangement of nanoscopic building blocks is insufficient. Then, the local structure of the building blocks on the nanoscale may lead to contributions to the SHG yield that go beyond those allowed by the macroscopic symmetry. This is similar to the case of incommensurate structures where long-wavelength spin structures were recently found to lead to SHG contributions that are forbidden by the point symmetry [181].

As for the origin of the local SHG contributions, one notes that whereas the metamaterials present an excellent homogeneity at the scale of hundreds of nanometers, this is no longer true on the order of the size of the building blocks. A multitude of surface defects with small radius of curvature are present [59, 60]. In spite of their random distribution they can interfere with the SHG process so that new SHG signals emerge that are normally canceled out due to destructive interference [182]. Also, “hot spots” with high charge density are associated with regions with small radius of curvature. By Gauss’s law, the electric field intensity is locally increased and multipoles of even higher order can be promoted.

A qualitative and quantitative evaluation of this interpretation is presently under development. An elaborate approach is found in the recent work of Kauranen et al. [183–185]. Their work

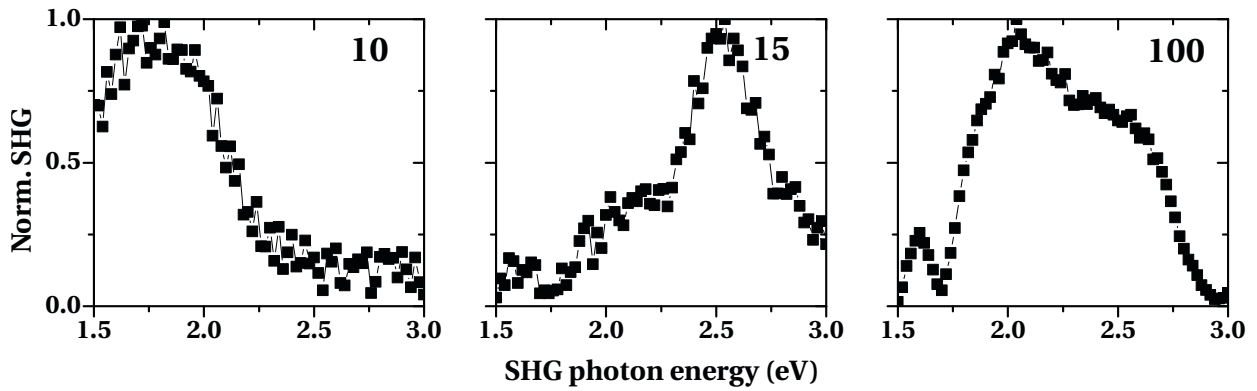


**Figure 4.15** – SHG acquisition reproducibility on a U-shaped metamaterial field. Three acquisitions of the  $\chi_{yyy}$  spectrum of the reference U-shape design. All three curves are obtained using the very same sample. The second spectrum was obtained immediately after completion of the first acquisition, on a single setup. Only the optical alignment of the field with respect to the laser was readjusted (field taken out and back in the beam). The third curve was obtained after the setup was rebuilt using another similar laser source. The lack of reproducibility is observed constantly also for other designs. The acquisition mismatch, even when leaving the setup untouched, can only be explained by an alteration of the sample itself.

makes use of an effective medium multipolar tensor analysis to demonstrate the presence of higher order contributions to the SHG signal due to local effects. The resulting inhomogeneity of the electric field may also lead to SHG contributions from the substrate [183, 186–188]. The relevance of local inhomogeneities for the SHG process is supported by linear extinction spectra and SEM measurements on the metamaterials subsequent to the SHG experiments. We observe that laser-induced modifications increasing the disorder of the building blocks do always occur up to partial detachment and relocation on the substrate as shown later in figure 4.17.

### Reproducibility Issues

As it has been mentioned at the beginning of this section, reproducibility is a major issue with the results presented above.

Figure 4.15 shows three acquisitions of the  $\chi_{yyy}$  spectrum of the reference U-shape design. All three curves are obtained using the very same sample. The second spectrum is obtained immediately after completion of the first acquisition, so that both use the same laser source (Legend Elite, TOPAS-C) and setup. Another laser source (Legend Elite Duo, OPerA Solo) is used to obtain the third curve, and the setup was rebuilt, although its operating principle is maintained. The lack of reproducibility is observed constantly also for other designs. The acquisition mismatch, even when leaving the setup untouched, can be explained either by minute changes in the beam position or by an alteration of the sample itself. The former can have a nonlinearly large effect as in sub-resolution SHG imaging. As for the latter and assuming a Gaussian beam an intensity of  $2.3\text{mJcm}^{-2}$  is considered to be safe for a gold sample, see section 3.7. From there, the damage threshold is overcome if the beam characteristics are modified (inhomogeneities, smaller beam diameter). Nanostructuring the gold sample might

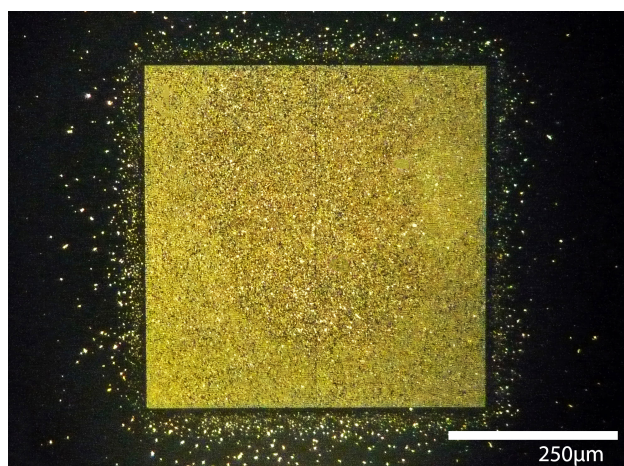


**Figure 4.16** – Optical microscope inspection of a damaged field of gold metamaterial structures. The image reveals inhomogeneity of the field as well as clusters of gold particles around the it at positions left clear from any lithographic process. One notices the longest exposure area in the center (about  $200\mu\text{m}$  beam diameter). However, the rest of the field is damaged as a consequence of further damage threshold tests.

also promote damage processes not predominant in the bulk test sample and for which the extra margin below the damage threshold is not sufficient to prevent alteration of the sample.

Effects due to beam profile variations are minimized by monitoring and optimizing the condition of the laser system (optical alignment, temperature stability, optics cleanliness) and e.g. via the normalization procedure detailed in section 3.6. However, one notices the narrow measurement window defined while evaluating the destruction threshold: A lower or higher fundamental intensity and the generated signals are too low to be measured or the sample is destroyed, respectively. Thus, even a moderate inhomogeneity of the beam profile potentially overcomes the destruction limit. Such a problem does not occur in natural crystal samples since they withstand much higher intensities of the fundamental.

As mentioned in section 3.7, sample damage can also occur due to the ultrafast processes induced by the 100 fs light pulses. The high pulse intensities obtained at a repetition rate of 1 kHz deposit a considerable amount of energy into the sample with the potential to cause damage. The plasmonic process drives the displacement of electrons within the metallic nanostructures. Although gold is the third best electrical conductor after silver and copper (at room temperature,  $4.5 \times 10^7 \text{ S m}^{-1}$  vs.  $6.2 \times 10^7 \text{ S m}^{-1}$  and  $5.9 \times 10^7 \text{ S m}^{-1}$ , respectively), it retains a finite resistivity and is hence subject to the Joule effect. Thus, the ultrafast light pulses trigger a nearly instantaneous heating of the gold volume and therewith thermal expansion. Different expansion coefficients for gold and glass hint at a possible mismatch at the gold-glass surface contact and with it at an alteration of the sample.

Naked-eye visual inspection proves inconclusive in detecting sample destruction: The gold layer is not vaporized as for damages of a plain gold film, and a nanostructure covered field remains observable. However, sample damage can be verified using a variety of methods. Corresponding illustrations are found in figure 4.16-4.18. By growing order of testing complexity, a first visual inspection under optical microscope shows inhomogeneities in the metamaterial fields, as well as presence of gold beyond the field boundaries. Second, the metamaterials lose their linear spectral features as soon as their meta-atoms are altered. For instance, after illumination of the sample, the extinction resonance obtained under  $y$ -polarized light excitation drops from 76% to 20%, as seen in figure 4.18. This reduction is accompanied by a moderate 0.08 eV blue-shift of the linear resonance, which hints at an alteration of the base unit. Third,

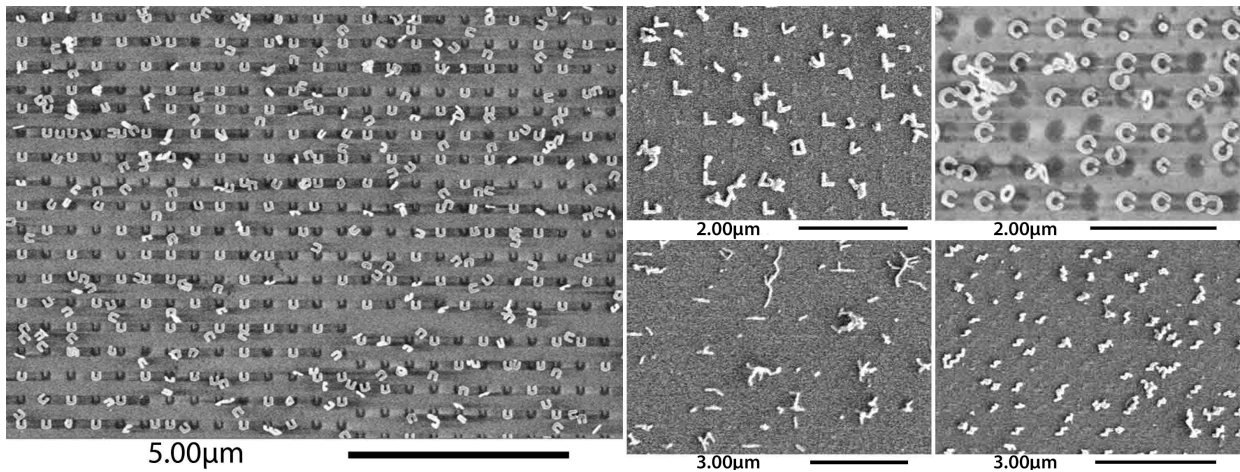


**Figure 4.17** – Normal incidence SEM micrographs of damaged gold structures (light gray) written on a glass substrate (dark gray). All images reveal distortions and randomizing of the nanostructures regardless of the symmetry design. Hardly any melting of the gold volumes is observed. Most structures are dislocated from their original position and are scattered around. Once displaced, they potentially remain in contact with a neighboring unit.

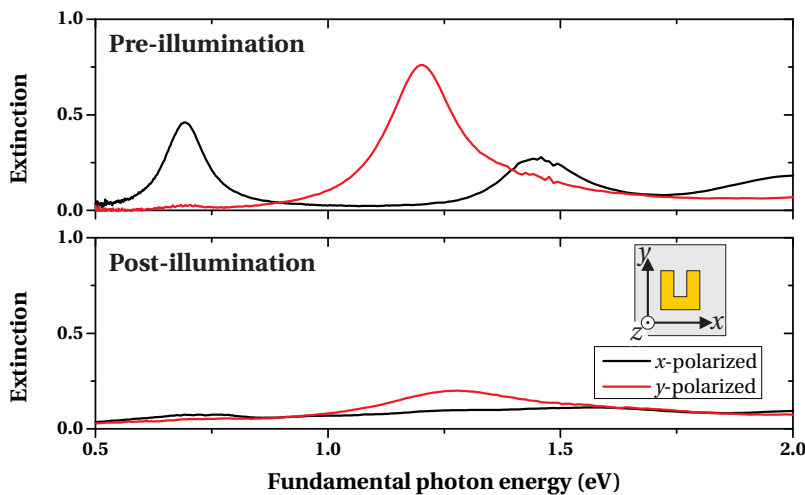


**Figure 4.18** – Linear spectra before (top) and after (bottom) illumination by femtosecond laser light pulses. The polarization of the excitation is along the  $x$ - (black) or  $y$ -axis (red). Most linear extinction resonances are virtually suppressed after exposure, while the remaining features are blue-shifted. The change is consistent with an alteration of the metamaterial building blocks' geometry and relative orientation.

direct SEM observation provides an actual view of the sample condition with meta-atoms either destroyed (e.g. partial or complete melting of the gold) or with their relative orientation randomized. The corresponding figure supports the hypothesis of a destruction induced by thermal expansion, see figure 4.17. Such a process leaves each meta-atom minimally altered in design, though not in their relative positioning. A few structures appear to hold in place: These explain the remaining *linear* spectral features seen in figure 4.18.

Thus, attempts were made at minimizing its effect. First, the Joule effect was decreased by reducing the temperature of the sample to 10K using vapor from liquid helium in a cryostat. A first cooling cycle without laser exposure together with a before/after comparison of the linear spectra allowed to verify that samples withstand progressive cooling. Heading to cryogenic temperatures dramatically lowers the resistivity of metals and cuts down the ohmic heating rate, see figure 4.19. It is stressed that linear spectral acquisitions were carried out at room

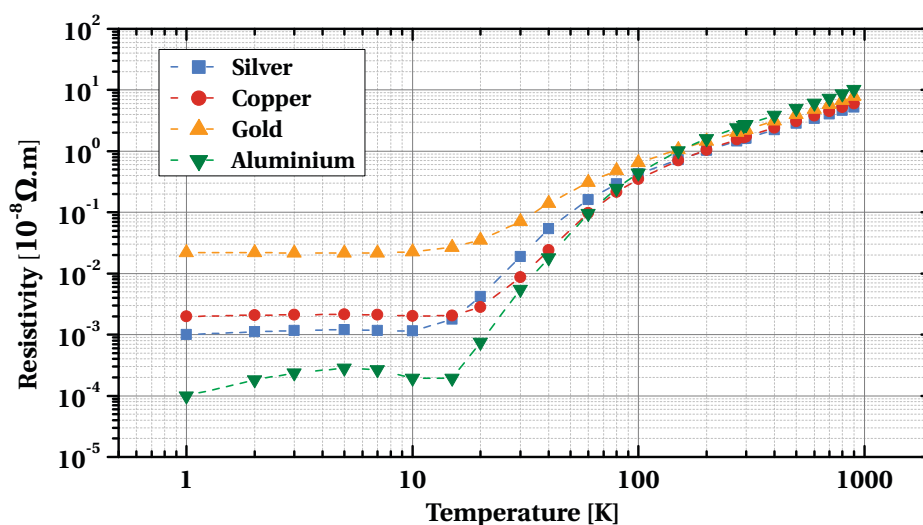


**Figure 4.19** – Resistivity of usual plasmonic metals versus temperature. While e.g. silver is less prone to resistive losses than gold, both at room and cryogenic temperatures, gold is usually preferred since it is not subject to oxidation. Data points computed on Wolfram Alpha ([www.wolframalpha.com](http://www.wolframalpha.com)), see sources therein.

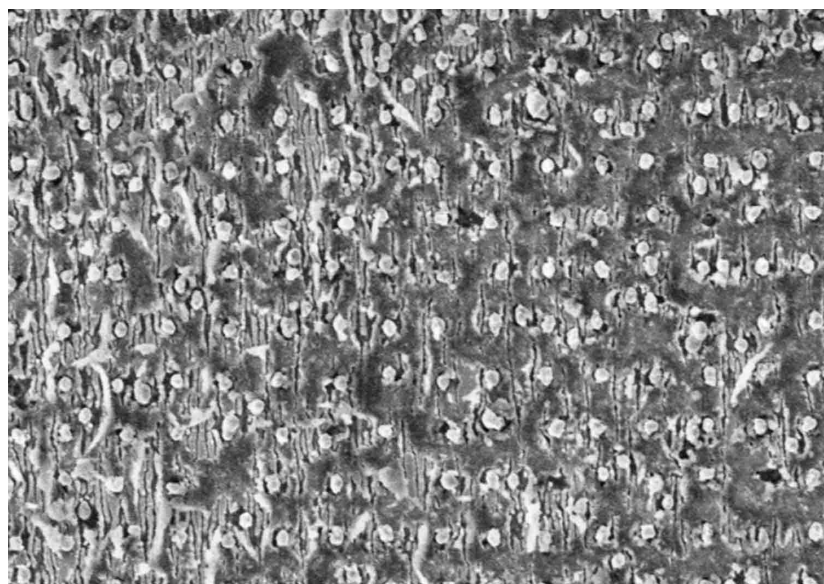


**Figure 4.20** – SEM acquisition of optically induced damage observed on a PMMA impregnated sample. A periodically arranged test sample made of simple gold dots was used to evaluate the stabilizing feature of an extra transparent PMMA layer deposited on top. After illumination under femtosecond light pulses, the PMMA layer is burnt and cracked. The underlying gold structures are deformed and disordered, therewith discarding the PMMA as a viable solution to sample destruction.

temperature, and that any shift of the plasmonic resonance due e.g. to thermal shrinkage is left unaccounted for. In any case, nonlinear measurements at low temperature showed no improvement in reproducibility, with SEM acquisitions demonstrating identical damages (not shown). The ultrafast process at play and the reduced gold volume that does not allow for thermal dissipation are conceivable explanations. Consequently, the further consideration to replace the glass substrate by sapphire, an excellent thermal conductor, was not intended. Also, doing so would have induced retuning the nanostructures' sizes due to the change in their environment's permittivity. At the time when this was considered, the target sizes would have been too small to be produced accurately, and the inhomogeneous broadening of the total linewidth might have become significant.

In another approach, an extra layer of PMMA (transparent plastic,  $n = 1.49$ ) was deposited on top of the metamaterials to try and hold the nanostructures in place. In doing so, the nanostructure design has to be adapted ("downsized" in an overly simplified picture) to accommodate for the higher permittivity of PMMA with respect to air, see section 1.3.1. Technical limitations prevented using a more stable sputtered silica glass at the time the measurements were carried out. Indeed, such an adaptation could not be achieved to keep the plasmonic resonance within the measurable spectrum allowed by the setup. Here, damages were observed on the PMMA protective layer, see figure 4.20. Again this was correlated with an alteration of the corresponding spectra, linear as well as nonlinear. However, it is mentioned that a 20nm thick protective layer of silica has since proved a suitable technique in at least one other group [185].

Another proposed alternative is to make use of Babinet's principle, i.e. working with complementary nanostructures, see §11.3 in reference [189], as well as [190, 191]. According to this principle, complementary structures exhibit both a complementary spectral response and field distribution of the respective eigenmodes. In this case, one would modify the manufacturing process to obtain nanostructures "carved out" of a gold film. An equivalence in the electromagnetic analysis is then obtained essentially by interchanging the  $\mathbf{E}$  and  $\mathbf{B}$  fields. The interested reader will find a more detailed procedure in the references mentioned above. In this way, one achieves very stable nanostructures, with a high damage threshold equivalent to that of a plain gold film. In principle, such a design also paves the way to the production of nanostructured free-standing films. Therewith, one suppresses complications due to the glass substrate. Among them one counts structural mismatch, back-reflections, plasmonic tuning related to the glass permittivity, and surface SHG at the gold/glass interface. Nevertheless, the decision was taken not to carry out this experiment and stick to more established split-ring resonator designs for easier comparison to other results delivered by the scientific community.

Based on the SEM acquisitions of the actual samples, one notices that a small proportion of the meta-atoms holds in place. It is tempting to believe that the measured SHG signals might come from these unaffected parts of the sample. However, this cannot be the case for at least two reasons: First, later recorded SHG are similar in intensity to the initial acquisition, although in all probability the amount of intact structures degrades with laser exposure time. Second, there is hardly any meta-atom in place that is not partly covered by one or more "randomized" nanostructures. This is a major issue since physical contact of the metallic volumes means electrical contact and therewith perturbation of the plasmonic process.

The damaged topography is consistent with the fact that one no longer observes linear optical resonances: The system displays very large inhomogeneous broadening of the total linewidth of the resonances, see section 1.3.3, rather than a summation of all linear resonances as projected onto the eigenpolarization axes, see section 4.1.1. In other words, although the meta-atoms roughly conserve their form, they do lose the plasmonic properties targeted through their design. For the same reason, the system cannot be seen as a "powder" of meta-atoms investigated by SHG. Moreover, such a behavior would have been inconsistent with the measured anisotropies, given that traditional crystal powder samples act as an isotropic source of second harmonic radiation [192]. The SHG generating system approximates a 2D gold film presenting randomly distributed facets and openings. This is a complex system,

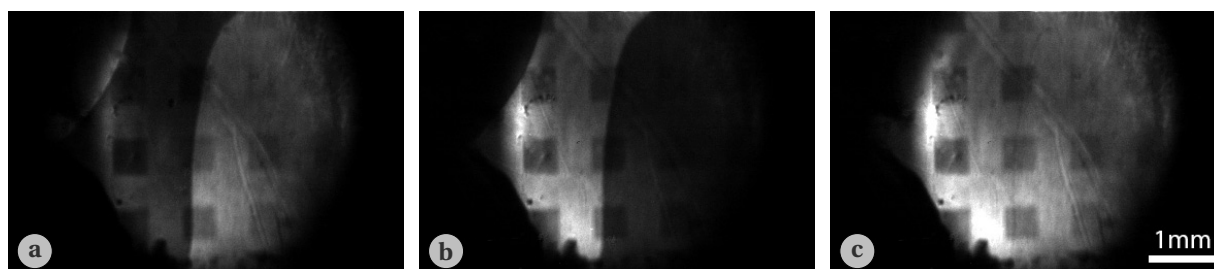


**Figure 4.21** – CCD acquisition of an antiferromagnetic domain topography of a nanostructure patterned  $\text{Cr}_2\text{O}_3$  surface (sample DMF18). Exposure time amounts to 60 min: Cosmic rays were removed using an image editing software. The measurements are performed below the Néel temperature,  $T < T_N$ , using a circularly polarized fundamental wave at 1.05 eV. Figures (a) and (b) show the topography of the SHG signal using  $\sigma_-$  and  $\sigma_+$ -polarized light, respectively. By superposing both previous images, figure (c) demonstrates the complementarity of the domains. The metamaterial fields are recognizable through the shadow they cast by partly attenuating the generated SHG. The domain boundary runs *unperturbed* through metamaterial fields: The nanostructures do not alter the host system.

very different from the initial motivation for this work. It requires a fundamentally different approach, in particular in characterizing the actual features of the gold distribution and the electric currents streaming therein.

#### 4.2.4 SHG Amplification

In this section, the application potential of metamaterials for enhanced nonlinear optical performance is considered. In a first approach, metamaterials in the form of wires are written on  $\text{Cr}_2\text{O}_3$  and multiferroic  $\text{RMnO}_3$  single crystals. The nanostructures are considered as an *optical catalyst* for enhancing the SHG conversion efficiencies of the nonlinear crystals, as explained in section 3.1.4. The feasibility of this approach is investigated in two steps: The *functionality* of the metamaterial is checked in the next section, followed by a spectral characterization of the *mechanism* of the signal remodeling induced by the metamaterial. These initial results lead to the investigation in a third section of SHG signals delivered by nanowires on top of amorphous glass, a nonlinear inactive host system.

##### Functionality: AFM Measurements

To start with, it is important to show that aside from potential field enhancement, the metamaterials do not affect the basic properties of the host material. This is best verified by concentrating investigations on the AFM domain structures. AFM domains, whether in  $\text{RMnO}_3$  or  $\text{Cr}_2\text{O}_3$ , are easily disturbed so that any perturbation by the gold wires applied on the sample are expected to influence or pin the position of AFM domain walls. AFM experiments have to be carried out below the Néel temperature, see section 3.1.4, and in the narrow spectral range in which an AFM SHG signal is present (2.30 eV to 2.80 eV and 1.80 eV to 3.00 eV for  $\text{RMnO}_3$  and  $\text{Cr}_2\text{O}_3$ , respectively). As mentioned in section 3.1.5, for these measurements the laser light is incident perpendicular to the surface of the sample.

Figure 4.21 shows the antiferromagnetic domain topography in  $\text{Cr}_2\text{O}_3$  after it has been poled using the magnetoelectric effect (sample DMF18, cosmic rays were removed for clarity). For this experiment, a nanosecond laser system was employed and tuned to deliver an SHG signal at 2.10 eV photon energy where the SHG yield is high and the contrast between AFM domains maximized, see section 3.5. Experimental details as well as the original acquisitions can be found in reference [172]. Figure 4.21c demonstrates the perfect complementarity of the domains and therewith their magnetic origin. It also illustrates the good homogeneity of the circular flat-top beam profile.

Most importantly, the CCD acquisition clearly shows that a domain boundary runs *unperturbed* through several metamaterial fields. This demonstrates that the presence of the metallic nanostructures does not alter the mechanisms at play in the host system. This is an essential prerequisite to use metamaterials as optical catalysts, boosting the SHG yield, without altering the underlying process studied.

One further notes that there is no increase but rather a decrease of the SHG where the crystal is nanopatterned. This is consistent with the use of nanosecond pulses for which the coherent interaction with particle plasmons is negligible, see section 1.3.3. All following measurements are carried out with the femtosecond laser system described in section 3.3.

Leaving the host system unperturbed is a necessary yet not sufficient condition to validate metamaterials as optical catalysts. One still has to link enhanced SHG signals with the original SHG processes from the host system. For that, one now concentrates on the AFM signal delivered by the bare host system. Indeed, AFM SHG features of the model systems, such as temperature dependence and six-fold anisotropy, are excellent candidates to provide potential evidences of the metamaterial functionality. Reference spectra are provided in figure A.13 and figure A.14 with a maximum SHG yield obtained near 2.44 eV and 2.20 eV for  $\text{RMnO}_3$  and  $\text{Cr}_2\text{O}_3$ , respectively.

Figure 4.22 shows isotropy measurements carried out on a  $\text{RMnO}_3$  system, in this case FG  $\text{HoMnO}_3$  (sample DMF13). Measurements were carried out in a row on the same setup and in the same environment (normal incidence,  $T = 50\text{K} < T_N$ , at 2.44 eV (a) and 2.07 eV (e,f) SHG photon energy). The crystal substrate is moved on micrometer translation stages to target different areas of the surface. Figure 4.22a displays the well-known six-fold AFM anisotropy from an unstructured  $\text{RMnO}_3$  crystal. The maximum intensity is used to normalize all curves presented in this graph. Maximum intensities are given in the top right inset of each graph. Both the form and intensity of the first graph serve as references to analyze figures 4.22(e)-(f), obtained from areas patterned with horizontal and vertical wires, respectively. Also for reference, figures 4.22(b)-(c) illustrate the results of a straightforward amplification of the incident electric field in the direction normal to the nanowires. The model used to compute the latter two figures is given in annex B.1. Here, the amplification value is arbitrary set at 50% to display all the anisotropy feature of the model. In other words, given an incident fundamental beam with electric field strength  $E_0$ , the crystal is excited by the amplified electric field  $E_a$  mediated by the nanostructures:  $E_a = 1.5E_0$  when impinging on the crystal with a polarization normal to the nanowires,  $E_a = E_0$  for a polarization along the nanowires long axis and neglecting absorption by them. Although the code used was developed to model SHG in  $\text{Cr}_2\text{O}_3$ , it remains suitable for this simulation: Given  $\mathbf{k} \propto \hat{\mathbf{e}}_z$ , there is a mathematical

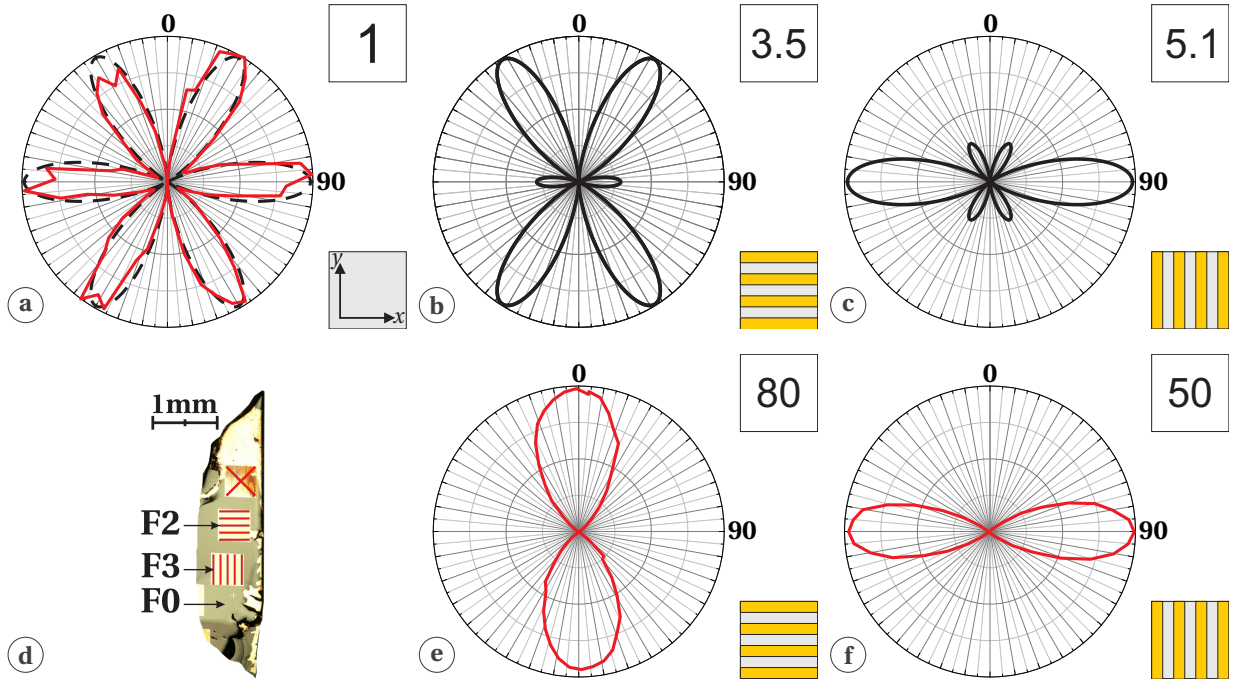


**Figure 4.22** – AFM SHG anisotropies in unstructured and nanowire-patterned  $RMnO_3$ . Measurements carried out at 40K, 2.44eV, and normal incidence. The measurement (red line) from the bare crystal (a) is a perfect match to the model used (dashed black line). Simulations based on a straight forward field amplification are provided in (b) and (c) for wires along the  $x$ - and  $y$ -axis, respectively. The maximum value and wire orientation are indicated in the top and bottom right inset, respectively. Numerical values are normalized to that obtained from the unstructured crystal. The actual measurements shown in (e) and (f) are carried out on the fields F2 and F3, respectively, with a linear resonance near the 1.03 eV target, where the crystal SHG yield is minute. For both orientations, a simple two-fold anisotropy is observed so that e.g. comparing (b) to (e) proves the simple amplification model wrong. The maxima are oriented normal to the wires' long axis, and the anisotropy function is properly fitted by a  $\cos^6\theta$  or  $\sin^6\theta$  function, depending on the wires' orientation. The  $HoMnO_3$  crystal topography is shown in (d).

form equivalence of the SHG sources between  $Cr_2O_3$  above its Néel temperature and  $RMnO_3$  compounds following the  $\alpha_y$  spin order below their Néel temperature. Only the strength of the tensor component at play changes, which is of no significance here.

The discrepancy between the amplification model and real-world measurements is two-fold. First, the form of the metamaterial-mediated anisotropies does not follow the amplification model. In fact, as for figure 4.22e, the anisotropy no longer exhibits the six lobes reflecting the  $Mn^{3+}$  spins' ordering. Second, the AFM origin of the SHG signals measured on patterned fields is further discarded by investigating the temperature dependence, see figure 4.23. While an unstructured field sees its signal vanish at the Néel temperature  $T_N = 76K$  there is no temperature dependence on patterned fields. The relative attenuation in the 32K to 45K range is an artifact related to the laser stability, *not* to a phase transition within the  $HoMnO_3$  crystal. Therewith, the affiliation of the modified SHG signals to the original SHG processes in the host system seems lost.

This initial result represents a setback with respect to the functionality of metamaterials

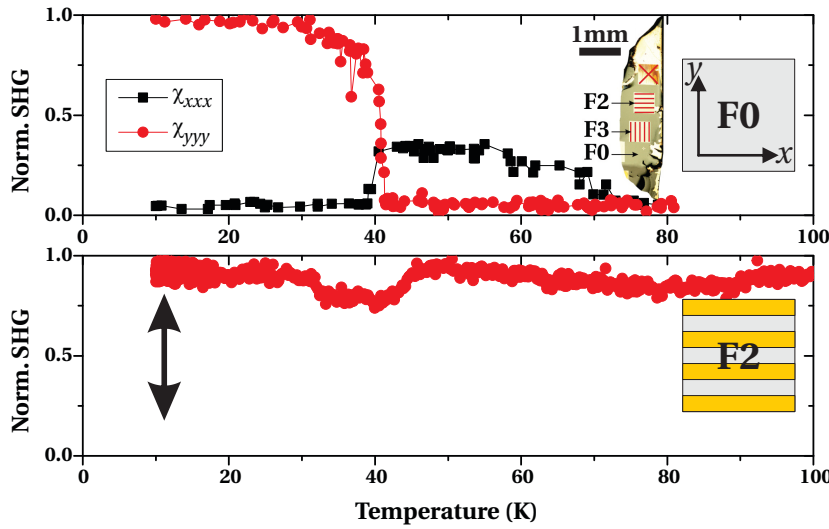


**Figure 4.23** – Temperature dependence of SHG signals obtained at 2.44 eV SHG from (un)structured  $\text{HoMnO}_3$  at normal incidence (sample DMF13 FG). At the unstructured location F0, the SHG yield displays a phase transition at 40 K and vanishes at the Néel temperature  $T_N = 76$  K. The AFM origin of the signal is therewith confirmed. On the contrary, signals from structured areas such as F2 display no temperature dependence and cannot be of AFM origin. Incoming and analyzed polarizations are set parallel to the arrow.

as an optical catalyst, at least in the approach guiding the current work. The application of nanowires to strengthen the SHG yield in an unsophisticated manner loses consistency, and a more challenging process may explain the measurements. Further insights into the mechanism of this process are gathered in the next section that concentrates on FEL SHG.

### Mechanism: FEL Measurements in $\text{RMnO}_3$

In this section, one further characterizes the spectral dependence of the amplification. For this purpose the FEL SHG signal in  $\text{RMnO}_3$  is employed. Spectrally broader than the AFM spectrum, it is generated in the entire spectral range accessible with our laser system. FEL signals are therefore better suited for studying the spectral aspects of nanostructure-mediated electric field amplification. Also, measurements are carried out under ambient conditions. Reference spectra are provided in figure A.12. In particular, the effect of tuning the linear resonance of the wires is investigated. As mentioned in section 3.1.5, the laser light is incident at  $45^\circ$  to the surface of the sample.

In such a configuration, it is stressed that the nanowires act as a grating at the wavelength range of the emitted light. However, the typical period  $d_p = 450$  nm between two nanowires does not prove to be an efficient grating configuration for the wavelength range of the fundamental, given that  $\lambda_{\text{fund}} > d_p$ . Nevertheless the tilted incidence of the light onto the sample is a source of complexity. In fact, horizontal wires tilted in the horizontal plane at  $45^\circ$  are analogous to a plain gold surface. Only the cover ratio is affected: Being unity for a gold film, it reaches a factor  $d_w/d_p$  for the field of wires, where  $d_w$  is the wires' width. In practice  $d_w/d_p$  varies from 0.25 to 0.70 depending on the nanowires' width i.e. linear resonance. In this way, any signal generated from tilted horizontal wires and under horizontally polarized light excitation is mixed with surface SHG from gold, as investigated in section 4.2.2. This consideration could be easily dismissed by employing crystals cut normal to the  $y$ -axis to investigate the FEL signals, as in reference [143]. Unfortunately, such crystals were not available during this work.

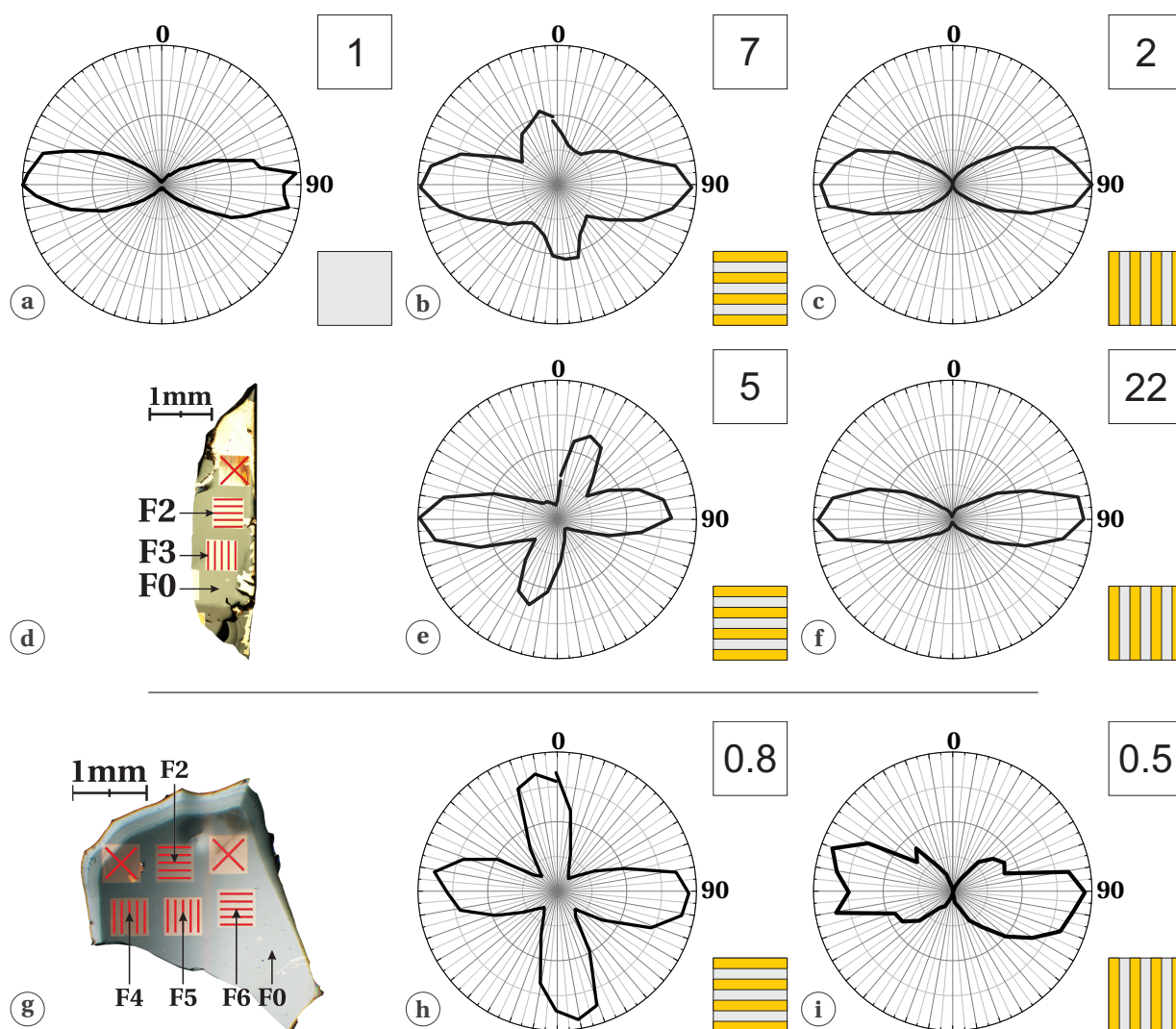


**Figure 4.24** – Normalized FEL SHG anisotropies in unstructured (a) and nanowire-patterned  $RMnO_3$  (b-i). All measurements are carried out at room temperature and  $45^\circ$  incidence. Polarizer and analyzer are rotated in parallel with  $0^\circ$  relative angle. Crystal topographies are shown in (d,g). SHG photon energy is 2.70 eV (a-c), 2.10 eV (e-f), and 2.60 eV (h-i). Measurements (a-f) are carried out on sample DMF13 (FG  $HoMnO_3$ ), on field F0 (a), F2 (b,e), and F3 (c,f). Measurements (g-i) are carried out on sample DMF15 (FG  $YbMnO_3$ ), on field F6 (h) and F5 (i). For both wire orientations, a signal is observed in the direction normal to the nanowire so that e.g. comparing (a) to (b,e, or h) proves the simple amplification model wrong. Maximum values are indicated as inset and are normalized to the maximum value measured from the bare crystal at 2.70 eV.

For  $z$ -cut crystals, care must be taken to compare SHG from metamaterial fields with  $x$ - or  $y$ -wires. In that respect, one notices in table 3.3 that the  $x$ - and  $y$ -axis are equivalent as far as ( $i$ )-type contributions are concerned. It follows that one can directly compare the signals from  $x$ -wires with  $y$ -wires provided the crystal is rotated by  $90^\circ$  around its  $z$ -axis from one case to the other. It was verified that the SHG signals from wires with orthogonal relative orientation and illuminated at  $45^\circ$  incidence are interchangeable when the crystal is rotated accordingly. Typical anisotropy measurements are displayed in figure 4.24. Three different cases are

considered, using two different samples whose topography is shown on the second and third graphic rows. First, the top line shows acquisitions carried out at the maximum FEL SHG yield, i.e. 2.70 eV, away from the nanostructures' linear resonance. The anisotropy measurement obtained from an unstructured region on a FG HoMnO<sub>3</sub> sample (DMF13) is compared to the measurements from the nanostructured fields F2 and F3 that differ in the orientation of their wires with respect to the crystal axes. In the second case, measurements are carried out on the same sample, but with a fundamental tuned to match the linear resonance of the nanowires, i.e. at 2.10 eV SHG, but *not* that of the crystal. Both field orientations are compared and shown on the second line. In the third and last case, new nanowires were produced on another sample (FG YbMnO<sub>3</sub> DMF15) to obtain a metamaterial resonance matching that of the host crystal at 2.60 eV. Again, anisotropy measurements for both field orientations are compared and shown on the third line.

A noticeable difference is observed depending on the wires orientation. Where the anisotropy shape is two-fold with horizontal lobes for vertical wires, it becomes four-fold for horizontal wires with an added pair of vertical lobes of a different amplitude. Both lobe sets follow a  $\cos^6 \theta$  or  $\sin^6 \theta$  function, similar to the lobes' shape matching the SHG signal discussed in the previous section. The latter vertical lobes are unexpected given that a vertical excitation cannot lead to a likewise vertical emission based on the symmetry analysis carried out in table 3.3. As such, one cannot relate this vertical signal to the host RMnO<sub>3</sub> system alone, as considered under a plane wave excitation. However, the vertical signal is obtained for a vertically-polarized excitation on horizontal nanowires. That is the required configuration to excite the plasmonic resonance, and potentially relates the signal directly to the nanostructures. Considering horizontal lobes, one has to distinguish the case of vertical and horizontal nanowires. For the former, the behavior is consistent with an amplification of the host system's signal. Yet the signal generation could follow the same undetermined process as for the vertical lobes discussed above. For the latter, the lobes cannot be linked to a plasmonic process given that no resonance occurs in horizontally oriented nanowires under horizontally polarized light. However, the SHG signal can be related either to the nanowires' material as surface SHG from tilted gold, or to the host crystal considering the less-than-unity cover factor of the nanowires. The last row of results is puzzling because one would expect the maximum recorded signal where the plasmonic resonance matches that of the host system. Instead the SHG strength is attenuated with respect to that on the bare crystal. Nevertheless, it is evident that something takes place under mediation of the nanostructures as shown by the modification of the anisotropies' shape and/or strength. The following spectral analysis is valuable to try and identify the proper mechanism.

Figure 4.25 displays the enhancement factor of the SHG obtained from nanostructured fields with respect to SHG from the unstructured RMnO<sub>3</sub> crystal. The maximum value of the horizontal lobes are being compared, i.e. both polarizer and analyzer are rotated horizontally. The amplification spectra show a pronounced difference depending on the nanowires' orientation. For sample DMF13 (bottom graph), a clear correlation to the linear resonance is noticeable for vertical wires. Not so for the amplification recorded on horizontal wires, which could match the surface SHG spectrum of gold, see figure 4.12. Sample DMF12 (top graph) delivers an ambiguous result given that the plasmonic linear resonance offers strong correlation with the latter. Furthermore, one lacks points in the 1.75 eV to 2.25 eV range to determine whether the

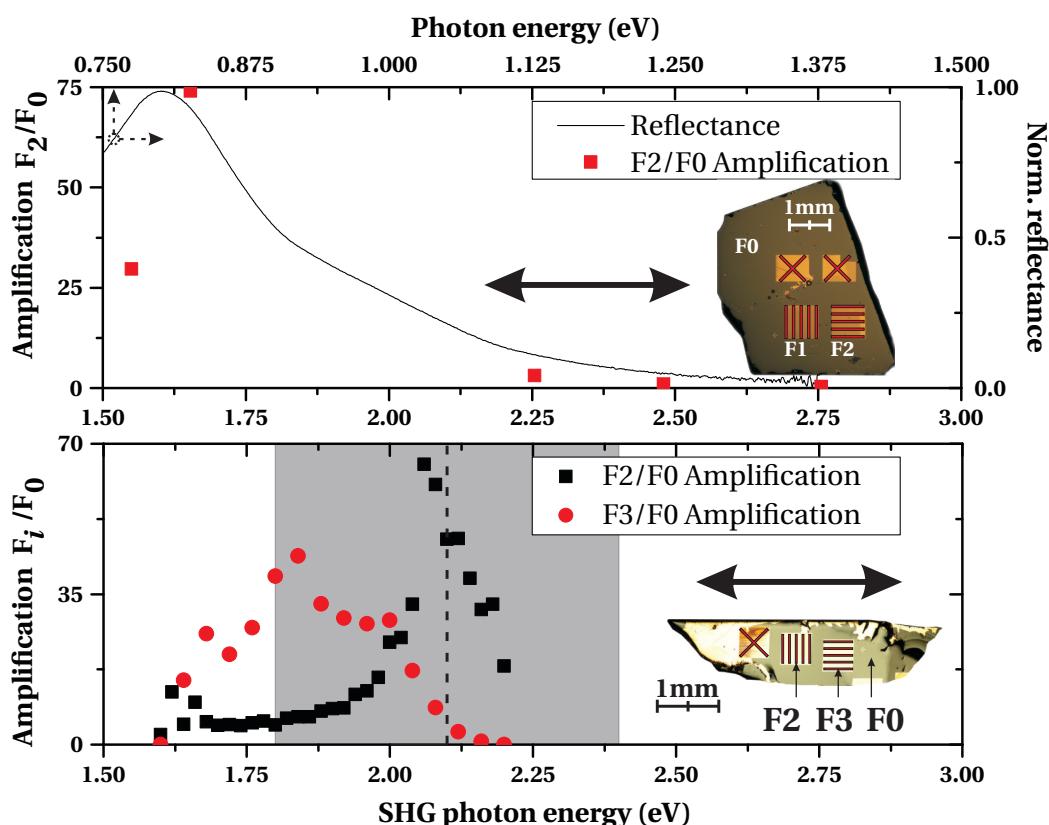


**Figure 4.25** – Amplification spectra of FEL SHG. SHG strength from metamaterial fields  $F_i$  as compared to SHG measured on an unstructured area  $F_0$  of the host crystal. The top graph is obtained from sample DMF12 (FZ YbMnO<sub>3</sub>). The bottom graph is obtained from sample DMF13 (FG HoMnO<sub>3</sub>); the plasmonic resonance peak and FWHM are indicated by a dashed line and gray area, respectively. The incoming and analyzed polarizations are indicated by an arrow beside the sample plans.

point of maximum amplification is indeed at 1.65 eV or if the amplification curve matches that of field F3 on sample DMF13. In any case, the similarity of the lobe shapes makes it difficult to identify the origin of the process at play and differentiate it with e.g. surface SHG. Cr<sub>2</sub>O<sub>3</sub> is a viable alternative host system since it features a distinctive six-fold anisotropy, yet remains an extensively investigated system. The investigation of a possible SHG signal amplification in such a system is the topic of the next section.

### Mechanism: MD Contribution in Cr<sub>2</sub>O<sub>3</sub>

Cr<sub>2</sub>O<sub>3</sub> crystals present the advantage of displaying a distinctive six-fold anisotropy shape. In addition, the high Néel temperature makes it convenient to investigate both (*i*)- and (*c*)-type signals. Both signal types are measurable under normal incidence, which allows to discriminate against surface effects. Also, the temperature dependence of the signal strength is well documented for bare crystals. Below the Néel temperature, (*c*)-type ED effects take place which results in a rotation of the anisotropy signal along the *z*-axis [151].

In contrast to the above mentioned features, measurements carried out on nanopatterned

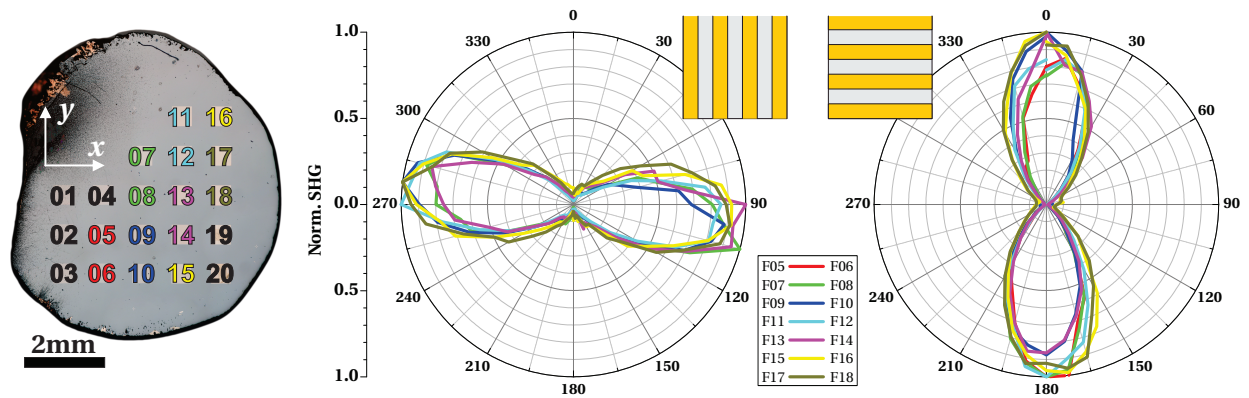


**Figure 4.26** –  $0^\circ$  relative anisotropy measured at 2.20eV SHG photon energy on nanostructured fields on  $\text{Cr}_2\text{O}_3$ . All curves are normalized to the SHG maximum intensity. The sample plan on the left shows the color-coded nanostructured field pairs. Black-numbered fields were destroyed during the production. Each pair consists of a field with  $x$ -wires and another field with  $y$ -wires sharing the same linear resonance. The lower the field number, the higher the resonance energy. Anisotropies are two-fold and oriented normal to the wires' long axis. The lobes follow a  $\cos^6\theta$  or  $\sin^6\theta$  fitting function according to the nanowires' orientation indicated in the inset at the top. The behavior is consistent across all fields.

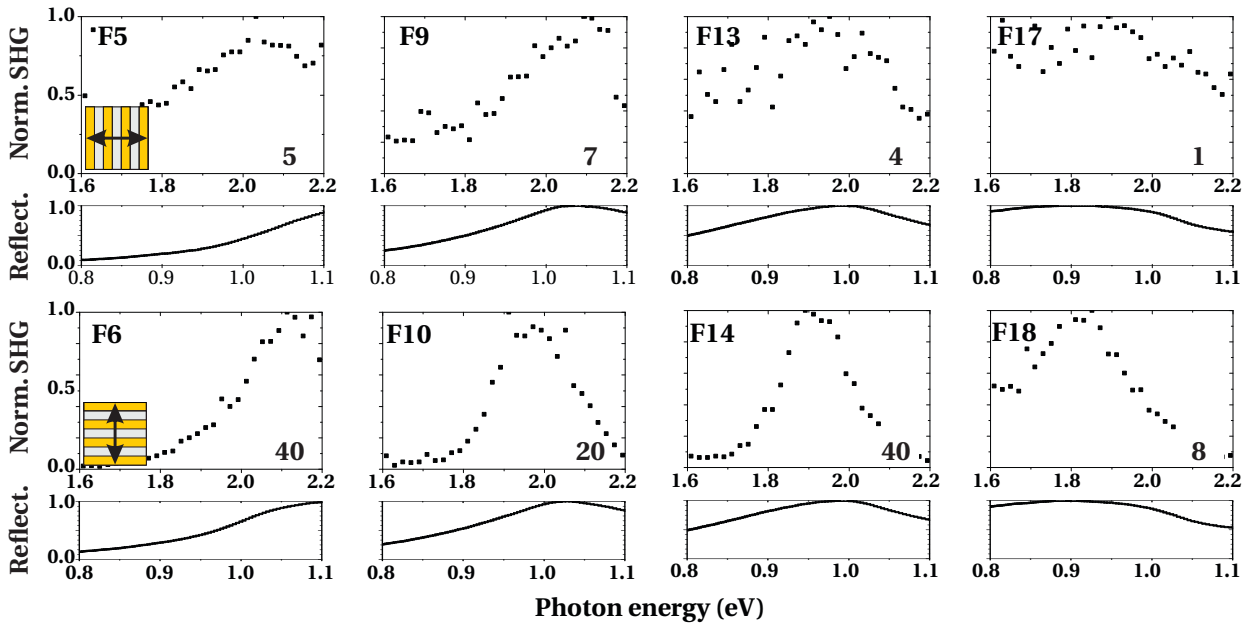


**Figure 4.27** – Correlation of SHG signal obtained from different nanostructured fields on  $\text{Cr}_2\text{O}_3$  (sample DMF18) with their linear resonance. A clear trend is noticeable displaying a direct projection of the plasmonic resonance features into the SHG spectral features. For each graph, the field number is indicated at the top left, and the maximum value before normalization is given as inset in the bottom right corner. For each row, the nanowire orientation and polarization of both the polarizer and analyzer are indicated as inset in the first graph. The linear spectra are free from any spectral features at the SHG photon energy and are not displayed for sake of clarity.

areas show a very different behavior. Nevertheless, they display reproducible results with predictable features. First, anisotropy measurements are always two-fold with a maximum obtained normal to the wires' long axis, see figure 4.26. Fitting curves follow a  $\sin^6 \theta$  function for  $y$ -wires ( $\cos^6 \theta$  for  $x$ -wires, respectively). This supports the hypothesis that the horizontal lobes recorded in the "FEL" anisotropies on horizontal nanowires on  $\text{RMnO}_3$  under  $45^\circ$  incidence is actually surface SHG from gold. Second, different metamaterial fields produce different SHG spectra in strong correlation with the linear plasmonic resonance of the nanowires. This correlation is reported in figure 4.27.

Neither varying the fundamental photon energy, nor varying the temperature 20K below or above the Néel temperature alters the anisotropy signal form or orientation (not shown, the interested reader will find further graphs in reference [172]). Although a continuous temperature dependence measurement down to cryogenic values was not carried out, it is not expected to present another trend given that no changes are known to occur in the system apart from a reduction of the Ohmic losses. In the following, all measurements are carried out just above the Néel temperature, i.e. concentrating on the MD contributions to SHG in  $\text{Cr}_2\text{O}_3$ .

One notes that  $y$ -wires fields present a considerably lower SHG yield with respect to the  $x$ -wires fields. It is reminded that the metamaterial fields are expected to vary only in their nanowires' orientation width, i.e. in their linear plasmonic resonance. However, the SHG yield variation for the two orientations might be explained by a difference in the quality factor of the structures, which is reported in figure 4.7, see also equation (1.40). There is a priori no fabrication process difference between the two wires orientation, written in the same batch. However,  $x$ -wires consistently present a lower resonant quality factor yet with a higher SHG yield. An explanation might be found during the lift-off process following the EBL and gold sputtering fabrication steps. During lift-off, the mask is mechanically removed by pulling it up from a side of the sample. This represents an anisotropic step in the fabrication process with a lift-off direction most often roughly parallel either to the  $x$ - or  $y$ -axis. It is hence conceivable that small defects might be preferably generated in a given set of wires. An alteration of the wires by increasing nanoscale defects would reduce the quality factor, yet has the potential to increase the SHG yield through hot spots. It would be interesting to vary the mask-stripping direction and verify whether the quality factor is indeed affected. Without direct access to a production facility, this could not be carried out in the time-frame of this work.

One then recalls that the SHG anisotropy measurement from the bare crystal delivers a maximum signal for a polarization along  $x$  and *no* signal along  $y$  above the Néel temperature and for a  $0^\circ$  polarizer-analyzer relative angle. One can think of two explanations for the discrepancy to figure 4.26: First, the nanowires could alter the incoming polarization in the near-field, consequently projecting or amplifying the fundamental light along directions other than that normal to the wires. In particular, a projection of the incoming light field along  $z$  would allow tensor components normally discarded by the setup configuration under far-field-only considerations. This is investigated in detail later on in section 4.2.4. Second, SHG could be generated from the nanostructures themselves. In this hypothesis, SHG recorded from  $x$ -wires (i.e. recorded signal and expected amplification are along the  $y$ -axis) originates from the nanostructures only since the host crystal alone does not produce SHG in that direction. In contrast, SHG from  $y$ -wires could interfere with nonlinear signals delivered by the bare

crystal. The absence of side-lobes along all  $x$ -axes of the crystal discards this hypothesis. Indeed, one should record SHG amplitudes from the bare crystal comparable to that from the nanostructures to explain the measured amplitudes (partial or total destructive interferences).

Another attempt was made to try and reveal a connection between the metamaterial-mediated SHG signal and the underlying nonlinear crystal. To do so, the linear polarized light out of the OPA was converted into right- or left-circular polarized light (later referred to as  $\sigma_+$  and  $\sigma_-$  polarizations) using a quarter-wave plate placed before the  $\text{Cr}_2\text{O}_3$  sample. The crystal was then cooled down into its AFM phase using a controlled flow of cold vapor from a liquid nitrogen dewar, see reference [172]. In this phase,  $\text{Cr}_2\text{O}_3$  presents a characteristic contrast between the two polarizations, see figure A.14. This contrast was already employed in figure 4.21 and is a distinct feature of the host crystal only. Indeed, the projection of both circular polarizations along the eigenpolarization axes of the nanowires is identical: No difference in the plasmonic conversion process of the electric field from far-field to near-field is expected. The crystal was verified to form a single AFM domain by rastering the unpatterned surface around and in-between the metamaterial fields and recording SHG strength for both circular polarizations: At 2.10 eV SHG, a constant contrast of about 5:1 was recorded across the whole unstructured sample, which demonstrates that the sample is in a magnetic single domain state.

Figure 4.28 shows the SHG amplitudes recorded at 2.10 eV on several metamaterial fields sorted according to their nanowires' orientation. First, the highest SHG yields are recorded on metamaterial fields with linear resonances in the 1.00 eV to 1.10 eV range for which the SHG yield of the host crystal is highest. A signal enhancement is recorded for these fields only. Second, there is indeed a contrast between signals obtained from two circular polarization excitation on metamaterial fields. These two first points support the hypothesis of an existing link between the SHG signals measured on nanostructured fields and the underlying crystal. However, while the SHG under  $\sigma_+$  excitation is larger than under  $\sigma_-$  for both the bare crystal and  $x$ -wires, the opposite is true for  $y$ -wires. Moreover, for both nanowire types the recorded contrast values are two orders of magnitude smaller than on the bare crystal. Also, the contrast trend with respect to the plasmonic resonance is roughly linear and does not present any maximum around 2.10 eV SHG. Finally, one notices the  $\cos^2\theta$  or  $\sin^2\theta$  emission polarization distribution, i.e. the anisotropic character of the emitted light. This differs from the purely isotropic character of SHG emitted by the bare crystal under circular polarization excitation. Since it seems quite clear that the circular polarization becomes scrambled as the light passes through the nanostructures, these last observations might not exclude a systematic enhancement with the plasmonic *and* the host resonance. Rather, the convolution of the observed features hints at an interaction between the crystal and the metamaterial systems according to a process that remains undetermined. To relate indubitably the recorded SHG with the host system, i.e. to verify that the crystal indeed plays a role in the SHG generation process, the experiment is carried out again in the next section where the host crystal is replaced by an amorphous fused silica substrate.

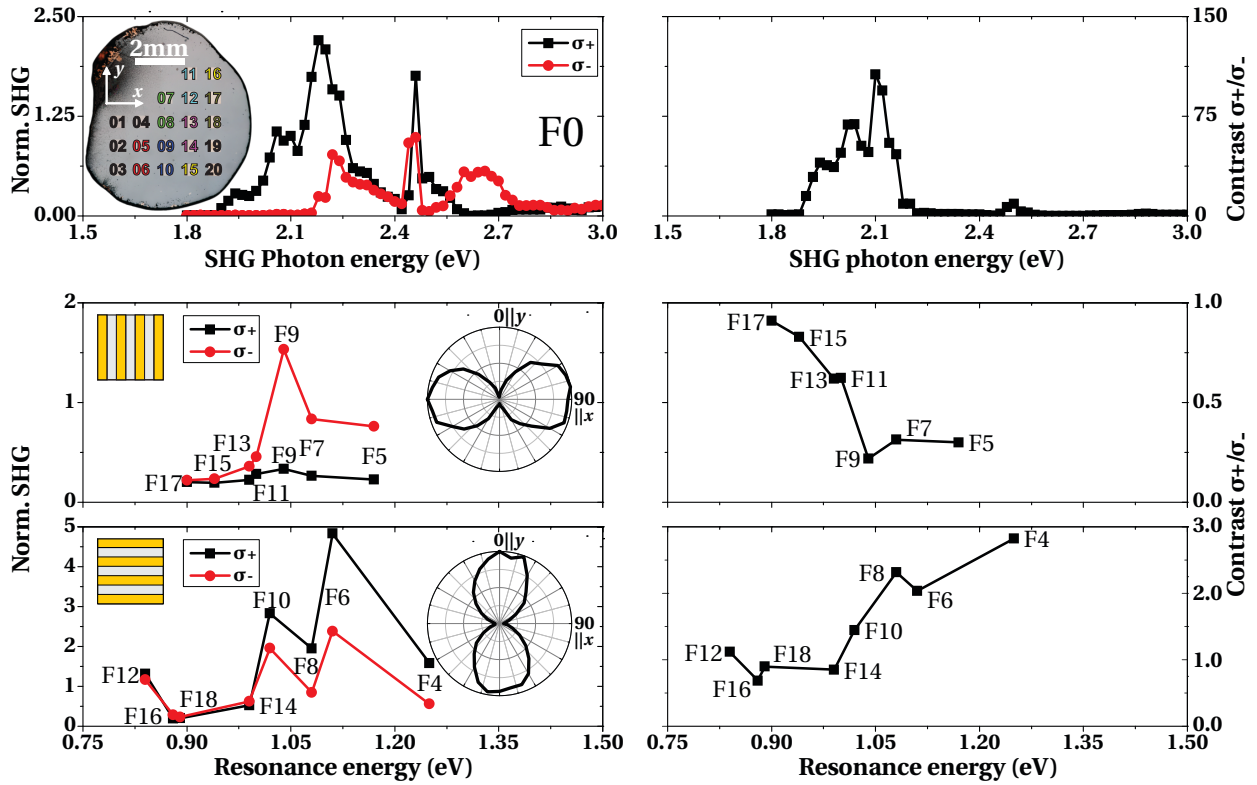


**Figure 4.28** – SHG strength and contrast under circular polarization and 2.10 eV SHG photon energy as a function of the plasmonic resonance energy for even and odd field number (bottom). Reference SHG spectra and  $\sigma_+/\sigma_-$  contrast values for Cr<sub>2</sub>O<sub>3</sub> at 10K are also reported from [151] (top). SHG strengths are normalized with respect to the maximum SHG measured on the bare crystal at 2.10 eV. For nanostructures fields, the data points are obtained for a photon energy of the fundamental beam at the plasmonic resonance by adding orthogonal SHG signals polarized along the  $x$ - and  $y$ -axis, which is equivalent to removing the analyzer. A typical analyzer measurement is shown in inset. The  $\cos^2\theta$  or  $\sin^2\theta$  distribution demonstrates the anisotropic character of the emitted light.

### Mechanism: Nanowires On Amorphous Glass

Here, nanowires are written on glass to investigate their behavior on an SHG-inactive substrate. Their linear resonance features were shown in figure 4.8 and proved to evolve linearly with increasing field number as the nanowire’s width is tuned. Likewise, the linear spectra reported in figure A.11 show a regular trend in the extinction, apart for the fields whose peak resonance is about 1.30 eV where the extinction is about 10% higher than the observed trend. The reason for this is unknown. It cannot a priori be related to the glass substrate which displays constant optical features in this range according to the manufacturer’s datasheet [193]. Neither does gold present any features in this range, see figure 1.1. Nevertheless, this observation seems to play a major role, as discussed below.

All 0° relative anisotropies present a  $\cos^6\theta$  shape similar to the measurements recorded on Cr<sub>2</sub>O<sub>3</sub> (not shown). However, the spectral features contrast with the case on Cr<sub>2</sub>O<sub>3</sub> for which a correlation to the linear resonance is observed. Here, all SHG spectra recorded from nanostructures on the glass substrate show a peak at a fundamental photon energy around

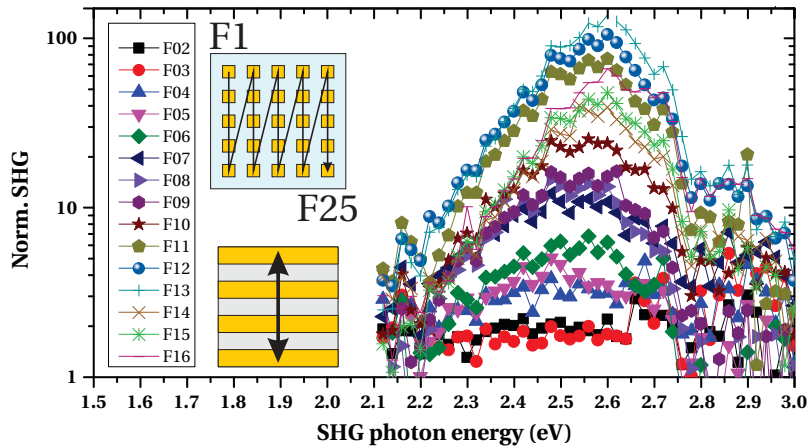


**Figure 4.29** – Normalized SHG spectra from nanowires on glass. Insets show the sample plan (top) as well as the nanowires horizontal orientation, and polarizer and analyzer polarization (bottom). The OPA signal range (1.50 eV to 2.22 eV) was not measured in the time frame of this work since all plasmonic resonances are higher-tuned. A logarithmic scale is used for clarity.

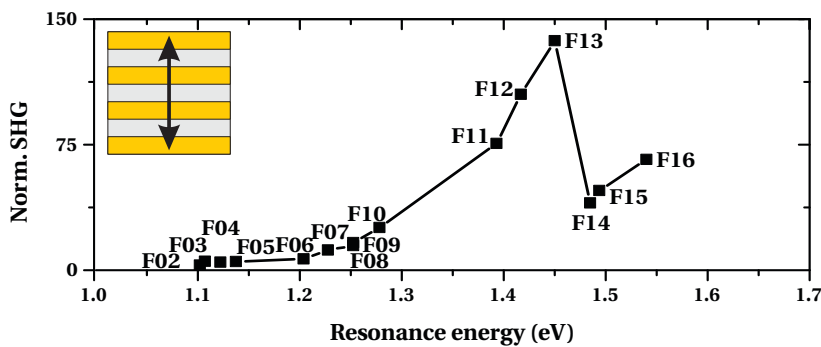


**Figure 4.30** – SHG strength versus plasmonic resonance for nanowires on glass. The nanowires horizontal orientation as well as the polarizer and analyzer vertical polarization are shown in inset. The OPA is set to deliver a fundamental photon energy where SHG is maximized, see previous graph. Lines are drawn to guide the eye.

the 1.30 eV range mentioned above. Although the linear resonances extend from 1.10 eV to 2.10 eV, see figure A.11, only a minimal shift of the SHG spectral peak is recorded from 2.40 eV to 2.60 eV with increasing field number, i.e. increasing linear resonance energy, see figure 4.29. It is not clear which process could explain the 0.20 eV spectral shift.

Figure 4.30 shows the SHG strength as a function of the linear plasmonic resonance. A general trend is noticeable with respect to the linear resonance: The higher the field number, the higher the SHG signal. This can be explained by a higher quality factor, see figure 4.8. An abrupt shift in the overall SHG strength is noticeable for field F14 and higher. This could not be explained by visual inspection for field damages, but could be related to nanoscopic defects induced in the lift-off process. One notices there is no direct correlation between the SHG yield peak at 2.60 eV and the plasmonic resonance, e.g. F13 delivers the strongest signal yet bares a plasmonic resonance at an unexpected 1.45 eV rather than 1.30 eV. This latter plasmonic resonance nearly matches the photoluminescence peak of gold at 2.40 eV. However, photoluminescence is again discarded by a rather sharp 0.06 eV SHG monochromaticity and a  $\cos^2 \theta$  analyzer measurement (not shown).

It is important to highlight two points: First, SHG is indeed recorded from nanostructures expected to be centrosymmetric and on an SHG inactive substrate. This occurs for an optical polarization allowing the plasmon excitation. This means that the symmetry analysis under plane-wave excitation fails to properly describes what actually occurs at the level of the nanostructures. Second, determining which feature(s) and according to which process the plasmonic nanostructures interact with the underlying substrate remain a challenge. As it

was shown in the previous section with a  $\text{Cr}_2\text{O}_3$  host, it is conceivable that the recorded SHG signals result from an overlap between the plasmonic resonance of the nanostructures and a sample-specific response determined by the underlying host substrate. However, as it is shown here with a glass substrate, this does not encompass the full picture and as closer look into more refined models is necessary. In the following section, one leaves the plane-wave amplification approach that guided the analysis, and tries to get an insight into what is happening on the near-field based on a nanoscale model.

### Near-Field Model Nanowire Model

The previous sections demonstrated the inability of a straightforward model to relate the measurements with the simple electric field amplification of the incoming light wave. In this section, an attempt is made to push the paradigm further and actually look at what happens at the nanoscale. It is stressed that this section is a proposition for a model that needs be further verified in the future: The definitiveness and correctness of the proposed tables and description are not yet given. In particular, the repercussion of the distance across the wire on phase-related effects as well as the  $\omega - 2\omega$  coupling are subject to discussion. In the following, one concentrates on the case of nanowires on a nonlinear crystal with normal incidence excitation. The extension to other incidence angles is straightforward and does not require a specific refinement of this approach.

As one excites the system with plane waves, a plasmon is generated with optical and electromagnetic features that partially depend on the nanostructures' environment, e.g. through the damping due to the polarization of the crystal, see section 1.3. Here, the key consideration is to recognize that the wire nanostructures not only potentially enhance the absolute electric field strength, as in the assumption motivating this work; they also convert the *far-field* plane wave into a *near-field* electric field distribution that looks nothing like a plane wave. Most notably, an electric field component normal to the surface is present in the near-field.

Moreover, the simple geometry of the wires results in the simple dipole-like field distribution of the system, which is *electrodynamic* and hence radiating. However, as discussed above one is interested in the near-field behavior of such an electrodynamic system, should it be used as an optical catalyst. Remarkably, the expression of a radiating electric dipole simplifies in the near-field to its *electrostatic* expression, as described in equation (1.32) [64, 189]. Such a problem is easy to simulate on a desktop PC, without expensive dedicated software: An unsophisticated model is proposed in the form of a Mathematica notebook, see code B.2. This model was used to compute the diagram shown in figure 3.5, in which one first demonstrates the few 10nm depth range where the nanostructures affect the crystal system. The volume of the host system being covered extends beyond that of any "monolayer" surface effect, but much less than the depth analyzed in a reflection experiment (about 100nm). This scale difference could be of major significance to explain the results and is discussed later in this section.

Based on this model, one gets qualitative access to the distribution and phase of the electric field and of its spatial derivative (for the EQ tensor components), see figure 4.31. In the reflection measurements carried out on the crystals, SHG produced below the wires is screened

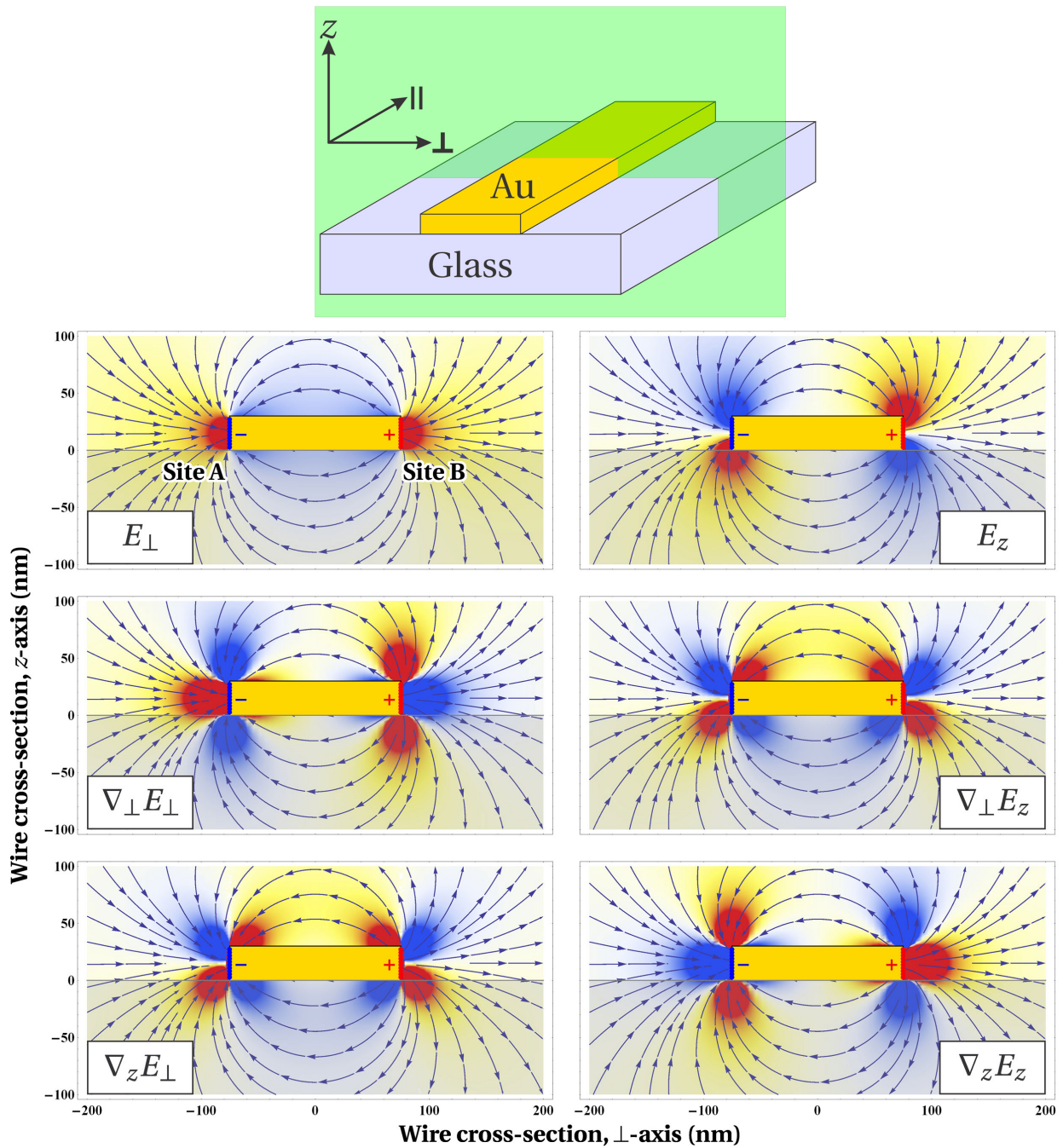


**Figure 4.31** – Overview and referential for a single nanowire (top). A green cross section is indicated for which the spatial distribution of the plasmonic electric field strength and its first partial spatial derivatives are given (bottom). The actual field lines are superimposed on each graph for reference. The model is based on the near-field only, which is equivalent to studying an electrostatic charge distribution. Here, the charge distribution consists of ten infinite wires normal to the illustrated cross-section and oppositely charged on opposite nanostructure edges. The effect of substrate polarization is unaccounted for without qualitative consequences. The phase and field strength are color coded: Positive in red, negative in blue, and saturation increasing with strength. Comparing sites A and B, the  $E_{\perp}$ ,  $\nabla_{\perp}E_{\perp}$ , and  $\nabla_z E_{\perp}$  field distributions are in phase, while the  $E_z$ ,  $\nabla_{\perp}E_z$ , and  $\nabla_z E_z$  field distributions are in antiphase. The  $z$ -axis is vertical in the plane of the page.  $\perp$  takes the value  $x$  or  $y$  depending on the orientation of the nanostructures's long axis out of the page along the  $y$ - or  $x$ -axis, respectively.

**Table 4.1** – Plasmonic wire amplification truth table. The subscript  $\perp$  indicates the direction normal to the nanowires' long axis being considered, i.e.  $\perp = x$  for  $y$ -wires and  $\perp = y$  for  $x$ -wires. Since no plasmonic excitation is excited with a fundamental light polarized parallel to the nanowires' long axis, the corresponding cases are not treated in this table. An analysis of the phase of the excitations allows for determining whether signals produced at sites A and B contribute to the measured SHG signal. Excitations in phase at both sites are highlighted in yellow. All other excitations are in antiphase at both sites. Where both fundamental excitations are in phase at sites A and B, constructive interference occurs in the far field and the signal can be detected. On the contrary, excitations in antiphase see their resulting SHG contribution cancel out: The corresponding tensor component does not contribute to plasmon-mediated SHG.

Plasmonic excitation			$P_{ED,j}^{NL}$	$M_j^{NL}$	$Q_{ij}^{NL}$
$E_k$	$E_l$	Sites A & B in phase	$\chi_{jkl}^{eee}$	$\chi_{jkl}^{mee}$	$\chi_{ijkl}^{qee}$
$E_{\perp}$	$E_{\perp}$	✓	$\chi_{j\perp\perp}^{eee}$	$\chi_{j\perp\perp}^{mee}$	$\chi_{ij\perp\perp}^{qee}$
$E_{\perp}$	$E_z$	×	$\chi_{j\perp z}^{eee}$	$\chi_{j\perp z}^{mee}$	$\chi_{ij\perp z}^{qee}$
$E_z$	$E_{\perp}$	×	$\chi_{jz\perp}^{eee}$	$\chi_{jz\perp}^{mee}$	$\chi_{ijz\perp}^{qee}$
$E_z$	$E_z$	×	$\chi_{jzz}^{eee}$	$\chi_{jzz}^{mee}$	$\chi_{ijzz}^{qee}$
Plasmonic excitation			$P_{MD-EQ,i}^{NL}$		
$E_j$	$\nabla_k E_l$	Sites A & B in phase	$\chi_{ijkl}^{eem,q}$		
$E_{\perp}$	$\nabla_{\perp} E_{\perp}$	×	$\chi_{i\perp\perp\perp}^{eem,q}$		
$E_{\perp}$	$\nabla_{\perp} E_z$	✓	$\chi_{i\perp\perp z}^{eem,q}$		
$E_{\perp}$	$\nabla_z E_{\perp}$	✓	$\chi_{i\perp z\perp}^{eem,q}$		
$E_{\perp}$	$\nabla_z E_z$	×	$\chi_{i\perp zz}^{eem,q}$		
$E_z$	$\nabla_{\perp} E_{\perp}$	×	$\chi_{iz\perp\perp}^{eem,q}$		
$E_z$	$\nabla_{\perp} E_z$	×	$\chi_{iz\perp z}^{eem,q}$		
$E_z$	$\nabla_z E_{\perp}$	×	$\chi_{izz\perp}^{eem,q}$		
$E_z$	$\nabla_z E_z$	×	$\chi_{izzz}^{eem,q}$		

by the gold and contributes only marginally to the measured SHG signal. Thus, one has to consider not one system but the two sub-systems made by each wire edge, called site A and site B. SHG can only be detected when SHG produced in site A and site B are in phase, i.e. interfere constructively. Checking the phase of the electric field based on the electrostatic model, one can derive a "truth table" describing which tensor component delivers SHG in (anti)phase at both sites, see table 4.1. One notices the list of tensor components producing measurable enhanced SHG differs from that obtained by studying the system under the assumption of a plane wave incident along the  $z$ -axis, as in section 3.1. Based on this new list, one obtains a list of tensor components susceptible to be catalyzed by the plasmonic process. These are all tensor components whose indices follow the patterns  $\chi_{j\perp\perp}^{eee}$ ,  $\chi_{j\perp\perp}^{mee}$ ,  $\chi_{ij\perp\perp}^{qee}$ ,  $\chi_{i\perp\perp z}^{eem,q}$ , and  $\chi_{i\perp z\perp}^{eem,q}$ , where the  $\perp$  indices can take either the value  $x$  or  $y$  depending on the nanowires'

orientation. For a given tensor component, all  $\perp$  indices must then take the same value. From this list, one derives the source terms of plasmonic origin for  $x$ - and  $y$ -wires and for each host material and setup configuration, see equations 4.1-(4.4).

SHG measurements always demonstrated the presence of an SHG signal varying with the nanowires' orientation, e.g. the anisotropies always show lobes normal to the nanowires. It is then remarkable that for each case,  $x$ - or  $y$ -wires, the source terms are identical in their mathematical form. In other words, the  $0^\circ$  relative anisotropy for  $y$ -wires should correspond to the  $90^\circ$  relative anisotropy for  $x$ -wires. The shape and orientation of these anisotropy measurements, if not the amplitude, should be identical. For instance, according to Equation (4.1) these should be two-fold anisotropies oriented along the  $x$ -axis. No signal is expected along  $y$ . Since this does not match the experimental results, either the catalyzing process is not the source of the SHG signal, or the model employed is wrong and a complete different story is taking place in the near-field.

It is important to consider also the depth reach of the plasmonic effects as it was mentioned above. It turns out that the plasmon-affected volume remains within the region altered during the polishing process. Indeed, it is typically considered that such processes induce crystallographic defects within a depth of about three times the grain size, i.e. about  $3\mu\text{m}$  in our case. The presence of such defects is illustrated in figure 4.32. Their magnitude and number decrease with the depth. Thus, the question arises whether the crystal volume susceptible to deliver an enhanced signal is still to be considered as a proper homogeneous crystallographic entity on which the selection rules apply, or if it should rather be assimilated to a polycrystalline volume. The effect of such a damaged layer is mostly irrelevant for measurements carried out without nanostructures because the actual volume being probed is larger as mentioned above. This was verified in many experiments within the research group. Nevertheless, this near-surface region becomes preponderant under the nanostructures' mediation if local field enhancement effectively takes place. The region most strongly catalyzed is also the most smeared out in its crystallographic structure.

Assimilating this region to a polycrystalline volume, SHG should be generated isotropically, before eventually canceling out in far field, but the optical catalyst feature is not isotropic: If at all, amplification takes place only for the projection of the incident electric field in the direction normal to the nanowire's long axis. In other words, the amplified SHG anisotropy of a polycrystalline volume would appear to be two-fold. In this hypothesis, a linear amplification model with respect to the fundamental electric field strength would feature both a  $\cos^2\theta$  or  $\sin^2\theta$  incident and emission anisotropies, depending on the nanowires' orientation. This is consistent with a  $\cos^6\theta$  or  $\sin^6\theta$  measurement for  $0^\circ$  relative anisotropies. This does match the shape of the registered lobes. This polycrystalline SHG hypothesis can be verified using samples that are not lapped or polished, but cleaved to offer a virgin surface on which to produce metamaterials.

Should this prove not to be the right explanation, one has to depart from an electric field amplification model and consider SHG generation directly within the gold structures as mentioned previously. Such a model would provide a meaningful explanation to the observation of similar signals on nonlinear crystal and glass host substrate, but also the lack of a temperature dependence on "AFM" signals. In that respect, the Maxwell-Vlasov theory [194, 195]

**RMnO<sub>3</sub> (c)-type plasmonic SHG ( $\alpha_y$  phase), normal incidence**

$$\mathbf{S}_{\text{pl}}^{\text{NL}}(c) = \begin{pmatrix} (\chi_{xxx}^{eee}(c) + \chi_{yyy}^{mee}(c) + \chi_{zxxx}^{qee}(c)) E_x^2 \\ \quad + \chi_{xxxz}^{eem,q}(c) E_x \nabla_x E_z \\ \quad + \chi_{xxzx}^{eem,q}(c) E_x \nabla_z E_x \\ 0 \\ 0 \end{pmatrix}, \quad \mathbf{S}_{\text{pl}}^{\text{NL}}(c) = - \begin{pmatrix} (\chi_{xxx}^{eee}(c) + \chi_{yyy}^{mee}(c) + \chi_{zxyy}^{qee}(c)) E_y^2 \\ \quad + \chi_{xyyz}^{eem,q}(c) E_y \nabla_y E_z \\ \quad + \chi_{xyzy}^{eem,q}(c) E_y \nabla_z E_y \\ 0 \\ 0 \end{pmatrix} \quad (4.1)$$

**RMnO<sub>3</sub> (i)-type plasmonic SHG, 45° incidence**

$$\mathbf{S}_{\text{pl}}^{\text{NL}}(i) = \begin{pmatrix} \chi_{xxx}^{qee}(i) E_x^2 \\ 0 \\ (\chi_{zxx}^{eee}(i) + \chi_{zzxx}^{qee}(i)) E_x^2 \\ \quad + \chi_{zxxz}^{eem,q}(i) E_x \nabla_x E_z \\ \quad + \chi_{zxzx}^{eem,q}(i) E_x \nabla_z E_x \end{pmatrix}, \quad \mathbf{S}_{\text{pl}}^{\text{NL}}(i) = \begin{pmatrix} \chi_{xxyy}^{qee}(i) E_y^2 \\ 0 \\ (\chi_{zxx}^{eee}(i) + \chi_{zzxx}^{qee}(i)) E_y^2 \\ \quad + \chi_{zxxz}^{eem,q}(i) E_y \nabla_y E_z \\ \quad + \chi_{zxzx}^{eem,q}(i) E_y \nabla_z E_y \end{pmatrix} \quad (4.2)$$

**Cr<sub>2</sub>O<sub>3</sub> (i)- and (c)-type plasmonic SHG signals, normal incidence**

$$\mathbf{S}_{\text{pl}}^{\text{NL}} = \begin{pmatrix} (\chi_{yyy}^{mee}(i) + \chi_{zxxx}^{qee}(i)) E_x^2 \\ \quad + \chi_{xxxz}^{eem,q}(i) E_x \nabla_x E_z \\ \quad + \chi_{xxzx}^{eem,q}(i) E_x \nabla_z E_x \\ -\chi_{yyy}^{eee}(c) E_x^2 \\ 0 \end{pmatrix}, \quad \mathbf{S}_{\text{pl}}^{\text{NL}} = - \begin{pmatrix} (\chi_{yyy}^{mee}(i) + \chi_{zxxx}^{qee}(i)) E_y^2 \\ \quad + \chi_{xxxz}^{eem,q}(i) E_y \nabla_y E_z \\ \quad + \chi_{xxzx}^{eem,q}(i) E_y \nabla_z E_y \\ -\chi_{yyy}^{eee}(c) E_y^2 \\ 0 \end{pmatrix} \quad (4.3)$$

**Nanowires on glass only, normal incidence**

$$\mathbf{S}_{\text{pl}}^{\text{NL}} = \begin{pmatrix} (-\chi_{yxx}^{mee}(i) + \chi_{zxxx}^{qee}(i)) E_x^2 \\ \quad + \chi_{xxxz}^{eem,q}(i) E_x \nabla_x E_z \\ \quad + \chi_{xxzx}^{eem,q}(i) E_x \nabla_z E_x \\ (\chi_{xxx}^{mee}(i) + \chi_{zyxx}^{qee}(i)) E_x^2 \\ \quad + \chi_{yxxz}^{eem,q}(i) E_x \nabla_x E_z \\ \quad + \chi_{yxzx}^{eem,q}(i) E_x \nabla_z E_x \\ 0 \end{pmatrix}, \quad \mathbf{S}_{\text{pl}}^{\text{NL}} = \begin{pmatrix} (-\chi_{yyy}^{mee}(i) + \chi_{zxyy}^{qee}(i)) E_y^2 \\ \quad + \chi_{xyyz}^{eem,q}(i) E_y \nabla_y E_z \\ \quad + \chi_{xyzy}^{eem,q}(i) E_y \nabla_z E_y \\ (\chi_{xyy}^{mee}(i) + \chi_{zyyy}^{qee}(i)) E_y^2 \\ \quad + \chi_{yyyz}^{eem,q}(i) E_y \nabla_y E_z \\ \quad + \chi_{yyzy}^{eem,q}(i) E_y \nabla_z E_y \\ 0 \end{pmatrix} \quad (4.4)$$

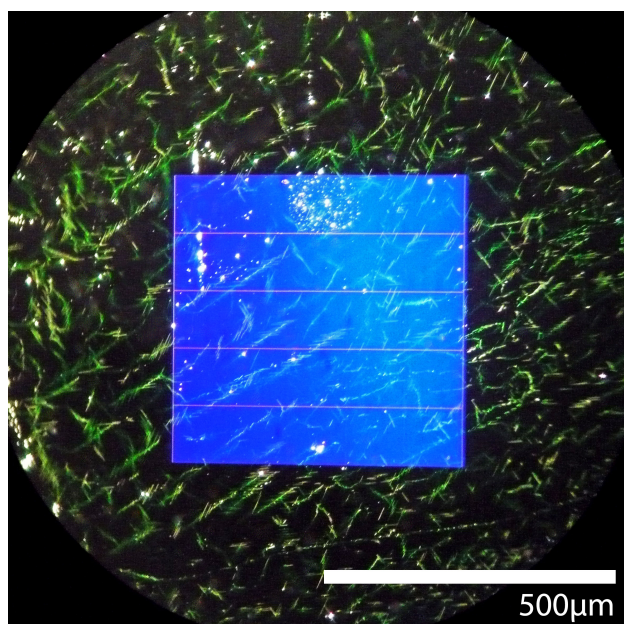


**Figure 4.32** – Dark field acquisition carried out on a nanostructured field on  $\text{Cr}_2\text{O}_3$ . Only the scattered light is collected, therewith revealing defects in the crystal. Their green tint is characteristic of  $\text{Cr}_2\text{O}_3$ . This demonstrates that scattering occurs within the crystal and is not due to surface contamination by e.g. dust. Much more numerous and finer cracks may be present but not detected in this way. Formation of such cracks occurs during the lapping and polishing phases with slurry solutions containing grains of  $3\mu\text{m}$  diameter. The affected crystal depth is typically considered to be a factor 3 larger than the grain size.

appears as an insightful and relevant approach to model the optical nonlinearity in metal nanostructures. In this framework, SHG occurs directly from the metal, and current densities plays a critical role. To properly investigate their effect, one would require a proper simulation software, whose scope is far beyond the simple mathematica model proposed in this work. One notices that the Maxwell-Vlasov theory seems also coherent with the above observations. In particular, the largest currents are present at the peak resonance and there is reminiscence of the underlying crystal due to its dielectric constant, i.e. damping of the plasmon via polarization of the crystal.



## Conclusion and Outlook

Beyond their linear features for which a proper model is at hand, metamaterials feature nonlinear properties with a challenging model description. In this work, one makes use of the symmetry sensitivity and spectral information carried in the nonlinear process of second harmonic generation (SHG). The approach in this work consists of carrying out a classical analysis of the tensor components at play based on a far-field excitation, i.e. using plane waves electromagnetic fields and a symmetry analysis of the material under investigation. To do so, the nanostructures are considered as perfect nanostructures identical from one building block to the other. Two types of investigations are carried out: First, gold nanostructures sharing symmetry feature variations are investigated to *characterize* the SHG in metamaterials. Second, simple gold nanowires are used to pattern the surface of an SHG-active host to investigate their *application* as an optical catalyst. The classical approach does not fully encompass the processes at play, yet SHG is recorded from a variety of nanostructures and valuable information is gained from the results.

The first part of this work is dedicated to SHG characterization of metamaterials. Here and for the first time, broad SHG spectra are recorded for a variety of nanostructures sharing geometrical features. SHG is measured even from structures described as centrosymmetric, or from tensor components expected to be symmetry forbidden. This unexpected observation has been reported by several groups [48, 54, 132, 196, 197]. The challenge lies in providing a proper model to these measurements. Together with the extreme variability of the SHG signal delivered by nanostructures, they hint at the potential role played by nanoscopic surface defects and irregularities resulting from the top-down EBL fabrication process. The fact that SHG signal is still recorded despite the meta-atoms being dislocated further supports this hypothesis, and dedicated experiments back this interpretation [198, 199]. The dislocation and orientation randomizing of the nanostructures under illumination might also explain the lack of correlation between the plasmonic linear resonance and the recorded SHG spectra. Improving the metamaterial volume and contour down to the atomic scale is an obvious step to further investigate the interesting nonlinear features of metamaterials [200, 201]. Suggestions regarding the nanostructures' mechanical stability are also proposed in this work.

The second part is dedicated to SHG amplification by metamaterials. Here, one investigates the use of metamaterials as optical catalysts based on the local field enhancement in their immediate vicinity. Here too, broad SHG spectra are reported for the first time for such an application of metamaterials. The concept of a simple and straightforward patterning of a nonlinear crystal for nonlinear optical catalysis is undermined by the absence of features such as temperature dependence on expected AFM signals. Moreover, here too, SHG is measured

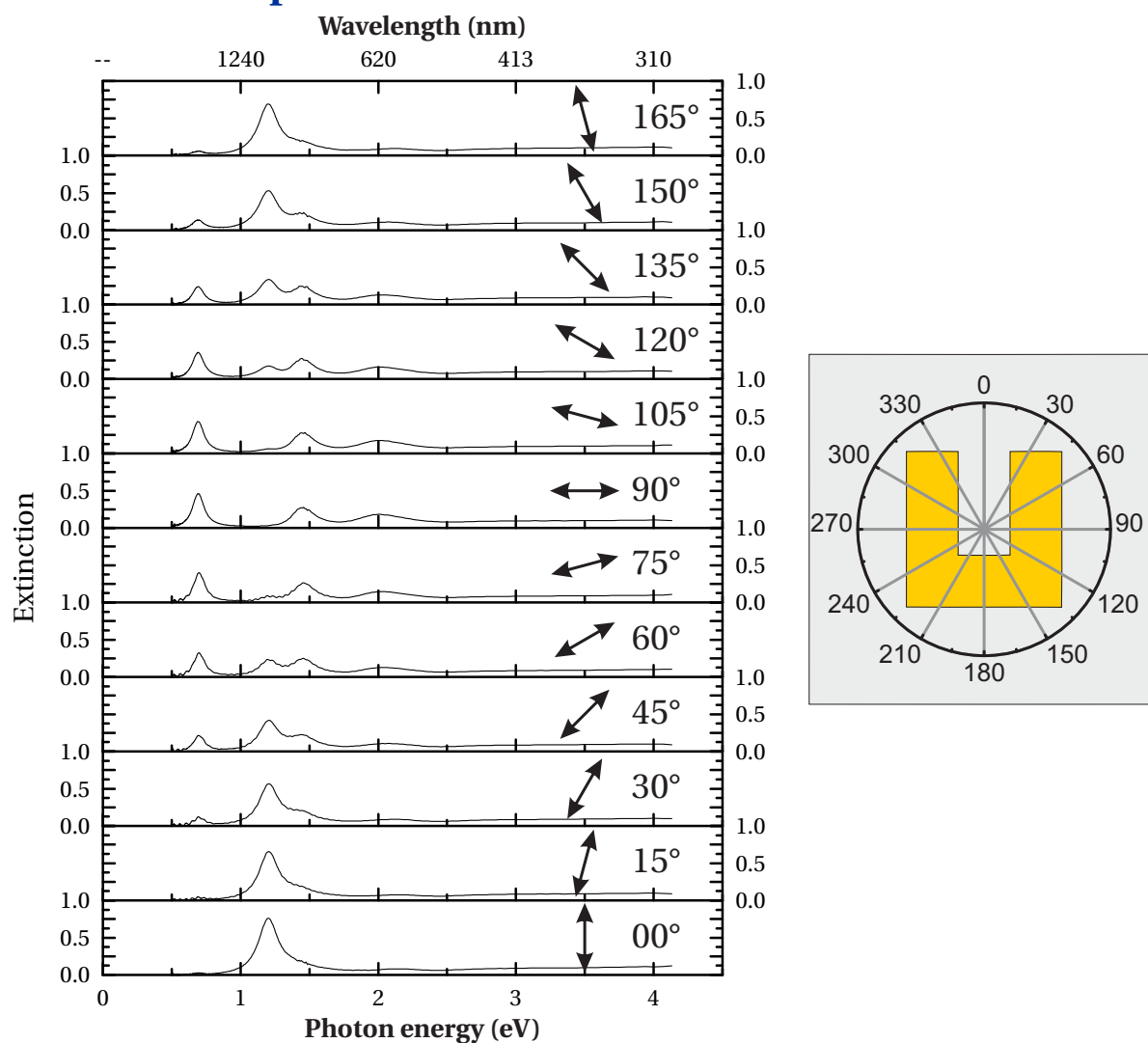
from nanowires expected to be centrosymmetric on an SHG inactive glass host. Nevertheless, similar nanostructures fabricated on the surface of  $R\text{MnO}_3$  and  $\text{Cr}_2\text{O}_3$  crystals display tweaked SHG features with respect to the known features from these nonlinear model systems. This is a clear indication of convolutions of the plasmonic process with a sample-specific response. Although the exact process could not be pinpointed, a certain dependence of the SHG yield on the environment of the nanowires has been highlighted and requires to take a closer look in future investigations.

First steps in that direction were made by proposing an evolution of the far-field plane-wave approach to include near-field effects. In this model, it was proposed that the recorded SHG intensities might be explained by constructive plasmonic interferences instead of macroscopic SHG selection rules. Based on perfect nanostructures and a defect-free crystal host, the near-field model cannot fully explain the recorded SHG signals. Again, this is consistent with SHG being potentially generated by random defects or hot spots. However, not only the nanowires might bear defects, but also the host substrate after it underwent the lapping and polishing preparation steps. While this effect is irrelevant for measurements carried out on bare crystals, it might not be so for their surface patterned with nanostructure due to the expected enhancement of the electric field in their few-nanometer vicinity. Indeed, it was shown that the anisotropy measurements recorded from nanostructure fields are also consistent with an anisotropic amplification of an isotropic polycrystalline volume. Working in the future with cleaved samples rather than polished ones would allow to clarify this hypothesis. Finally, addressing the question where the light conversion takes place, whether within the crystal or within the nanostructures is key. In the latter case, a future analysis of the internal currents based e.g. on the Maxwell-Vlasov theory might explain the process of SHG in nearly centrosymmetric nanostructures. It would also help to understand the spectral SHG modulation by the crystal/environment, and therewith corroborate whether one observes a metamaterial-mediated amplification of SHG from the host substrate or a host-mediated SHG from plasmon-driven nanostructures.

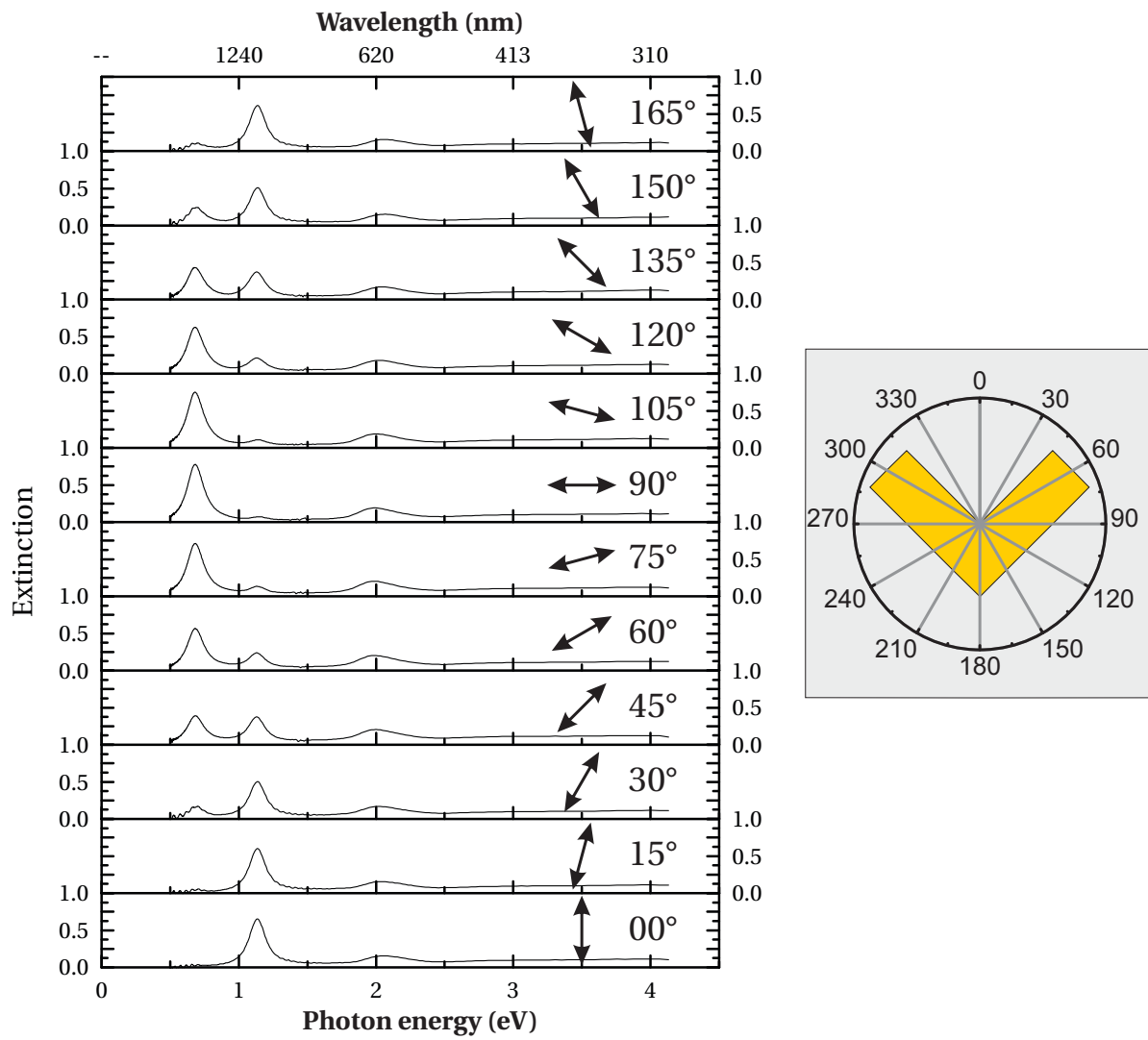
# Appendix A

## Spectra

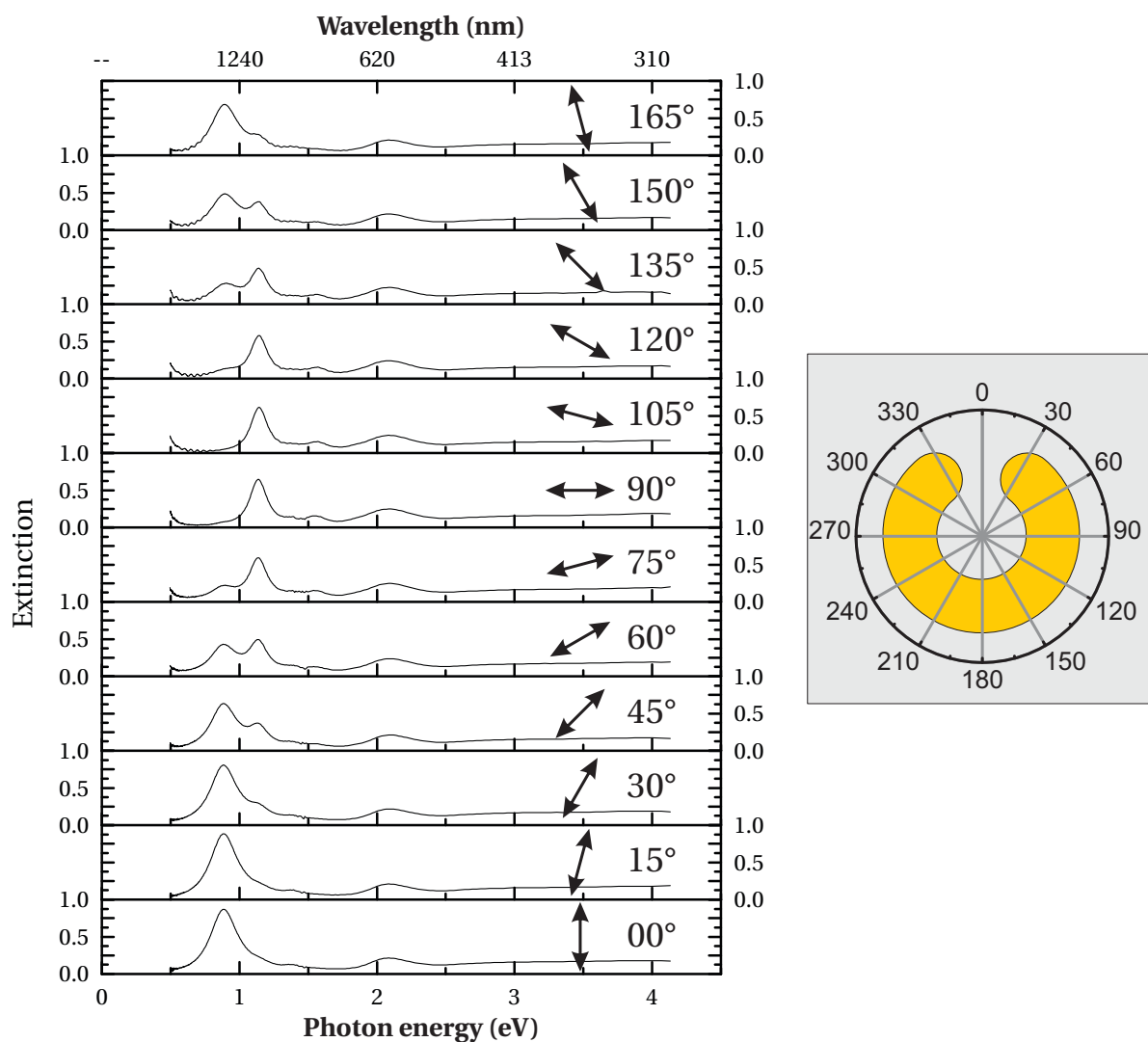
### A.1 Linear Spectra



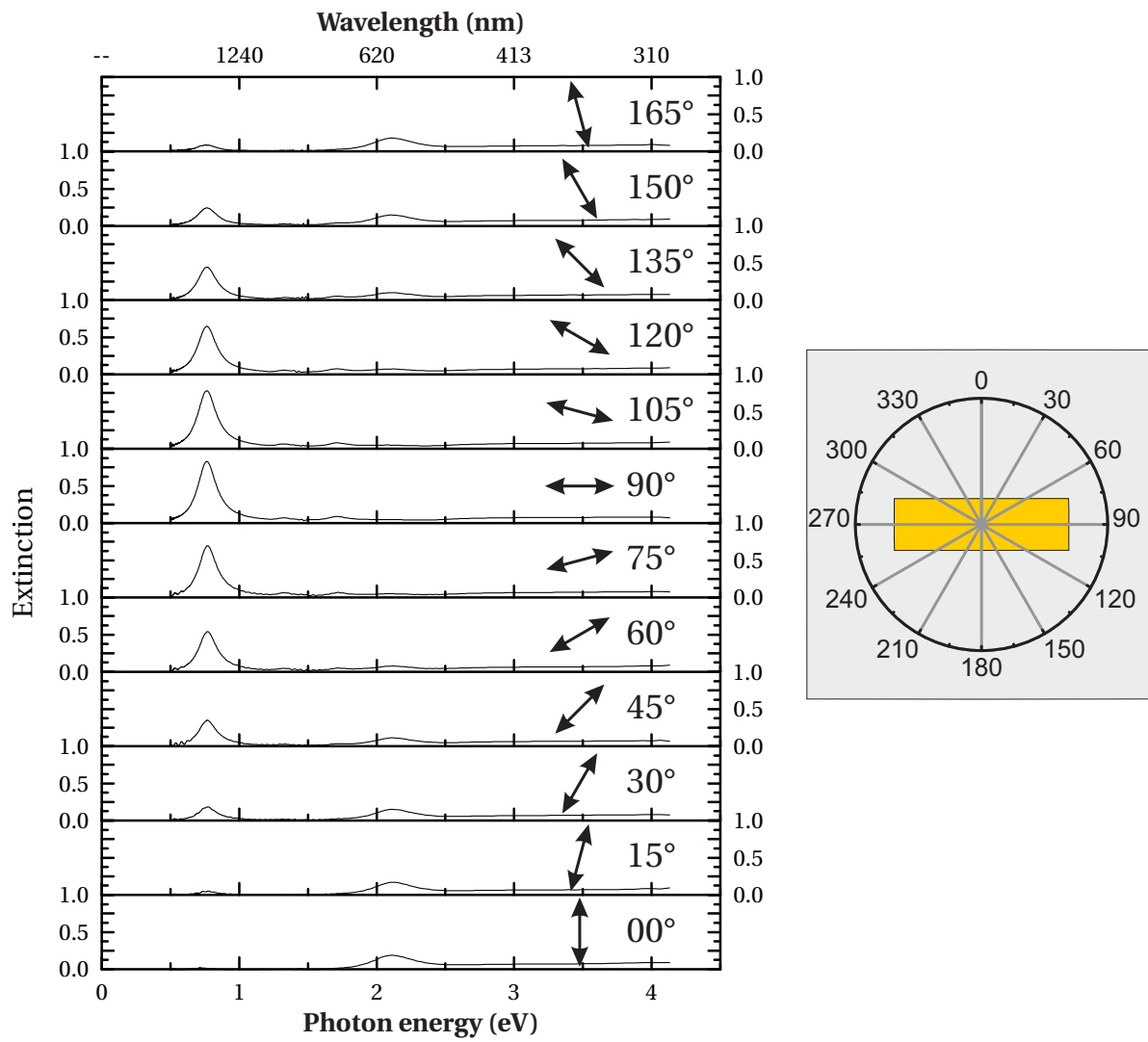
**Figure A.1** – U-shaped metamaterial linear spectra versus driving light polarization. The incident light polarization angle is displayed as inset. The evolution of the spectra demonstrates the presence of eigenpolarizations at 0° and 90°.



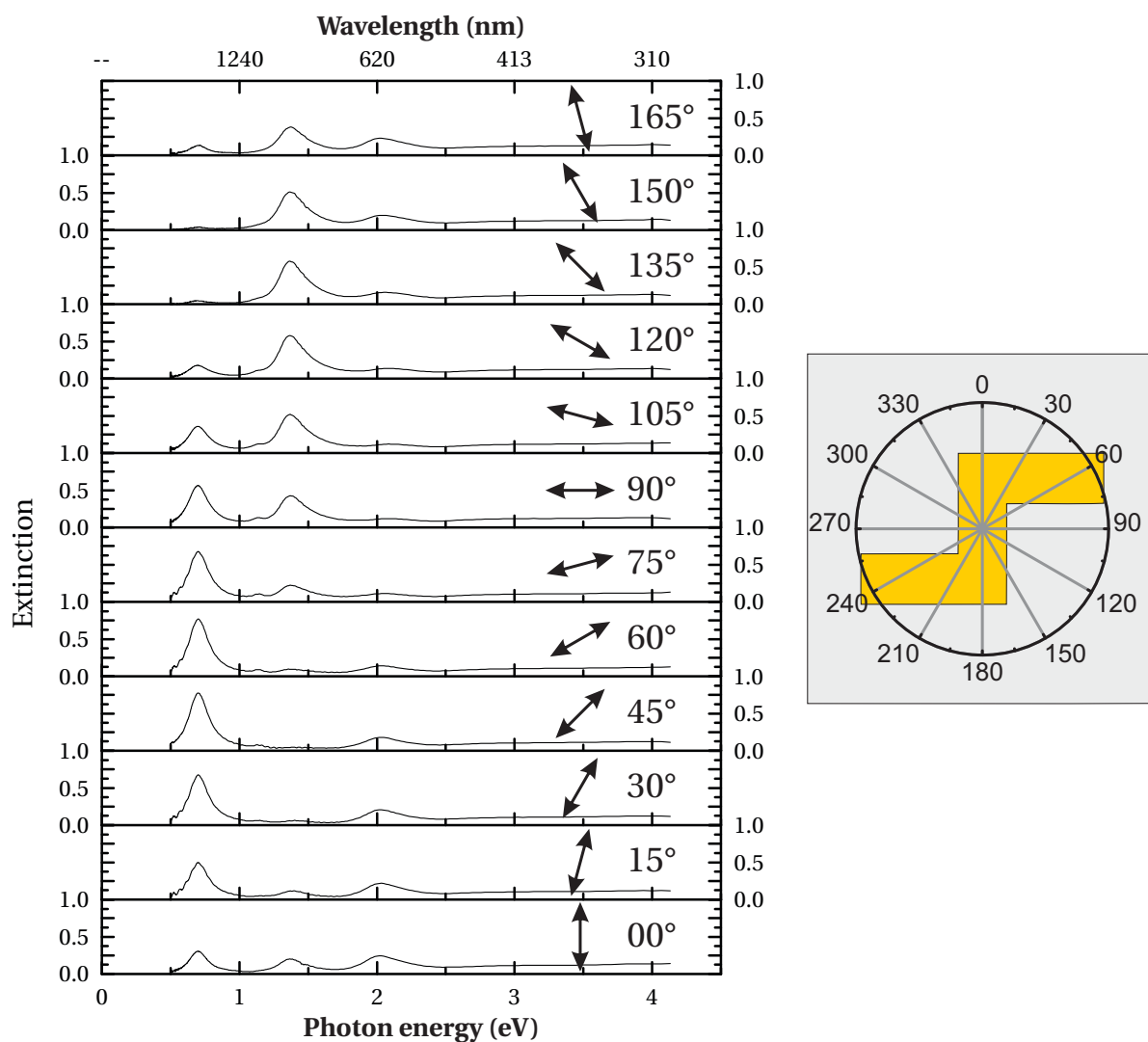
**Figure A.2** – L-shaped metamaterial linear spectra versus driving light polarization. The incident light polarization angle is displayed as inset. The evolution of the spectra demonstrates the presence of eigenpolarizations at 0° and 90°.



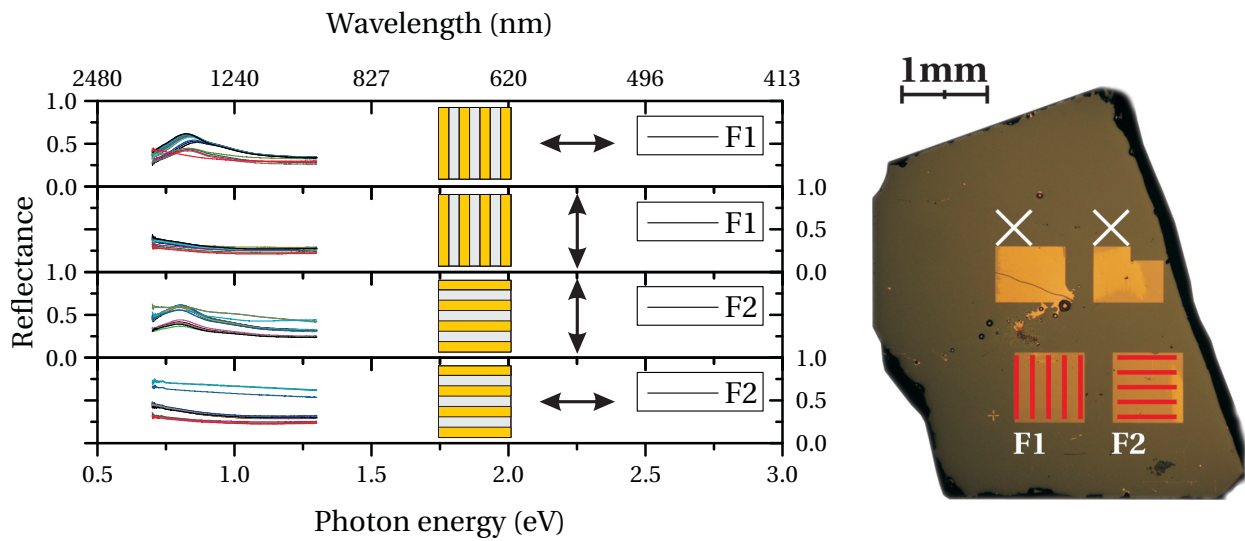
**Figure A.3** – C-shaped metamaterial linear spectra versus driving light polarization. The incident light polarization angle is displayed as inset. The evolution of the spectra demonstrates the presence of eigenpolarizations at  $0^\circ$  and  $90^\circ$ .



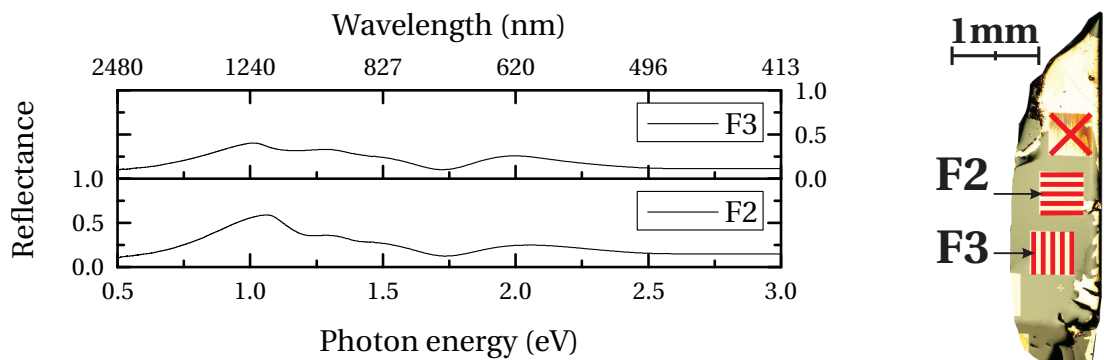
**Figure A.4** – I-shaped metamaterial linear spectra versus driving light polarization. The incident light polarization angle is displayed as inset. The evolution of the spectra demonstrates the presence of eigenpolarizations at 0° and 90°.



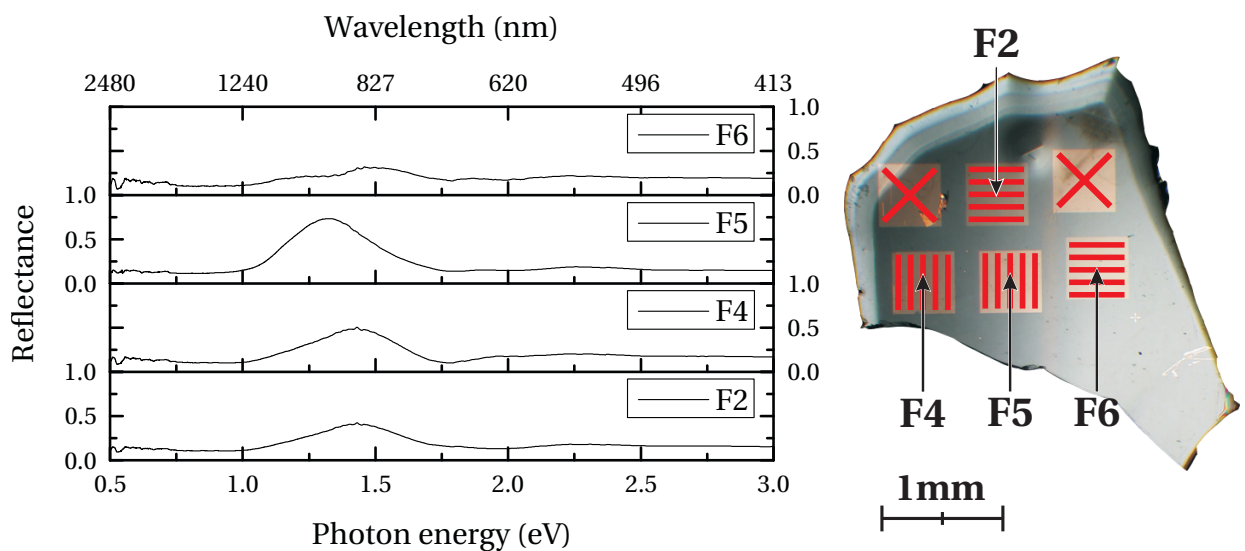
**Figure A.5** – Z-shaped metamaterial linear spectra versus driving light polarization. The incident light polarization angle is displayed as inset. The evolution of the spectra demonstrates the presence of eigenpolarizations at 45° and 135°.



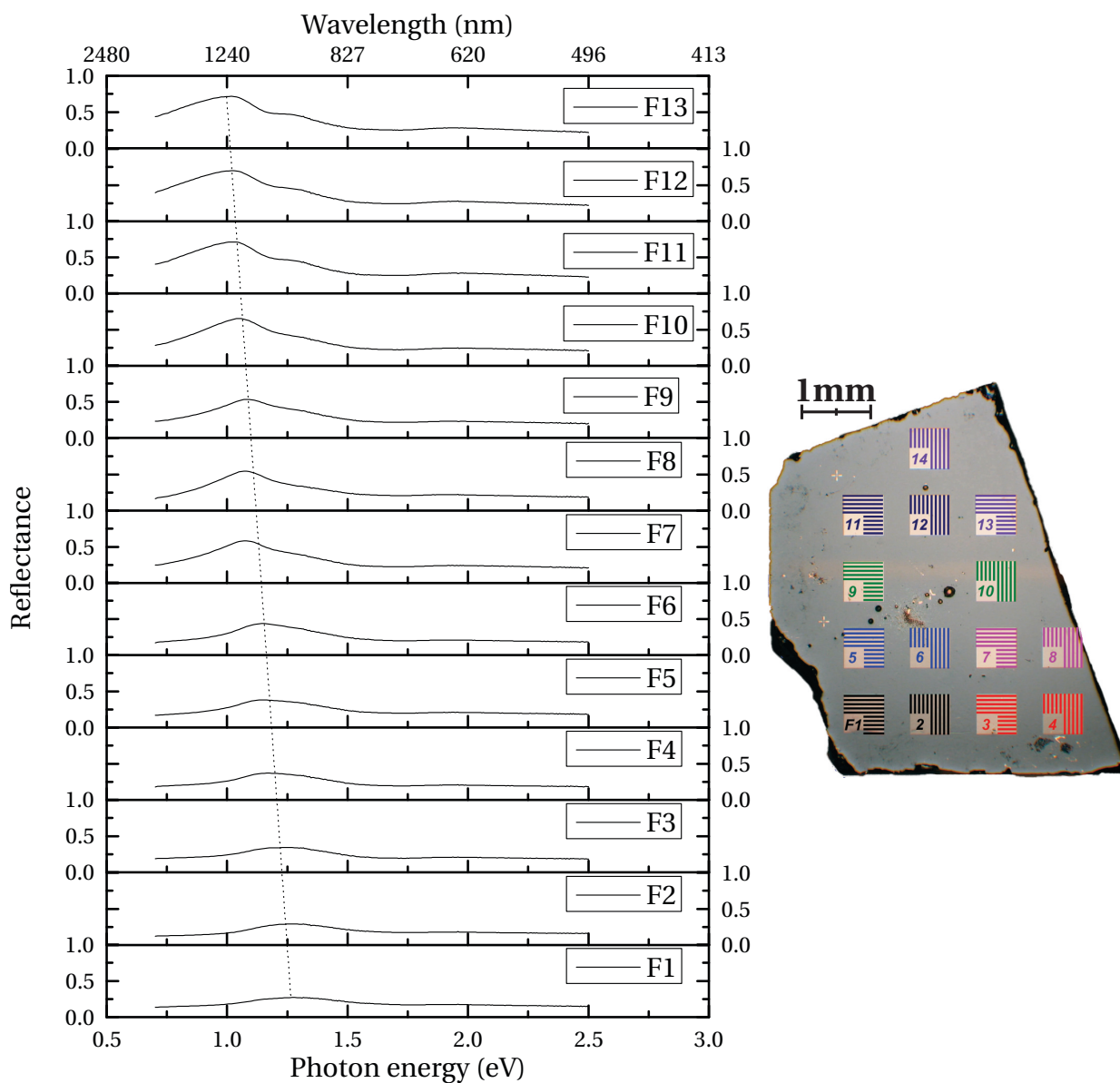
**Figure A.6** – Linear spectra of sample DMF12 FZ  $\text{YbMnO}_3$ . Reflectance spectra are shown for both excitation polarizations on both field orientations. Each field is rastered and a square of  $100 \times 100 \mu\text{m}^2$  only is measured (one curve per measurement), therewith demonstrating the good overall homogeneity of each field.



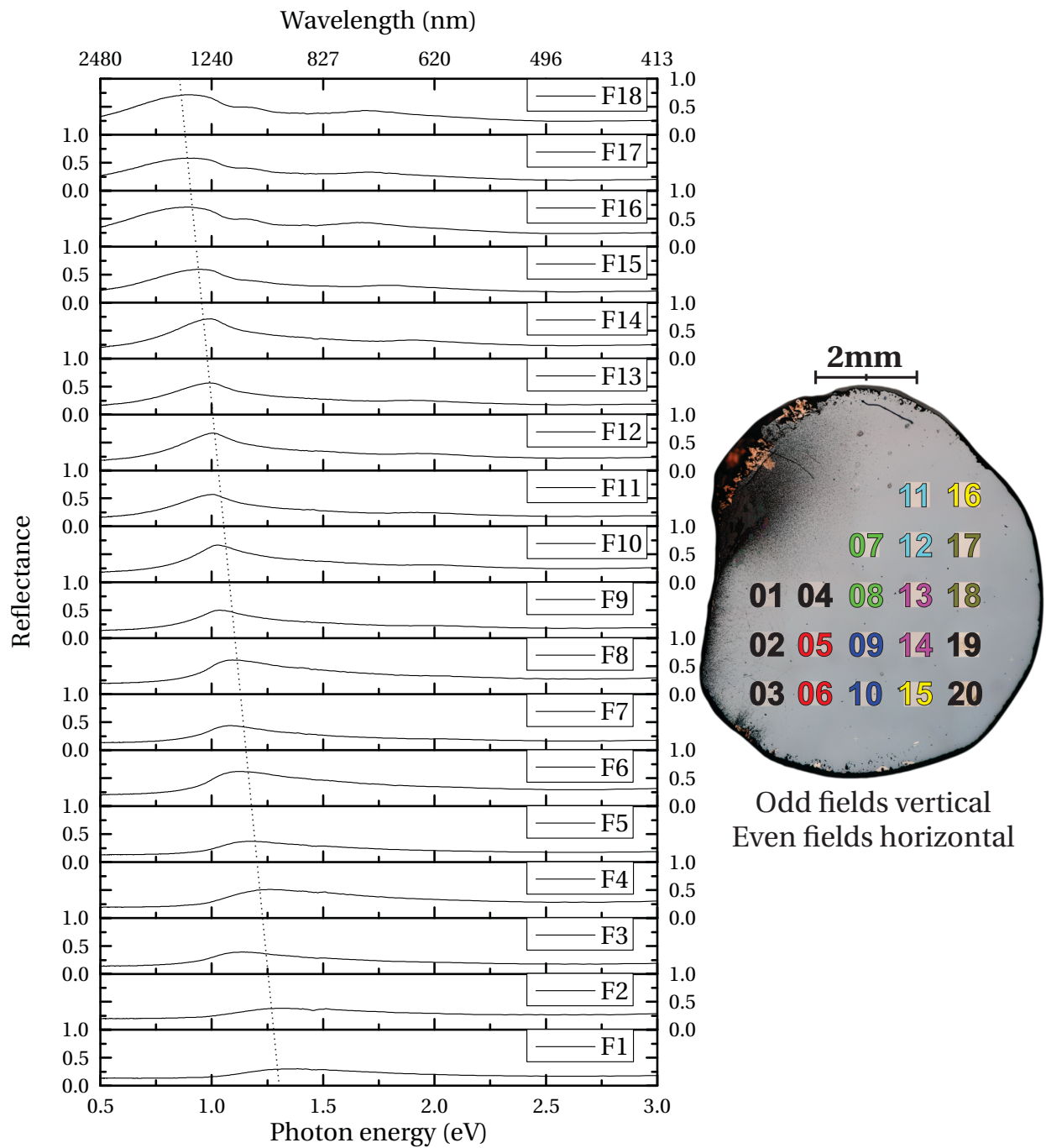
**Figure A.7** – Linear spectra of sample DMF13 FG  $\text{HoMnO}_3$ . Excitation polarization normal to the nanowires.



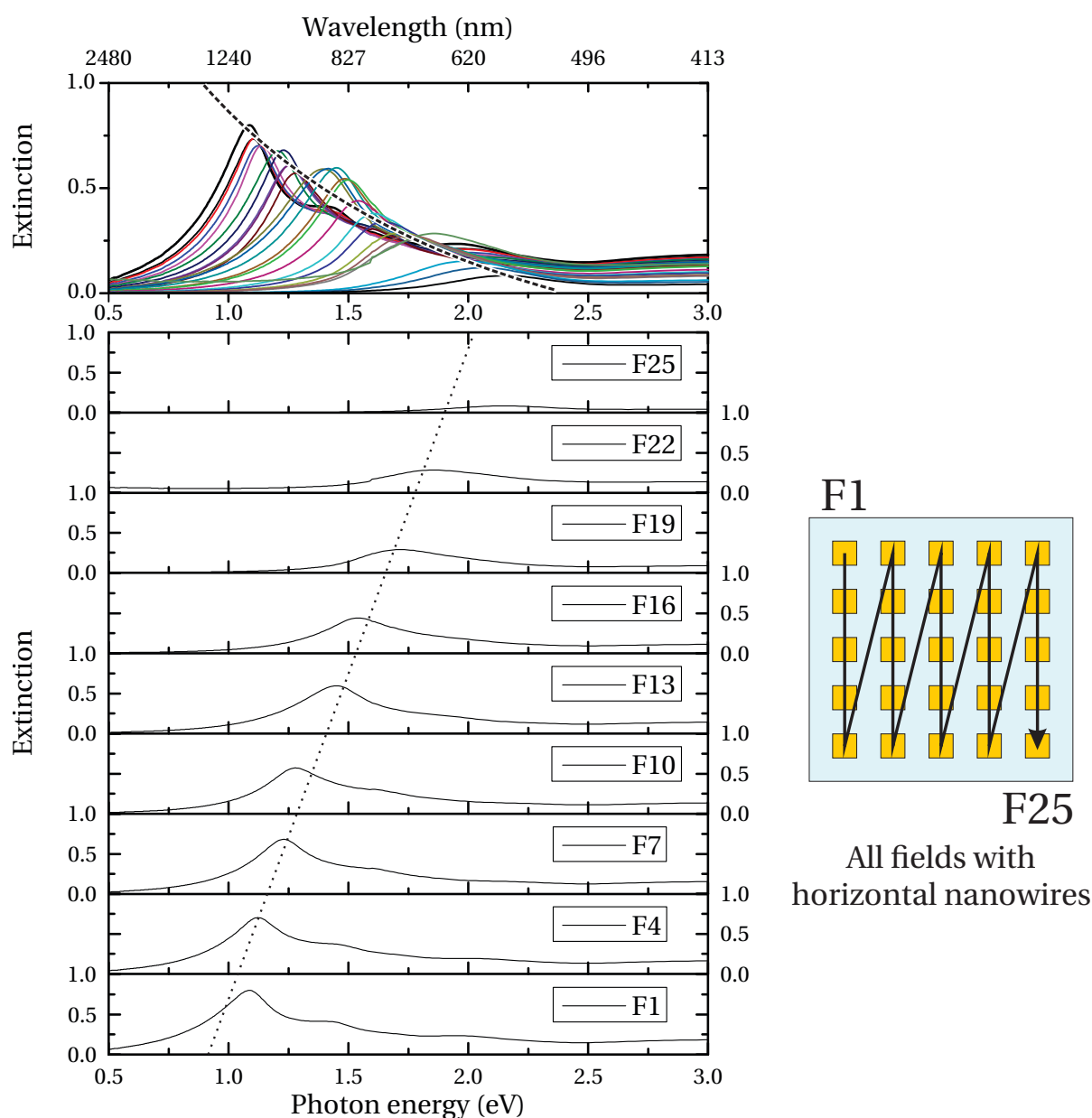
**Figure A.8** – Linear spectra of sample DMF15 FG  $\text{YbMnO}_3$ . Excitation polarization normal to the nanowires.



**Figure A.9** – Linear spectra of sample DMF16 FZ  $\text{YbMnO}_3$ . Excitation polarization normal to the nanowires. A dotted line is traced to guide the eye and demonstrate the linear variation of the plasmonic resonance with the field number, i.e. the nanowires' width.

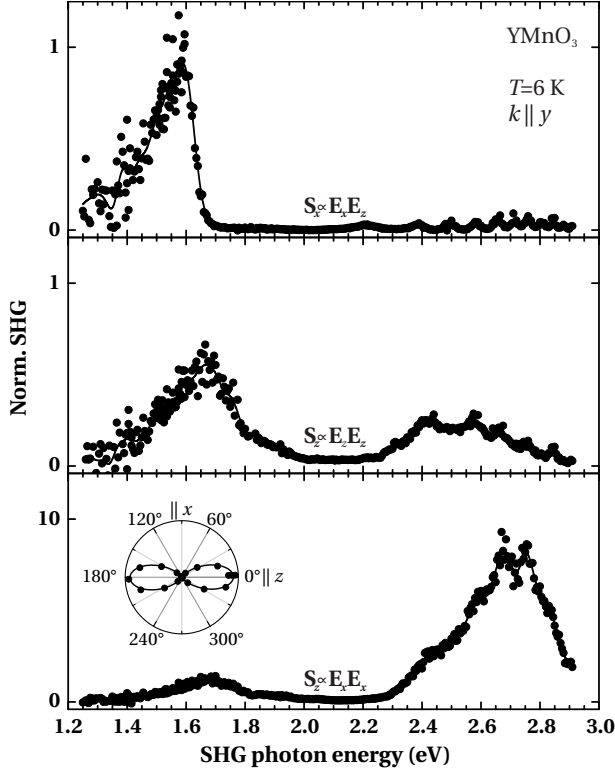


**Figure A.10** – Linear spectra of sample DMF18  $\text{Cr}_2\text{O}_3$ . Excitation polarization normal to the nanowires. A dotted line is traced to guide the eye and demonstrate the linear variation of the plasmonic resonance with the field number, i.e. the nanowires' width.

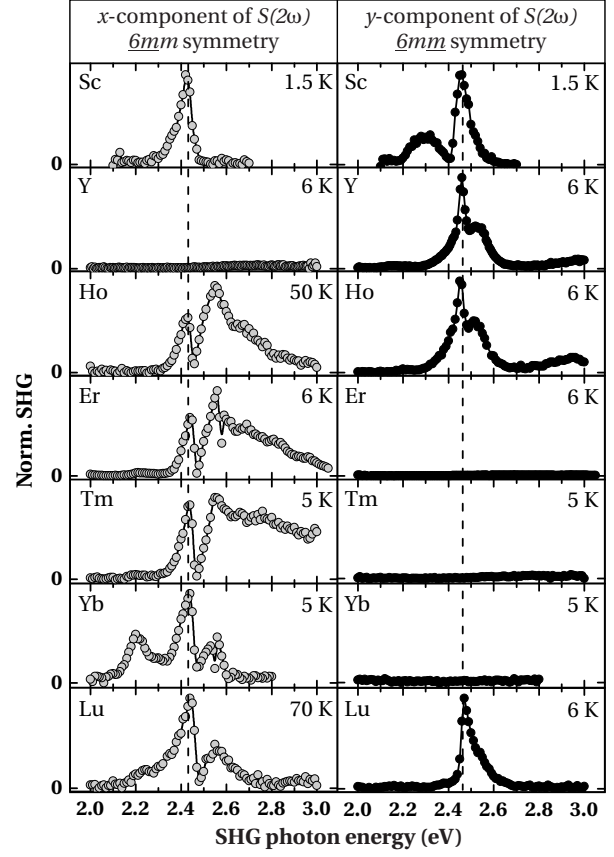


**Figure A.11** – Linear spectra of sample WoG (wires on glass). Excitation polarization normal to the nanowires. The extinction is superposed for all fields in the top graph together with a dashed line showing the trend of the maximum extinction. This dashed line is not straight as a result of both the quality factor and the cover ratio varying with field number. A selection of every third field is displayed in the bottom part together with a dotted line traced to guide the eye and demonstrate the linear variation of the plasmonic resonance with the field number, i.e. the nanowires' width.

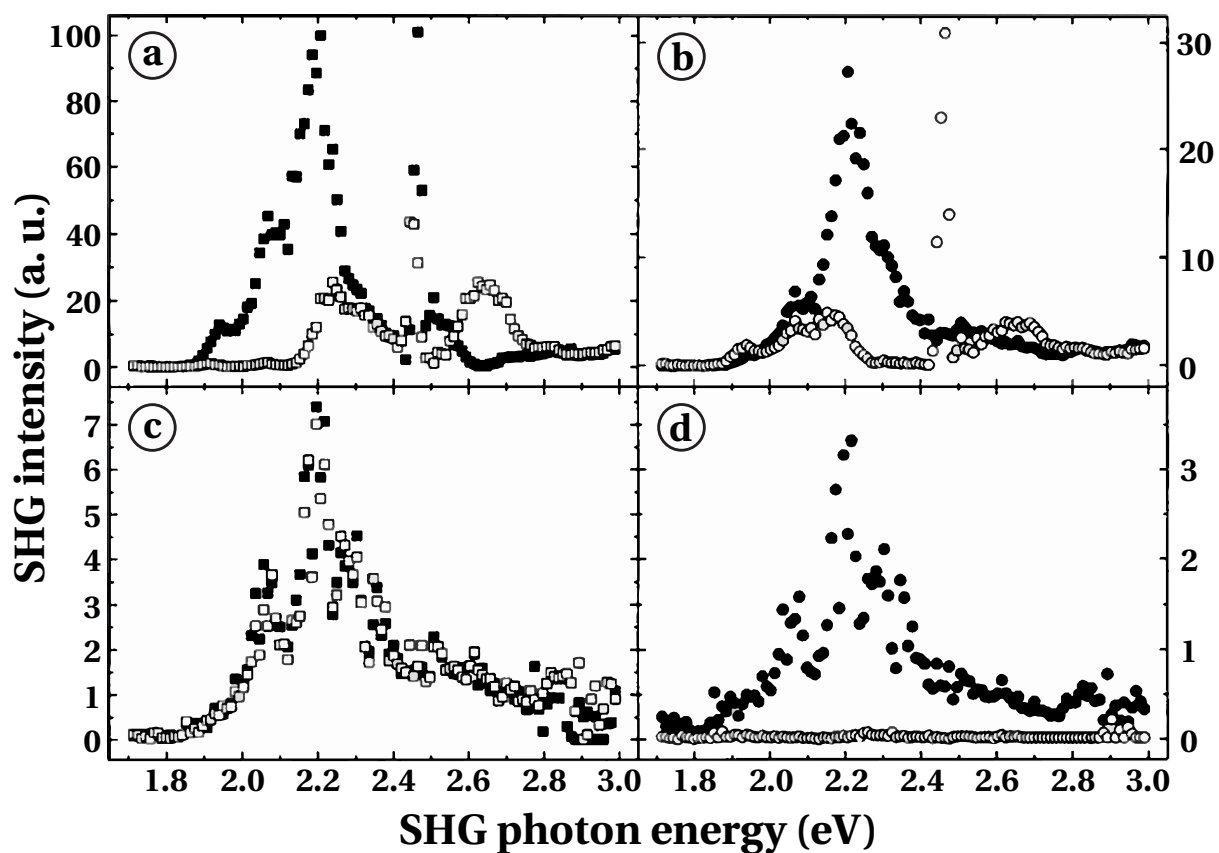
## A.2 $\text{RMnO}_3$ Reference SHG Spectra



**Figure A.12** –  $i$ -tensor SHG contributions in  $\text{YMnO}_3$ . The diagrams show the spectral dependence of the  $\chi_{xxz}$ ,  $\chi_{zzz}$ , and  $\chi_{zxx}$  components of the  $\chi^{\text{ED}}(i)$  tensor at  $T = 6\text{K}$ . The spectra were measured on a sample surface normal to the  $y$ -axis. The dominant contribution is the  $\chi_{zxx}$  component in the 2.70 eV range. The inset anisotropy measured at  $E_{\text{SH}} = 2.65\text{eV}$  reflects the two-fold polarization dependence of the  $\chi_{zxx}$  component. Graphic taken from [143].



**Figure A.13** –  $c$ -tensor SHG contributions in hexagonal manganites  $\text{RMnO}_3$ . The diagrams show the spectra for various  $\text{RMnO}_3$  compounds measured below their Néel temperature in the 2.44 eV resonance range for  $k \propto \hat{e}_z$ . In  $\text{ErMnO}_3$ ,  $\text{TmMnO}_3$ ,  $\text{YbMnO}_3$ , and  $\text{YMnO}_3$  SHG contributions polarized *only* in the  $x$ - or  $y$ -direction occur. In these compounds, antiferromagnetic orders exist that follow the  $\alpha_y$ - (point group  $\bar{6}mm$ ) or  $\alpha_x$  model (point group  $\bar{6}mm$ ), respectively. In the other compounds, more than one  $\alpha$  spin order occur. Graphic taken from [143].

A.3  $\text{Cr}_2\text{O}_3$  Reference SHG Spectra

**Figure A.14** –  $c$ - (ED) and  $i$ -type (MD/EQ) SHG contributions in  $\text{Cr}_2\text{O}_3$ . The diagrams show the breakdown of the spectra obtained with circular-polarized light (a, c) into the  $c$ -type ( $\propto |\chi_e(c)|^2$ ) and  $i$ -type  $\propto |\chi_{m,q}(i)|^2$  contributions (b, d). The measurements were performed at  $T = 10\text{K}$  (a, b), and  $T = 325\text{K}$  (c, d). Closed and open squares correspond to right- and left-circular polarized light, closed and open circles correspond to the MD/EQ- and the ED-contribution of the signal. Graphic taken from [151].



# Appendix B

## Mathematica 8 Notebooks

### B.1 Cr<sub>2</sub>O<sub>3</sub> SHG Model

This model allows for computing the SHG polarization measurements as a function of temperature on a Cr<sub>2</sub>O<sub>3</sub> crystal whose surface is cut and illuminated along its *c*-axis. Above the Néel temperature, the source terms being mathematically equivalent, the model can also be used to simulate the shape (but not the temperature dependence) of polarization measurements for FEL SHG signals on RMnO<sub>3</sub>. Functions prefixed with an "A" refer to a straightforward amplification process in the direction normal to the nanowires long axis .

```
(*Light electric field *)
EE[ $\theta_{pol}$ ] := {Sin[ $\theta_{pol}$ ], Cos[ $\theta_{pol}$ ], 0};
Ex[ $\theta_{pol}$ ] := EE[ $\theta_{pol}$ ][[1]];
Ey[ $\theta_{pol}$ ] := EE[ $\theta_{pol}$ ][[2]];
Ez[ $\theta_{pol}$ ] := EE[ $\theta_{pol}$ ][[3]];

(*Amplified electric field =Incoming light-Absorbed light+Plasmonic amplification *)
AEE[ $\theta_{pol}$ ,  $\theta_{wire}$ , Amp, Absorption] := (1 - Absorption) * EE[ $\theta_{pol}$ ]
+ {-Amp Sin[ $\theta_{wire}$  -  $\theta_{pol}$ ] Cos[ $\theta_{wire}$ ], Amp Sin[ $\theta_{wire}$  -  $\theta_{pol}$ ] Sin[ $\theta_{wire}$ ], Abs[Amp Sin[ $\theta_{wire}$  -  $\theta_{pol}$ ]]};

AEx[ $\theta_{pol}$ ,  $\theta_{wire}$ , Amp, Absorption] := AEE[ $\theta_{pol}$ ,  $\theta_{wire}$ , Amp, Absorption][[1]];
AEy[ $\theta_{pol}$ ,  $\theta_{wire}$ , Amp, Absorption] := AEE[ $\theta_{pol}$ ,  $\theta_{wire}$ , Amp, Absorption][[2]];
AEz[ $\theta_{pol}$ ,  $\theta_{wire}$ , Amp, Absorption] := AEE[ $\theta_{pol}$ ,  $\theta_{wire}$ , Amp, Absorption][[3]];

(*Temperature dependency of tensor components*)
MQ[Temp] := Piecewise[{{.7 * (1 - (Temp / 800)), Temp  $\leq$  800}, 0];
ED[Temp] := Piecewise[{{((308 - Temp) ^ .5) / (308 ^ .5), Temp  $\leq$  308}, 0];

(*Source term*)
S[ $\theta_{pol}$ , Temp] := {MQ[Temp] (Ex[ $\theta_{pol}$ ] ^ 2 - Ey[ $\theta_{pol}$ ] ^ 2) + 2 ED[Temp] Ex[ $\theta_{pol}$ ] Ey[ $\theta_{pol}$ ],
-2 MQ[Temp] Ex[ $\theta_{pol}$ ] Ey[ $\theta_{pol}$ ] + ED[Temp] (Ex[ $\theta_{pol}$ ] ^ 2 - Ey[ $\theta_{pol}$ ] ^ 2),
0};
Sx[ $\theta_{pol}$ , Temp] := S[ $\theta_{pol}$ , Temp][[1]];
Sy[ $\theta_{pol}$ , Temp] := S[ $\theta_{pol}$ , Temp][[2]];
Sz[ $\theta_{pol}$ , Temp] := S[ $\theta_{pol}$ , Temp][[3]];
```

(\*code continues on next page\*)

```
(*Amplified source term*)
AS[ $\theta_{pol}$ ,  $\theta_{wire}$ , Amp, Absorption, Temp] := {
  (MQ[Temp] + EDp[Temp]) (AEx[ $\theta_{pol}$ ,  $\theta_{wire}$ , Amp, Absorption]^2 - AEy[ $\theta_{pol}$ ,  $\theta_{wire}$ , Amp, Absorption]^2)
  + 2 ED[Temp] AEx[ $\theta_{pol}$ ,  $\theta_{wire}$ , Amp, Absorption] AEy[ $\theta_{pol}$ ,  $\theta_{wire}$ , Amp, Absorption]
  , -2 (MQ[Temp] + EDp[Temp]) AEx[ $\theta_{pol}$ ,  $\theta_{wire}$ , Amp, Absorption] AEy[ $\theta_{pol}$ ,  $\theta_{wire}$ , Amp, Absorption]
  + ED[Temp] (AEx[ $\theta_{pol}$ ,  $\theta_{wire}$ , Amp, Absorption]^2 - AEy[ $\theta_{pol}$ ,  $\theta_{wire}$ , Amp, Absorption]^2)
  , 0
};
ASx[ $\theta_{pol}$ ,  $\theta_{wire}$ , Amp, Absorption, Temp] := AS[ $\theta_{pol}$ ,  $\theta_{wire}$ , Amp, Absorption, Temp][[1]];
ASy[ $\theta_{pol}$ ,  $\theta_{wire}$ , Amp, Absorption, Temp] := AS[ $\theta_{pol}$ ,  $\theta_{wire}$ , Amp, Absorption, Temp][[2]];
ASz[ $\theta_{pol}$ ,  $\theta_{wire}$ , Amp, Absorption, Temp] := AS[ $\theta_{pol}$ ,  $\theta_{wire}$ , Amp, Absorption, Temp][[3]];

(*SHG expressions*)
SHGSignal[ $\theta_{ana}$ ,  $\theta_{pol}$ , Temp] := (Sin[ $\theta_{ana}$ ] Sx[ $\theta_{pol}$ , Temp] + Cos[ $\theta_{ana}$ ] Sy[ $\theta_{pol}$ , Temp])^2;
Aniso[RelativeAngle,  $\theta_{ana}$ , Temp] := SHGSignal[ $\theta_{ana}$ ,  $\theta_{ana}$  - RelativeAngleDegree, Temp];
(*Amplified SHG expressions*)
ASHGSignal[ $\theta_{ana}$ ,  $\theta_{pol}$ ,  $\theta_{wire}$ , Amp, Absorption, Temp] := (Sin[ $\theta_{ana}$ ] ASx[ $\theta_{pol}$ ,  $\theta_{wire}$ , Amp, Absorption, Temp]
  + Cos[ $\theta_{ana}$ ] ASy[ $\theta_{pol}$ ,  $\theta_{wire}$ , Amp, Absorption, Temp])^2;
AAAniso[RelativeAngle,  $\theta_{ana}$ ,  $\theta_{wire}$ , Amp, Absorption, Temp] :=
  ASHGSignal[ $\theta_{ana}$ ,  $\theta_{ana}$  - RelativeAngleDegree,  $\theta_{wire}$ , Amp, Absorption, Temp];

(*Plot SHG intensity*)
Manipulate[
  ParametricPlot[
    Tooltip[{Sin[ $\theta$ ], Cos[ $\theta$ ]} Aniso[RelativeAngle,  $\theta$ , Temp], "AnisoRelAng"
    , Tooltip[{Sin[ $\theta$ ], Cos[ $\theta$ ]} AAAniso[RelativeAngle,  $\theta$ ,  $\theta_{wire}$ , Amp, Absorption, Temp], "AAAnisoRelAng"
    ], { $\theta$ , 0, 2  $\pi$ }, PlotRange -> All]
  , { $\theta_{wire}$ , {0, 30  $\pi$ /180, 45  $\pi$ /180, 60  $\pi$ /180, 90  $\pi$ /180}}
  , {{Amp, 1}, 0, 10}, {{Absorption, .5}, 0, 1}
  , {{CurrentAngle, 2  $\pi$ }, 0, 2  $\pi$ }
  , { $\theta_{pol}$ , {0, 45  $\pi$ /180, 90  $\pi$ /180, 135  $\pi$ /180, 180  $\pi$ /180}}
  , { $\theta_{ana}$ , {0, 45  $\pi$ /180, 90  $\pi$ /180, 135  $\pi$ /180, 180  $\pi$ /180}}
  , {RelativeAngle, {0, 90}}
  , {{Temp, 400}, 0, 1000}
]

```

Code B.1 – SHG model in Cr<sub>2</sub>O<sub>3</sub>

## B.2 Nanowire-Mediated SHG Amplification Model

This model provides access to the electric field strength and its spatial derivatives within and around a nanowire as a function of the amplification of the driving electric field. Dielectric polarization compensation is not taken into account for sake of simplicity since it does not alter the qualitative investigation. The model charge distribution is discretized into a discrete number of infinite charged wires at both ends of the gold nanostructure. The theorem of superposition is then employed to compute the global field distribution. The structure is represented geometrically as having perfect sharp edges yet only the charge separation is taken into consideration, *not* the presence of hot-spots or sharp edges. Figures 3.5 and 4.31 were produced based on this model.

```

Clear["Global`*"]; GoldThickness = 30; OutputSize = 525; OutputRatio = 2;
(*Component of the electric field due to a given charge; x, y are the "test charge" space coordinate; xq, yq are the charge coordinate and qn, its value*)
Ex[x_, y_, xq_, yq_, qn_] := ((x - xq) qn) / ((x - xq)^2 + (y - yq)^2); Ey[x_, y_, xq_, yq_, qn_] := ((y - yq) qn) / ((x - xq)^2 + (y - yq)^2); (*Line charge*)
(* Rough approximation to have an electric field value of Amplification *ExcitationField in the center of the nanostructure *)
DiscreteCharge[ChargeSeparation_, Amplification_, NbCharges_ : 11] := Amplification * ChargeSeparation / (4 * NbCharges) (*Line charge*)
(*Theorem of superposition*)
ExTotal[x_, y_, ChargeSeparation_, Amplification_, ExcitationField_, NbCharges_] :=
  Sum[Ex[x, y, -ChargeSeparation/2, i * GoldThickness / (NbCharges + 1), -DiscreteCharge[ChargeSeparation, Amplification, NbCharges]], {i, 1, NbCharges}] +
  Sum[Ex[x, y, ChargeSeparation/2, i * GoldThickness / (NbCharges + 1), +DiscreteCharge[ChargeSeparation, Amplification, NbCharges]], {i, 1, NbCharges}] + ExcitationField;
EyTotal[x_, y_, ChargeSeparation_, Amplification_, ExcitationField_, NbCharges_] :=
  Sum[Ey[x, y, -ChargeSeparation/2, i * GoldThickness / (NbCharges + 1), -DiscreteCharge[ChargeSeparation, Amplification, NbCharges]], {i, 1, NbCharges}] +
  Sum[Ey[x, y, ChargeSeparation/2, i * GoldThickness / (NbCharges + 1), +DiscreteCharge[ChargeSeparation, Amplification, NbCharges]], {i, 1, NbCharges}];
(*Partial electric field derivatives*)
dExdx[x_, y_, ChargeSeparation_, Amplification_, ExcitationField_, NbCharges_] = D[ExTotal[x, y, ChargeSeparation, Amplification, ExcitationField, NbCharges], x];
dExdy[x_, y_, ChargeSeparation_, Amplification_, ExcitationField_, NbCharges_] = D[ExTotal[x, y, ChargeSeparation, Amplification, ExcitationField, NbCharges], y];
dEydx[x_, y_, ChargeSeparation_, Amplification_, ExcitationField_, NbCharges_] = D[EyTotal[x, y, ChargeSeparation, Amplification, ExcitationField, NbCharges], x];
dEydY[x_, y_, ChargeSeparation_, Amplification_, ExcitationField_, NbCharges_] = D[EyTotal[x, y, ChargeSeparation, Amplification, ExcitationField, NbCharges], y];
(* Graphic representation of the system *)
SystemGraphics[ChargeSeparation_, FOV_, NbCharges_] = Hold[
  Graphics[{
    RGBColor[{1, 0.84, 0}], Rectangle[{-ChargeSeparation/2, 0}, {ChargeSeparation/2, GoldThickness}]
    , RGBColor[{0, 0, 0}], Line[{{-ChargeSeparation/2, 0}, {-ChargeSeparation/2, GoldThickness}}, {ChargeSeparation/2, GoldThickness}, {ChargeSeparation/2, 0}, {-ChargeSeparation/2, 0}]
    , RGBColor[ {.5, .5, .5}], Opacity[.2], Rectangle[{-FOV, 0}, {FOV, -FOV/OutputRatio}], Opacity[1], Line[{{-FOV, 0}, {FOV, 0}}]
    , RGBColor[{0, 0, 1}], PointSize[.01], Table[Point[{-ChargeSeparation/2, i * GoldThickness / (NbCharges + 1)}], {i, 1, NbCharges}]
    , RGBColor[{1, 0, 0}], PointSize[.01], Table[Point[+ChargeSeparation/2, i * GoldThickness / (NbCharges + 1)}], {i, 1, NbCharges}]
    , RGBColor[{0, 0, 1}], Text[Style["-", 20, Bold], {-ChargeSeparation/2 + 10, GoldThickness/2}]
    , RGBColor[{1, 0, 0}], Text[Style["+", 20, Bold], {+ChargeSeparation/2 - 10, GoldThickness/2}]
  ]
];
(* Field components and resulting SHG amplitude at the crystal surface *)
Manipulate[
  Grid[{
    {
      Plot[{ExTotal[x, y, ChargeSeparation, Amplification, ExcitationField, NbCharges]}, {x, -FOV, FOV}, PlotRange -> All, ImageSize -> {OutputSize, OutputSize/OutputRatio}]
      , Plot[{EyTotal[x, y, ChargeSeparation, Amplification, ExcitationField, NbCharges]}, {x, -FOV, FOV}, PlotRange -> All, ImageSize -> {OutputSize, OutputSize/OutputRatio}]
    }, {
      Plot[{ExTotal[x, y, ChargeSeparation, Amplification, ExcitationField, NbCharges]^4}, {x, -FOV, FOV}, PlotRange -> All, ImageSize -> {OutputSize, OutputSize/OutputRatio}]
      , Plot[{EyTotal[x, y, ChargeSeparation, Amplification, ExcitationField, NbCharges]^4}, {x, -FOV, FOV}, PlotRange -> All, ImageSize -> {OutputSize, OutputSize/OutputRatio}]
    }
  ]
], {{y, 0, "y"}, -FOV, FOV, 5, Appearance -> "Labeled"}
, {{FOV, 200, "FOV"}, 2000, 50, Appearance -> "Labeled"}
, {{ExcitationField, 1, "ExcitationField"}, 0, 1, 1, Appearance -> "Labeled"}
, {{NbCharges, 3, "NbCharges"}, 0, 100, 1, Appearance -> "Labeled"}
, {{ChargeSeparation, 150, "ChargeSeparation"}, 0, 1000, 10, Appearance -> "Labeled"}
, {{Amplification, 4, "Amplification"}, 0, 100, .1, Appearance -> "Labeled"}
, ContinuousAction -> False, TrackedSymbols -> True]

```

(\* Field components and derivatives around the crystal surface \*)

```

Manipulate[
  Grid[
    {
      Show[
        Quiet@DensityPlot[
          ExTotal[x, y, ChargeSeparation, Amplification, ExcitationField, NbCharges]
          , {x, -FOV, FOV}, {y, -FOV/OutputRatio, FOV/OutputRatio}, AspectRatio -> 1/OutputRatio, ColorFunction -> "TemperatureMap", ClippingStyle -> Automatic, PlotPoints -> Discretization
        ], Quiet@StreamPlot[
          {ExTotal[x, y, ChargeSeparation, Amplification, ExcitationField, NbCharges], EyTotal[x, y, ChargeSeparation, Amplification, ExcitationField, NbCharges]}
          , {x, -FOV, FOV}, {y, -FOV/OutputRatio, FOV/OutputRatio}, AspectRatio -> 1/OutputRatio, StreamPoints -> Medium
        ], ReleaseHold[SystemGraphics[ChargeSeparation, FOV, NbCharges]], ImageSize -> {OutputSize, OutputSize/2}, FrameTicksStyle -> Directive[Bold, 14]
      ], Show[
        Quiet@DensityPlot[
          EyTotal[x, y, ChargeSeparation, Amplification, ExcitationField, NbCharges]
          , {x, -FOV, FOV}, {y, -FOV/OutputRatio, FOV/OutputRatio}, AspectRatio -> 1/OutputRatio, ColorFunction -> "TemperatureMap", ClippingStyle -> Automatic, PlotPoints -> Discretization
        ], Quiet@StreamPlot[
          {ExTotal[x, y, ChargeSeparation, Amplification, ExcitationField, NbCharges], EyTotal[x, y, ChargeSeparation, Amplification, ExcitationField, NbCharges]}
          , {x, -FOV, FOV}, {y, -FOV/OutputRatio, FOV/OutputRatio}, AspectRatio -> 1/OutputRatio, StreamPoints -> Medium
        ], ReleaseHold[SystemGraphics[ChargeSeparation, FOV, NbCharges]], ImageSize -> {OutputSize, OutputSize/OutputRatio}, FrameTicksStyle -> Directive[Bold, 14]
      ]
    ]
  ], {
    Show[
      Quiet@DensityPlot[
        dExdx[x, y, ChargeSeparation, Amplification, ExcitationField, NbCharges]
        , {x, -FOV, FOV}, {y, -FOV/OutputRatio, FOV/OutputRatio}, AspectRatio -> 1/OutputRatio, ColorFunction -> "TemperatureMap", ClippingStyle -> Automatic, PlotPoints -> Discretization
      ], Quiet@StreamPlot[
        {ExTotal[x, y, ChargeSeparation, Amplification, ExcitationField, NbCharges], EyTotal[x, y, ChargeSeparation, Amplification, ExcitationField, NbCharges]}
        , {x, -FOV, FOV}, {y, -FOV/OutputRatio, FOV/OutputRatio}, AspectRatio -> 1/OutputRatio, StreamPoints -> Medium
      ], ReleaseHold[SystemGraphics[ChargeSeparation, FOV, NbCharges]], ImageSize -> {OutputSize, OutputSize/2}, FrameTicksStyle -> Directive[Bold, 14]
    ], Show[
      Quiet@DensityPlot[
        dEydx[x, y, ChargeSeparation, Amplification, ExcitationField, NbCharges]
        , {x, -FOV, FOV}, {y, -FOV/OutputRatio, FOV/OutputRatio}, AspectRatio -> 1/OutputRatio, ColorFunction -> "TemperatureMap", ClippingStyle -> Automatic, PlotPoints -> Discretization
      ], Quiet@StreamPlot[
        {ExTotal[x, y, ChargeSeparation, Amplification, ExcitationField, NbCharges], EyTotal[x, y, ChargeSeparation, Amplification, ExcitationField, NbCharges]}
        , {x, -FOV, FOV}, {y, -FOV/OutputRatio, FOV/OutputRatio}, AspectRatio -> 1/OutputRatio, StreamPoints -> Medium
      ], ReleaseHold[SystemGraphics[ChargeSeparation, FOV, NbCharges]], ImageSize -> {OutputSize, OutputSize/OutputRatio}, FrameTicksStyle -> Directive[Bold, 14]
    ]
  ]
  ], {
    Show[
      Quiet@DensityPlot[
        dExdy[x, y, ChargeSeparation, Amplification, ExcitationField, NbCharges]
        , {x, -FOV, FOV}, {y, -FOV/OutputRatio, FOV/OutputRatio}, AspectRatio -> 1/OutputRatio, ColorFunction -> "TemperatureMap", ClippingStyle -> Automatic, PlotPoints -> Discretization
      ], Quiet@StreamPlot[
        {ExTotal[x, y, ChargeSeparation, Amplification, ExcitationField, NbCharges], EyTotal[x, y, ChargeSeparation, Amplification, ExcitationField, NbCharges]}
        , {x, -FOV, FOV}, {y, -FOV/OutputRatio, FOV/OutputRatio}, AspectRatio -> 1/OutputRatio, StreamPoints -> Medium
      ], ReleaseHold[SystemGraphics[ChargeSeparation, FOV, NbCharges]], ImageSize -> {OutputSize, OutputSize/OutputRatio}, FrameTicksStyle -> Directive[Bold, 14]
    ]
  ]
  ]

```

```

], ReleaseHold[SystemGraphics[ChargeSeparation, FOV, NbCharges]], ImageSize -> {OutputSize, OutputSize/2}, FrameTicksStyle -> Directive[Bold, 14]
], Show[
Quiet@DensityPlot[
  dEydy[x, y, ChargeSeparation, Amplification, ExcitationField, NbCharges]
  , {x, -FOV, FOV}, {y, -FOV/OutputRatio, FOV/OutputRatio}, AspectRatio -> 1/OutputRatio, ColorFunction -> "TemperatureMap", ClippingStyle -> Automatic, PlotPoints -> Discretization
], Quiet@StreamPlot[
  {ExTotal[x, y, ChargeSeparation, Amplification, ExcitationField, NbCharges], EyTotal[x, y, ChargeSeparation, Amplification, ExcitationField, NbCharges]}
  , {x, -FOV, FOV}, {y, -FOV/OutputRatio, FOV/OutputRatio}, AspectRatio -> 1/OutputRatio, StreamPoints -> Medium
], ReleaseHold[SystemGraphics[ChargeSeparation, FOV, NbCharges]], ImageSize -> {OutputSize, OutputSize/OutputRatio}, FrameTicksStyle -> Directive[Bold, 14]
]
}
}]
, {{FOV, 200, "FOV"}, 2000, 50, Appearance -> "Labeled"}
, {{ExcitationField, 0, "ExcitationField"}, 0, 1, 1, Appearance -> "Labeled"}
, {{NbCharges, 10, "NbCharges"}, 0, 100, 1, Appearance -> "Labeled"}
, {{Discretization, 75, "Discretization"}, 0, 50, 5, Appearance -> "Labeled"}
, {{ChargeSeparation, 150, "ChargeSeparation"}, 0, 1000, 10, Appearance -> "Labeled"}
, {{Amplification, 5, "Amplification"}, 0, 100, .1, Appearance -> "Labeled"}
, ContinuousAction -> False, TrackedSymbols -> True
]
Export["WireField.jpg", %, ImageResolution -> 300, "CompressionLevel" -> 0];

```



# Bibliography

- [1] U. Leonhardt. “Optical metamaterials: Invisibility cup”. In: *Nature Photonics* 1 (2007), p. 207. DOI: [10.1038/nphoton.2007.38](https://doi.org/10.1038/nphoton.2007.38).
- [2] S. A. Maier. *Plasmonics: Fundamentals and Applications*. Springer, 2007. URL: <http://www.amazon.com/dp/1441941134>.
- [3] G. Mie. “Beiträge zur Optik trüber Medien, speziell kolloidaler Metallösungen”. In: *Annalen der Physik* 330.3 (1908), p. 377. DOI: [10.1002/andp.19083300302](https://doi.org/10.1002/andp.19083300302).
- [4] V. G. Veselago. “The electrodynamics of substances with simultaneously negative values of  $\epsilon$  and  $\mu$ ”. In: *Soviet Physics Uspekhi* 10.4 (1968), p. 509. DOI: [10.1070/PU1968v010n04ABEH003699](https://doi.org/10.1070/PU1968v010n04ABEH003699).
- [5] J. Pendry et al. “Magnetism from conductors and enhanced nonlinear phenomena”. In: *IEEE Transactions on Microwave Theory and Techniques* 47.11 (1999), p. 2075. DOI: [10.1109/22.798002](https://doi.org/10.1109/22.798002).
- [6] D. R. Smith et al. “Composite medium with simultaneously negative permeability and permittivity”. In: *Physical Review Letters* 84.18 (2000), p. 4184. DOI: [10.1103/PhysRevLett.84.4184](https://doi.org/10.1103/PhysRevLett.84.4184).
- [7] D. R. Smith, J. B. Pendry, and M. C. K. Wiltshire. “Metamaterials and negative refractive index”. In: *Science* 305.5685 (2004), p. 788. DOI: [10.1126/science.1096796](https://doi.org/10.1126/science.1096796).
- [8] C. M. Soukoulis, S. Linden, and M. Wegener. “Negative refractive index at optical wavelengths”. In: *Science* 315.5808 (2007), p. 47. DOI: [10.1126/science.1136481](https://doi.org/10.1126/science.1136481).
- [9] C. Soukoulis, M. Kafesaki, and E. N. Economou. “Negative-index materials: New frontiers in optics”. In: *Advanced Materials* 18.15 (2006), p. 1941. DOI: [10.1002/adma.200600106](https://doi.org/10.1002/adma.200600106).
- [10] V. M. Shalaev. “Optical negative-index metamaterials”. In: *Nature Photonics* 1.1 (2007), p. 41. DOI: [10.1038/nphoton.2006.49](https://doi.org/10.1038/nphoton.2006.49).
- [11] S. Linden and M. Wegener. “Metamaterialien werden „sichtbar“”. In: *Physik Journal* 5.12 (2006), p. 29. URL: <http://www.pro-physik.de/details/articlePdf/1105495/issue.html>.
- [12] U. Kreibig and P. Zacharias. “Surface plasma resonances in small spherical silver and gold particles”. In: *Zeitschrift für Physik A: Hadrons and Nuclei* 231 (1970), p. 128. DOI: [10.1007/BF01392504](https://doi.org/10.1007/BF01392504).

- [13] M.-C. Daniel and D. Astruc. “Gold nanoparticles: Assembly, supramolecular chemistry, quantum-size-related properties, and applications toward biology, catalysis, and nanotechnology”. In: *Chemical Reviews* 104.1 (2004), p. 293. DOI: [10.1021/cr030698+](https://doi.org/10.1021/cr030698+).
- [14] V. A. Podolskiy, A. K. Sarychev, and V. M. Shalaev. “Plasmon modes and negative refraction in metal nanowire composites”. In: *Optics Express* 11.7 (2003), p. 735. DOI: [10.1364/OE.11.000735](https://doi.org/10.1364/OE.11.000735).
- [15] V. A. Podolskiy et al. “Resonant light interaction with plasmonic nanowire systems”. In: *Journal of Optics A: Pure and Applied Optics* 7.2 (2005), S32. DOI: [10.1088/1464-4258/7/2/004](https://doi.org/10.1088/1464-4258/7/2/004).
- [16] S. Linden et al. “Magnetic response of metamaterials at 100 terahertz”. In: *Science* 306.5700 (2004), p. 1351. DOI: [10.1126/science.1105371](https://doi.org/10.1126/science.1105371).
- [17] S. Zhang et al. “Near-infrared double negative metamaterials”. In: *Optics Express* 13.13 (2005), p. 4922. DOI: [10.1364/OPEX.13.004922](https://doi.org/10.1364/OPEX.13.004922).
- [18] G. Dolling et al. “Simultaneous negative phase and group velocity of light in a metamaterial”. In: *Science* 312.5775 (2006), p. 892. DOI: [10.1126/science.1126021](https://doi.org/10.1126/science.1126021).
- [19] M. S. Rill et al. “Photonic metamaterials by direct laser writing and silver chemical vapour deposition”. In: *Nature Materials* 7.7 (2008), p. 543. DOI: [10.1038/nmat2197](https://doi.org/10.1038/nmat2197).
- [20] H. Schweizer et al. “Negative permeability around 630 nm in nanofabricated vertical meander metamaterials”. In: *Physica Status Solidi A: Applications and materials science* 204 (2007), p. 3886. DOI: [10.1002/pssa.200776412](https://doi.org/10.1002/pssa.200776412).
- [21] G. Dolling et al. “Cut-wire pairs and plate pairs as magnetic atoms for optical metamaterials”. In: *Optics Express* 30.23 (2005), p. 3198. DOI: [10.1364/OL.30.003198](https://doi.org/10.1364/OL.30.003198).
- [22] J. B. Pendry et al. “Extremely low frequency plasmons in metallic mesostructures”. In: *Physical Review Letters* 76.25 (1996), p. 4773. DOI: [10.1103/PhysRevLett.76.4773](https://doi.org/10.1103/PhysRevLett.76.4773).
- [23] J. B. Pendry, D. Schurig, and D. R. Smith. “Controlling electromagnetic fields”. In: *Science* 312.5781 (2006), p. 1780. DOI: [10.1126/science.1125907](https://doi.org/10.1126/science.1125907).
- [24] D. Schurig et al. “Metamaterial electromagnetic cloak at microwave frequencies”. In: *Science* 314.5801 (2006), p. 977. DOI: [10.1126/science.1133628](https://doi.org/10.1126/science.1133628).
- [25] J. K. Rowling. *Harry Potter and the philosopher's stone*. Bloomsbury, 1997. ISBN: 0747532699. URL: <http://www.amazon.com/dp/0747532699>.
- [26] J. Valentine et al. “An optical cloak made of dielectrics”. In: *Nature Materials* 8.7 (2009), p. 568. DOI: [10.1038/nmat2461](https://doi.org/10.1038/nmat2461).
- [27] J. B. Pendry. “Negative refraction makes a perfect lens”. In: *Physical Review Letters* 85.18 (2000), p. 3966. DOI: [10.1103/PhysRevLett.85.3966](https://doi.org/10.1103/PhysRevLett.85.3966).
- [28] N. Fang et al. “Sub-diffraction-limited optical imaging with a silver superlens”. In: *Science* 308.5721 (2005), p. 534. DOI: [10.1126/science.1108759](https://doi.org/10.1126/science.1108759).
- [29] Z. Liu et al. “Far-field optical hyperlens magnifying sub-diffraction-limited objects”. In: *Science* 315.5819 (2007), p. 1686. DOI: [10.1126/science.1137368](https://doi.org/10.1126/science.1137368).

- [30] C. L. Baciú et al. “Protein-membrane interaction probed by single plasmonic nanoparticles”. In: *Nano Letters* 8 (2008), p. 1724. DOI: [10.1021/nl080805l](https://doi.org/10.1021/nl080805l).
- [31] N. Liu et al. “Planar metamaterial analogue of electromagnetically induced transparency for plasmonic sensing”. In: *Nano Letters* 10 (2010), p. 1103. DOI: [10.1021/nl902621d](https://doi.org/10.1021/nl902621d).
- [32] P. Zijlstra, J. W. M. Chon, and M. Gu. “Five-dimensional optical recording mediated by surface plasmons in gold nanorods”. In: *Nature* 459 (2009), p. 410. DOI: [10.1038/nature08053](https://doi.org/10.1038/nature08053).
- [33] D. Brinks et al. “Visualizing and controlling vibrational wave packets of single molecules”. In: *Nature* 465 (2010), p. 905. DOI: [10.1038/nature09110](https://doi.org/10.1038/nature09110).
- [34] O. L. Muskens et al. “Strong enhancement of the radiative decay rate of emitters by single plasmonic nanoantennas”. In: *Nano Letters* 7 (2007), p. 2871. DOI: [10.1021/nl0715847](https://doi.org/10.1021/nl0715847).
- [35] M. Pfeiffer et al. “Enhancing the optical excitation efficiency of a single self-assembled quantum dot with a plasmonic nanoantenna”. In: *Nano Letters* 10 (2010), p. 4555. DOI: [10.1021/nl102548t](https://doi.org/10.1021/nl102548t).
- [36] C. Loo et al. “Immunotargeted nanoshells for integrated cancer imaging and therapy”. In: *Nano Letters* 5 (2005), p. 709. DOI: [10.1021/nl050127s](https://doi.org/10.1021/nl050127s).
- [37] H. A. Atwater and A. Polman. “Plasmonics for improved photovoltaic devices”. In: *Nature Materials* 9 (2010), p. 205. DOI: [10.1038/nmat2629](https://doi.org/10.1038/nmat2629).
- [38] M. A. Green and S. Pillai. “Harnessing plasmonics for solar cells”. In: *Nature Photonics* 6 (2012), p. 130. DOI: [10.1038/nphoton.2012.30](https://doi.org/10.1038/nphoton.2012.30).
- [39] N. Engheta. “Circuits with light at nanoscales: Optical nanocircuits inspired by metamaterials”. In: *Science* 317 (2007), p. 1698. DOI: [10.1126/science.1133268](https://doi.org/10.1126/science.1133268).
- [40] N. I. Zheludev and Y. S. Kivshar. “From metamaterials to metadevices”. In: *Nature Materials* 11 (2012), p. 917. DOI: [10.1038/nmat3431](https://doi.org/10.1038/nmat3431).
- [41] Y. Gong et al. “Highly flexible all-optical metamaterial absorption switching assisted by Kerr-nonlinear effect”. In: *Optics Express* 19 (2011), p. 10193. DOI: [10.1364/OE.19.010193](https://doi.org/10.1364/OE.19.010193).
- [42] F. Zhang et al. “Ultrafast all-optical tunable Fano resonance in nonlinear metamaterials”. In: *Applied Physics Letters* 102 (2013), p. 181109. DOI: [10.1063/1.4804436](https://doi.org/10.1063/1.4804436).
- [43] P. A. Franken et al. “Generation of optical harmonics”. In: *Physical Review Letters* 7.4 (1961), p. 118. DOI: [10.1103/PhysRevLett.7.118](https://doi.org/10.1103/PhysRevLett.7.118).
- [44] N. Bloembergen. *Nonlinear optics*. 4th. World Scientific Publishing Company, 1996. ISBN: 9789810225995. URL: <http://www.amazon.com/dp/9810225997>.
- [45] Y. R. Shen. *The principles of nonlinear optics*. Wiley-Interscience, 2002. ISBN: 0471430803. URL: <http://www.amazon.com/dp/0471430803>.
- [46] R. W. Boyd. *Nonlinear optics*. 3rd. Academic Press, 2008. ISBN: 0123694701. URL: <http://www.amazon.com/dp/0123694701>.

- [47] K. H. Bennemann. *Nonlinear optics in metals*. Oxford University Press, USA, 1999. ISBN: 9780198518938. URL: <http://www.amazon.com/dp/0198518935>.
- [48] M. W. Klein et al. “Second-harmonic generation from magnetic metamaterials”. In: *Science* 313 (2006), p. 502. DOI: [10.1126/science.1129198](https://doi.org/10.1126/science.1129198).
- [49] M. W. Klein et al. “Experiments on second- and third-harmonic generation from magnetic metamaterials”. In: *Optics Express* 15.8 (2007), p. 5238. DOI: [10.1364/OE.15.005238](https://doi.org/10.1364/OE.15.005238).
- [50] R. Singh et al. “The impact of nearest neighbor interaction on the resonances in terahertz metamaterials”. In: *Applied Physics Letters* 94.2, 021116 (2009), p. 021116. DOI: [10.1063/1.3063051](https://doi.org/10.1063/1.3063051).
- [51] N. Liu and H. Giessen. “Coupling effects in optical metamaterials”. In: *Angewandte Chemie - International Edition* 49.51 (2010), p. 9838. DOI: [10.1002/anie.200906211](https://doi.org/10.1002/anie.200906211).
- [52] H. J. Simon, D. E. Mitchell, and J. G. Watson. “Optical second-harmonic generation with surface plasmons in silver films”. In: *Physical Review Letters* 33.26 (1974), p. 1531. DOI: [10.1103/PhysRevLett.33.1531](https://doi.org/10.1103/PhysRevLett.33.1531).
- [53] A. Lesuffleur, L. K. S. Kumar, and R. Gordon. “Enhanced second harmonic generation from nanoscale double-hole arrays in a gold film”. In: *Applied Physics Letters* 88 (2006), p. 261104. DOI: [10.1063/1.2218057](https://doi.org/10.1063/1.2218057).
- [54] J. A. H. van Nieuwstadt et al. “Strong modification of the nonlinear optical response of metallic subwavelength hole arrays”. In: *Physical Review Letters* 97.14 (2006), p. 146102. DOI: [10.1103/PhysRevLett.97.146102](https://doi.org/10.1103/PhysRevLett.97.146102).
- [55] N. Feth et al. “Second-harmonic generation from complementary split-ring resonators”. In: *Optics Letters* 33.17 (2008), p. 1975. DOI: [10.1364/OL.33.001975](https://doi.org/10.1364/OL.33.001975).
- [56] E. Kim et al. “Nonlinear optical spectroscopy of photonic metamaterials”. In: *Physical Review B* 78.11 (2008), p. 113102. DOI: [10.1103/PhysRevB.78.113102](https://doi.org/10.1103/PhysRevB.78.113102).
- [57] Y. Zeng et al. “Classical theory for second-harmonic generation from metallic nanoparticles”. In: *Physical Review B* 79.23 (2009), p. 235109. DOI: [10.1103/PhysRevB.79.235109](https://doi.org/10.1103/PhysRevB.79.235109).
- [58] F. B. P. Niesler et al. “Second-harmonic optical spectroscopy on split-ring-resonator arrays”. In: *Optics Letters* 36 (2011), p. 1533. DOI: [10.1364/OL.36.001533](https://doi.org/10.1364/OL.36.001533).
- [59] M. Lippitz, M. A. van Dijk, and M. Orrit. “Third-harmonic generation from single gold nanoparticles”. In: *Nano Letters* 5 (2005), p. 799. DOI: [10.1021/nl10502571](https://doi.org/10.1021/nl10502571).
- [60] B. K. Canfield et al. “Local field asymmetry drives second-harmonic generation in noncentrosymmetric nanodimers”. In: *Nano Letters* 7.5 (2007), p. 1251. DOI: [10.1021/nl10701253](https://doi.org/10.1021/nl10701253).
- [61] V. K. Valev et al. “Asymmetric optical second-harmonic generation from chiral G-shaped gold nanostructures”. In: *Physical Review Letters* 104 (2010), p. 127401. DOI: [10.1103/PhysRevLett.104.127401](https://doi.org/10.1103/PhysRevLett.104.127401).
- [62] M. P. Marder. *Condensed matter physics*. Wiley, 2010. ISBN: 0470617985. URL: <http://www.amazon.com/dp/0470617985>.

- [63] J. D. Jackson. *Classical electrodynamics*. 3rd. Wiley, 1998. ISBN: 047130932X. URL: <http://www.amazon.com/dp/047130932X>.
- [64] D. J. Griffiths. *Introduction to electrodynamics*. 3rd. Benjamin Cummings, 1999. ISBN: 013805326X. URL: <http://www.amazon.com/dp/013805326X>.
- [65] P. Drude. “Zur Elektronentheorie der Metalle”. In: *Annalen der Physik* 306.3 (1900), p. 566. DOI: [10.1002/andp.19003060312](https://doi.org/10.1002/andp.19003060312).
- [66] N. W. Ashcroft and N. D. Mermin. *Solid state physics*. Brooks Cole, 1976. ISBN: 0030839939. URL: <http://www.amazon.com/dp/0030839939>.
- [67] P. B. Johnson and R. W. Christy. “Optical constants of the noble metals”. In: *Physical Review B* 6.12 (1972), p. 4370. DOI: [10.1103/PhysRevB.6.4370](https://doi.org/10.1103/PhysRevB.6.4370).
- [68] F. Reinert and S. Hüfner. “Photoemission spectroscopy – From early days to recent applications”. In: *New Journal of Physics* 7 (2005), p. 97. DOI: [10.1088/1367-2630/7/1/097](https://doi.org/10.1088/1367-2630/7/1/097).
- [69] N. E. Christensen and B. O. Seraphin. “Relativistic band calculation and the optical properties of gold”. In: *Physical Review B* 4 (1971), p. 3321. DOI: [10.1103/PhysRevB.4.3321](https://doi.org/10.1103/PhysRevB.4.3321).
- [70] R. Keyling. “Ab-initio Berechnung der ultraschnellen Dynamik angeregter Elektronen in Volumen- und Oberflächenzuständen von Metallen”. PhD thesis. Freie Universität Berlin, 2002. URL: [http://www.diss.fu-berlin.de/diss/receive/FUDISS\\_thesis\\_000000000707](http://www.diss.fu-berlin.de/diss/receive/FUDISS_thesis_000000000707).
- [71] J. Pendry. “Photonics: Metamaterials in the sunshine”. In: *Nature Materials* 5 (2006), p. 599. DOI: [10.1038/nmat1697](https://doi.org/10.1038/nmat1697).
- [72] K. L. Kelly et al. “The optical properties of metal nanoparticles: The influence of size, shape, and dielectric environment”. In: *Journal of Physical Chemistry B* 107 (2003), p. 668. DOI: [10.1021/jp026731y](https://doi.org/10.1021/jp026731y).
- [73] U. Kreibig and M. Vollmer. *Optical properties of metal clusters*. 1st ed. Springer, 1995. ISBN: 9783540578369. URL: <http://www.amazon.com/dp/3540578366>.
- [74] A. Gonzalez and C. Noguez. “Influence of morphology on the optical properties of metal nanoparticles”. In: *Journal of Computational and Theoretical Nanoscience* 4 (2007), p. 231. DOI: [doi:10.1166/jctn.2007.005](https://doi.org/10.1166/jctn.2007.005).
- [75] E. C. Stoner. “The demagnetizing factors for ellipsoids”. In: *Philosophical Magazine Series* 7 36 (1945), p. 803. DOI: [10.1080/14786444508521510](https://doi.org/10.1080/14786444508521510).
- [76] J. A. Osborn. “Demagnetizing factors of the general ellipsoid”. In: *Physical Review* 67 (1945), p. 351. DOI: [10.1103/PhysRev.67.351](https://doi.org/10.1103/PhysRev.67.351).
- [77] E. David. “Deutung der Anomalien der optischen Konstanten dünner Metallschichten”. In: *Zeitschrift für Physik A: Hadrons and Nuclei* 114 (1939), p. 389. DOI: [10.1007/BF01329519](https://doi.org/10.1007/BF01329519).
- [78] P. Bharadwaj, B. Deutsch, and L. Novotny. “Optical antennas”. In: *Advances in Optics and Photonics* 1 (2009), p. 438. DOI: [10.1364/AOP.1.000438](https://doi.org/10.1364/AOP.1.000438).

- [79] L. Novotny and N. van Hulst. “Antennas for light”. In: *Nature Photonics* 5 (2011), p. 83. DOI: [10.1038/nphoton.2010.237](https://doi.org/10.1038/nphoton.2010.237).
- [80] C. F. Bohren and D. R. Huffman. *Absorption and scattering of light by small particles*. Wiley-VCH, 1998. ISBN: 0471293407. URL: <http://www.amazon.com/dp/0471293407>.
- [81] M. Husnik et al. “Quantitative experimental determination of scattering and absorption cross-section spectra of individual optical metallic nanoantennas”. In: *Physical Review Letters* 109 (2012), p. 233902. DOI: [10.1103/PhysRevLett.109.233902](https://doi.org/10.1103/PhysRevLett.109.233902).
- [82] J. Gersten. “Surface enhanced Raman scattering”. In: ed. by R. Chang and T. Furtak. Plenum Press, New York, 1982. Chap. Surface shape resonances. ISBN: 0306409070. URL: <http://www.amazon.com/dp/0306409070>.
- [83] U. Kreibig, B. Schmitz, and H. D. Breuer. “Separation of plasmon-polariton modes of small metal particles”. In: *Physical Review B* 36 (1987), p. 5027. DOI: [10.1103/PhysRevB.36.5027](https://doi.org/10.1103/PhysRevB.36.5027).
- [84] U. Kreibig. “Small silver particles in photosensitive glass: Their nucleation and growth”. In: *Applied Physics A: Materials & Processing* 10 (1976), p. 255. DOI: [10.1007/BF00897225](https://doi.org/10.1007/BF00897225).
- [85] L. Novotny. “Effective wavelength scaling for optical antennas”. In: *Physical Review Letters* 98 (26 2007), p. 266802. DOI: [10.1103/PhysRevLett.98.266802](https://doi.org/10.1103/PhysRevLett.98.266802).
- [86] A. Taflove and S. C. Hagness. *Computational electrodynamics: The finite-difference time-domain method*. 3rd. Artech House, 2005. ISBN: 9781580538329. URL: <http://www.amazon.com/dp/1580538320>.
- [87] B. T. Draine and P. J. Flatau. “Discrete-dipole approximation for scattering calculations”. In: *Journal of the Optical Society of America A* 11 (1994), p. 1491. DOI: [10.1364/JOSAA.11.001491](https://doi.org/10.1364/JOSAA.11.001491).
- [88] J. Katsikadelis. *Boundary elements: Theory and applications*. Elsevier Science, 2002. ISBN: 0080441076. URL: <http://www.amazon.com/dp/0080441076>.
- [89] C. Altman and K. Suchy. *Reciprocity, spatial mapping and time reversal in electromagnetics (Developments in electromagnetic theory and applications)*. Springer, 1991. ISBN: 0792313399. URL: <http://www.amazon.com/dp/0792313399>.
- [90] L. Li. “Formulation and comparison of two recursive matrix algorithms for modeling layered diffraction gratings”. In: *Journal of the Optical Society of America A* 13 (1996), p. 1024. DOI: [10.1364/JOSAA.13.001024](https://doi.org/10.1364/JOSAA.13.001024).
- [91] L. Li. “Fourier modal method for crossed anisotropic gratings with arbitrary permittivity and permeability tensors”. In: *Journal of Optics A: Pure and Applied Optics* 5 (2003), p. 345. DOI: [10.1088/1464-4258/5/4/307](https://doi.org/10.1088/1464-4258/5/4/307).
- [92] E. J. Heilweil and R. M. Hochstrasser. “Nonlinear spectroscopy and picosecond transient grating study of colloidal gold”. In: *Journal of Chemical Physics* 82 (1985), p. 4762. DOI: [10.1063/1.448693](https://doi.org/10.1063/1.448693).
- [93] C. Sönnichsen et al. “Drastic reduction of plasmon damping in gold nanorods”. In: *Physical Review Letters* 88 (7 2002), p. 077402. DOI: [10.1103/PhysRevLett.88.077402](https://doi.org/10.1103/PhysRevLett.88.077402).

- [94] A. Kawabata and R. Kubo. “Electronic properties of fine metallic particles. II. Plasma resonance absorption”. In: *Journal of the Physical Society of Japan* 21 (1966), p. 1765. DOI: [10.1143/JPSJ.21.1765](https://doi.org/10.1143/JPSJ.21.1765).
- [95] J. Crowell and R. H. Ritchie. “Radiative decay of Coulomb-stimulated plasmons in spheres”. In: *Physical Review* 172 (1968), p. 436. DOI: [10.1103/PhysRev.172.436](https://doi.org/10.1103/PhysRev.172.436).
- [96] T. Zentgraf. “Optische Eigenschaften und Dynamik von photonisch gekoppelten Metall-Partikel-Plasmonen”. ger. PhD thesis. Universität Stuttgart, 2006. URL: <http://elib.uni-stuttgart.de/opus/volltexte/2006/2764>.
- [97] H. Hövel et al. “Width of cluster plasmon resonances: Bulk dielectric functions and chemical interface damping”. In: *Physical Review B* 48 (1993), p. 18178. DOI: [10.1103/PhysRevB.48.18178](https://doi.org/10.1103/PhysRevB.48.18178).
- [98] A. Matthiessen and C. Vogt. “On the influence of temperature on the electric conducting-power of alloys”. In: *Philosophical Transactions of the Royal Society of London* 154 (1864), p. 167. URL: <http://www.jstor.org/stable/108867>.
- [99] L. Genzel and U. Kreibig. “Dielectric function and infrared absorption of small metal particles”. In: *Zeitschrift für Physik B: Condensed Matter* 37 (1980), p. 93. DOI: [10.1007/BF01365365](https://doi.org/10.1007/BF01365365).
- [100] B. Persson. “Polarizability of small spherical metal particles: Influence of the matrix environment”. In: *Surface Science* 281 (1993), p. 153. DOI: [10.1016/0039-6028\(93\)90865-H](https://doi.org/10.1016/0039-6028(93)90865-H).
- [101] K.-P. Charlé et al. “The Surface Plasmon Resonance of Free and Embedded Ag-Clusters in the Size Range  $1,5 \text{ nm} < D < 30 \text{ nm}$ ”. In: *Crystal Research and Technology* 33 (1998), p. 1085. DOI: [10.1002/\(SICI\)1521-4079\(199810\)33:7/8<1085::AID-CRAT1085>3.0.CO;2-A](https://doi.org/10.1002/(SICI)1521-4079(199810)33:7/8<1085::AID-CRAT1085>3.0.CO;2-A).
- [102] U. Kreibig and L. Genzel. “Optical absorption of small metallic particles”. In: *Surface Science* 156 (1985), p. 678. DOI: [10.1016/0039-6028\(85\)90239-0](https://doi.org/10.1016/0039-6028(85)90239-0).
- [103] A. Wokaun, J. P. Gordon, and P. F. Liao. “Radiation damping in surface-enhanced Raman scattering”. In: *Physical Review Letters* 48 (14 1982), p. 957. DOI: [10.1103/PhysRevLett.48.957](https://doi.org/10.1103/PhysRevLett.48.957).
- [104] M. Meier and A. Wokaun. “Enhanced fields on large metal particles: Dynamic depolarization”. In: *Optics Letters* 8 (1983), p. 581. DOI: [10.1364/OL.8.000581](https://doi.org/10.1364/OL.8.000581).
- [105] S.-Y. Wang and L.-C. Chu. “Radiation damping in the scattering of light by a metal sphere”. In: *Physical Letters A* 115 (1986), p. 297. DOI: [10.1016/0375-9601\(86\)90557-8](https://doi.org/10.1016/0375-9601(86)90557-8).
- [106] L. Allen and J. H. Eberly. *Optical resonance and two-level atoms*. Dover Publications, 1987. ISBN: 0486655334. URL: <http://www.amazon.com/dp/0486655334>.
- [107] N. D. Lang and W. Kohn. “Theory of metal surfaces: Charge density and surface energy”. In: *Physical Review B* 1 (1970), p. 4555. DOI: [10.1103/PhysRevB.1.4555](https://doi.org/10.1103/PhysRevB.1.4555).
- [108] J. Tiggesbäumker et al. “Blue shift of the Mie plasma frequency in Ag clusters and particles”. In: *Physical Review A* 48 (3 1993), R1749. DOI: [10.1103/PhysRevA.48.R1749](https://doi.org/10.1103/PhysRevA.48.R1749).

- [109] M. Quinten et al. “Electromagnetic energy transport via linear chains of silver nanoparticles”. In: *Optics Letters* 23 (1998), p. 1331. DOI: [10.1364/OL.23.001331](https://doi.org/10.1364/OL.23.001331).
- [110] J.-C. Weeber et al. “Plasmon polaritons of metallic nanowires for controlling submicron propagation of light”. In: *Physical Review B* 60 (12 1999), p. 9061. DOI: [10.1103/PhysRevB.60.9061](https://doi.org/10.1103/PhysRevB.60.9061).
- [111] M. Meier, A. Wokaun, and P. F. Liao. “Enhanced fields on rough surfaces: dipolar interactions among particles of sizes exceeding the Rayleigh limit”. In: *Journal of the Optical Society of America B* 2 (1985), p. 931. DOI: [10.1364/JOSAB.2.000931](https://doi.org/10.1364/JOSAB.2.000931).
- [112] B. Lamprecht et al. “Metal nanoparticle gratings: Influence of dipolar particle interaction on the plasmon resonance”. In: *Physical Review Letters* 84 (2000), p. 4721. DOI: [10.1103/PhysRevLett.84.4721](https://doi.org/10.1103/PhysRevLett.84.4721).
- [113] R. W. Wood. “Anomalous diffraction gratings”. In: *Physical Review* 48 (12 1935), p. 928. DOI: [10.1103/PhysRev.48.928](https://doi.org/10.1103/PhysRev.48.928).
- [114] S. Zou, N. Janel, and G. C. Schatz. “Silver nanoparticle array structures that produce remarkably narrow plasmon lineshapes”. In: *Journal of Chemical Physics* 120 (2004), p. 10871. DOI: [10.1063/1.1760740](https://doi.org/10.1063/1.1760740).
- [115] T. H. Maiman. “Stimulated optical radiation in ruby”. In: *Nature* 187.4736 (1960), p. 493. DOI: [10.1038/187493a0](https://doi.org/10.1038/187493a0).
- [116] B. Lamprecht, A. Leitner, and F. Aussenegg. “SHG studies of plasmon dephasing in nanoparticles”. In: *Applied Physics B: Laser and Optics* 68 (1999), p. 419. DOI: [10.1007/s003400050643](https://doi.org/10.1007/s003400050643).
- [117] P. S. Pershan. “Nonlinear optical properties of solids: Energy considerations”. In: *Physical Review* 130 (1963), p. 919. DOI: [10.1103/PhysRev.130.919](https://doi.org/10.1103/PhysRev.130.919).
- [118] N. Bloembergen et al. “Optical second-harmonic generation in reflection from media with inversion symmetry”. In: *Physical Review* 174 (1968), p. 813. DOI: [10.1103/PhysRev.174.813](https://doi.org/10.1103/PhysRev.174.813).
- [119] P. Guyot-Sionnest and Y. R. Shen. “Bulk contribution in surface second-harmonic generation”. In: *Physical Review B* 38 (1988), p. 7985. DOI: [10.1103/PhysRevB.38.7985](https://doi.org/10.1103/PhysRevB.38.7985).
- [120] R. R. Birss. *Symmetry and magnetism*. 2nd. Elsevier Science Publishing Co Inc., U.S., 1966. ISBN: 9780720414530. URL: <http://www.amazon.com/dp/0720414539>.
- [121] P. Guyot-Sionnest, W. Chen, and Y. R. Shen. “General considerations on optical second-harmonic generation from surfaces and interfaces”. In: *Physical Review B* 33.12 (1986), p. 8254. DOI: [10.1103/PhysRevB.33.8254](https://doi.org/10.1103/PhysRevB.33.8254).
- [122] M. Göppert-Mayer. “Über Elementarakte mit zwei Quantensprüngen”. In: *Annalen der Physik* 401 (1931), p. 273. DOI: [10.1002/andp.19314010303](https://doi.org/10.1002/andp.19314010303).
- [123] W. Kaiser and C. G. B. Garrett. “Two-photon excitation in  $\text{CaF}_2: \text{Eu}^{2+}$ ”. In: *Physical Review Letters* 7 (1961), p. 229. DOI: [10.1103/PhysRevLett.7.229](https://doi.org/10.1103/PhysRevLett.7.229).

- [124] P. Biagioni et al. “Dependence of the two-photon photoluminescence yield of gold nanostructures on the laser pulse duration”. In: *Physical Review B* 80 (2009), p. 045411. DOI: [10.1103/PhysRevB.80.045411](https://doi.org/10.1103/PhysRevB.80.045411).
- [125] A. Mooradian. “Photoluminescence of metals”. In: *Physical Review Letters* 22 (1969), p. 185. DOI: [10.1103/PhysRevLett.22.185](https://doi.org/10.1103/PhysRevLett.22.185).
- [126] K. Imura, T. Nagahara, and H. Okamoto. “Near-field two-photon-induced photoluminescence from single gold nanorods and imaging of plasmon modes”. In: *Journal of Physical Chemistry B* 109 (2005), p. 13214. DOI: [10.1021/jp051631o](https://doi.org/10.1021/jp051631o).
- [127] W. Gotschy et al. “Thin films by regular patterns of metal nanoparticles: Tailoring the optical properties by nanodesign”. In: *Applied Physics B: Laser and Optics* 63 (1996), p. 381. DOI: [10.1007/s003400050099](https://doi.org/10.1007/s003400050099).
- [128] N. Liu. “Three-dimensional optical metamaterials”. PhD thesis. Universität Stuttgart, 2009. URL: <http://elib.uni-stuttgart.de/opus/volltexte/2009/4522>.
- [129] A. Boltasseva and V. M. Shalaev. “Fabrication of optical negative-index metamaterials: Recent advances and outlook”. In: *Metamaterials* 2 (2008), p. 1. DOI: [10.1016/j.metmat.2008.03.004](https://doi.org/10.1016/j.metmat.2008.03.004).
- [130] M. Agio and A. Alù, eds. *Optical antennas*. Cambridge University Press, 2013. ISBN: 110701414X. URL: <http://www.amazon.com/dp/110701414X>.
- [131] H. Tuovinen et al. “Linear and second-order nonlinear optical properties of arrays of noncentrosymmetric gold nanoparticles”. In: *Journal of Nonlinear Optical Physics & Materials* 11 (2002), p. 421. DOI: [10.1142/S0218863502001103](https://doi.org/10.1142/S0218863502001103).
- [132] B. Canfield et al. “Linear and nonlinear optical responses influenced by broken symmetry in an array of gold nanoparticles”. In: *Optics Express* 12 (2004), p. 5418. DOI: [10.1364/OPEX.12.005418](https://doi.org/10.1364/OPEX.12.005418).
- [133] B. K. Canfield et al. “Polarization effects in the linear and nonlinear optical responses of gold nanoparticle arrays”. In: *Journal of Optics A: Pure and Applied Optics* 7 (2005), S110. DOI: [10.1088/1464-4258/7/2/015](https://doi.org/10.1088/1464-4258/7/2/015).
- [134] B. Wanklyn. “Flux growth of some complex oxide materials”. In: *Journal of Materials Science* 7 (1972), p. 813. DOI: [10.1007/BF00549910](https://doi.org/10.1007/BF00549910).
- [135] D. Prabhakaran et al. “Growth of large  $\text{La}_{1-x}\text{Sr}_x\text{MnO}_3$  single crystals under argon pressure by the floating-zone technique”. In: *Journal of Crystal Growth* 237 (2002), p. 806. DOI: [10.1016/S0022-0248\(01\)02035-8](https://doi.org/10.1016/S0022-0248(01)02035-8).
- [136] T. Katsufuji et al. “Dielectric and magnetic anomalies and spin frustration in hexagonal  $\text{RMnO}_3$  ( $R=\text{Y}$ ,  $\text{Yb}$ , and  $\text{Lu}$ )”. In: *Physical Review B* 64 (2001), p. 104419. DOI: [10.1103/PhysRevB.64.104419](https://doi.org/10.1103/PhysRevB.64.104419).
- [137] H. L. Yakel Jnr et al. “On the crystal structure of the manganese(III) trioxides of the heavy lanthanides and yttrium”. In: *Acta Crystallographica* 16 (1963), p. 957. DOI: [10.1107/S0365110X63002589](https://doi.org/10.1107/S0365110X63002589).
- [138] F. C. Lissalde and J. C. Peuzin. “A new surface effect exhibited by the ferroelectric  $\text{YMnO}_3$ ”. In: *Ferroelectrics* 4 (1972), p. 159. DOI: [10.1080/00150197208235758](https://doi.org/10.1080/00150197208235758).

- [139] M. Fiebig. “Revival of the magnetoelectric effect”. In: *Journal of Physics D: Applied Physics* 38 (2005), R123. DOI: [10.1088/0022-3727/38/8/R01](https://doi.org/10.1088/0022-3727/38/8/R01).
- [140] M. Fiebig et al. “Determination of the magnetic symmetry of hexagonal manganites by second harmonic generation”. In: *Physical Review Letters* 84.24 (2000), p. 5620. DOI: [10.1103/PhysRevLett.84.5620](https://doi.org/10.1103/PhysRevLett.84.5620).
- [141] M. Fiebig, T. Lottermoser, and R. V. Pisarev. “Spin-rotation phenomena and magnetic phase diagrams of hexagonal  $RMnO_3$ ”. In: *Journal of Applied Physics* 93 (2003), p. 8194. DOI: [10.1063/1.1544513](https://doi.org/10.1063/1.1544513).
- [142] D. Sa, R. Valentí, and C. Gros. “A generalized Ginzburg-Landau approach to second harmonic generation”. In: *European Physical Journal B - Condensed Matter and Complex Systems* 14 (2 2000), p. 301. DOI: [10.1007/s100510050133](https://doi.org/10.1007/s100510050133).
- [143] T. Lottermoser. “Elektrische und magnetische Ordnung hexagonaler Manganite”. PhD thesis. Universität Dortmund, 2002.
- [144] D. Kinloch and C. Birchenall. “Verneuil crystals of chromic oxide via the argon plasma”. In: *Journal of Crystal Growth* 19 (1973), p. 105. DOI: [10.1016/0022-0248\(73\)90017-1](https://doi.org/10.1016/0022-0248(73)90017-1).
- [145] I. Dzyaloshinskii. “A thermodynamic theory of “weak” ferromagnetism of antiferromagnetics”. In: *Journal of Physics and Chemistry of Solids* 4 (1958), p. 241. DOI: [10.1016/0022-3697\(58\)90076-3](https://doi.org/10.1016/0022-3697(58)90076-3).
- [146] I. E. Dzyaloshinskii. “On the magnetoelectric effect in antiferromagnets”. In: *Soviet Physics JETP-USSR* 10 (1960), p. 628.
- [147] E. B. Graham and R. E. Raab. “Magnetic effects in antiferromagnetic crystals in the electric quadrupole-magnetic dipole approximation”. In: *Philosophical Magazine B* 66 (1992), p. 269. DOI: [10.1080/13642819208224589](https://doi.org/10.1080/13642819208224589).
- [148] L. M. Corliss et al. “Magnetic structure of  $Cr_2O_3$ ”. In: *Journal of Applied Physics* 36 (1965), p. 1099. DOI: [10.1063/1.1714118](https://doi.org/10.1063/1.1714118).
- [149] T. H. O’Dell. *Electrodynamics of Magneto-electric Media*. Elsevier Science Publishing Co Inc., U.S., 1970. ISBN: 072041461X. URL: <http://www.amazon.com/dp/072041461X>.
- [150] B. Krichevtsov, V. Pavlov, and R. Pisarev. “Nonreciprocal optical effects in antiferromagnetic  $Cr_2O_3$  subjected to electric and magnetic fields”. In: *Soviet Physics JETP-USSR* 67 (1988), p. 378. URL: <http://www.jetp.ac.ru/cgi-bin/e/index/e/67/2/p378?alist>.
- [151] M. Fiebig. “Nichtlineare Spektroskopie und Topographie an antiferromagnetischen Domänen”. PhD thesis. Universität Dortmund, 1996.
- [152] M. Fiebig et al. “Domain topography of antiferromagnetic  $Cr_2O_3$  by second-harmonic generation”. In: *Applied Physics Letters* 66 (1995), p. 2906. DOI: [10.1063/1.113699](https://doi.org/10.1063/1.113699).
- [153] G. W. Fynn and W. J. A. Powell. *Cutting and polishing optical and electronic materials*. Adam Hilger, 1988. ISBN: 0852743734. URL: <http://www.amazon.com/dp/0852743734>.
- [154] C. Enkrich. “Magnetic metamaterials for photonics”. PhD thesis. Universität Karlsruhe, 2006. URL: <http://d-nb.info/980842522>.

- [155] D. Strickland and G. Mourou. “Compression of amplified chirped optical pulses”. In: *Optics Communications* 56 (1985), p. 219. ISSN: 0030-4018. DOI: [10.1016/0030-4018\(85\)90120-8](https://doi.org/10.1016/0030-4018(85)90120-8).
- [156] S. Backus et al. “High power ultrafast lasers”. In: *Review of Scientific Instruments* 69 (1998), p. 1207. DOI: [10.1063/1.1148795](https://doi.org/10.1063/1.1148795).
- [157] *Guide to streak cameras*. Hamamatsu Photonics K.K. 2008. URL: [http://sales.hamamatsu.com/assets/pdf/catsandguides/e\\_streakh.pdf](http://sales.hamamatsu.com/assets/pdf/catsandguides/e_streakh.pdf).
- [158] Y. Tsuchiya. “Advances in streak camera instrumentation for the study of biological and physical processes”. In: *IEEE Journal of Quantum Electronics* 20 (1984), p. 1516. DOI: [10.1109/JQE.1984.1072316](https://doi.org/10.1109/JQE.1984.1072316).
- [159] A. Velten et al. “Slow art with a trillion frames per second camera”. In: *ACM SIGGRAPH 2011 Posters*. SIGGRAPH '11. 2011, 13:1. ISBN: 978-1-4503-0971-4. DOI: [10.1145/2037715.2037730](https://doi.org/10.1145/2037715.2037730).
- [160] C. Rulliere, ed. *Femtosecond laser pulses: Principles and experiments*. Springer, 2010. ISBN: 1441918507. URL: <http://www.amazon.com/dp/1441918507>.
- [161] C. Daniel et al. “Deciphering the reaction dynamics underlying optimal control laser fields”. In: *Science* 299 (2003), p. 536. DOI: [10.1126/science.1078517](https://doi.org/10.1126/science.1078517).
- [162] F. Träger, ed. *Springer handbook of lasers and optics*. Springer, 2012. ISBN: 3642194087. URL: <http://www.amazon.com/dp/3642194087>.
- [163] R. Trebino. *Frequency-resolved optical gating: The measurement of ultrashort laser pulses*. Springer, 2002. ISBN: 1402070667. URL: <http://www.amazon.com/dp/1402070667>.
- [164] R. Trebino et al. “Measuring ultrashort laser pulses in the time-frequency domain using frequency-resolved optical gating”. In: *Review of Scientific Instruments* 68 (1997), p. 3277. DOI: [10.1063/1.1148286](https://doi.org/10.1063/1.1148286).
- [165] V. Petrov, F. Seifert, and F. Noack. “High repetition rate traveling wave optical parametric generator producing nearly bandwidth limited 50 fs infrared light pulses”. In: *Applied Physics Letters* 65 (1994), p. 268. DOI: [10.1063/1.112367](https://doi.org/10.1063/1.112367).
- [166] R. Laenen et al. “Parametric generation of femtosecond and picosecond pulses for spectroscopic applications”. In: *Journal of the Optical Society of America B* 10 (1993), p. 2151. DOI: [10.1364/JOSAB.10.002151](https://doi.org/10.1364/JOSAB.10.002151).
- [167] T. Günter. “Aufbau und Charakterisierung eines Femtosekunden-Lasersystems”. Diploma thesis. Universität Bonn, 2008.
- [168] R. Paschotta. *Encyclopedia of laser physics and technology*. Wiley-VCH, 2008. ISBN: 3527408282. URL: <http://www.amazon.com/dp/3527408282>.
- [169] A. E. Siegman. *Lasers*. University Science Books, 1986. ISBN: 0935702113. URL: <http://www.amazon.com/dp/0935702113>.
- [170] A. H. Firester, M. E. Heller, and P. Sheng. “Knife-edge scanning measurements of subwavelength focused light beams”. In: *Applied Optics* 16.7 (1977), p. 1971. DOI: [10.1364/AO.16.001971](https://doi.org/10.1364/AO.16.001971).

- [171] J. M. Khosroffian and B. A. Garetz. “Measurement of a Gaussian laser beam diameter through the direct inversion of knife-edge data”. In: *Applied Optics* 22.21 (1983), p. 3406. DOI: [10.1364/AO.22.003406](https://doi.org/10.1364/AO.22.003406).
- [172] W. Tievesch. “Verstärkung nichtlinear optischer Prozesse durch Metamaterialien”. Diploma thesis. Universität Bonn, 2012.
- [173] D. Meier. “Order parameters and domain topology in magnetically-induced ferroelectrics”. PhD thesis. Universität Bonn, 2009.
- [174] A. Habenicht. “Dynamik metallischer Nanotröpfchen”. PhD thesis. Universität Konstanz, 2007. URL: <http://nbn-resolving.de/urn:nbn:de:bsz:352-opus-58450>.
- [175] B. Bai et al. “Determination of the eigenpolarizations in arbitrary diffraction orders of planar periodic structures under arbitrary incidence”. In: *Physical Review A* 85 (2012), p. 053808. DOI: [10.1103/PhysRevA.85.053808](https://doi.org/10.1103/PhysRevA.85.053808).
- [176] F. Brown, R. E. Parks, and A. M. Sleeper. “Nonlinear optical reflection from a metallic boundary”. In: *Physical Review Letters* 14 (1965), p. 1029. DOI: [10.1103/PhysRevLett.14.1029](https://doi.org/10.1103/PhysRevLett.14.1029).
- [177] D. Krause, C. W. Teplin, and C. T. Rogers. “Optical surface second harmonic measurements of isotropic thin-film metals: Gold, silver, copper, aluminum, and tantalum”. In: *Journal of Applied Physics* 96 (2004), p. 3626. DOI: [10.1063/1.1786341](https://doi.org/10.1063/1.1786341).
- [178] C. Rockstuhl et al. “On the reinterpretation of resonances in split-ring-resonators at normal incidence”. In: *Optics Express* 14 (2006), p. 8827. DOI: [10.1364/OE.14.008827](https://doi.org/10.1364/OE.14.008827).
- [179] S. Linden et al. “Photonic metamaterials: Magnetism at optical frequencies”. In: *IEEE Journal of selected topics in quantum electronics* 12 (2006), p. 1097. DOI: [10.1109/JSTQE.2006.880600](https://doi.org/10.1109/JSTQE.2006.880600).
- [180] C. Rockstuhl et al. “Resonances of split-ring resonator metamaterials in the near infrared”. In: *Applied Physics B: Laser and Optics* 84 (2006), p. 219. DOI: [10.1007/s00340-006-2205-2](https://doi.org/10.1007/s00340-006-2205-2).
- [181] D. Meier et al. “Second harmonic generation on incommensurate structures: The case of multiferroic  $\text{MnWO}_4$ ”. In: *Physical Review B* 82 (2010), p. 155112. DOI: [10.1103/PhysRevB.82.155112](https://doi.org/10.1103/PhysRevB.82.155112).
- [182] J. Butet, K. Thyagarajan, and O. J. F. Martin. “Ultrasensitive optical shape characterization of gold nanoantennas using second harmonic generation”. In: *Nano Letters* 13 (2013), p. 1787. DOI: [10.1021/nl400393e](https://doi.org/10.1021/nl400393e).
- [183] B. K. Canfield et al. “A macroscopic formalism to describe the second-order nonlinear optical response of nanostructures”. In: *Journal of Optics A: Pure and Applied Optics* 8.4 (2006), S278. DOI: [10.1088/1464-4258/8/4/S30](https://doi.org/10.1088/1464-4258/8/4/S30).
- [184] M. Kauranen and S. Cattaneo. “Chapter 2: Polarization techniques for surface nonlinear optics”. In: *Progress in Optics*. Vol. 51. Progress in Optics. Elsevier, 2008, p. 69. DOI: [10.1016/S0079-6638\(07\)51002-4](https://doi.org/10.1016/S0079-6638(07)51002-4).
- [185] M. Zdanowicz et al. “Effective medium multipolar tensor analysis of second-harmonic generation from metal nanoparticles”. In: *New Journal of Physics* 13 (2011), p. 023025. DOI: [10.1088/1367-2630/13/2/023025](https://doi.org/10.1088/1367-2630/13/2/023025).

- [186] S. Cattaneo and M. Kauranen. “Polarization-based identification of bulk contributions in surface nonlinear optics”. In: *Physical Review B* 72.3 (2005), p. 033412. DOI: [10.1103/PhysRevB.72.033412](https://doi.org/10.1103/PhysRevB.72.033412).
- [187] F. J. Rodriguez et al. “Multipolar tensor analysis of second-order nonlinear optical response of surface and bulk of glass”. In: *Optics Express* 15.14 (2007), p. 8695. DOI: [10.1364/OE.15.008695](https://doi.org/10.1364/OE.15.008695).
- [188] F. J. Rodriguez, F. X. Wang, and M. Kauranen. “Calibration of the second-order nonlinear optical susceptibility of surface and bulk of glass”. In: *Optics Express* 16.12 (2008), p. 8704. DOI: [10.1364/OE.16.008704](https://doi.org/10.1364/OE.16.008704).
- [189] M. Born and E. Wolf. *Principles of Optics: Electromagnetic Theory of Propagation, Interference and Diffraction of Light*. Cambridge University Press, 1999. ISBN: 0521642221. URL: <http://www.amazon.com/dp/0521642221>.
- [190] T. Zentgraf et al. “Babinet’s principle for optical frequency metamaterials and nanoantennas”. In: *Physical Review B* 76.3 (2007), p. 033407. DOI: [10.1103/PhysRevB.76.033407](https://doi.org/10.1103/PhysRevB.76.033407).
- [191] C. Rockstuhl et al. “Resonances in complementary metamaterials and nanoapertures”. In: *Optics Express* 16 (2008), p. 2080. DOI: [10.1364/OE.16.002080](https://doi.org/10.1364/OE.16.002080).
- [192] S. K. Kurtz and T. T. Perry. “A powder technique for the evaluation of nonlinear optical materials”. In: *Journal of Applied Physics* 39 (1968), p. 3798. DOI: [10.1063/1.1656857](https://doi.org/10.1063/1.1656857).
- [193] Heraeus-Quarzglas. *Quartz glass Suprasil®1, Standard Optics Information*. URL: [http://optics.heraeus-quarzglas.com/en/productsapplications/productdetail\\_4101.aspx](http://optics.heraeus-quarzglas.com/en/productsapplications/productdetail_4101.aspx).
- [194] T. J. M. Boyd and J. J. Sanderson. *The Physics of Plasmas*. Cambridge University Press, 2003. ISBN: 9780521459129. URL: <http://www.amazon.com/dp/0521459125>.
- [195] *Optimal second-harmonic generation in split-ring resonator arrays*. Vol. 8623. Ultrafast Phenomena and Nanophotonics XVII. Proc. SPIE. 2013, pp. 86230L–9. DOI: [10.1117/12.2003279](https://doi.org/10.1117/12.2003279).
- [196] M. Gentile et al. “Investigation of the nonlinear optical properties of metamaterials by second harmonic generation”. In: *Applied Physics B: Laser and Optics* 105 (2011), p. 149. DOI: [10.1007/s00340-011-4766-y](https://doi.org/10.1007/s00340-011-4766-y).
- [197] J. Berthelot et al. “Silencing and enhancement of second-harmonic generation in optical gap antennas”. In: *Optics Express* 20 (2012), p. 10498. DOI: [10.1364/OE.20.010498](https://doi.org/10.1364/OE.20.010498).
- [198] R. Czaplicki et al. “Dipole limit in second-harmonic generation from arrays of gold nanoparticles”. In: *Optics Express* 19 (2011), p. 26866. DOI: [10.1364/OE.19.026866](https://doi.org/10.1364/OE.19.026866).
- [199] C. Awada et al. “Polarized second harmonic response of square, hexagonal and random arrays of gold metallic nanocylinders”. In: *Optical Materials* 33 (2011), p. 1440. DOI: [10.1016/j.optmat.2011.02.045](https://doi.org/10.1016/j.optmat.2011.02.045).
- [200] J.-S. Huang et al. “Atomically flat single-crystalline gold nanostructures for plasmonic nanocircuitry”. In: *Nature Communications* 1 (2010), p. 150. DOI: [10.1038/ncomms1143](https://doi.org/10.1038/ncomms1143).

- [201] B. Hecht et al. "Single crystalline optical antennas". In: *CLEO/Europe and EQEC 2011 Conference Digest*. 2011. URL: [http://www.opticsinfobase.org/abstract.cfm?URI=CLEO\\_Europe-2011-CK3\\_1](http://www.opticsinfobase.org/abstract.cfm?URI=CLEO_Europe-2011-CK3_1).

# Publications and Presentations

## Publications

- (1) M. Gentile, M. Hentschel, R. Taubert, H. Guo, H. Giessen, M. Fiebig, "Investigation of the nonlinear optical properties of metamaterials by second harmonic generation" In: *Applied Physics B* 105 (2011), pp. 149-162, DOI: [10.1007/s00340-011-4766-y](https://doi.org/10.1007/s00340-011-4766-y)

## Conference Contributions

- (5) DPG conference, Berlin (Germany), March 25<sup>th</sup>-30<sup>th</sup> 2012: Enhancement of non-linear effects using nano-wires, W. Tielech, M. Gentile, M. Hentschel, H. Giessen, and M. Fiebig (Talk)
- (4) Advanced DPG-School on Physics: Nanoantennas and Hybrid Quantum Systems, Bad Honnef (Germany), September 25<sup>th</sup>-30<sup>th</sup> 2011: Nonlinear Optical Spectroscopy of Metamaterials, M. Gentile, M. Hentschel, R. Taubert, H. Guo, H. Giessen, and M. Fiebig (Poster)
- (3) DPG conference, Regensburg (Germany), March 21<sup>st</sup>-26<sup>th</sup> 2010: Nonlinear Optical Spectroscopy of Metamaterials, M. Gentile, R. Taubert, M. Hentschel, H. Giessen, and M. Fiebig, (Poster)
- (2) DPG conference, Dresden (Germany), March 22<sup>nd</sup>-27<sup>th</sup> 2009: Nonlinear Optical Spectroscopy of Metamaterials, M. Gentile, M. Hentschel, H. Guo, H. Giessen, and M. Fiebig (Talk)
- (1) DPG conference, Berlin (Germany), February 25<sup>th</sup>-29<sup>th</sup> 2008: Transmission of light through subwavelength holes in thin metal films M. Gentile, F. Kalkum, M. Fiebig, and K. Buse (Poster)